CMS physics technical design report, volume II: Physics performance

Chapter 11. MSSM Higgs Bosons

11.1. Introduction

Supersymmetric extensions of the SM [516–520] are strongly motivated by the idea of providing a solution of the hierarchy problem in the Higgs sector. They allow for a light Higgs particle in the context of GUTs [521], in contrast with the SM, where the extrapolation requires an unsatisfactory fine-tuning of the SM parameters. Supersymmetry is a symmetry between fermionic and bosonic degrees of freedom and thus the most general symmetry of the S-matrix. The minimal supersymmetric extension of the SM (MSSM) yields a prediction of the Weinberg angle in agreement with present experimental measurements if embedded in a SUSY–GUT [522, 523]. Moreover, it does not exhibit any quadratic divergences, in contrast with the SM Higgs sector. Owing to the large top quark mass SUSY-GUTs develop electroweak symmetry breaking at the electroweak scale dynamically [524–527]. The lightest supersymmetric particle offers a proper candidate for the Cold Dark Matter content of the universe, if R-parity is conserved. Finally, local supersymmetry enforces gravitational interactions.

In the MSSM two isospin Higgs doublets have to be introduced in order to preserve supersymmetry [525, 528, 529]. After the electroweak symmetry-breaking mechanism, three of the eight degrees of freedom are absorbed by the Z and W gauge bosons, leading to the existence of five elementary Higgs particles. These consist of two CP-even neutral (scalar) particles h, H, one CP-odd neutral (pseudoscalar) particle A, and two charged particles $H^{\pm}$. In order to describe the MSSM Higgs sector one has to introduce four masses M_h, M_H, M_A and $M_{H^{\pm}}$ and two additional parameters, which define the properties of the scalar particles and their interactions with gauge bosons and fermions: the mixing angle β, related to the ratio of the two vacuum expectation values, $\tan\beta = v_2/v_1$, and the mixing angle α in the neutral CP-even sector. Due to supersymmetry there are several relations among these parameters, and only two of them are independent at leading order. In the absence of CP-violation they are usually chosen as M_A and $\tan\beta$. The other Higgs-boson masses and mixing angles are calculable in terms of the other MSSM parameters. Measuring the masses and angles will constitute an important consistency check of the MSSM.

At tree-level the following mass hierarchies hold: $M_h < M_Z$, $M_A < M_H$ and $M_W < M_{H^{\pm}}$. The tree-level bound on M_h receives large corrections from SUSY-breaking effects in the Yukawa sector of the theory. The leading one-loop correction is proportional to m_t^4. The leading logarithmic one-loop term (for vanishing mixing between the scalar top quarks) reads [530–536]

$$\Delta M_h^2 = \frac{3 G_\mu m_t^4}{\sqrt{2}\,\pi^2 \sin^2\beta} \ln\left(\frac{m_{\tilde{t}_1} m_{\tilde{t}_2}}{m_t^2}\right), \tag{11.1}$$

where G_μ is the Fermi constant, and $m_{\tilde{t}_{1,2}}$ are the two stop masses. Corrections of this kind have drastic effects on the predicted value of M_h and many other observables in the MSSM Higgs sector. The higher-order contributions can shift M_h by 50–100% [143, 144, 537–548]. The corrections to the MSSM Higgs boson sector have been evaluated in several approaches. The status of the available calculations can be summarised as follows. For the one-loop part, the complete result within the MSSM is known [530–532, 536, 549–552]. The by far dominant one-loop contribution is the $\mathcal{O}(\alpha_t)$ term due to top and stop loops ($\alpha_t \equiv h_t^2/(4\pi)$, h_t being the top-quark Yukawa coupling). Concerning the two-loop effects, their computation is quite advanced and has now reached a stage such that all the presumably dominant contributions are known [143, 538–543, 545–548, 553–563]. They include (evaluated for vanishing external momenta) the strong corrections, $\mathcal{O}(\alpha_t\alpha_s)$, and Yukawa corrections, $\mathcal{O}(\alpha_t^2)$, to the dominant

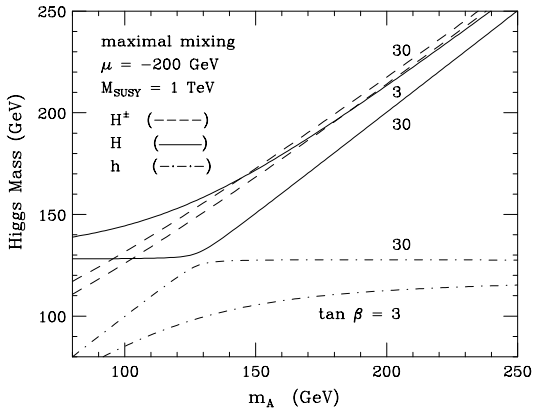

Figure 11.1. The CP-even and charged MSSM Higgs boson masses as a function of M_A for $\tan\beta = 3$ and 30, including radiative corrections [565].

one-loop $\mathcal{O}(\alpha_t)$ term, as well as the strong corrections to the bottom/sbottom one-loop $\mathcal{O}(\alpha_b)$ term ($\alpha_b \equiv h_b^2/(4\pi)$), i.e. the $\mathcal{O}(\alpha_b\alpha_s)$ contribution. The latter can be relevant for large values of $\tan\beta$. For the (s)bottom corrections the all-order resummation of the $\tan\beta$-enhanced terms, $\mathcal{O}(\alpha_b(\alpha_s\tan\beta)^n)$, has also been computed. Finally, the $\mathcal{O}(\alpha_t\alpha_b)$ and $\mathcal{O}(\alpha_b^2)$ corrections have been obtained. The higher-order corrections shift the upper bound of M_h to $M_h \lesssim 135\,\text{GeV}$ [143, 144]. The remaining theoretical uncertainty on M_h has been estimated to be below $\sim 3\,\text{GeV}$[144, 564]. Besides the masses of the Higgs bosons, also their couplings are affected by large higher-order corrections (see below).

An important feature of the MSSM Higgs sector is that for large pseudoscalar masses M_A the light scalar Higgs mass reaches its upper bound and becomes SM-like. Moreover, for large values of $\tan\beta$ the down(up)-type Yukawa couplings are strongly enhanced (suppressed) apart from the region, where the light (heavy) scalar is at its upper (lower) mass bound. The radiatively corrected Higgs masses are depicted in Fig. 11.1.

The LEP experiments have searched for the MSSM Higgs bosons via the Higgs-strahlung process $e^+e^- \to Z + h/H$ and the associated production $e^+e^- \to A + h/H$ for the neutral Higgs particles and $e^+e^- \to H^+H^-$ for the charged Higgs bosons. Neutral Higgs masses $M_A \lesssim 91.9\,\text{GeV/c}^2$ and $M_{h/H} \lesssim 91\,\text{GeV/c}^2$ are excluded [566] as well as charged Higgs masses $M_{H^\pm} \lesssim 78.6\,\text{GeV/c}^2$ [567].

The lightest Higgs boson h will mainly decay into $b\bar{b}$ and $\tau^+\tau^-$ pairs, since its mass is below $\sim 135\,\text{GeV/c}^2$, see Fig. 11.2a. Close to its upper bound in mass all decay modes as for the SM Higgs boson open up rapidly. For large values of $\tan\beta$ the heavy scalar and pseudoscalar Higgs particles H, A will decay predominantly into $b\bar{b}$, $\tau^+\tau^-$ pairs, too, due to the enhanced Yukawa couplings for down-type fermions. The branching ratios for the decays into $b\bar{b}$ and $\tau^+\tau^-$ are about 90% and 10% respectively. Other heavy scalar Higgs decay modes as $H \to t\bar{t}$, W^+W^-, ZZ, hh, AA develop sizeable branching ratios only for small values of $\tan\beta$ (see Fig. 11.2b) and analogously the pseudoscalar Higgs decays $A \to t\bar{t}$, gg, Zh (see Fig. 11.2c). The charged Higgs bosons decay mainly into $\tau\nu_\tau$ pairs for $M_{H^\pm} \lesssim 180\,\text{GeV/c}^2$ and into tb final states above (see Fig. 11.2d). All other decay modes do not acquire branching ratios larger than a few per cent. The (SUSY–)QCD [385–391, 549, 562, 568] and (SUSY–)electroweak corrections [392–395, 568, 569] to the fermionic decay modes are sizeable. In addition to the usual large QCD corrections, significant corrections arise from

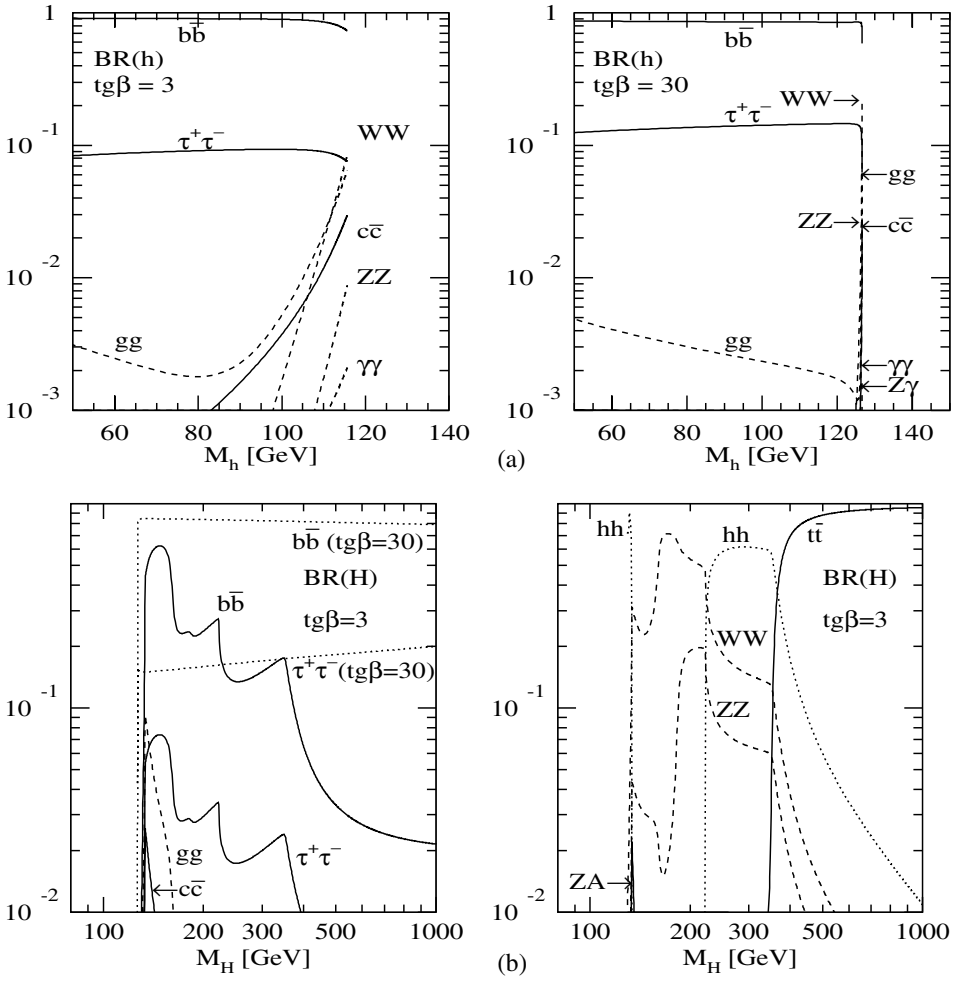

Figure 11.2. Branching ratios of the MSSM Higgs bosons h, H, A, $H^{\pm}$ for non-SUSY decay modes as a function of the masses for two values of $\tan\beta = 3$, 30 and maximal mixing. The common squark mass has been chosen as $M_S = 1\,\mathrm{TeV/c^2}$. The other SUSY–parameters have been chosen as $M_2 = m_{\tilde{g}} = \mu = 1$ TeV/c^2 and $A_{t,b} = 2783\,(2483)\,\mathrm{TeV/c^2}$ for $\tan\beta = 3(30)$. (Continued on next page.)

virtual sbottom/stop and gluino/gaugino exchange contributions in the h, H, $A \to b\bar{b}$ and $H^{\pm} \to tb$ decay modes [549,562,568,569]. The dominant part of the latter corrections can be absorbed in improved bottom Yukawa couplings. In this way these contributions can also be resummed up to all orders thus yielding reliable perturbative results [560,563]. The rare photonic decay modes h, H, $A \to \gamma\gamma$ are mediated by W, t, b loops as in the SM Higgs case and additional contributions from charged Higgs bosons, charginos and sfermions, if these virtual particles are light enough [20,369,370]. The QCD corrections to these decay modes can reach a few per cent in the relevant mass regions [396–402]. If decays into supersymmetric particles, i.e. gauginos and sfermions, are possible, they acquire significant branching ratios and can even be the dominant decay modes [20,369,370,570,571]. In contrast to the SM the

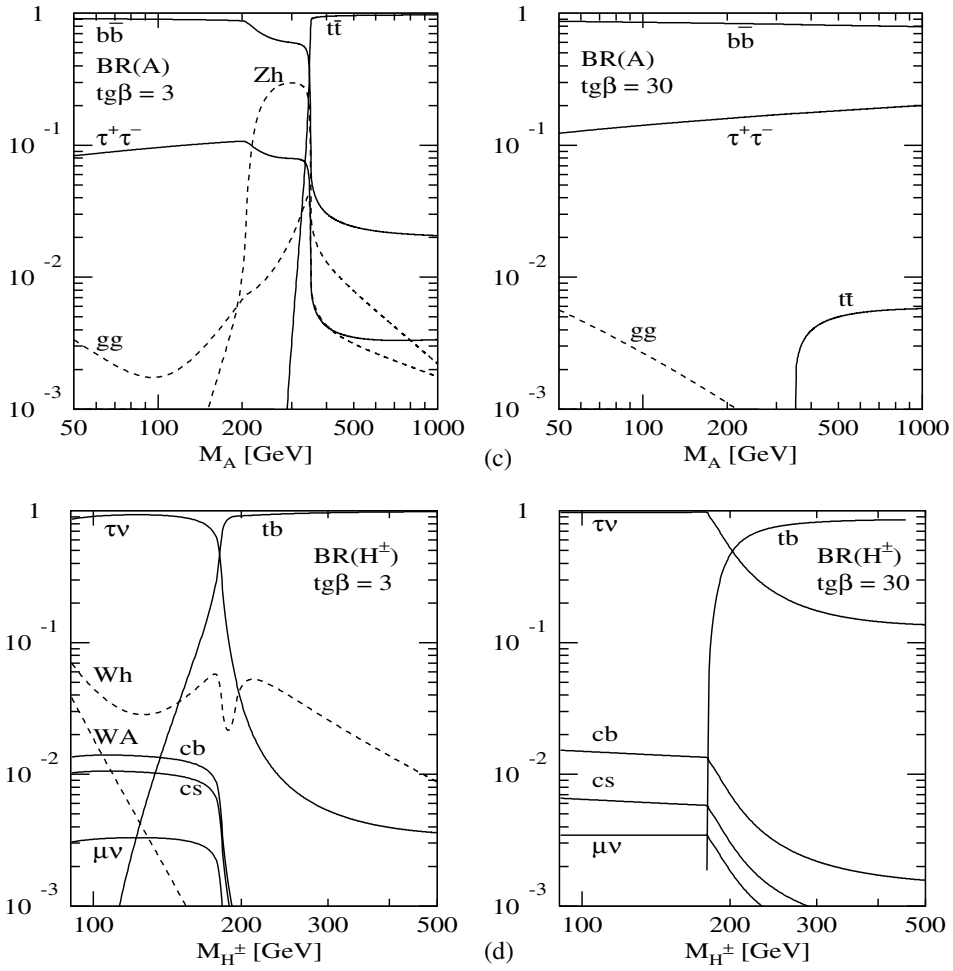

Figure 11.2. Continued.

total widths of the MSSM Higgs bosons do not exceed several tens of GeV, so that the MSSM Higgs particles appear as narrow resonances.

The dominant neutral MSSM Higgs production mechanisms for small and moderate values of $\tan\beta$ are the gluon fusion processes

$$gg \to h, H, A$$

which are mediated by top and bottom loops as in the SM case, but in addition by stop and sbottom loops for the scalar Higgs bosons h, H, if the squark masses are below about $400\,\mathrm{GeV}/c^2$ [572]. The NLO QCD corrections to the quark loops are known in the heavy quark limit as well as including the full quark mass dependence [409–411, 413–416]. They increase the cross sections by up about 100% for smaller $\tan\beta$ and up to about 40% for very large $\tan\beta$, where the bottom loop contributions become dominant due to the strongly enhanced bottom Yukawa couplings. The limit of heavy quarks is only applicable for $\tan\beta \lesssim 5$ within about 20–25%, if full mass dependence of the LO terms is taken into

account [20,369,370,412]. Thus the available NNLO QCD corrections in the heavy quark limit [417–420] can only be used for small and moderate $\tan\beta$, while for large $\tan\beta$ one has to rely on the fully massive NLO results [409–411]. The QCD corrections to the squark loops are only known in the heavy squark limit [572] and the full SUSY–QCD corrections in the limit of heavy squarks and gluinos [573–576]. The pure QCD corrections are of about the same size as those to the quark loops thus rendering the total K factor of similar size as for the quark loops alone with a maximal deviation of about 10% [572]. The pure SUSY–QCD corrections are small [573–576]. The NNLL resummation of the SM Higgs cross section [421] can also be applied to the scalar MSSM Higgs cross sections in the regions, where the heavy quark and squark limits are valid. The same is also true for the NLO QCD corrections to the p_T distributions [428–432] and the NNLL resummation of soft gluon effects [433–443], i.e. for small values of $\tan\beta$, M_H and p_T only. However, for large values of $\tan\beta$ the p_T distributions are only known at LO, since the bottom loops are dominant and the heavy top limit is not valid. An important consequence is that the p_T distributions of the neutral Higgs bosons are softer than for small values of $\tan\beta$ [577].

The vector-boson fusion processes [449,451]

$$pp \to qq \to qq + WW/ZZ \to qq + h/H$$

play an important role for the light scalar Higgs boson h close to its upper mass bound, where it becomes SM-like, and for the heavy scalar Higgs particle H at its lower mass bound. In the other regions the cross sections are suppressed by the additional SUSY-factors of the Higgs couplings. The NLO QCD corrections to the total cross section and the distributions can be taken from the SM Higgs case and are of the same size [452,453]. The SUSY–QCD corrections mediated by virtual gluino and squark exchange at the vertices turned out to be small [578].

Higgs-strahlung off W, Z gauge bosons [454,455]

$$pp \to q\bar{q} \to Z^*/W^* \to H + Z/W$$

does not play a major role for the neutral MSSM Higgs bosons at the LHC. The NLO [456] and NNLO [457] QCD corrections are the same as in the SM case, and the SUSY–QCD corrections are small [578]. The SUSY–electroweak corrections are unknown.

Higgs radiation off top quarks [459–463]

$$pp \to q\bar{q}/gg \to h/H/A + t\bar{t}$$

plays a significant role at the LHC for the light scalar Higgs particle only. The NLO QCD corrections are the same as for the SM Higgs boson with modified top and bottom Yukawa couplings and are thus of moderate size [162,464,465]. The SUSY–QCD corrections have been computed recently for the light scalar case [579]. They are of moderate size.

For large values of $\tan\beta$ Higgs radiation off bottom quarks [459–463]

$$pp \to q\bar{q}/gg \to h/H/A + b\bar{b}$$

constitutes the dominant Higgs production process. The NLO QCD corrections can be taken from the analogous calculation involving top quarks. However, they turn out to be very large [580,581]. The main reason is that the integration over the transverse momenta of the final state bottom quarks generates large logarithmic contributions. The resummation of the latter requires the introduction of bottom quark densities in the proton, since the large logarithms are related to the DGLAP-evolution of these densities. Their DGLAP-evolution

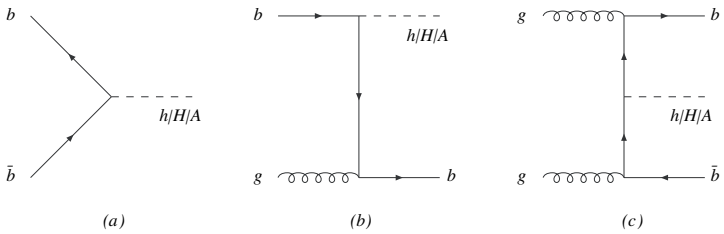

Figure 11.3. Typical diagrams for all Higgs boson production mechanisms related to Higgs radiation off bottom quarks at leading order: (a) $b\bar{b} \to h/H/A$, (b) $gb \to b + h/H/A$, (c) $gg \to b\bar{b} + h/H/A$.

resums them. This leads to an approximate approach starting from the process [582] (see Fig. 11.3a)

$$pp \to b\bar{b} \to h/H/A$$

at LO, where the transverse momenta of the incoming bottom quarks, their masses and their off-shellness are neglected. The NLO [583,584] and NNLO [585] QCD corrections to this bottom-initiated process are known and of moderate size, if the running bottom Yukawa coupling at the scale of the Higgs mass is introduced. At NNLO the full process $gg \to h/H/A + b\bar{b}$ (see Fig. 11.3c) contributes for the first time. At this order a proper matching to the fully massive result for this process can be performed [586,587] so that the final expression provides an improved result, which takes into account the resummation of the large logarithms and mass effects. The fully exclusive $gg \to h/H/A + b\bar{b}$ process, calculated with four active parton flavours in a fixed flavour number scheme (FFNS), and this improved resummed result, calculated with 5 active parton flavours in the variable flavour number scheme (VFNS), will converge against the same value at higher perturbative orders. The best agreement between the NLO FFNS and NNLO VFNS is achieved, if the factorisation scale of the bottom quark densities is chosen as about a quarter of the Higgs mass [588,589]. If only one of the final state bottom jets accompanying the Higgs particle is tagged, the LO bottom-initiated process is $gb \to b + h/H/A$ (see Fig. 11.3b), the NLO QCD corrections of which have been calculated [589,590]. They turn out to reach $\mathcal{O}(40-50\%)$. The situation concerning the comparison with the FFNS at NLO is analogous to the total cross section. Agreement within the respective theoretical uncertainties is found for a factorisation scale of about a quarter of the Higgs mass [588]. If both bottom jets accompanying the Higgs boson in the final state are tagged, one has to rely on the fully exclusive calculation for $gg \to b\bar{b} + h/H/A$.

All neutral MSSM Higgs production cross sections including the NLO QCD corrections are shown in Fig. 11.4.

The dominant charged Higgs production process is the associated production with heavy quarks [591–593] (see Fig. 11.5a)

$$pp \to q\bar{q}, gg \to H^- + t\bar{b} \qquad \text{and c.c.}$$

The NLO QCD and SUSY–QCD corrections have very recently been computed [594]. They are of significant size due to the large logarithms arising from the transverse-momentum integration of the bottom quark in the final state and the large SUSY–QCD corrections to the bottom Yukawa coupling. The large logarithms can be resummed by the introduction of bottom quark densities in the proton in complete analogy to the neutral Higgs case. In this

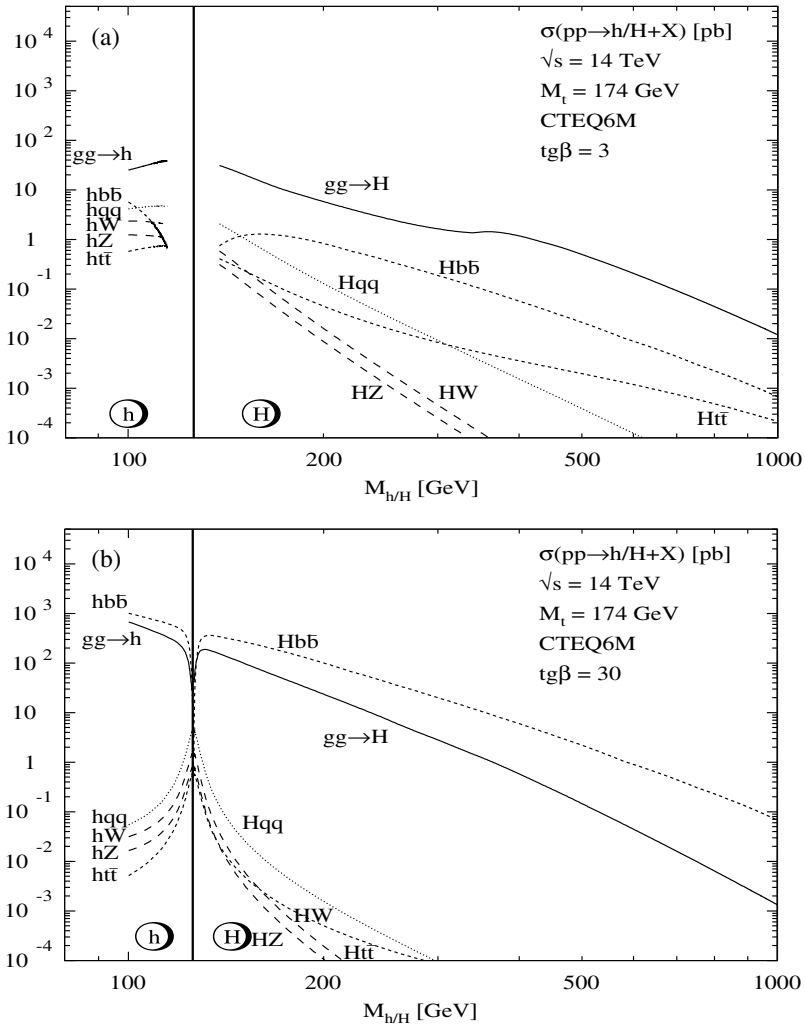

Figure 11.4. Neutral MSSM Higgs production cross sections at the LHC for gluon fusion $gg \to \Phi$, vector-boson fusion $qq \to qqVV \to qqh/qqH$, Higgs-strahlung $q\bar{q} \to V^* \to hV/HV$ and the associated production $gg, q\bar{q} \to b\bar{b}\Phi/t\bar{t}\Phi$, including all known QCD corrections. (a) h, H production for $\tan\beta = 3$, (b) h, H production for $\tan\beta = 30$, (c) A production for $\tan\beta = 3$, (d) A production for $\tan\beta = 30$. The same parameters as in Fig. 11.2 have been adopted. (Continued on next page.)

approach the LO process is $gb \to H^- t$ and the charge conjugate. The NLO SUSY–QCD corrections have been derived in [595–598] and found to be of significant size. This process, however, relies on the same approximations as all bottom-initiated processes. A quantitative comparison of the processes $gb \to H^- t$ and $gg \to H^- + t\bar{b}$ at NLO is missing so far.

The second important charged Higgs production process is charged Higgs pair production in a Drell–Yan type process (see Fig. 11.5b)

$$pp \to q\bar{q} \to H^+ H^-$$

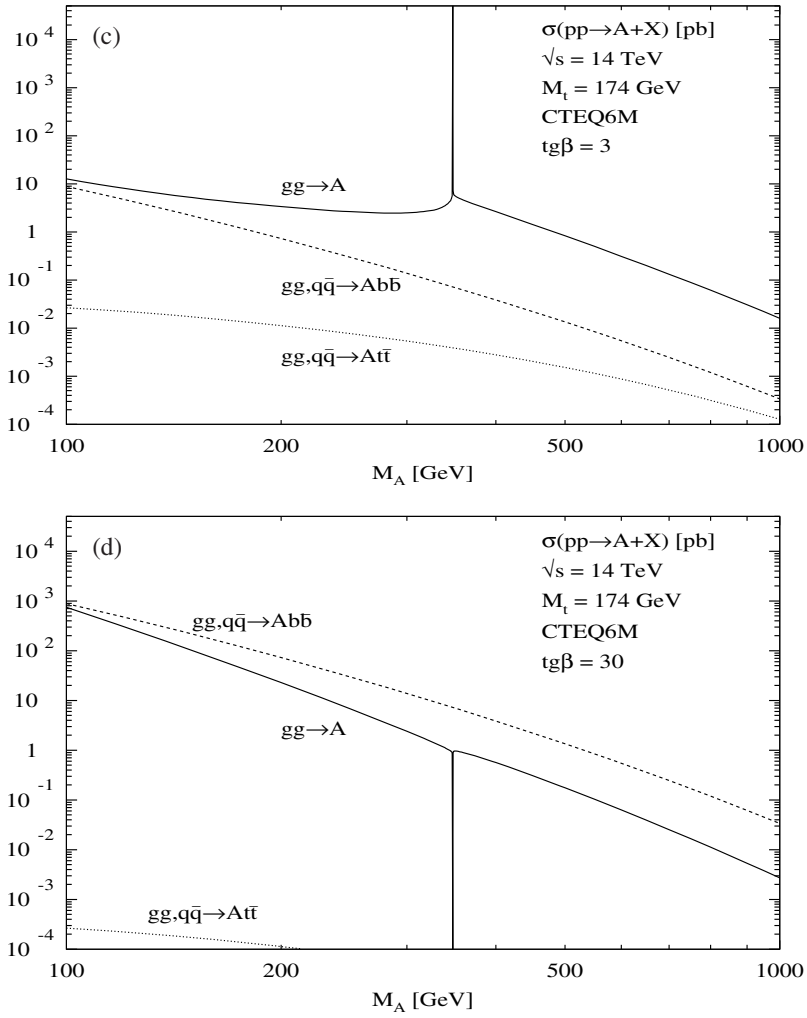

Figure 11.4. Continued.

which is mediated by s-channel photon and Z-boson exchange. The NLO QCD corrections can be taken from the Drell–Yan process and are of moderate size as in the case of the neutral Higgs-strahlung process discussed before. The genuine SUSY–QCD corrections, mediated by virtual gluino and squark exchange in the initial state, are small [578].

Charged Higgs pairs can also be produced from gg initial states by the loop-mediated process [599–603] (see Fig. 11.5c)

$$pp \to gg \to H^+H^-$$

where the dominant contributions emerge from top and bottom quark loops as well as stop and sbottom loops, if the squark masses are light enough. The NLO corrections to this process are unknown. This cross section is of similar size as the bottom-initiated process [603] (see Fig. 11.5e)

$$pp \to b\bar{b} \to H^+H^-$$

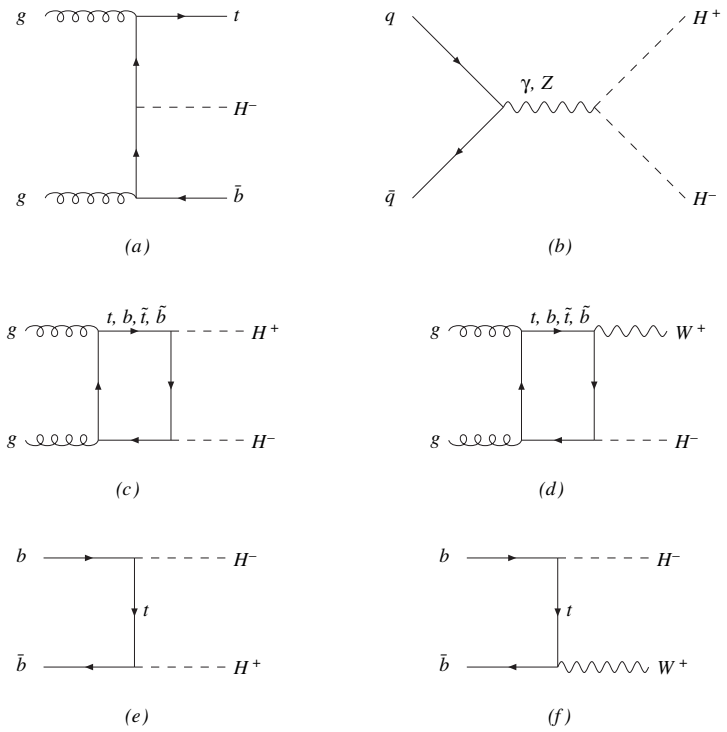

Figure 11.5. Typical diagrams for charged Higgs boson production mechanisms at leading order: (a) $gg \to H^- t\bar{b}$, (b) $q\bar{q} \to H^+H^-$, (c) $gg \to H^+H^-$, (d) $gg \to W^+H^-$, (e) $b\bar{b} \to H^+H^-$, (f) $b\bar{b} \to W^+H^-$.

which relies on the approximations required by the introduction of the bottom densities as discussed before and is known at NLO [604]. The SUSY–QCD corrections are of significant size. The pure QCD corrections and the genuine SUSY–QCD corrections can be of opposite sign.

Finally, charged Higgs bosons can be produced in association with a W boson [605–607] (see Fig. 11.5d)

$$pp \to gg \to H^+W^- \qquad \text{and c.c.}$$

which is generated by top-bottom quark loops and stop-sbottom loops, if the squark masses are small enough. This process is known at LO only. The same final state also arises from the process [605, 606, 608] (see Fig. 11.5f)

$$pp \to b\bar{b} \to H^+W^- \qquad \text{and c.c.}$$

which is based on the approximations of the VFNS. The QCD corrections have been calculated and turn out to be of moderate size [609, 610].

11.2. Higgs boson channels

11.2.1. Associated $b\bar{b}H$ production with $H \to \tau\tau \to e^{\pm}\mu^{\mp} + E_{\mathrm{T}}^{\mathrm{miss}}$

Compared to the hadronic and semi-leptonic final states described in Section 5.2, the fully leptonic final states are suppressed by relatively small branching ratio $\mathrm{BR}(\tau \to \mu\nu\nu) \sim 0.174$ and $\mathrm{BR}(\tau \to e\nu\nu) \sim 0.178$, but the signal is clean and easy to trigger.

The signal consists of events in which the Higgs boson decays into two tau leptons which in turn decay leptonically. Two possibilities exist, either to select any-two-lepton final states, which have larger signal rate, or electron + muon final states for which the background is easier to suppress. Here the electron + muon final state is chosen.

The main backgrounds for $H/A \to \tau\tau$ with $e\mu$ final state are the Drell–Yan $\tau\tau$ production, the $t\bar{t}$ and the Wt production where the W boson coming from top quark decay decays leptonically, the $\tau\tau b\bar{b}$ production, and the $b\bar{b}$ background with b quarks decaying semi-leptonically. Other backgrounds are pairs of vector bosons WW or WZ decaying into leptonic final states, but their contribution is small. The $\tau\tau c\bar{c}$ background is also found negligible. The most biggest background arises from those $t\bar{t}$ and Drell–Yan events which involve genuine τ's and b jets and produce events very similar to the signal. No SUSY particle background is assumed.

A detailed description of the analysis can be found in [611].

11.2.1.1. Event generation. The Higgs boson signal is generated with PYTHIA [246]. The signal cross sections and branching ratios are calculated with FEYNHIGGS [142]. TAUOLA package [155] is used for leptonic τ decays in the signal events.

The Drell–Yan $\tau\tau$ production, $b\bar{b}$, WW, WZ and ZZ backgrounds are generated with PYTHIA. The Drell–Yan $\tau\tau$ next-to-leading order cross section of 1891 pb calculated with the program MCFM [56] for $M_{\tau\tau} > 80\,\mathrm{GeV/c^2}$ is used. The $\tau\tau b\bar{b}$ background is generated with COMPHEP [43] with no p_T and η cuts applied on b quarks and the leading order cross section calculated with COMPHEP are used. The Z/γ^* generation is split into two bins of generated $\tau\tau$ mass $m_{\tau\tau}$: 80–100 $\mathrm{GeV/c^2}$ and $> 100\,\mathrm{GeV/c^2}$, and the $\tau\tau b\bar{b}$ is generated in the $\tau\tau$ mass bins of 60–100 $\mathrm{GeV/c^2}$ and $> 100\,\mathrm{GeV/c^2}$.

The $t\bar{t}$ background is generated with TOPREX [44] and PYTHIA and the single top (Wt) events are generated with TOPREX. A cross section of 840 and 60 pb is used for $t\bar{t}$ and Wt events, respectively.

11.2.1.2. Level-1 and HLT selections. The events are triggered with the single and the double electron and muon triggers. The p_T threshold for single muons is 19 GeV/c, for single electrons 26 GeV/c, for double muons 7 GeV/c and for double electrons 14.5 GeV/c. The Level 1 trigger efficiency for the signal of $M_A = 200\,\mathrm{GeV/c^2}$ is 0.96, and the overall trigger efficiency including the HLT is 0.82. The corresponding trigger efficiencies for the Drell–Yan $\tau\tau$, the $\tau\tau b\bar{b}$, the $t\bar{t}$ and the Wt backgrounds are 0.18, 0.29, 0.68 and 0.68, respectively.

In the future also a combined e+mu trigger with symmetric thresholds of 10 GeV/c for the electron and muon will be included. No large gain is expected since events passing e+mu trigger are most probably already triggered by the single muon trigger.

11.2.1.3. Offline selections. The basic event selection is a requirement of two isolated leptons (one e and one μ) with $p_T > 20\,\mathrm{GeV/c}$ in the central detector acceptance region $|\eta| < 2.5$ coming from a reconstructed primary vertex (PV). The electron candidates are required to pass electron identification cuts described in [156]. The efficiency for the electron identification is about 90% for electrons passing the trigger. The leptons are defined isolated when there are no other tracks from the primary vertex with $p_T > 1\,\mathrm{GeV/c}$ within a cone $\Delta R = \sqrt{\Delta\varphi^2 + \Delta\eta^2} \leqslant 0.4$ around the lepton. The p_T cut and the isolation reduce efficiently the backgrounds with soft leptons ($b\bar{b}$, $c\bar{c}$, ..).

The b jets associated with the Higgs boson provide a powerful tool to separate the $b\bar{b}H/A$ events from the Drell–Yan background. The Drell–Yan background in which Z/γ^* decay into a tau pair has a large cross section compared to the Higgs production. However, these

events are mostly produced with no associated jets, and if they have associated jets they are mostly light quark and gluon jets. Therefore the Drell–Yan background can be suppressed by requiring a reconstructed jets present in the event, and even further by requiring that the associated jets are identified as b jets. The b jets associated with the Higgs bosons are generally very soft, which makes their tagging a challenging task. For low jet E_T values the track multiplicity and momenta tend to be low, and many jets do not have enough significant tracks to be identified as a b jet. As a consequence the b tagging efficiency is not very high. The b tagging efficiency of 43% per jet for the signal events with 2% of the mistagging rate is found.

The $t\bar{t}$ background cannot be suppressed with b tagging due the presence of two energetic genuine b jets in the event. In fact, the jet reconstruction and the b-tagging efficiencies are higher for b jets in $t\bar{t}$ events than for those associated with the signal. This can be exploited using a central jet veto: if more than one jet is found, the event is rejected. The threshold of 20 GeV is set on the calibrated E_T for the jets within the tracker acceptance region, $|\eta| < 2.5$. A suppression factor of 8 is obtained against the $t\bar{t}$ background with an efficiency of 60% for the signal.

A missing energy measurement is needed for estimating the fraction of the energy carried away by neutrinos. This information is used in the Higgs boson mass reconstruction. The amount of missing transverse energy is small and close to the detector resolution.

The τ's from the Higgs boson with $M_A = 200\,\mathrm{GeV/c^2}$ travel on average about 5 mm before they decay. Therefore the leptons coming from τ decays are displaced relative to the primary vertex [612]. The track impact parameter measurements in the transverse plane for the two leptons are combined quadratically into one variable $\sigma_{ip} = \sigma_{ip}(\tau_1) \oplus \sigma_{ip}(\tau_2)$, where $\sigma_{ip}(\tau_1, \tau_2)$ are significances of the lepton impact parameters. The leptons in $t\bar{t}$ background come mostly from W decays. The $t\bar{t}$ events with two intermediate τ's cannot be suppressed by using impact parameter.

The neutrinos-charged lepton collinear approximation method for the mass reconstruction in $H/A \to \tau\tau$ is described in section 5.2.5. The mass reconstruction is possible when the two leptons are not in a back-to-back configuration. The back-to-back events are removed with a cut on the angle between the two leptons in the transverse plane $\Delta\varphi(e, \mu) < 175^\circ$. Uncertainties of the missing transverse energy measurement can lead to negative neutrino energies. For the signal $\sim 40\%$ of events are lost when the positive neutrino energies are required. This requirement, however, yields a further suppression of the $t\bar{t}$ and Wt backgrounds, since for these backgrounds the neutrinos are generally not emitted along the lepton directions. The efficiencies of $E_{\nu 1,\nu 2} > 0$ cut for these backgrounds are about 17% and 15%, respectively. The reconstructed $\tau\tau$ mass with $30\,\mathrm{fb}^{-1}$ after all selections, but the mass window, is shown in Fig. 11.6. In the figure the signal of $M_A = 140$, $\tan\beta = 20$ and $200\,\mathrm{GeV/c^2}$, $\tan\beta = 25$ in the m_h^{max} scenario and the backgrounds are presented.

11.2.1.4. Expected number of events. Table 11.1 shows the cross section times branching ratio for the backgrounds for each step of the selections. The signal cross sections for $M_A = 140, 200$ and $250\,\mathrm{GeV/c^2}$ and $\tan\beta = 20$ in the m_h^{max} scenario are shown in Table 11.2. The expected number of events with $30\,\mathrm{fb}^{-1}$ after all cuts, but mass window, is also shown in Tables 11.1 and 11.2. The expected number of events after all cuts including the mass window is shown for the signal and the total background in Table 11.3.

11.2.1.5. Systematic uncertainties and the discovery reach. The uncertainty of the event selection efficiency is related to the uncertainty of the lepton identification efficiency, the jet

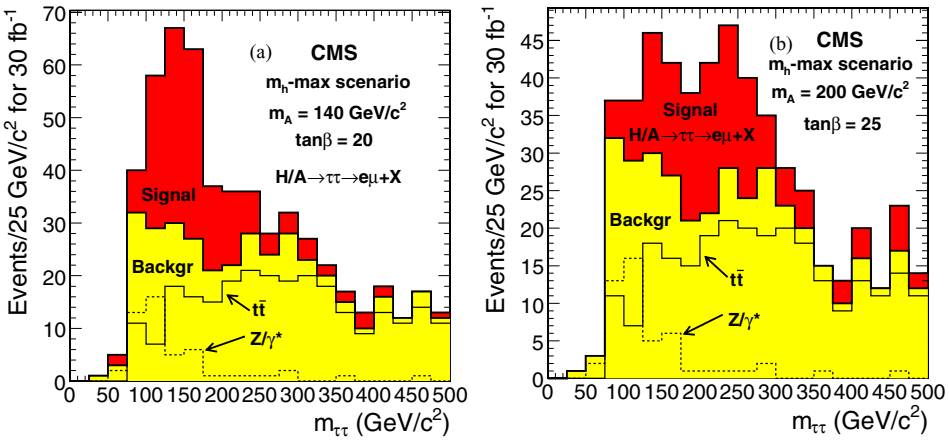

Figure 11.6. The $\tau\tau$ reconstructed mass with 30 fb^{-1} after all selections, but the mass window. The signal in the m_h^{max} scenario and the backgrounds are shown for (a) $M_A = 140\,GeV/c^2$, $\tan\beta = 20$ and (b) $M_A = 200\,GeV/c^2$ and $\tan\beta = 25$.

Table 11.1. The background cross section times branching ratio (in pb) for each step of the selections. The expected number of events at 30 fb^{-1} is also shown.

	Z,γ^*	bbZ,γ^*	tt	tW	bb	VV
$\sigma \times BR$	233.1	3.422	86.2	6.16	36170	7.88
Level 1	83.9	1.85	72.2	5.37	811	5.16
HLT	42.6	0.981	53.7	4.17	78.0	4.10
reconstructed PV	40.8	0.952	53.3	4.11	78.1	3.92
isol e + μ,p_T cut	1.10	0.0270	5.65	0.452	0.0378	0.288
$Q_e + Q_\mu = 0$	1.09	0.0268	5.62	0.451	0.0374	0.248
$\sigma_{ip}(e) \oplus \sigma_{ip}(\mu)$	0.296	0.00745	0.791	0.0550	0.0254	0.0255
N jets > 0	0.0127	0.00527	0.778	0.0509	0.00654	0.0115
b tagging	0.00457	0.00289	0.608	0.0341	0.00312	0.000547
jet veto	0.00344	0.00124	0.0745	0.0166	0.000179	0.000265
$\Delta\varphi(e, \mu)$	0.00295	0.00116	0.0696	0.0159	0.000142	0.000259
$E_{\nu 1,\nu 2} > 0$	0.00124	0.000486	0.0119	0.00246	0.0000661	0.0000546
N_{ev} at 30 fb^{-1}	37.1	14.6	355.8	73.7	2.0	1.6

energy and the missing energy scale and the b tagging efficiency. The jet energy and the missing energy scale uncertainty gives the uncertainty of 7.3% on the $t\bar{t}$ background, which is the dominant background. The uncertainty of the lepton identification efficiency of 2% is used for both electrons and muons. The uncertainty of the b tagging efficiency, 5%, can be estimated from $t\bar{t}$ events as in Ref. [83]. The 5% uncertainty of the mistagging efficiency is assumed [613]. The 5.8% uncertainty of the theoretical prediction of the $t\bar{t}$ cross section is taken. The total systematic uncertainty including the luminosity uncertainty 3% yields a 12% uncertainty for the total background.

The signal significance S with 30 fb^{-1} for the signal of $M_A = 140$, 200 and 250 GeV/c^2 and $\tan\beta = 20$ in the m_h^{max} scenario is shown in Table 11.2 without and with the background systematic uncertainty taken into account. Figure 11.7 shows the discovery reach in the $M_A - \tan(\beta)$ plane in the m_h^{max} scenario with 30 fb^{-1}. The lower (upper) curve corresponds to the case when the background systematic uncertainty is not taken (taken) into account.

Table 11.2. The signal cross section times branching ratio (in pb) for $M_A = 140$, 200 and 250 GeV/c^2 and $\tan\beta = 20$ in the m_h^{max} scenario for each step of the selections. The expected number of events at 30 fb^{-1} is also shown.

m_A	140	200	250
$\sigma \times BR$ (pb)	3.468	1.123	0.493
L1	3.238	1.079	0.479
HLT	2.585	0.923	0.419
reconstructed PV	2.434	0.866	0.395
isol $e^+\mu$, p_T cut	0.258	0.116	0.0613
$Q_e + Q_\mu = 0$	0.256	0.116	0.0612
$\sigma_{ip}(e) \oplus \sigma_{ip}(\mu)$	0.0859	0.044	0.0260
N jets > 0	0.0375	0.0216	0.0130
b tagging	0.0177	0.0104	0.00649
jet veto	0.0115	0.00619	0.00390
$\Delta\varphi(e, \mu)$	0.0106	0.00554	0.00351
$E_{\nu 1,\nu 2} > 0$	0.00601	0.00340	0.00222
N_{ev} at 30 fb^{-1}	180	102	67

Table 11.3. The expected number of the signal plus background and the background events in a given mass windows for 30 fb^{-1} and the signal significance S without and with the background systematic uncertainty taken into account.

	$\Delta m_{\tau\tau}$	N_S+N_B	N_B	$S_{no\,syst.}$	$S_{syst.}$
$m_A = 140$ GeV/c^2, $\tan\beta = 20$	100–200 GeV/c^2	225	107	9.9	7.3
$m_A = 200$ GeV/c^2, $\tan\beta = 20$	140–250 GeV/c^2	163	109	4.8	3.1
$m_A = 250$ GeV/c^2, $\tan\beta = 20$	160–380 GeV/c^2	244	204	2.7	1.4

11.2.2. Associated $b\bar{b}H$ production with $H \to \mu^+\mu^-$

The Higgs boson production in association with b quarks, $pp \to b\bar{b}\phi$ ($\phi = h, H, A$) followed by the $\phi \to \mu\mu$ decay can provide the best measurement for the mass and width of the heavy MSSM Higgs bosons H and A. At high $\tan\beta$ the natural width, sensitive to the $\tan\beta$ value, is comparable or dominates the dimuon mass experimental resolution, thus the measured width can be used to constrain the $\tan\beta$.

This analysis uses the dimuon trigger (Level-1 and HLT) stream. Despite of the small $\phi \to \mu\mu$ branching ratio ($\simeq 10^{-4}$) the precise measurement of the dimuon mass in off-line provides an excellent possibility to suppress the $t\bar{t}$ background. The associated Higgs boson production with b quarks is exploited to suppress the huge Drell–Yan $\mu\mu$ background using the b tagging. Irreducible background from $\mu\mu b\bar{b}$ process was also considered and found to be small.

The analysis was performed in the m_h^{max} scenario for three regions of M_A:

- the so-called decoupling regime, $M_A \gg M_h$, where $M_A \sim M_H$. The Higgs bosons A and H with $M_{A(H)} \geqslant 150$ GeV/c^2 and $\tan\beta \geqslant 15$ were generated.
- the "intensive-coupling regime" $M_A \sim M_h$ defined in [614, 615], where the three neutral Higgs bosons have comparable masses, $M_A \simeq M_H \simeq M_h$ The h, A and H bosons were generated for three mass points of $M_A = 125$, 130 and 135 GeV/c^2 at $\tan\beta = 30$.
- the low M_A regime, $M_A < M_h$, where $M_A \sim M_h$. The Higgs bosons h and A were generated at $M_A = 100$ GeV/c^2 and $\tan\beta \geqslant 20$ points.

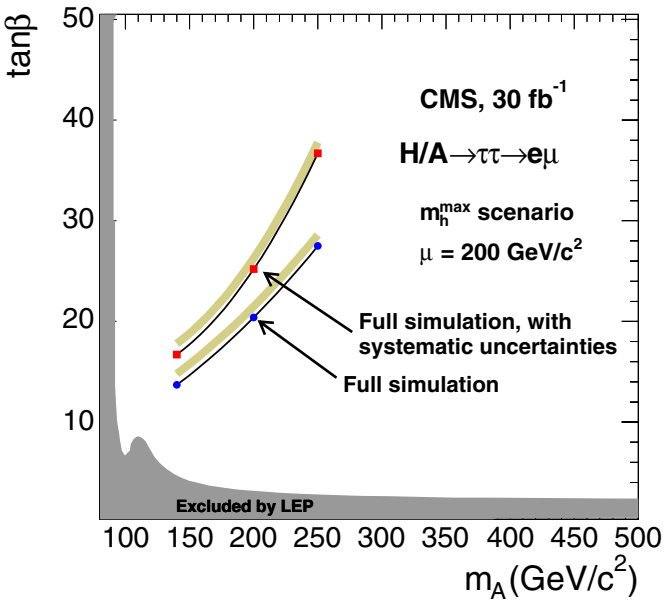

Figure 11.7. The discovery region for $gg \to b\bar{b}H/A, H/A \to \tau\tau \to e\mu + X$ channel in M_A-tan β in the m_h^{max} scenario with 30 fb^{-1}.

11.2.2.1. Event generation. The Higgs boson production $pp \to b\bar{b}\phi$ and decay was generated with PYTHIA for the decoupling and low M_A regimes. For the "intensive-coupling regime" events were generated by COMPHEP as described in [615]. The Higgs boson production cross section and branching ratio were evaluated using FeynHiggs 2.3.2 [142–144]. The mass relations between A, H and h bosons and widths were obtained with HDECAY [41] for the "intensive-coupling regime".

The Drell–Yan and $t\bar{t}$ backgrounds were generated with PYTHIA. The Drell–Yan events with b quarks in the final state were excluded to avoid double counting with $\mu\mu b\bar{b}$ background generated with COMPHEP.

11.2.2.2. Offline selection.

Muon identification. The signal is characterised by two well reconstructed, isolated muons. Therefore the event is accepted if there are at least two muons, with opposite charge, both satisfying the following conditions:

- muon transverse momentum $p_T > 20\,GeV/c$;
- a cone of $\Delta R = \sqrt{\Delta\eta^2 + \Delta\phi^2} = 0.35$ is defined around the reconstructed muon track. Then the variable E_{iso} is evaluated as the sum of the energies measured by all the detectors (tracker, ECAL, HCAL) inside this cone with muon momentum excluded. The muon is defined *isolated* if $E_{iso} < 10\,GeV$.

Rejection of $t\bar{t}$ background. The rejection of $t\bar{t}$ events is based on two selection cuts and exploits the presence of the neutrino in the top decay chain and of two well reconstructed energetic jets.

The event is accepted if the following conditions are satisfied:

- the missing transverse energy is less than 40 GeV;
- the jets, reconstructed with the Iterative Cone Algorithm [314], must have transverse energy less than 45 GeV and $|\eta| < 5.0$.

B tagging. The presence of b jets in the Higgs boson production is exploited to suppress Drell–Yan $\mu\mu$ background, which otherwise be dominant, especially for dimuon invariant masses below 200 GeV/c^2.

The b quarks in signal events are mainly produced in the forward region, with lower p_T with respect to the b quarks coming from $t\bar{t}$ background.

Two different strategies, based on two distinct cuts, have been developed for the b tagging:

1. The event must contain at least one jet tagged as b jet with the Combined B-Tagging algorithm [616]. This algorithm has been designed to tag mainly central b jets of high transverse energy, thus it is not optimised for the b jets of the signal. In the following this cut will be refereed to as *hard b-tag*.
2. The tracks in the event are classified as *good tracks* if they satisfy:
   - at least 6 hits in the tracker of which at least two belonging to the pixel detectors;
   - transverse momentum $p_T > 2.4$ GeV/c;
   - pseudorapidity $|\eta| < 2.4$;
   - transverse impact parameter IP < 0.5 cm;
   - track fit quality $\chi^2/ndf < 5$.

   The event must contain at least two good tracks with transverse impact parameter (IP) in the range $0.01 < IP < 0.1$ cm (only one track if $0.02 < IP < 0.075$ cm).

The first strategy consists on applying selection 1) only. The second strategy is the logical OR between selection 1) and 2) (this strategy will be refereed to as *soft b-tag*).

Results have been calculated for both selections and the one with the best signal significance has been considered.

11.2.2.3. Fitting procedure. Figure 11.8 shows the distribution of reconstructed dimuon invariant mass after all selections for the backgrounds and, as an example, for the signal of $M_A = 150$ GeV/c^2 and $\tan\beta = 40$. The plot has been obtained assuming an integrated luminosity of 30 fb^{-1} and the hard b-tag. The signal is visible as a peak over a background that exponentially decreases with increasing $M_{\mu\mu}$.

The background is estimated by fitting the dimuon mass distribution in the off-peak regions, where the signal is not present. To identify this region, the *TSpectrum* class in root is used: this class allows to find a signal peak over a background distribution.

The function used in this analysis to parameterise the background has three free parameters:

$$f_B(M_{\mu\mu}; P_0, P_1, P_2) = P_0 \times \frac{\Gamma_Z}{2\pi\left(\left(M_{\mu\mu} - M_Z\right)^2 + \left(\frac{\Gamma_Z}{2}\right)^2\right)} + P_1 + P_2 \times M_{\mu\mu}. \tag{11.2}$$

After the background parametrisation function is determined by fitting the background in the off-peak region, a binned likelihood fit method, with three free parameters, is applied over the whole $M_{\mu\mu}$ range using the function:

$$f_{tot}(M_{\mu\mu}; M_A, \sigma_{\mu\mu}, \Gamma_A, N_S) = (N_{TOT} - N_S) \times pdf_B(M_{\mu\mu}) + N_S \times V(M_{\mu\mu}; M_A, \sigma_{\mu\mu}, \Gamma_A) \tag{11.3}$$

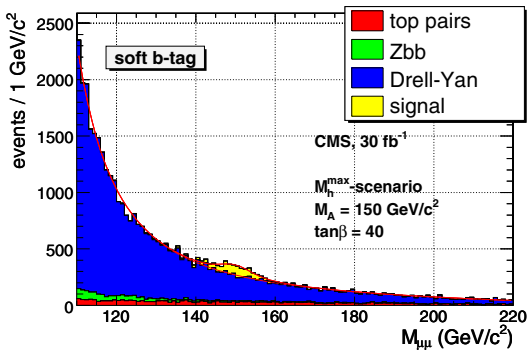

Figure 11.8. Fitting procedure applied to the dimuon reconstruction mass for the main background and for the signal sample with $M_A = 150\,\mathrm{GeV/c^2}$ and $\tan\beta = 40$.

Table 11.4. Effect of the selection cuts on the background and signal cross section (all values in pb). Efficiency w.r.t. previous cut in % is shown in brackets. The *no cut* value for the top pair background refers to the inclusive $t\bar{t}$ production.

	top pairs	Drell–Yan $M_{\mu\mu} > 115\,\mathrm{GeV/c^2}$	Zbb $M_{\mu\mu} > 100\,\mathrm{GeV/c^2}$	signal $\mathrm{M_A} = 130, \tan\beta = 30$
No cuts	840	27.8	1.05	0.309
pre-selection cut	20.9 (2.5)	13.0 (46.8)	0.778 (74.1)	0.245 (79.2)
Level-1	19.8 (94.7)	11.9 (91.3)	0.720 (92.5)	0.226 (92.2)
HLT	17.1 (86.1)	11.8 (99.3)	0.712 (98.9)	0.223 (98.7)
Muon Id	5.23 (30.7)	10.4 (87.9)	0.569 (79.9)	0.183 (81.8)
Missing Et	1.20 (23)	9.51 (91.7)	0.503 (88.4)	0.163 (89.2)
Jet Veto	0.317 (26.4)	8.37 (88.1)	0.418 (83.1)	0.138 (84.5)
Soft b-tag	0.238 (75.2)	0.916 (10.9)	0.146 (35.0)	0.0424 (30.9)
$\mathrm{N_{ev}}$ at 30 $\mathrm{fb^{-1}}$	7140	27480	4380	1272
Hard b-tag	0.173 (54.7)	0.0697 (0.83)	0.0616 (14.7)	0.0154 (11.2)
$\mathrm{N_{ev}}$ at 30 $\mathrm{fb^{-1}}$	5190	2091	1848	462

where $pdf_B(M_{\mu\mu})$ is the probability distribution function for the background with fixed parameters, and the second is the Voigt function, i.e. the convolution function between Gaussian and Breit–Wigner functions. The three free parameters are the number of signal events (N_S), the MSSM Higgs boson mass (M_A) and width (Γ_A). The quantity $\sigma_{\mu\mu}$ is the CMS resolution for $M_{\mu\mu}$ and it's value is found from the fit of the Z peak in the Drell–Yan distribution.

To estimate the significance for the potential discovery of the Higgs boson, the likelihood fit is performed in the *signal+background* hypothesis (L_{S+B}) and in the *background* hypothesis (L_B). The significance is defined [102] as:

$$S_L = \sqrt{2\,(\ln L_{S+B} - \ln L_B)}. \tag{11.4}$$

11.2.2.4. Results. Table 11.4 summarises the selection cut efficiency for background and signal. The first set of cuts, down to the Jet Veto cut, is always applied. After that two different b-tags are considered.

Table 11.5. Significance for the decoupling regimes.

Luminosity (fb^{-1})	$\tan\beta = 30$	$\tan\beta = 40$	$\tan\beta = 50$
	$M_A = 150\,GeV/c^2$ - soft b-tag		
10	-	6.5	7.9
20	7.2	10.3	12.1
30	9.7	13.0	15.4
	$M_A = 150\,GeV/c^2$ - hard b-tag		
10	3.8	5.7	6.7
20	6.2	7.3	9.8
30	8.8	9.8	13.1
	$M_A = 200\,GeV/c^2$ - soft b-tag		
20	-	3.1	5.2
30	-	4.7	5.7

Table 11.6. Significance for the intensive coupling regime as a function of the integrated luminosity, for different M_A values.

Luminosity (fb^{-1})	$M_A = 125\,GeV/c^2$	$M_A = 130\,GeV/c^2$	$M_A = 135\,GeV/c^2$
20	7.1	5.4	5.1
30	9.8	7.6	7.1

The systematic effects may be introduced by the experimental technique to fit the background. To estimate such effects, the fitting procedure has been repeated fixing one of the parameters to the measured value increased by its error.

Decoupling regime. Table 11.5 shows the significance as a function of $\tan\beta$, for an Higgs mass of 150 and $200\,GeV/c^2$. In general, where the fitting procedure works properly, the significance is greater then five. Best results are obtained for low values of M_A (as the cross section increases with decreasing Higgs mass) and for high values of $\tan\beta$ (the cross section is proportional to $\tan^2\beta$).

Low M_A regime. In the low M_A regime the background is large due to the presence of the Z^0 peak, thus the signal peak is hidden for the integrated luminosity considered in this study. Better results could be obtained in the LHC high luminosity phase.

Intensive coupling regime. The intensive coupling regime is interesting because all the three neutral Higgs bosons contribute to the signal peak of dimuon mass. Each Higgs boson has rather small intrinsic width (less then $3\,GeV/c^2$ for $\tan\beta = 30$) which is smaller then the mass difference. However, once the mass resolution is taken into account, it becomes impossible to separate the three peaks.

The significance, on the other hand, is quite good despite the vicinity of the Z^0 peak, because the signal cross section is large, thus the discovery can be already done with an integrated luminosity of $20\,fb^{-1}$. Table 11.6 summarises the significance obtained for the three signal samples as a function of the integrated luminosity.

Figure 11.9 shows the discovery contour plot in the plane (M_A, $\tan\beta$) obtained with this analysis. The signal significance inside the grey area is >5 with an integrated luminosity of $30\,fb^{-1}$. The structure of the contour plot near the minimum is due to the features of the signal in the intense coupling regime. The dashed line refers to the analysis without systematic uncertainties. It must be pointed out that the contour of the grey area does not correspond to a significance equal to 5 for $M_A < 180\,GeV/c^2$. The contour for $M_A < 180\,GeV/c^2$ is actually

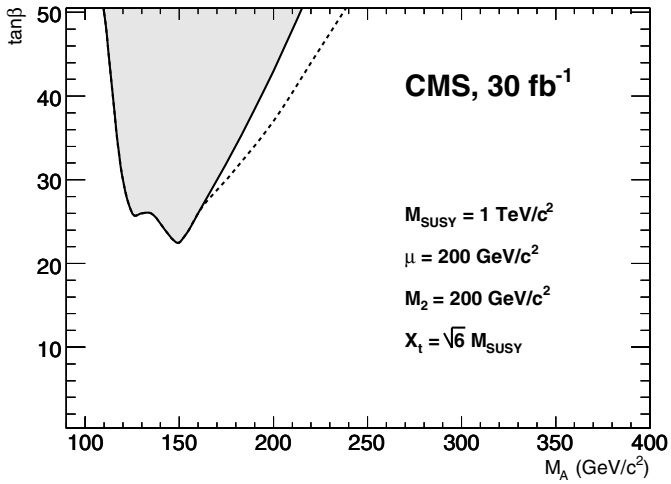

Figure 11.9. Discovery contour plot for the MSSM neutral Higgs in dimuon analysis. The signal significance inside the grey area is > 5 with an integrated luminosity of 30 fb^{-1}.

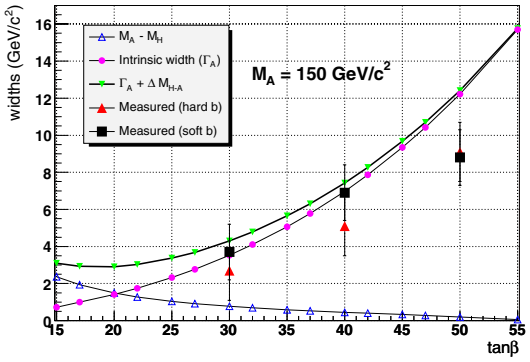

Figure 11.10. The comparison between the expected Higgs boson width and the measured one as a function of $\tan\beta$ for $M_A = 150\,\mathrm{GeV/c^2}$.

determined by the possibility to perform a successful fit to the data, due to the low statistics and the contour plot corresponds to a significance which is actually slightly larger than 5. Only for $M_A > 180\,\mathrm{GeV/c^2}$ the contour corresponds to the signal significance equal to 5. This explains why the effect of the inclusion of the systematic uncertainty is visible only in this mass range. For $M_A < 180\,\mathrm{GeV/c^2}$, the fit fails even if systematic uncertainties are not included in the analysis, and the contour plot does not change.

11.2.2.5. tan β measurement. The peculiar feature of the dimuon channel at high tan β is the possibility of the direct measurement of the Higgs boson width, $\Gamma_{\mathrm{H/A}}$, which is sensitive to $\tan\beta$ value. Therefore, it is possible to constrain $\tan\beta$ using the measured width. Figures 11.10 compares the intrinsic Higgs boson width (shown as solid circles) with the measured one (solid triangles and solid squares) for $M_A = 150\,\mathrm{GeV/c^2}$. Fitting the mass distribution with a Voigt function, the contribution to the Higgs peak from the muon

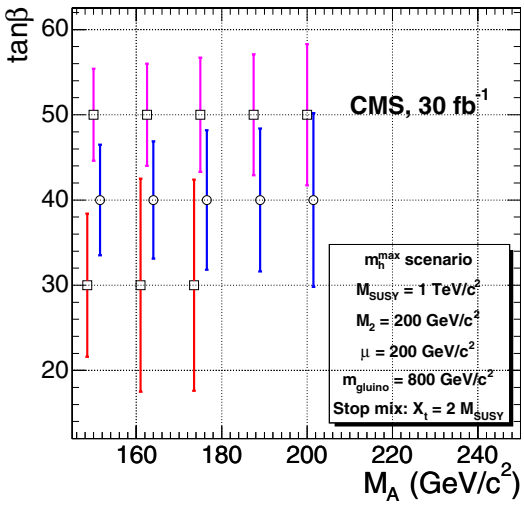

Figure 11.11. Uncertainty on the $\tan\beta$ measurement obtained from the Higgs boson width measurement with an integrated luminosity of 30 fb^{-1}.

invariant mass resolution is subtracted. However, another effect must be taken in account: the degeneracy of the two neutral Higgs bosons, A and H, is not perfect. The value of $M_A - M_H$ is plotted as a function of $\tan\beta$ (open triangles). The effect is particularly evident for $M_A = 150\,\mathrm{GeV/c^2}$ and for low $\tan\beta$, where the mass difference is greater then the intrinsic width. Thus the measured effective width is not the intrinsic one, but it is the sum of the intrinsic width and of Higgs mass difference (inverted triangles): $\Gamma_A + (M_H - M_A)$.

Figure 11.11 shows the uncertainty on the $\tan\beta$ measurement that can be obtained if the MSSM relation between the Higgs boson width and $\tan\beta$ is exploited in the m_h^{max} scenario. A theoretical uncertainty of 15% [560] is included. The $\tan\beta$ can be further constrained using the cross section measurement and exploiting the $\tan\beta$ dependance, $\sigma \times \mathrm{Br} \sim \tan^2\beta_{\mathrm{eff}}$.

11.2.3. Associated $b\bar{b}H$ production with $H \to b\bar{b}$

At high $\tan\beta$ the associated $b\bar{b}H/A$ production followed by the $H/A \to b\bar{b}$ decay has the biggest cross section. Nevertheless, the challenge of observing this channel is driven by the huge QCD multi-jet background expected for the final signature of two soft b-jets from associated Higgs boson production plus two hard b jets from the Higgs boson decay.

In this analysis [617] a study of the observability of this channel is performed using the fast simulation framework of CMS, FAMOS [11]. Signal is also studied with the full GEANT4 [9] CMS detector simulation [8] which allows to validate the fast simulation samples.

This channel can be considered as a cross-check for the discovery once it is known which Higgs boson mass (observed for instance in $b\bar{b}H/A \to b\bar{b}\tau^+\tau^-$ channel) must be looked at. In combination with the $\tau\tau$ mode it can be used to evaluate the ratio of $A(H)b\bar{b}$ and $A(H)\tau\tau$ Yukawa couplings.

11.2.3.1. Event generation. Signal events $b\bar{b}H$, $H \to b\bar{b}$ were produced using PYTHIA for 4 values of M_A: 200, 500, 600 and 800 $\mathrm{GeV/c^2}$. The signal cross sections and branching ratios were calculated with FeynHiggs 2.3.2 [142–144] in the m_h^{max} scenario. The $\tan\beta$ value chosen

Table 11.7. Off-line selection cuts on E_T of the jets (in GeV) for different Higgs boson mass values considered.

M_A	200	500	600	800
E_T^{j1}	90	200	220	260
E_T^{j2}	80	180	200	240
E_T^{j4}		30		

for generation was 50. In the considered M_A-tan β region, A and H Higgs bosons have almost the same mass and can not be distinguished.

Among the Standard Model processes, backgrounds for this channel come mainly from QCD multi-jet production which includes events with four real b jets. Background has been generated with PYTHIA QCD dijet production processes where additional jets are produced from gluon splitting and from the initial and the final state radiation in PYTHIA.

The generation of backgrounds has been weighted in order to get a similar statistics in the whole relevant $\hat{p_T}$ range. Production was split in $\hat{p_T}$ bins of 50 GeV/c from 50 to 1000 GeV/c.

11.2.3.2. Event pre-selection. About 800 million Monte-Carlo events were generated and passed to a pre-selection, requiring a final state containing at least three heavy (b or c) quarks and four jets reconstructed with PYCELL PYTHIA jet finder in the $|\eta| < 4.5$ region, using cone size of 0.5. The thresholds $E_{T_2} > 50$ GeV/c and $E_{T_4} > 10$ GeV/c were applied on the second and fourth highest E_T jet respectively. The QQ + jj background (with Q=b, c and j=light quark or gluon) was estimated to be less than 10% of the total QCD multi-jet background after final selection cuts. After pre-selection, around 30 million events were passed to the detector simulation.

11.2.3.3. Online selection. This channel is triggered at Level 1 by the standard single and multi-jet triggers. At High Level, the inclusive single b-jet trigger [618] stream has been used. The implementation of the High Level double b-jet trigger and relaxing the jet energy thresholds could improve the observability of the signal, especially for low mass Higgs boson ($\sim 200\,\mathrm{GeV/c^2}$).

11.2.3.4. Off-line selection. Analysis has been performed with fast simulated signal and background samples where pile-up was not included, once it was checked with full simulation on signal events that its effect was not significant after requiring jets with reconstructed $E_T > 30$ GeV.

The jets are reconstructed with the iterative cone algorithm [314] using cone size of 0.5. The calorimeter towers with the energy thresholds tuned to minimise the fake jet rate were used as an input for the jet finder. The jet energy corrections were applied using Monte Carlo calibration [619].

The event was required to have at least four jets with the transverse energy of 1st, 2nd and 4th jet greater than thresholds depending upon the M_A point considered, according to Table 11.7. The cut on the 4th jet E_T is motivated by reliability of the analysis simulation without pile-up.

Subsequently, the jets were required to be in the range of the tracker acceptance, $|\eta| < 2.4$. Combined b tagging as described in [616] has been used. At least three b-tagged jets (with discriminant variable > 2), among the 4 highest E_T jets, are requested in the analysis; two of them must be the two highest E_T jets. It would also have been possible to be less restrictive

Table 11.8. Signal selection cumulative efficiencies for $M_A = 600\,GeV/c^2$, $\tan\beta = 50$ and background cumulative efficiencies. The signal to background ratio, S/B, is also shown.

Selection	Signal efficiency	Background efficiency	S/B (full mass range)
None	1	1	1.85×10^{-7}
Pre-selection	5.14E−01	5.94E−03	1.60×10^{-5}
At least 4 jets	5.01E−01	5.85E−03	1.58×10^{-5}
E_T^{j1}	3.10E−01	1.57E−04	3.66×10^{-4}
E_T^{j2}	1.86E−01	4.76E−05	7.21×10^{-4}
E_T^{j4}	1.02E−01	3.24E−05	5.82×10^{-4}
Jets in $\|\eta\| \leqslant 2.4$	8.25E−02	2.26E−05	6.73×10^{-4}
b tagging of 1 jet	3.61E−02	2.44E−06	2.73×10^{-3}
b tagging of 2 jets	1.69E−02	2.81E−07	1.11×10^{-2}
b tagging of 3 jets	8.57E−03	5.62E−08	2.82×10^{-2}
centrality > 0.7	7.05E−03	3.69E−08	3.52×10^{-2}

and accept events where only three of the four jets are in the tracker acceptance, with the other outside the tracker acceptance, but this option is not considered in this analysis.

Finally, the centrality variable, defined as

$$C = \frac{\sum E_T}{\sqrt{(\sum E)^2 + (\sum E_z)^2}} \tag{11.5}$$

using the four highest E_T jets in the event, is used to discriminate between signal and background, given its independence from the signal mass. The analysis uses the discrimination power of this variable to reject background events with C lower than 0.7.

Table 11.8 summarises the selection cut efficiencies for background and signal. The signal to background ratio, S/B, is also shown. The event samples used to calculate numbers given in this table are statistically independent from the ones used to optimise the cuts.

11.2.3.5. Signal significance. The criterion for the presence of signal is based on the distribution of the reconstructed Higgs boson mass, considering as mass estimator the invariant mass distribution of the two leading E_T jets. The signal significance, $S/\sqrt{(B)}$ is calculated in the mass window which maximises this ratio. Figure 11.12 shows the reconstructed Higgs boson mass distribution for signal and background after all selections as expected for $60\,fb^{-1}$.

The signal significances in the optimised mass window after all the cuts applied excluding and including the HLT in the analysis chain, can be found in Table 11.9. The HLT decreases the significance up to a factor 10 for low masses ($M_A = 200\,GeV/c^2$). For higher masses, this factor is reduced to less than 2.

11.2.3.6. Background uncertainty and discovery reach in the $M_A - tan\,\beta$ plane. Given the low S/B ratio and the similarities of the signal and background distributions, a careful evaluation of the background has to be performed. The best source of background events will come from real data samples, when available, as it is being done at the Tevatron experiments [620]. The QCD multi-jet background will be determined from data by normalising distributions outside of the signal region, once the mass of the Higgs is known from other channels for example. Data will be also used to extract the background shape with possibly the help of Monte Carlo.

Figure 11.13 shows the effect of the background uncertainty on the discovery reach (with two sigma signal significance) in the M_A-tan β plane. Different curves correspond to the

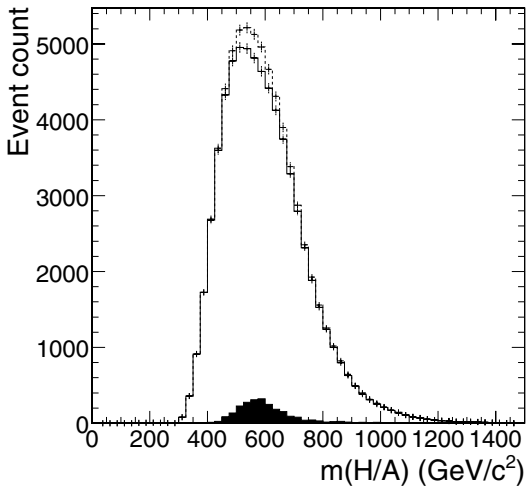

Figure 11.12. The Higgs boson mass distributions after all selections for the signal of $M_A = 600\,GeV/c^2$, $\tan\beta = 50$ in the m_h^{max} scenario (black in foreground), background (solid line) and signal plus background (dashed line) for $60\,fb^{-1}$.

Table 11.9. Signal significance $S/\sqrt{B}$ in optimised mass window after all selections with and without HLT filtering included. The last line shows the low limit of $\tan\beta$ where the 5σ discovery is possible with $60\,fb^{-1}$ in the absence of systematics.

M_A	200	500	600	800
No HLT	30.9	10.4	7.7	2.3
With HLT	2.9	6.4	5.6	3.4
$\tan\beta$ where significance is 5	71	44	47	62

different assumptions on the background uncertainty, from zero uncertainty to 2%. The signal significance is defined as $s = \frac{S}{\sqrt{B+(\varepsilon B)^2}}$, where S is the number of signal events in the mass window, B is the number of background events in the same window and ε is the relative background uncertainty.

The discovery potential of this channel is limited by the low signal-to-background ratio and the similarity of the signal and background distribution shapes. So far, it is not known how well the background can be measured at LHC, thus it is difficult to make predictions about the possibility to observe the MSSM Higgs bosons in the four-b final state.

11.2.4. Charged Higgs boson of $M_H < m_t$ in $t\bar{t} \to H^\pm W^\mp b\bar{b}$ production with $H^\pm \to \tau^\pm\nu$, $\tau \to \nu + hadrons$ and $W^\mp \to \ell^\mp\nu$

A detailed description of the analysis can be found in [621].

11.2.4.1. Event generation and cross sections of signal and background events. The charged Higgs boson in the MSSM can be produced in top quark decays, $t \to H^+b$, if $m_{H^\pm} < m_t - m_b$. The branching ratio of top decay to charged Higgs boson depends on both $m_{H^\pm}$ and $\tan\beta$ as shown in Fig. 11.14a. The corresponding top decay to $W^\pm b$ decreases with increasing $\tan\beta$ so as to keep the sum of branching ratios almost at unity. While the top decay to $H^\pm$ or $W^\pm$

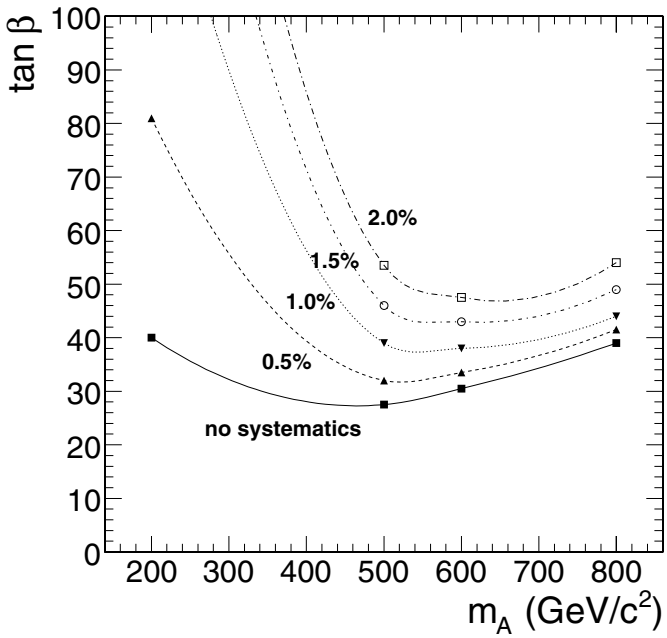

Figure 11.13. Two-sigma significance contours with different assumptions on the background uncertainty at 60 fb^{-1} in the m_h^{max} scenario.

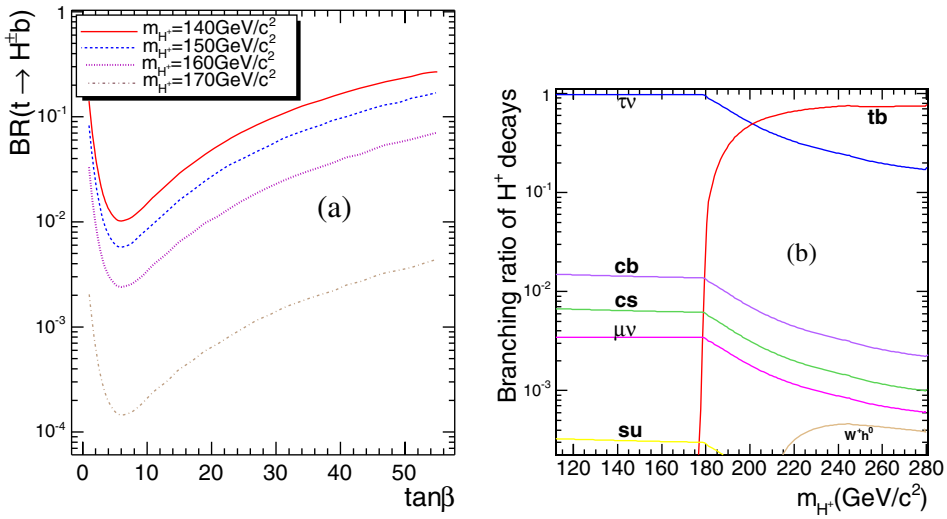

Figure 11.14. (a) Branching ratio of top decay to $H^{\pm}$ vs tan β, and (b) branching ratios for charged Higgs boson decaying to different final states for tan $\beta = 20$.

depends on tan β, the light charged Higgs boson decay to $\tau\nu$ is almost independent of tan β (for tan $\beta > 10$) and is $\sim 98\%$ for all tan $\beta > 10$ and $m_{H^{\pm}} < m_t$ as shown in Fig. 11.14b.

There are two different final states for $t\bar{t} \to H^{\pm}W^{\mp}b\bar{b}$ events depending on $W^{\pm}$ decay to leptons or jets. In this analysis the leptonic decay of $W^{\pm}$ boson is chosen and signal

Table 11.10. Cross section times branching ratio of $t\bar{t} \to H^{\pm}W^{\mp}b\bar{b} \to \tau\nu_{\tau}\ell\nu_{\ell}b\bar{b}$, $\tau \to$ hadrons for $\tan\beta = 20$.

$m_{H^{\pm}}$ (GeV/c^2)	140	150	160	170
Cross section [pb]	10.70	5.06	1.83	0.16

Table 11.11. Cross section times branching ratio of signal events for $m_{H^{\pm}} \simeq m_t$ according to NLO calculations in [597] for $\tan\beta = 20$.

Channel	$gb \to tH^{\pm} \to \ell\nu_{\ell}b\tau\nu_{\tau}$ ($\tau \to$ hadrons) $m_{H^{\pm}} = 170\,\text{GeV/c}^2$	$gg \to tbH^{\pm} \to \ell\nu_{\ell}bb\tau\nu_{\tau}$ ($\tau \to$ hadrons) $m_{H^{\pm}} = 170\,\text{GeV/c}^2$
Cross section [pb]	0.14	0.30

Table 11.12. Cross section times branching ratio of background events.

Channel	$t\bar{t} \to W^+W^-b\bar{b}$ $\to \ell\nu_{\ell}\tau\nu_{\tau}b\bar{b}$ ($\tau \to$ hadrons)	$t\bar{t} \to W^+W^-b\bar{b}$ $\to \ell\nu_{\ell}\ell'\nu_{\ell'}b\bar{b}$ $\ell, \ell' =$ e or μ	$t\bar{t} \to W^+W^-b\bar{b}$ $\to \ell\nu_{\ell}jjb\bar{b}$	$W^{\pm} + 3$ jets $W^{\pm} \to$ e or μ
Cross section [pb]	25.8	39.7	245.6	840

events are triggered by the single lepton trigger (e or μ). The τ lepton is forced to decay to hadrons. Table 11.10 shows the cross section times branching ratio of $t\bar{t} \to H^{\pm}W^{\mp}b\bar{b}$ events for $\tan\beta = 20$. In this analysis for $m_{H^{\pm}} = 170\,\text{GeV/c}^2$ both $t\bar{t}$ + gb and $gg \to t\bar{b}H^{\pm}$ production processes were used for comparison. The NLO cross section times branching ratio of signal events with $m_{H^{\pm}} \simeq m_t$ is listed in Table 11.11.

The background channels consist of $t\bar{t}$ events with at least a single lepton (e or μ) and τ-jets or jets which could fake τ-jets, $W^{\pm} + 3$ jet events and also single top (Wt) events which have a small contribution. The cross section of main background channels are shown in Table 11.12.

The $t\bar{t}$, $gb \to tH^{\pm}$ and $gg \to t\bar{b}H^{\pm}$ processes were generated by PYTHIA. The Wt background was generated with TOPREX and the W+3j background was generated by MADGRAPH. The production cross sections for the background processes were normalised to the NLO cross sections (except W + 3 jet).

11.2.4.2. Online event selection and offline reconstruction. Events are triggered by the single lepton triggers (e or μ) at Level 1 and HLT.

In the offline $\geqslant 3$ jets are required to suppress $W^{\pm}$ + njets background with $n < 3$. The jet reconstruction is performed using the iterative cone algorithm and the jet energy corrections, evaluated from γ+jet calibration, were applied. A jet is accepted if it has calibrated $E_T > 40\,\text{GeV}$. Only one b-tagged jet is required in this analysis.

Since events are triggered by lepton from $W \to \ell\nu$ decay, τ jets are identified with an offline τ-tagging algorithm which uses Level 1 τ objects as seeds for τ-jet reconstruction. The first, highest E_T, jet satisfying the conditions of $E_T > 20\,\text{GeV}$ and hottest HCAL tower $E_T > 2\,\text{GeV}$ is used as a τ candidate. A matching cone with $R_m = 0.1$, an isolation cone with $R_i = 0.4$ and a signal cone with $R_S = 0.07$ are defined for checking isolation requirements in the tracker. The ECAL isolation requirement is defined as

$$P_{\text{isol.}} = \sum_{\text{crystals},\,\Delta R_{\text{crystal},\tau-\text{jet}}<0.4} E_{T\text{crystal}} - \sum_{\text{crystals},\,\Delta R_{\text{crystal},\tau-\text{jet}}<0.13} E_{T\text{crystal}} < 5.6\,\text{GeV}. \tag{11.6}$$

Table 11.13. List of selection cuts and their efficiencies for signal events with $m_{H^\pm} < 170\,GeV/c^2$ for $\tan\beta = 20$. Numbers in each row show the remaining cross section after applying the corresponding cut. Numbers in parentheses are relative efficiencies in percent.

	$t\bar{t} \to H^\pm W^\mp b\bar{b}$ $\to \ell\nu_\ell\tau\nu_\tau b\bar{b}$ $m_{H^\pm} = 140\,GeV/c^2$	$t\bar{t} \to H^\pm W^\mp b\bar{b}$ $\to \ell\nu_\ell\tau\nu_\tau b\bar{b}$ $m_{H^\pm} = 150\,GeV/c^2$	$t\bar{t} \to H^\pm W^\mp b\bar{b}$ $\to \ell\nu_\ell\tau\nu_\tau b\bar{b}$ $m_{H^\pm} = 160\,GeV/c^2$
$\sigma \times BR$[fb]	10.7×10^3	5060	1830
L1 + HLT	5170.5(48.3)	2456.3(48.5)	888.9(48.6)
$\geqslant 3$ jets	1889.7(36.5)	795.0(32.4)	264.3(29.7)
$\geqslant 1$ b jet	1103.5(58.4)	427.4(53.8)	131.4(49.7)
< 2 b jets	883.0(80.0)	358.7(83.9)	119.2(90.7)
L1 τ exists	878.4(99.5)	357.4(99.6)	119.0(99.8)
τ-jet reconstruction	875.0(99.6)	356.5(99.7)	118.8(99.8)
Hottest HCAL tower $E_T > 2.GeV$	778.0(88.9)	316.1(88.6)	105.9(89.1)
Tracker isolation	378.2(48.6)	163.5(51.7)	52.7(49.8)
Ecal isolation	292.9(77.4)	134.2(82.1)	43.1(81.8)
$\tau\ E_T > 40\,GeV$	244.3(83.4)	113.0(84.2)	36.5(84.7)
$p_{\text{leading track}}/E_{\tau-\text{jet}} > 0.8$	102.3(41.9)	50.7(44.8)	16.8(45.9)
$Q(\ell) + Q(\tau) = 0$	88.0(86.0)	42.4(83.6)	14.6(87.0)
$E_T^{miss} > 70\,GeV$	51.0(58.0)	25.4(59.9)	9.2(63.3)
Expected Number of events after $10\,fb^{-1}$	510	254	92

When the tracker and ECAL isolation cuts are applied, the τ-jet E_T is required to be more than 40 GeV and the leading track of τ jet is required to carry at least 80% of the visible τ-lepton energy; finally the charges of the τ lepton and the lepton in the event should satisfy the requirement $Q(\ell) + Q(\tau) = 0$.

The missing E_T is reconstructed with the energy corrections applied to jets (Type 1 E_T^{miss} [147, 148]) and a cut on the reconstructed missing E_T ($E_T^{miss} > 70\,GeV$) is applied as a rejection tool against background events, especially $W^\pm + 3$jets.

11.2.4.3. Selection efficiencies and expected number of events. Tables 11.13, 11.14, 11.15 show the selection cuts and their efficiencies for signal and background samples. Other background events such as Wbb, Zbb with $W \to \ell\nu$ ($\ell = e, \mu$) and $Z \to ee$, or $\tau\tau$ turned out to be negligible. Single top background contribution is also small but was considered in the analysis for signal significance calculations.

11.2.4.4. Systematic uncertainties. The systematic uncertainties in the signal significance calculation include the experimental selection uncertainty of the background events and the theoretical cross section calculation uncertainty of the tt and single top background. The $t\bar{t}$ background uncertainty is taken into account as in Eq. 11.7:

$$\Delta^{t\bar{t}}_{sys.} = \Delta_{\text{lepton reconstruction}} \oplus \Delta_{\geqslant 3\,\text{jet selection}} \oplus \Delta_{1\,\text{b-jet tagging}} \oplus \Delta_{1\,\tau\,\text{tagging}} \oplus \Delta_{\text{lumi.}} \oplus \Delta^{tt}_{\text{theo.}}. \quad (11.7)$$

The $W^\pm + 3$ jets background is assumed to be measured from the real data. The uncertainty of the measurement is estimated by propagating the contribution of events counted in the background area to the signal area and cancelling the common selection cuts

Table 11.14. List of selection cuts and their efficiencies for signal events with $m_{H^\pm} = 170\,\mathrm{GeV/c^2}$ for $\tan\beta = 20$. Numbers in each row show the remaining cross section after applying the corresponding cut. Numbers in parentheses are relative efficiencies in percent.

	$t\bar{t} \to H^\pm W^\mp b\bar{b}$ $\to \ell\nu_\ell\tau\nu_\tau b\bar{b}$ $m_{H^\pm} = 170\,\mathrm{GeV/c^2}$	$gb \to tH^\pm$ $\to \ell\nu_\ell\tau\nu_\tau b$ $m_{H^\pm} = 170\,\mathrm{GeV/c^2}$	$gg \to t\bar{b}H^\pm$ $\to \ell\nu_\ell\tau\nu_\tau b\bar{b}$ $m_{H^\pm} = 170\,\mathrm{GeV/c^2}$
$\sigma \times$ BR[fb]	157	140	297
L1 + HLT	78.0(49.7)	70.5(50.4)	145.4(48.9)
$\geqslant 3$ jets	23.2(29.7)	21.7(30.7)	55.3(38.0)
$\geqslant 1$ bjet	11.5(49.4)	11.7(54.1)	31.9(57.7)
< 2 b jets	10.9(94.8)	10.0(85.5)	25.8(80.9)
L1 τ exists	10.8(99.8)	10.0(99.6)	25.7(99.4)
τ-jet reconstruction	10.8(99.9)	10.0(99.9)	25.5(99.1)
Hottest HCAL tower $E_T > 2.\,GeV$	9.6(88.4)	8.9(88.8)	22.6(88.9)
Tracker isolation	4.9(51.3)	5.1(57.2)	11.4(50.5)
Ecal isolation	4.2(84.9)	4.3(84.5)	9.6(84.4)
$\tau\ E_T > 40.GeV$	3.8(90.9)	3.9(90.6)	8.6(89.2)
$p_{\text{leading track}}/E_{\tau-\text{jet}} > 0.8$	1.6(41.7)	1.8(45.9)	3.4(39.6)
$Q(\ell) + Q(\tau) = 0$	1.3(84.4)	1.6(87.2)	2.8(82.6)
$E_T^{\text{miss}} > 70\,\mathrm{GeV}$	0.8(61.7)	1.0(65.2)	1.6(55.3)
Expected Number of events after $10\,\mathrm{fb}^{-1}$	8	10	16

Table 11.15. List of selection cuts and their efficiencies for background events. Numbers in each row show the remaining cross section after applying the corresponding cut. Numbers in parentheses are relative efficiencies in percent.

	$t\bar{t} \to W^+W^-b\bar{b}$ $\to \ell\nu_\ell\tau\nu_\tau b\bar{b}$	$t\bar{t} \to W^+W^-b\bar{b}$ $\to \ell\nu_\ell\ell'\nu_{\ell'}b\bar{b}$	$t\bar{t} \to W^+W^-b\bar{b}$ $\to \ell\nu_\ell jjb\bar{b}$	$W^\pm + 3$ jets $W^\pm \to \ell\nu_\ell$
$\sigma \times$ BR [fb]	25.8×10^3	39.8×10^3	245.6×10^3	$840. \times 10^3$
L1 + HLT	12101.2(46.9)	28429.1(71.4)	99506.6(40.5)	287280(34.2)
$\geqslant 3$ jets	5105.2(42.2)	11306.6(39.8)	66038.6(66.4)	114050(39.7)
$\geqslant 1$ b jet	3428.3(67.1)	7622.0(67.4)	43433.0(65.8)	24292.7(21.3)
< 2 b jets	2325.7(67.8)	5262.7(69.0)	29003.4(66.8)	21207.5(87.3)
L1 τ exists	2310.7(99.3)	5233.7(99.4)	28698.8(98.9)	20613.7(97.2)
τ-jet reconstruction	2303.6(99.7)	5224.4(99.8)	28465.0(99.2)	19438.7(94.3)
Hottest HCAL tower $E_T > 2.GeV$	2034.1(88.3)	3850.6(73.7)	26635.1(93.6)	17125.5(88.1)
Tracker isolation	798.7(39.3)	1120.6(29.1)	6653.3(25.0)	5411.7(31.6)
Ecal isolation	545.6(68.3)	519.5(46.3)	2952.8(44.4)	2554.3(47.2)
$\tau\ E_T > 40.GeV$	405.8(74.4)	341.8(65.8)	1946.8(65.9)	1312.9(51.4)
$p_{\text{leadingtrack}}/E_{\tau-\text{jet}} > 0.8$	123.5(30.4)	131.9(38.6)	377.9(19.4)	224.5(17.1)
$Q(\ell) + Q(\tau) = 0$	95.7(77.5)	56.7(43.0)	78.8(20.9)	27.1(12.1)
$E_T^{\text{miss}} > 70\,\mathrm{GeV}$	51.6(53.9)	29.3(51.8)	36.6(46.4)	10.7(39.3)
Expected Number of events after $10\,\mathrm{fb}^{-1}$	516	293	366	107

uncertainties. Eq. 11.8 describes how systematic uncertainties are taken into account in W+3 jets cross section measurement.

$$\Delta_{\text{sys.}}^{W^\pm+3\,\text{jets}} = \Delta_{\text{stat.}} \oplus \frac{\Delta N_B^{t\bar{t}}}{N_B^{W^\pm+3\,\text{jets}}} \oplus \Delta_{3\,\text{non-b-jet}} \oplus \Delta_{\text{b-jet mistagging}} \oplus \Delta_{\tau\ \text{mistagging}}. \tag{11.8}$$

Table 11.16. The values of different selection uncertainties for $t\bar{t}$ and $W^{\pm}+3$ jets background events at 30 fb^{-1}.

Scale uncertainty of $t\bar{t}$ cross section	5%
PDF uncertainty of $t\bar{t}$ cross section	2.5%
b tagging	5%
τ tagging	4%
Lepton identification	2%
Jet energy scale	3%
Mistagging a non-b jet as a b jet	5%
Mistagging a jet as a τ jet	2%
Non-b-jet identification (anti-b-tagging)	5%
Luminosity uncertainty	5%

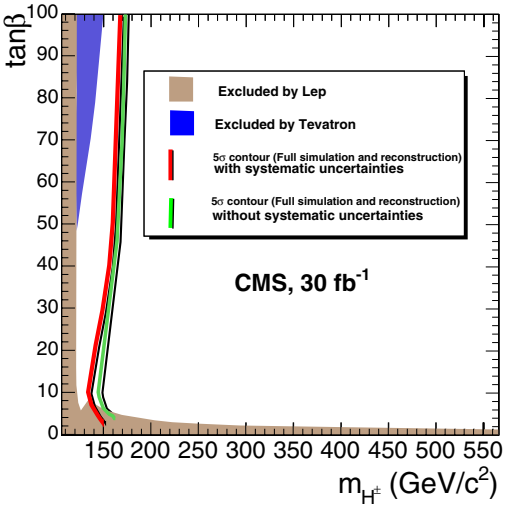

Figure 11.15. The 5σ contour in the $(M_{H^+}, \tan\beta)$ plane for light charged Higgs boson discovery at 30 fb^{-1} including the effect of systematic uncertainties.

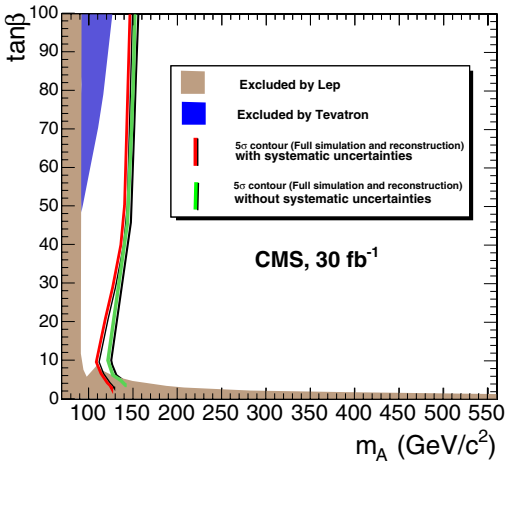

Figure 11.16. The 5σ contour in the $(M_A, \tan\beta)$ plane for light charged Higgs boson discovery at 30 fb^{-1} including the effect of systematic uncertainties.

Table 11.16 lists different sources of systematic uncertainties and their used values corresponding to 30 fb^{-1} in this analysis.

11.2.4.5. Discovery reach in the $M_{A(H^{\pm})} - tan\,\beta$ plane. Figures 11.15 and 11.16 show the 5σ discovery region in the $(M_{H^+}, \tan\beta)$ and $(M_A, \tan\beta)$ planes including the systematic uncertainties. It should be noted that this analysis is systematics dominated and there could be alternative approaches where the systematic uncertainties cancel down to a reasonable level.

11.2.5. Charged Higgs boson of $M_H > m_t$ in $gg \to tbH^{\pm}$ production with $H^{\pm} \to \tau^{\pm}\nu, \tau \to hadrons\ \nu$ and $W^{\mp} \to jj$

The $H^{\pm} \to \tau^{\pm}\nu_{\tau}$ decay mode with fully hadronic final state of the charged Higgs boson in the associated production with a top quark has been shown to lead to a clean and almost background-free signature at large $\tan\beta$ in several particle level [622] and fast

simulation [383, 384, 623, 624] studies. The advantages of this decay mode in association with top quark are the large missing transverse energy from $H^{\pm}$, the possibility to disentangle the hadronic τ decay from the hadronic jets, the possibility to reconstruct the top mass to suppress the multi-jet backgrounds, and, in particular, τ helicity correlations favouring the $H^{\pm} \to \tau^{\pm}\nu_{\tau}$ decay over the $W^{\pm} \to \tau^{\pm}\nu_{\tau}$ decay (from the $t\bar{t}$ background). The main backgrounds are due to genuine τ's in multi-jet events from $t\bar{t}$ with $t_1 \to b\tau\nu_{\tau}$, $t_2 \to bqq$, Wt with $W_1 \to \tau\nu_{\tau}$, $W_2 \to qq'$ and W+3 jets with $W \to \tau\nu_{\tau}$. The hadronic QCD multi-jet events can lead to a background through fake τ's and the uncertainty of E_T^{miss} measurement.

A detailed description of the analysis can be found in [625].

11.2.5.1. Helicity correlations. The polarisation states for the τ^+ from $H^+ \to \tau^+\nu_{\tau}$ and from $W^+ \to \tau^+\nu_{\tau}$ are opposite due to the spin-parity properties of the decaying particle. The angular distribution of a pion from the $\tau^{\pm} \to \pi^{\pm}\nu$ decay in the CM frame has the form $(1 + P_{\tau}\cos\theta)$, which leads to more energetic pions in the laboratory frame for the signal ($P_{\tau} = 1$) than for the background ($P_{\tau} = -1$) [622, 626]. The $\tau^{\pm} \to \pi^{\pm}\nu_{\tau}$ decay channel presents 12.5% of the hadronic decay modes. Similarly, the signal pions are more energetic in the τ decays to vector mesons and subsequent decays to one charged pion in the longitudinal polarisation states of the vector meson, $\tau^{\pm} \to \rho^{\pm}_{L}\nu_{\tau} \to \pi^{\pm}\pi^{\circ}\nu_{\tau}$ (26%) and $\tau^{\pm} \to a^{\pm}_{1L}\nu_{\tau} \to \pi^{\pm}\pi^{\circ}\pi^{\circ}\nu_{\tau}$ (7.5%). For the transverse polarisation states of the vector meson the situation is opposite with more energetic pions from the background. The small contributions from K^* and K in the τ decays lead to similar effects. The helicity correlations can be expressed as a function of the τ-jet momentum fraction carried by the charged pion $R_{\tau} = p_{\pi}/p_{\tau jet}$. As is shown in Refs. [622, 626] the $\tau^{\pm} \to \pi^{\pm}\nu_{\tau}$ decay leads to a δ-function at $R_{\tau} = 1$, the $\rho^{\pm}_{L}\nu_{\tau} \to \pi^{\pm}\pi^{\circ}\nu_{\tau}$ has contributions at $R_{\tau} \sim 1$ and $R_{\tau} \sim 0$, $\rho^{\pm}_{T}\nu_{\tau} \to \pi^{\pm}\pi^{\circ}\nu_{\tau}$ and $a^{\pm}_{1T}\nu_{\tau} \to \pi^{\pm}\pi^{\circ}\pi^{\circ}\nu_{\tau}$ have largest contributions around $R_{\tau} \sim 0.5$ while $a^{\pm}_{1L}\nu_{\tau} \to \pi^{\pm}\pi^{\circ}\pi^{\circ}\nu_{\tau}$ peaks at $R_{\tau} \sim 0$.

11.2.5.2. Event generation and simulation. The $gb \to tH^{\pm}$ and $gg \to tbH^{\pm}$ processes contribute to the production of a heavy single charged Higgs boson in association with top quark. In the $gb \to tH^{\pm}$ process the b quark is considered as a massless parton of the incoming proton. Logarithmic factors of the form $\log(p_T^b/m_b)$, due to the collinear b quarks, can be resumed to give a well defined cross section. The $gg \to tbH^{\pm}$ process, where the bottom quarks from the incoming gluons are considered massive, is of the order α_s^2 and is part of the next-to-leading order (LNO) corrections to the leading order (LO) process $gb \to tH^{\pm}$. These processes lead to somewhat different dynamics of the final state objects, visible in particular as a more energetic associated b quark in the $gg \to tbH^{\pm}$ process [627]. Near the top threshold, $m_{H^{\pm}} \sim m_t$, only the exclusive process $gg \to tbH^{\pm}$ can lead to a correct event description. As the correct description of merging these two processes is not possible in the full simulation, signal events were generated with the $gg \to tbH^{\pm}$ process over the full mass range with PYTHIA [69]. The cross sections were normalised to the NLO results of Refs. [597, 628]. The mass of the charged Higgs boson and the $H^{\pm} \to \tau\nu_{\tau}$ branching fraction were calculated with FeynHiggs2.3.2 [142–144] in the m_h^{max} scenario. The $t\bar{t}$ background was generated with PYTHIA, the Wt background with TOPREX [44], the W+3jet background with MADGRAPH [81] and the QCD multi-jet background with PYTHIA. The production cross sections for the background processes were normalised to the NLO cross sections (except $W + 3$jet). Pre-selections at the particle level, requiring at least one jet with $E_T > 80\,GeV$, reconstructed with the PYTHIA PYCELL routine with a cone size of 0.5, and containing at least one charged hadron with $p_T > 60\,GeV/c$, were applied to the $t\bar{t}$ and Wt backgrounds. The τ decays were performed with TAUOLA [155] for the signal and backgrounds. The τ from

Table 11.17. Cross section times branching fraction for $gg \to tbH^{\pm}$, $H^{\pm} \to \tau^{\pm}\nu$, $\tau \to$ hadrons + ν, efficiency for the selection cuts and final number of events for $m_T(\tau\,\text{jet}, E_T^{miss}) > 100\,GeV/c^2$ and for $\Delta\phi(\tau\,\text{jet}, E_T^{miss}) > 60^{\circ}$ with an integrated luminosity of $30\,fb^{-1}$ for the signal events with $m_{H^{\pm}} = 170, 180, 200$ and $400\,GeV/c^2$ and $\tan\beta = 30$.

$m_{H^{\pm}}$ (GeV/c^2)	171.6	180.4	201.0	400.4
σ(NLO) × BR (fb)	1359	1238	776	38
Level-1 trigger	729.9 (53.7%)	688.1 (55.6%)	451.3 (58.2%)	28.5 (75.6%)
HLT trigger	121.0 (16.6%)	128.6 (18.7%)	95.9 (21.2%)	12.1 (42.4%)
Primary vertex	119.9 (99.1%)	127.5 (99.2%)	95.1 (99.2%)	12.0 (99.2%)
Isolated lepton veto	94.4 (78.8%)	104.2 (81.7%)	78.2 (82.2%)	10.1 (85.0%)
$E_T^{miss} > 100\,GeV$	66.7 (70.6%)	70.0 (67.2%)	53.3 (68.2%)	8.2 (80.7%)
$E_T^{\tau jet} > 100\,GeV$	33.7 (50.5%)	36.7 (52.4%)	27.8 (52.1%)	6.7 (81.8%)
$R_\tau > 0.8$	11.2 (33.4%)	11.6 (31.5%)	9.5 (34.2%)	2.3 (34.2%)
1 or 3 signal tracks	10.7 (95.3%)	11.2 (97.1%)	9.1 (95.9%)	2.2 (97.0%)
Tracker isolation	10.0 (93.2%)	10.5 (94.0%)	8.6 (94.9%)	2.1 (93.7%)
ECAL isolation	9.4 (94.4%)	10.0 (95.0%)	8.3 (95.7%)	2.0 (95.8%)
$E_T^{max(HCAL\ cell)} > 2\,GeV$	9.1 (96.5%)	9.4 (93.3%)	7.9 (95.5%)	2.0 (98.7%)
$IP_T^{leading\ track} < 0.3\,mm$	9.0 (97.8%)	9.2 (98.2%)	7.8 (99.0%)	2.0 (99.3%)
$N_{hits}^{leading\ track} \geqslant 10$	8.6 (95.9%)	8.4 (96.5%)	7.4 (94.6%)	2.0 (96.5%)
$\geqslant 3$ jets, $E_T > 20\,GeV$	6.4 (74.4%)	7.2 (80.9%)	5.7 (77.4%)	1.4 (71.9%)
$140 < m_{top} < 210\,GeV/c^2$	4.6 (72.6%)	4.8 (67.2%)	3.6 (63.7%)	0.93 (66.6%)
b discriminator > 1.5	2.0 (43.7%)	2.0 (39.9%)	1.6 (42.7%)	0.37 (40.3%)
$E_T^{bjet} > 30\,GeV$	1.9 (93.2%)	1.8 (95.2%)	1.4 (91.6%)	0.33 (88.2%)
Jet veto, $E_T^{jet} > 25\,GeV$	0.65 (35.2%)	0.63 (34.6%)	0.52 (36.4%)	0.14 (40.9%)
$E_T^{Higgs} > 50\,GeV$	0.61 (91.9%)	0.63 (100%)	0.52 (100%)	0.13 (95.1%)
$m_T > 100\,GeV/c^2$	0.47 (77.3%)	0.49 (78.4%)	0.39 (74.9%)	0.12 (94.8%)
N^{ev}, $m_T > 100\,GeV/c^2$	14.1 ± 3.4	14.7 ± 3.2	11.7 ± 2.3	3.6 ± 0.5
$\Delta\phi(\tau, E_T^{miss}) > 60^0$	0.20 (31.9%)	0.18 (28.5%)	0.28 (53.9%)	0.12 (93.1%)
N^{ev}, $\Delta\phi(\tau, E_T^{miss}) > 60^0$	6.0 ± 2.2	5.4 ± 2.0 (28.5%)	8.3 ± 2.0	3.6 ± 0.5

$H^{\pm}$ was forced to decay to hadrons in the signal samples while all τ decays were generated for the backgrounds.

The analysis was based on event samples from full detector simulation and digitisation at low luminosity $2 \times 10^{33}\,cm^{-2}s^{-1}$.

11.2.5.3. Event selection. Due to an energetic τ jet from $H^{\pm}$ the $gg \to tbH^{\pm}$, $H^{\pm} \to \tau^{\pm}\nu$ ($\tau \to$ hadrons ν, $W^{\mp} \to jj$) events can be most efficiently triggered at the Level-1 with a single τ-jet trigger [76, 280]. At the HLT, a combined E_T^{miss}-τ trigger was used. For this trigger the τ-jet identification was performed in the full tracker (Tracker Tau trigger) [146]. Efficiencies of the Level 1 and HLT triggers are shown in Tables 11.17 and 11.18 for the signal and backgrounds, respectively. Purity of the τ trigger for the signal events is higher than 80%.

In the off-line reconstruction the transverse mass from the τ jet and missing transverse energy requires a fully hadronic event, where E_T^{miss} originates mainly from the $H^{\pm}$. Other sources of E_T^{miss} in the signal events are the leptonic W decays and the semi-leptonic b quark decays. The events with leptonic W decays can be removed with a veto on isolated leptons. The reconstructed electrons and muons were first required to be isolated in the tracker demanding that no track with $p_T > 1\,GeV/c$ was found in a cone of $\Delta R = 0.4$ around the lepton direction. The fraction of events containing at least one muon candidate with $p_T > 15\,GeV/c$ is 24.1%. An isolated muon is found in 8.9% of the signal events.

Table 11.18. Cross section times branching fraction, efficiency for the selection cuts and final number of events for $m_T(\tau\,\text{jet}, E_T^{miss}) > 100\,GeV/c^2$ and for $\Delta\phi(\tau\,\text{jet}, E_T^{miss}) > 60^\circ$ with an integrated luminosity of $30\,fb^{-1}$ for the $t\bar{t}$, Wt, $W^\pm + 3$jets and QCD multi-jet backgrounds background.

	$t\bar{t}$	Wt	$W^\pm$+ 3jets
σ(NLO) × BR (fb)	123820	9140	4.19×10^5
Pre-selection	6440 (5.2%)	237.6 (2.6%)	
Level-1 trigger	4730 (73.4%)	185.6 (78.1%)	1.25×10^5 (29.8%)
HLT trigger	320 (6.9%)	20.5 (11.1%)	4.19×10^3 (3.4%)
Primary vertex	319 (99.8%)	20.4 (99.7%)	4190 (100%)
Isolated lepton veto	314 (89.4%)	18.4 (89.9%)	3456 (82.5%)
$E_T^{miss} > 100\,GeV$	267.4 (85.1%)	15.9 (86.6%)	2674 (77.1%)
$E_T^{\tau\,jet} > 100\,GeV$	167.4 (62.6%)	10.7 (67.2%)	1280 (69.2%)
$R_\tau > 0.8$	35.5 (21.2%)	2.53 (23.7%)	175.4 (13.7%)
1 or 3 signal tracks	31.2 (88.0%)	2.37 (93.7%)	149.3 (85.1%)
Tracker isolation	27.8 (89.1%)	2.18 (91.9%)	132.9 (89.2%)
ECAL isolation	26.1 (93.7%)	2.07 (94.9%)	125.1 (94.1%)
$E_T^{max(HCAL\,cell)} > 2\,GeV$	24.1 (92.4%)	1.95 (94.2%)	105.1 (84.0%)
$IP_T^{leading\,track} < 0.3$	21.4 (88.8%)	1.92 (98.3%)	88.4 (84.1%)
$N_{hits}^{leading\,track} \geqslant 10$	19.9 (92.9%)	1.81 (94.4%)	84.6 (95.7%)
$\geqslant 3$ jets, $E_T > 20\,GeV$	17.3 (87.0%)	1.04 (57.6%)	67.5 (79.8%)
$140 < m_{top} < 210\,GeV/c^2$	12.2 (70.4%)	0.71 (67.7%)	26.6 (39.4%)
b discriminator > 1.5	5.81 (47.7%)	0.34 (48.1%)	1.09 (4.1%)
$E_T^{b\,jet} > 30\,GeV$	5.27 (90.6%)	0.30 (89.2%)	0.82 (75.1%)
Jet veto, $E_T^{jet} > 25\,GeV$	1.48 (28.1%)	0.24 (78.0%)	0.14 (17.2%)
$E_T^{Higgs} > 50\,GeV$	1.44 (97.1%)	0.23 (98.6%)	0.14 (98.3%)
$m_T(\tau\,\text{jet}, E_T^{miss}) > 100\,GeV/c^2$	0.03 (2.0%)	0.003 (1.3%)	0.02 (10.3%)
Events for $m_T > 100\,GeV/c^2$	0.86 ± 0.33	0.09 ± 0.04	0.60 ± 0.60
$\Delta\phi(\tau\text{jet}, E_T^{miss}) > 60^\circ$	0.01 (1.0%)	9.2×10^{-4} (0.4%)	0.013 (6.7%)
Events for $\Delta\phi(\tau\text{jet}, E_T^{miss}) > 60^\circ$	0.30 ± 0.25	0.03 ± 0.02	0.39 ± 0.39

About 84% of these muons were found to originate from $W \to \mu\nu_\mu$. The fraction of events containing at least one electron candidate with $p_T > 15\,GeV/c$ is 72.4% and an isolated electron candidate 41.7%. The final electron identification was done following the methods described in Ref. [156]. The fraction of events removed with a veto on the identified electrons is 7.9%, from which 93.3% are due to genuine electrons from $W \to e\nu_e$.

The missing transverse energy (E_T^{miss}) was reconstructed from the full calorimeter response summing the calorimeter towers and applying the jet energy corrections (Type 1 E_T^{miss} [147, 148]). The hadronic jets with $E_T^{raw} > 20\,GeV$ were calibrated using the corrections from γ+jet calibration. The τ jet was reconstructed in the calorimeter around the Level-1 τ-jet direction in a cone of 0.4 applying energy corrections evaluated for one- and three-prong τ decays. The offline E_T cut on the τ jet was taken to be $E_T^{\tau jet} > 100$ GeV, close to the Level-1 threshold of 93GeV. The tracks were reconstructed inside the jet reconstruction cone. The leading track was searched for in a cone of $R_m = 0.1$ around the τ-jet direction. For an efficient isolation against the hadronic jets a small signal cone of $R_S = 0.04$ was selected. The isolation cone size was taken to be the same as in the HLT Tau trigger, $R_i = 0.4$. The τ-jet isolation in the electromagnetic calorimeter was also applied as described in [280]. The fraction of signal events with $m_{H^\pm} = 200\,GeV/c^2$, where the one-prong (three-prong) τ decays lead to one (three) reconstructed track(s) with $p_T > 1\,GeV/c$ in the signal cone, was found to be in

92.3% (64%). Accidental track reconstruction problems, like shared hits, can lead to fake large-p_T tracks in the hadronic jets [7, 280]. These fake leading tracks are possible in the hadronic multi-jet events but can appear also in the $t\bar{t}$, Wt and W + 3 jet backgrounds if the E_T of the τ jet is below the trigger threshold and the event is triggered with a τ-like hadronic jet. The fake tracks can be suppressed with an upper bound in the transverse impact parameter of the leading track ($IP_T^{\text{leading track}} < 0.3$ mm) and requiring at least 10 hits in the full tracker. The fraction of the $\tau \to e\nu\nu$ events passing the full τ selection was found to be 3% for the $t\bar{t}$ background. This contamination can be efficiently suppressed requiring that the most energetic HCAL tower inside the τ-jet candidate ($E_T^{\text{max(HCAL cell)}}$) has the transverse energy greater than 2 GeV [280].

The τ helicity correlations are best exploited requiring the leading track to carry at least 80% of the τ jet energy. The efficiencies for the $t\bar{t}$ and Wt events, shown in Tables 11.17 and 11.18, are affected by the pre-selection cuts and do not show the expected background suppression for $R_\tau > 0.8$. This cut suppresses the three-prong τ decays leaving 3.1% as the fraction of three-prong τ decays for the signal events with $m_{H^\pm} = 200\,\text{GeV}/c^2$ after all selection cuts.

Due to a limited MC statistics, the trigger simulation was not used in the estimation of the QCD multi-jet background. Events with at least one jet with $E_T > 100$ GeV, containing a track with $p_T > 80$ GeV/c, were used for further analysis. Efficiency for this selection was found to be 5.55×10^{-3} for the QCD multi-jet events generated within the $\hat{p}_T$ interval of $170 < \hat{p}_T < 380\,\text{GeV}/c$. The τ selection cuts, except the E_T^{jet} threshold, are not correlated with the E_T^{miss} cut. Therefore the selection was factorised to E_T^{miss} and τ selections. The efficiency of the τ-selection cuts on the pre-selected events was found to be 1.65%. Combined with the pre-selection, the full τ-selection efficiency for the hadronic multi-jet events in the $\hat{p}_T$ interval considered was found to be 9.2×10^{-5}.

The $gg \to tbH^\pm$ events contain two b jets, one from the decay of the top quark and one associated b jet from the production process. The associated b quark is preferentially emitted in the forward directions and is distributed at smaller p_T values than the b quark from top decay. In about 20% of the signal events, however, this b quark is more energetic than the b quark from the top decay thus contaminating the spectrum of the identified b jet for the top reconstruction. The event reconstruction was performed for events where at least three hadronic jets with $E_T^{\text{jet}} > 20$ GeV were found. A probabilistic secondary vertex algorithm with a discriminator cut was used for b tagging [157]. The fraction of events where the best b-tagged jet is the b jet from $t \to bW$ was found to be 61%. The corresponding fractions for the associated b jets and the quark jets from $W \to qq$ decay were found to be $\sim 26\%$ and $\sim 8\%$, respectively.

The top-quark mass was reconstructed minimising the χ^2 distribution made from the reconstructed and nominal top and W masses, $\chi^2 = ((m_{jj} - m_W)/\sigma_W)^2 + ((m_{jjj} - m_{top})/\sigma_{top})^2$, where m_{jj} and m_{jjj} are the invariant masses of all two- and three-jet combinations in the event and σ_W and σ_{top} are the gaussian widths of the reconstructed true W and top mass distributions. The jet assigned to the top but not to the W presents the b jet from top. For a better reconstruction efficiency, in the presence of a significant contamination from the associated b quark, any of the three jets assigned to the top were tagged requiring the value of the discriminator greater than 1.5 and $E_T > 30$ GeV. A mass resolution of $\sim 11\%$ and a mean reconstructed mass of $\sim 176\ \text{GeV}/c^2$ were obtained, with a fraction of about 40% of correct jet assignments. For a further suppression of the $t\bar{t}$ background, the ordinal jets after top reconstruction were searched for within $|\eta| < 2.5$ and a jet veto was applied. The E_T threshold for the jet veto was set to 25 GeV. The efficiency of this method has decreased compared to

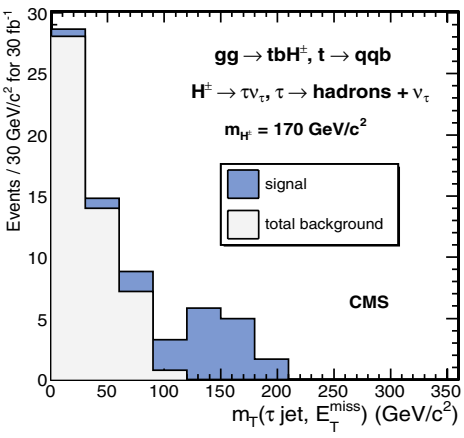

Figure 11.17. Transverse mass reconstructed from the τ jet and missing transverse energy for the $gg \to tbH^{\pm}$, $t \to bW$, $W^{\mp} \to jj$ signal (dark histogram) with $m_{H^{\pm}} = 170\,\mathrm{GeV/c^2}$, $\tan\beta = 30$ and for the total background (light histogram) for an integrated luminosity of $30\,\mathrm{fb}^{-1}$.

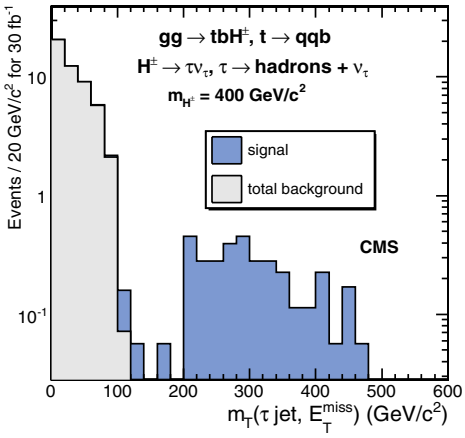

Figure 11.18. Transverse mass reconstructed from the τ jet and missing transverse energy for the $gg \to tbH^{\pm}$, $t \to bW$, $W^{\mp} \to jj$ signal (dark histogram) with $m_{H^{\pm}} = 400\,\mathrm{GeV/c^2}$, $\tan\beta = 30$ and for the total background (light histogram) for an integrated luminosity of $30\,\mathrm{fb}^{-1}$.

the fast simulation results [623] mainly due to more energetic associated b jets in $gg \to btH^{\pm}$ with respect to the $gb \to tH^{\pm}$ events.

For the $t\bar{t}$, Wt and W + 3jet backgrounds the configuration with large E_T^{miss} and large $E_T^{\tau\,jet}$ can be reached only for strongly boosted W. Therefore to suppress the background from events triggered with a fake τ from a hadronic jet recoiling against the genuine τ jet, a lower bound ($E_T^H > 50\,\mathrm{GeV}$) was set on the Higgs boson p_T reconstructed from the τ jet and the missing transverse energy.

The large E_T thresholds lead to an almost two-body (Jacobian peak) situation between the τ jet and missing transverse energy. Therefore an upper edge can be expected in the transverse mass $m_T = \sqrt{2 \times E_T^{\tau jet} \times E_T^{miss} \times (1 - \Delta\phi(\tau\mathrm{jet}, E_T^{miss}))}$ at $m_{H^{\pm}}$ for the signal and at m_W for the $t\bar{t}$, Wt and W+3jet backgrounds. The boost required for the $t\bar{t}$, Wt and W+3jet backgrounds to pass the E_T thresholds, leads to small opening angles $\Delta\phi(\tau$ jet, $E_T^{miss})$ in the transverse plane. Requiring $\Delta\phi > 60^{\circ}$ removes most of the remaining background for $m_T < 100\,\mathrm{GeV/c^2}$. The m_T distributions for the signal and total background are shown in Figs. 11.17 and 11.18 for $m_{H^{\pm}} = 170$ and $400\,\mathrm{GeV/c^2}$ and $\tan\beta = 30$, without a cut on $\Delta\phi(\tau$ jet, $E_T^{miss})$.

Tables 11.17 and 11.18 show the cross sections and efficiency for the selection cuts for the signal events with $m_{H^{\pm}} = 170$, 180, 200 and $400\,\mathrm{GeV/c^2}$ and $\tan\beta = 30$. The trigger efficiency and the efficiency of the primary vertex reconstruction are also shown. Table 11.18 shows the same for the $t\bar{t}$, Wt and W+3jet backgrounds. For the QCD multi-jet background the number of events where at least three jets are found after the E_T^{miss} and τ selections was estimated without the τ selection cuts. At this level of selection the QCD multi-jet events can be assumed to be similar to the W + 3jet events at the same selection level. Therefore the efficiency of the remaining selection cuts was taken from the W+3jet events yielding an estimate of 0.1 ± 0.1 events for $m_T(\tau$ jet, $E_T^{miss}) > 100\,\mathrm{GeV/c^2}$.

11.2.5.4. Systematic uncertainties on background determination. The background in the signal region $m_T(\tau$ jet, $E_T^{miss}) > 100\,\mathrm{GeV/c^2}$ may arise from two main sources, the tail due to measurement uncertainties in the backgrounds with $W \to \tau\nu$ decays, and the possibility of

Table 11.19. Value of $\tan\beta$, cross section times branching fraction for $gg \to tbH^{\pm}$, $H^{\pm} \to \tau^{\pm}\nu$, $\tau \to$ hadrons $+\,\nu$, number of selected signal events and the statistical significance (S) for the total background of 1.7 ± 1.0 events with ($S_{syst.}$) and without ($S_{no\,syst.}$) background uncertainty, for the signal with $m_{H^{\pm}} = 170$ to 600 GeV/c^2 ($m_A = 150$ to 600 GeV/c^2) and for an integrated luminosity of 30 fb^{-1}.

$m_{H^{\pm}}$ (GeV/c^2)	171.6	180.4	201.0	300.9	400.7	600.8
$\tan\beta$	30	30	30	30	50	50
σ(NLO) $\times$ BR (fb)	1359.2	1237.6	775.5	118.3	104.9	15.7
Events for 30 fb^{-1}	14.1 ± 1.6	14.7 ± 3.2	11.7 ± 2.3	8.3 ± 1.2	10.0 ± 1.4	2.0 ± 0.2
$S_{no\,syst.}$	6.4	6.6	5.5	4.2	4.9	1.2
$S_{syst.}$	5.0	5.2	4.3	3.3	3.8	1.0

fake τ jets, mainly in the QCD multi-jet events. The level of the backgrounds with $W \to \tau\nu$ decays can be measured from data exploiting the precise muon momentum measurement in the W+3jets, $W \to \mu\nu$ events, selecting events in the tail of the transverse mass distribution. The probability of a hadronic jet faking the τ jet can be measured exploiting the γ+jet events, as proposed in Ref. [280]. For this work a Monte-Carlo method was chosen assuming that the probability of the background events to migrate to the signal area depends mainly on the precision of the jet energy and E_T^{miss} measurements. The systematic uncertainty due to the energy scale was estimated varying the jet energy and the E_T^{miss} values with the expected energy scale uncertainties yielding the average values of 3% and 2% for the uncertainties on the efficiency of the E_T^{miss} cut and the efficiency of the selection of three hadronic jets for top reconstruction, respectively. The uncertainty of the τ identification has been estimated to be 8% for the E_T interval of τ jets from $Z \to \tau\tau$ decays [149]. For the b-tagging uncertainty a conservative estimate of 5% was taken. The theoretical uncertainty on the $t\bar{t}$ cross section due to a variation of the scale and PDF has been estimated to be 5.6% [159]. These values yield 11% for the total systematic uncertainty for the $t\bar{t}$ background. For the W+3jet and QCD multi-jet backgrounds the uncertainties due to present MC statistics strongly dominate the measurement uncertainties and therefore the MC statistical uncertainties were used. The total number of background events in the signal region $m_T(\tau\,\text{jet}, E_T^{miss}) > 100$GeV, is 1.7 ± 1.0 events, including the systematic and MC uncertainties.

11.2.5.5. Discovery potential. Table 11.19 shows the number of signal events for $m_{H^{\pm}} = 170$ to 300 GeV/c^2 with $\tan\beta = 30$ and for $m_{H^{\pm}} = 400$ to 600 GeV/c^2 with $\tan\beta = 50$ and the signal significance (S) calculated according to Poisson statistics [498] with (S_{syst}) and without ($S_{no\,syst.}$) background uncertainty for the total background of 1.7 ± 1.0 events. The cut in the transverse mass $m_T(\tau\,\text{jet}, E_T^{miss}) > 100$ GeV/c^2 is used to select the signal area. The results are shown for an integrated luminosity of 30 fb^{-1}. For the $t\bar{t}$ background the estimated systematic uncertainty of 11% is included. Figure 11.19 shows the 5σ-discovery region in the $m_A - \tan\beta$ plane in the maximal mixing scenario with $\mu = 200$ GeV/c^2 with and without systematic uncertainties at 30 fb^{-1}.

11.2.6. Charged Higgs boson of $M_H > m_t$ *in* $gg \to tbH^{\pm}$ *production with* $H^{\pm} \to tb$

The branching fractions for the decay channels of the charged Higgs boson depend strongly on its mass (see Fig. 11.2). For masses above $m_t + m_b$, the channel $H^{\pm} \to tb$ opens up. Two production channels and corresponding final states were considered in the search for charged Higgs bosons in the $H^{\pm} \to tb$ decay channel [629]:

$$gb \to tH^{\pm} \to ttb \to W^+W^-bbb \to qq'\mu\nu_\mu bbb, \tag{11.9}$$

$$gg \to tH^{\pm}b \to ttbb \to W^+W^-bbbb \to qq'\mu\nu_\mu bbbb. \tag{11.10}$$

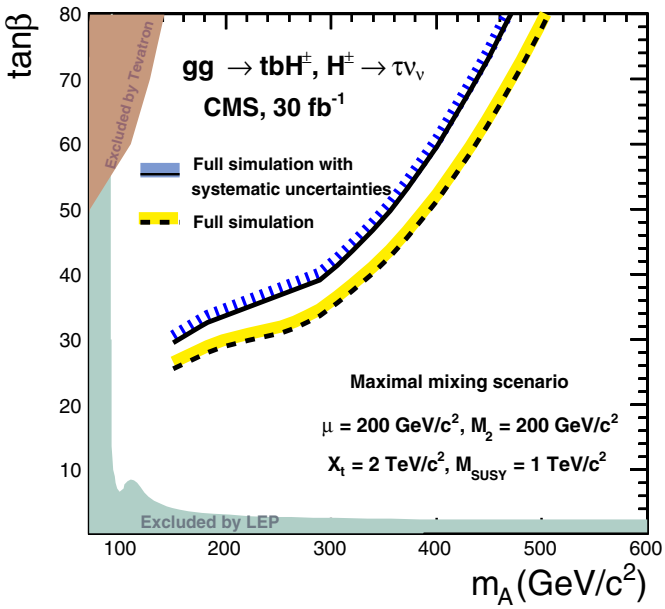

Figure 11.19. The 5σ-discovery region in the m_A-tan β plane for $gg \to tbH^{\pm}$, $H^{\pm} \to \tau\nu_{\tau}$ with an integrated luminosity of 30 fb^{-1} in the maximal mixing scenario with $\mu = 200$ GeV/c^2. The discovery regions with and without systematic uncertainties are shown. The regions excluded by the LEP and Tevatron searches are also shown in the figure.

These final states are the most interesting from the experimental point of view because an isolated muon is present to trigger on and the branching fraction into this decay is high ($\sim 30\%$).

The inclusive final state (11.9) is studied using triple b tagging within the parameterised simulation framework of CMS [11]. The final state (11.10), where a fourth b jet is resolved in the detector, is studied with full GEANT4 [9] CMS detector simulation [8]. Production of the $H^{\pm}$ bosons through heavy sparticle cascades is not taken into account. In addition, supersymmetric particles are supposed to be heavy enough, such that supersymmetric decays of the $H^{\pm}$ can be neglected.

A detailed description of the analysis can be found in [629].

11.2.6.1. Signal and background simulation. Events from the process (11.9) are modelled by considering the initial b quark as a massless parton from the corresponding parton density in the proton. On the other hand, events from the process (11.10) are described with massive spectator b quarks.

The calculation of the total signal cross section was performed at NLO [628], starting from the process (11.9). When calculating the cross section for both processes (11.9) and (11.10) to all orders, however, one expects to obtain the same result, as they both describe the same physics. Therefore, for both processes, the cross section was rescaled to the NLO result for the $pp \to tH^{\pm}X$ channel.

The signal cross section is sensitive to the two parameters $\tan\beta$ and $m_{H^{\pm}}$ (Fig. 11.20). The cross section is enhanced at small and large values of $\tan\beta$, with a minimum at $\tan\beta = \sqrt{m_t/m_b} \approx 6$. Furthermore, the cross section decreases rapidly with rising $m_{H^{\pm}}$. The generation of both processes (11.9) and (11.10) was performed with PYTHIA [69], forcing the

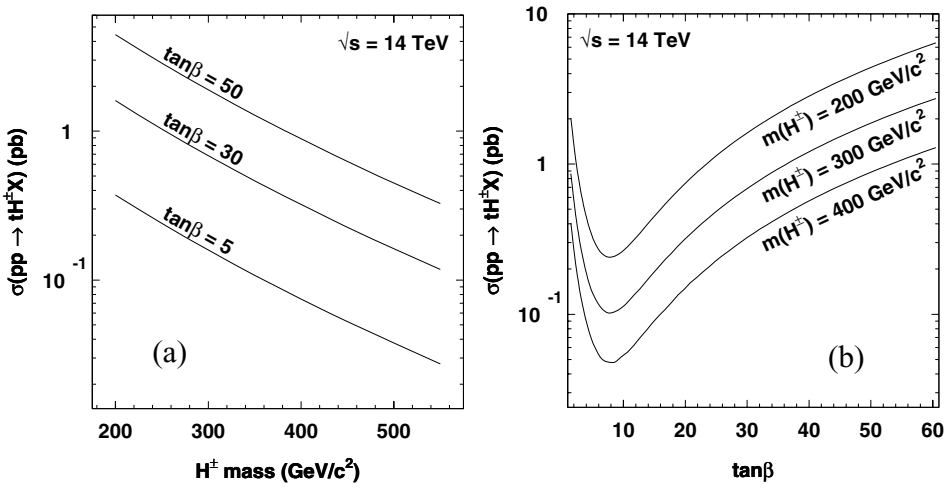

Figure 11.20. NLO cross section for $pp \to tH^{\pm}X$ as a function of (a) $m_{H^{\pm}}$ and (b) $\tan\beta$.

decay $H^{\pm} \to tb$ of the charged Higgs boson. The branching fraction $BR(H^{\pm} \to tb)$ for this decay process was calculated with HDECAY 3.0 [41].

The main background to charged Higgs boson production and decay through $pp \to tH^{\pm}(b) \to ttb(b)$ is the Standard Model top-quark pair production with additional jets. Other potential multi-jet backgrounds are much smaller and neglected.

In the case of process (11.9), the leading order background comes from SM $pp \to t\bar{t}b$ and $pp \to t\bar{t}$ + jet production, where in the latter the extra jet is misidentified as a b jet. The event simulation was performed using the matrix element generator `MadGraph/MadEvent` [81], interfaced to PYTHIA for parton shower, fragmentation and hadronisation, with a cut $p_T > 10\,\text{GeV/c}$ on the transverse momentum and $|\eta| < 2.5$ on the pseudorapidity of the extra jet. This resulted in a cross section of 678 pb.

The background for process (11.10) consists of the irreducible $pp \to t\bar{t}b\bar{b}$ and the reducible $pp \to t\bar{t}jj$ process, where in the latter two jets are misidentified as b jets. Both these backgrounds were simulated using the COMPHEP generator [43]. The generator level cuts $p_T > 15\,\text{GeV}$ and $|\eta| < 3$ were applied on the partons produced in association with the $t\bar{t}$ pair. A separation cut $\Delta R > 0.3$ was also imposed. This resulted in a cross section of 3.285 pb for the $pp \to t\bar{t}b\bar{b}$ process and 507.8 pb for $pp \to t\bar{t}jj$ production. Care was taken to avoid double counting between the $pp \to t\bar{t}b\bar{b}$ and $pp \to t\bar{t}jj$ processes and the cross section for $pp \to t\bar{t}jj$ was scaled to the result from a similar ALPGEN generation, where a jet matching technique was applied to more rigourously handle the transition between the hard interaction and the parton shower.

11.2.6.2. Event selection and reconstruction. On the final states (11.9) and (11.10) a basic event selection is applied on the reconstructed objects (Tables 11.20 and 11.21). Events passing the single muon HLT trigger are required to have at least one muon with $p_T > 20\,\text{GeV}$ and $|\eta| < 2.5$, at least respectively five or six calibrated jets with $E_T > 25\,\text{GeV}$ and $|\eta| < 2.5$ and at least respectively three or four of these jets tagged as b jet with a secondary vertex-based algorithm [157].

In both final states (11.9) and (11.10) the best jet association is selected with a likelihood ratio technique, which combines information from kinematical properties of the extra jets,

Table 11.20. Event selection yield for $\tan\beta = 30$ and an integrated luminosity of $30\,\mathrm{fb}^{-1}$.

$30\,\mathrm{fb}^{-1}$	$t\bar{t}b/t\bar{t}j$	$gb \to tH^{\pm}$ ($\tan\beta = 30$)					
$m_{H^{\pm}}$ ($\mathrm{GeV/c^2}$)		263	311	359	408	457	506
cross section × BR (pb)	678	0.850	0.570	0.377	0.251	0.169	0.116
# events before cuts	20.3M	25 489	17 088	11 319	7 529	5 063	3 472
single muon HLT	17%	16%	16%	16%	16%	16%	16%
1 muon	95%	95%	95%	95%	96%	96%	96%
5 jets	18%	35%	42%	44%	46%	49%	51%
3 b-tagged jets	6%	27%	29%	30%	32%	31%	29%
# remaining events	32 880	364	314	230	171	116	80

Table 11.21. Event selection yield for $\tan\beta = 30$ and an integrated luminosity of $30\,\mathrm{fb}^{-1}$.

$30\,\mathrm{fb}^{-1}$	$t\bar{t}b\bar{b}$	$t\bar{t}jj$	$gg \to tbH^{\pm}$ ($\tan\beta = 30$)					
$m_{H^{\pm}}$ ($\mathrm{GeV/c^2}$)			263	311	359	408	457	506
cross section × BR (pb)	2.386	235.8	0.850	0.570	0.377	0.251	0.169	0.116
# events before cuts	71 580	7.07M	25 489	17 088	11 319	7 529	5 063	3 472
single muon HLT	19%	19%	13%	13%	13%	13%	13%	13%
1 muon	96%	97%	96%	95%	97%	97%	97%	97%
6 jets	19%	23%	19%	23%	25%	26%	28%	31%
4 b-tagged jets	7%	0.55%	6%	5%	7%	7%	5%	6%
# remaining events	179	1 623	37	24	25	18	9	8

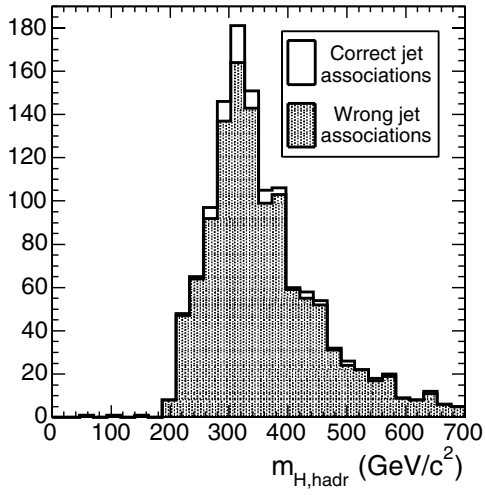

Figure 11.21. Reconstructed $H^{\pm}$ mass with hadronically decaying top for the chosen jet association ($m_{H^{\pm}} = 311\,\mathrm{GeV/c^2}$).

b-tagging of all jets and the result of a kinematic fit on the $t\bar{t}$ system, imposing both $W^{\pm}$ and t mass constraints. Starting from the chosen jet association the Higgs boson mass was reconstructed. An ambiguity remains, as it is not possible to know which top quark candidate the additional b jet should be combined with. In Fig. 11.21 the reconstructed charged Higgs boson mass with hadronically decaying top is shown for correct and wrong jet pairings in the case of three tagged b jets and for $m_{H^{\pm}} = 311\mathrm{GeV}/c^2$. Due to the large combinatorial

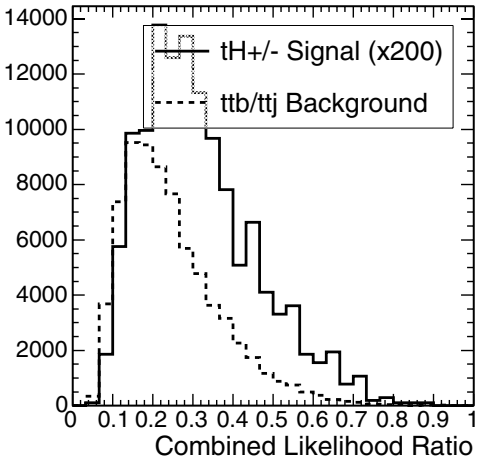

Figure 11.22. Distribution of the discriminator used to distinguish between signal 11.9 and background.

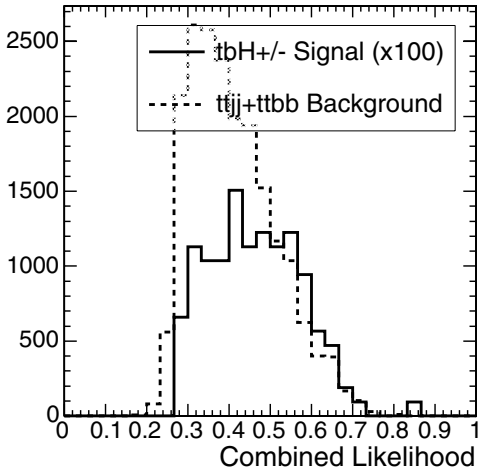

Figure 11.23. Distribution of the discriminator used to distinguish between signal 11.10 and background.

background, the mass information is of limited use for the separation between signal and background, and is therefore not used further on in the analysis.

11.2.6.3. Background suppression. To suppress the large $\mathrm{t\bar{t}}$ + jets background, observables were identified that have different properties for signal and background events. These observables were combined into an overall discriminator. In the case of process (11.9) the b-tagging information for the extra jet was used, together with the p_{T} of the softest jet from the $\mathrm{W}^{\pm}$ decay and the ratio of the E_{T} of the sixth jet and the fifth. For the process (11.10) only the b-tagging information for the two extra jets was used. In Figs. 11.22 and 11.23 the resulting discriminator distributions are shown for the process (11.9) and (11.10) respectively.

11.2.6.4. Discovery reach and systematics. A cut on the discriminating variables of Figs. 11.22 and 11.23 was optimised to obtain the maximal statistical significance for an integrated luminosity of $30\,\mathrm{fb}^{-1}$. The signal cross section required for a significance of 5, corresponding to a discovery, was derived and translated into a minimal value of $\tan\beta$ needed for a discovery for a given value of m_{A}. Performing this analysis and optimisation at different values of m_{A} a discovery contour was obtained in the MSSM ($\tan\beta$, m_{A}) plane.

The background is large in both final states and therefore the effect of systematic uncertainties on the knowledge of the background is important. A possible way to estimate the background level from data is to require one b-tagged jet less. After such a selection it is possible to calculate the expected number of background events plus its uncertainty, when tagging a third or fourth b jet. Optimistically the uncertainty on the mistag rate can be taken as 5%. Possible large theoretical uncertainties related to this method, like the ratio of events with real extra b jets and events with only light extra jets, should still be accounted for.

Depending on the expected systematic uncertainty on the background level the maximal significance was searched. In Fig. 11.24 the discovery contours are plotted for the final states (11.9) and (11.10) respectively, when supposing perfect knowledge of the background cross section ($\varepsilon = 0$), a 1% uncertainty ($\varepsilon = 0.01$), and a 3% uncertainty ($\varepsilon = 0.03$). From

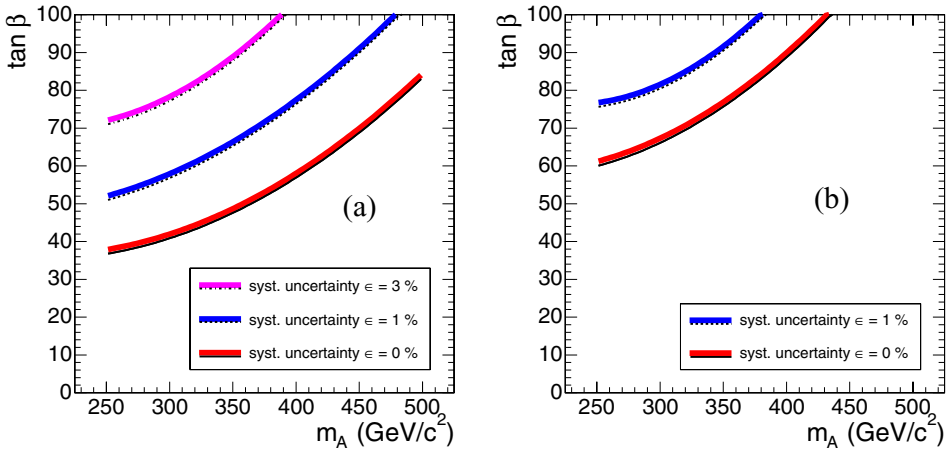

Figure 11.24. Discovery contour for the charged Higgs boson in the $H^{\pm} \to tb$ decay for 30 fb^{-1}, (a) applying 3 b tags, (b) applying 4 b tags; systematic uncertainties on the background of $\varepsilon = 0\%$, $\varepsilon = 1\%$ and $\varepsilon = 3\%$ are taken into account.

the above estimate of the systematic uncertainty on the number of background events, the conclusion is drawn that, neglecting SUSY cascade decays, no visibility for this channel is obtained in the MSSM parameter space during the low luminosity phase of LHC.

11.2.7. Search for the $A \to Zh$ decay with $Z \to \ell^+\ell^-$, $h \to b\bar{b}$

The observation of the CP-odd pseudo-scalar Higgs (A) via its decay into a Z boson and the lighter CP-even scalar Higgs (h) followed by $Z \to e^+e^-$, $\mu^+\mu^-$ and $h \to b\bar{b}$ decays provides an interesting way to detect A and h simultaneously. The largest branching ratio of the $A \to Zh$ appears for low $\tan\beta$ and $m_Z + m_h \leqslant m_A \leqslant 2m_{top}$ mass region. The main production mechanism for A at low $\tan\beta$ is via gg, qq$\to$ A.

The decays of the A into charginos and neutralinos ($A \to \chi\chi$), however, can dominate at certain values of μ and M_2 (Higgs-Higgsino and SU(2) gaugino mass parameters) since the masses of charginos and neutralinos as well as their couplings to the Higgs bosons depend on μ and M_2 (in addition to $\tan\beta$ and M_A). Large values of μ and M_2 are more favourable for the observation of the $A \to Zh$ channel.

In Fig. 11.25 the production cross section multiplied by the appropriate branching ratios (including $Z \to e^+e^-$, $\mu^+\mu^-$ and $h \to b\bar{b}$ decays) is shown as a function of M_A in the m_h^{max} scenario with $\mu = M_2 = 200\,GeV/c^2$ and $\mu = M_2 = 600\,GeV/c^2$ for two values of $\tan\beta$, 1 and 5. One can see that the difference in the total cross sections for the two choices of the μ and M_2 parameters can be as large as one order of magnitude. The $A \to Zh$ analysis and the discovery reach presented below was evaluated in the m_h^{max} scenario with $\mu = M_2 = 600\,GeV/c^2$.

11.2.7.1. Event generation, simulation and reconstruction. The Higgs boson production processes, gg$\to$ A and pp $\to$ A $b\bar{b}$, were generated using PYTHIA 6.225 [69] for three values of M_A (250, 300, 350 GeV/c^2) and two values of $\tan\beta$ (1.0, 5.0). No pre-selection at generation level was applied. The Standard Model backgrounds considered are: the $Zb\bar{b}$ generated with COMPHEP [355] and ZZ, ZW, Z+jets, W+jets and $t\bar{t}$ generated with PYTHIA 6.215. Events were fully simulated and digitised with pile-up corresponding to a luminosity of $2 \times 10^{33} cm^{-2} s^{-1}$.

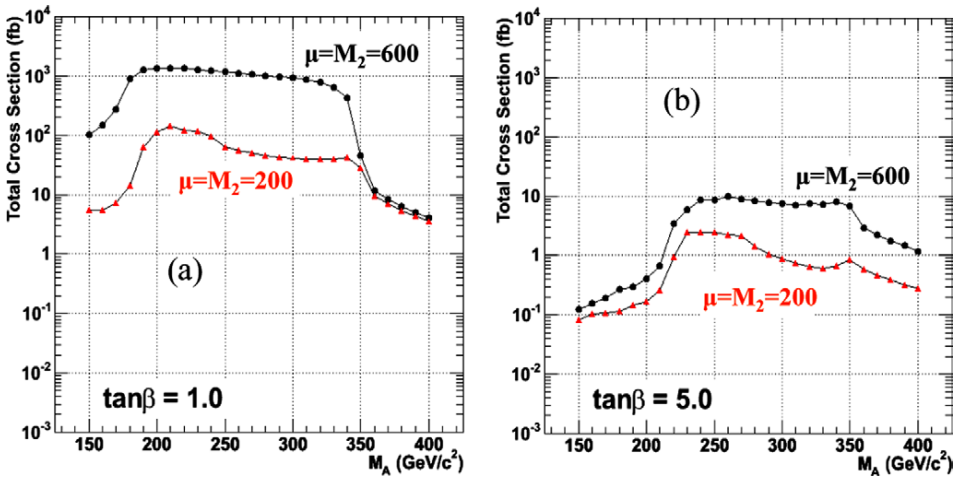

Figure 11.25. The production cross-section multiplied by appropriate branching ratios as a function of M_A in the m_h^{max} scenario with $\mu = M_2 = 600\,\mathrm{GeV/c^2}$ (circles) and $\mu = M_2 = 200\,\mathrm{GeV/c^2}$ (triangles) for (a) $\tan\beta = 1$ and (b) $\tan\beta = 5$.

Offline reconstruction of electrons, muons, jets and b tagging were performed using standard algorithms.

11.2.7.2. Online selection. The events are required to pass the global Level-1 (L1) and High Level Trigger (HLT) dimuon or dielectron selections since there will always be a real Z in the event decaying into two high p_T electrons or muons. The inclusion of the single muon and electron triggers does not improve the discovery reach in the M_A-$\tan\beta$ plane.

11.2.7.3. Off-line event selection. The baseline selection requires two opposite sign high p_T isolated leptons (e or μ) and two high E_T tagged b-jets separated from the leptons with $\Delta R(\ell, j) > 0.7$. Muons must have $|\eta| < 2.4$ and electrons should be in the ECAL fiducial region ($|\eta| < 2.5$ with $1.444 < |\eta| < 1.566$ region excluded). The event is required to have small missing E_T and reconstructed invariant mass of the leptons close to the Z mass in order to reject a significant fraction of the $t\bar{t}$ background.

Table 11.22 summarises the basic selection variables and thresholds. The variation of the signal significance with the change of the p_T thresholds on the electrons, muons and b-jets, and the thresholds on the b-tagging discriminant for the two tagged jets has been checked. No significant variation was found with small changes of the cut values presented in Table 11.22.

11.2.7.4. Results. The selection efficiencies for the signal vary from 5% to 12% depending on the M_A and $\tan\beta$ values as well as the production mechanism. The details can be found in [630]. The next-to-leading order (NLO) background cross sections before and after selections are shown in Table 11.23.

The signal and the background distributions of $M_{b\bar{b}}$ and $M_{\ell^+\ell^- b\bar{b}}$ after selections are shown in Fig. 11.26 and Fig. 11.27 respectively for $30\,\mathrm{fb}^{-1}$ of integrated luminosity.

11.2.7.5. Systematic uncertainties. The method to evaluate the background from the real data measuring the background in the signal free (normalisation) region is proposed.

Table 11.22. Selection variables and thresholds.

Selection Variable	Threshold
most energetic electron/muon p_T	> 30 GeV/c
second-most energetic electron/muon p_T	> 15 GeV/c
most energetic b-jet E_T	> 25 GeV
second-most energetic b-jet E_T	> 20 GeV
missing E_T	< 60 GeV
most energetic b-jet discriminator	> 1.5
second-most energetic b-jet discriminator	> 0.5
Z mass cut	$84\,\mathrm{GeV/c^2} < M_Z < 96\,\mathrm{GeV/c^2}$
Z p_T	> 30.0 GeV/c

Table 11.23. Background cross sections.

	NLO cross sections (fb)	
	before selection	after selection
$Zb\bar{b}$, $Z \to ee, \mu\mu, \tau\tau$	112830	415.26
$t\bar{t}$, $W \to e\nu, \mu\nu, \tau\nu$	88500	70.8
Z+jets, $Z \to ee, \mu\mu, \tau\tau$	5300000	83.05
W+jets, $W \to e\nu, \mu\nu, \tau\nu$	47900000	0.0
ZZ (inclusive)	14985	7.34
ZW (inclusive)	49422	1.98

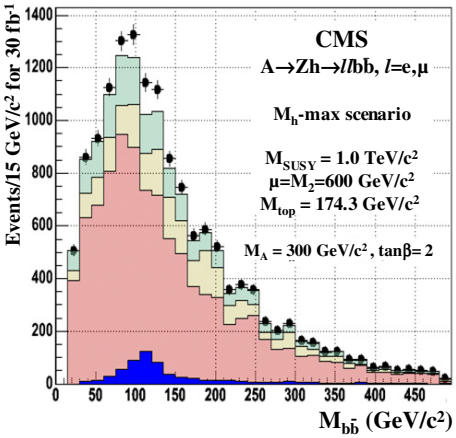

Figure 11.26. Distribution of $M_{b\bar{b}}$ for signal and background after event selection for $30\,\mathrm{fb}^{-1}$ of integrated luminosity. Red (dark gray), yellow (light gray) and green (medium gray) distributions represent the $Zb\bar{b}$, $t\bar{t}$ and Z+jets backgrounds. Blue (black) distribution is the signal ($M_A = 300$, $\tan\beta = 2$) and black dots the data (sum of the signal and the background).

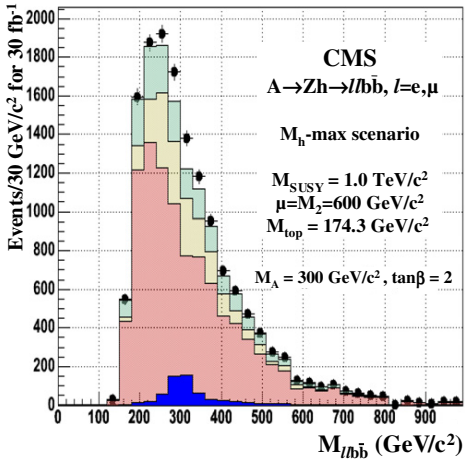

Figure 11.27. Distribution of $M_{\ell^+\ell^-b\bar{b}}$ for signal and background after event selection for $30\,\mathrm{fb}^{-1}$ of integrated luminosity. Red (dark gray), yellow (light gray) and green (medium gray) distributions represent the $Zb\bar{b}$, $t\bar{t}$ and Z+jets backgrounds. Blue (black) distribution is the signal ($M_A = 300$, $\tan\beta = 2$) and black dots the data (sum of the signal and the background).

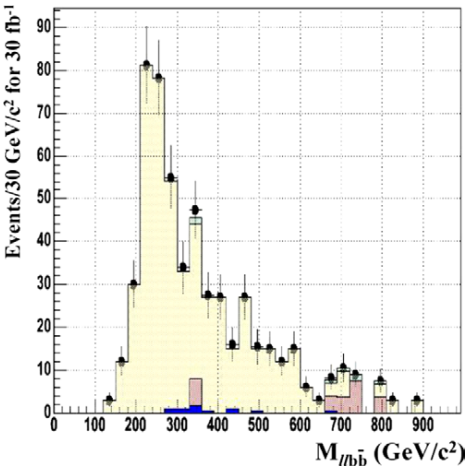

Figure 11.28. Distribution of $M_{\ell^+\ell^-b\bar{b}}$ in the $t\bar{t}$ background normalisation region. Colour code is as in Fig. 11.27.

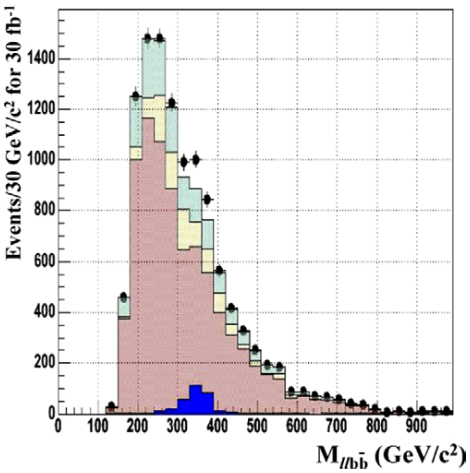

Figure 11.29. Distribution of $M_{\ell^+\ell^-b\bar{b}}$ used in the $Zb\bar{b}$ background estimation. Colour code is as in Fig. 11.27.

The background uncertainty then consists of the statistical uncertainty of the background measurement in the normalisation region and the systematic uncertainty of the ratio of the background in the signal and the normalisation region.

The normalisation region for the $t\bar{t}$ background is defined by the same selection as for the signal search, except the missing E_T which is required to be bigger than 120 GeV. With such a selection 544 events were found for 30 fb^{-1} with high purity (93.4%), thus giving the statistical uncertainty of 4.4%. The distribution of $M_{\ell^+\ell^-b\bar{b}}$ in the $t\bar{t}$ normalisation region can be seen in Figure 11.28. The contamination comes mainly from $Zb\bar{b}$ events (6%). The 5% missing E_T scale uncertainty gives 18.5% uncertainty on the number of the $t\bar{t}$ events in the signal region. Therefore the overall uncertainty in the estimation of the $t\bar{t}$ background is 19.0%.

For the irreducible $Zb\bar{b}$ background a similar idea can be used. In order to suppress the $t\bar{t}$ contribution as much as possible, missing $E_T < 40$ GeV was used. Applying a lower cut in the $M_{\ell^+\ell^-b\bar{b}}$ distribution of 500 GeV/c^2, 920 Zbb events were found with a purity of around 95% for 30 fb^{-1}. Contamination comes mainly from $t\bar{t}$ events. The accuracy of measuring the $Zb\bar{b}$ background is around 3.4% taking into account only statistics. The distribution of $M_{\ell^+\ell^-b\bar{b}}$ for those events can be seen in Figure 11.29 before the application of the $M_{\ell^+\ell^-b\bar{b}}$ 500 GeV/c^2 cut. The uncertainty of 5% on the missing E_T scale and the uncertainty of 3% on the jet energy scale lead to correspondingly 3.6% and 2.5% of the uncertainty of the $Zb\bar{b}$ background estimate in the signal region. Thus the overall uncertainty in the estimation of the $Zb\bar{b}$ background is 5.6%.

11.2.7.6. Discovery reach in the $M_A - \tan\beta$ plane. Figure 11.30 shows the 5 σ discovery contours in the (M_A, $\tan\beta$) plane for 30 and 60 fb^{-1} of integrated luminosity in the m_h^{max} scenario with $\mu = M_2 = 600\,GeV/c^2$. For the calculation of the signal significance the signal and background events were counted in mass windows of $\pm 1.5\sigma$ around the reconstructed masses of M_h and M_A. Since only three different M_A masses and two $\tan\beta$ values were available, the estimations for the rest of M_A, $\tan\beta$ parameter space was done using extra/interpolations of the signal efficiencies from the available parameter points. The

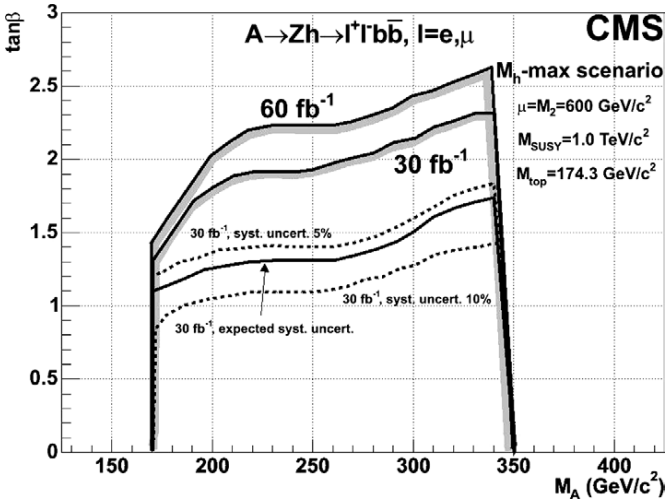

Figure 11.30. The 5σ discovery contours for 30 and 60 fb^{-1} integrated luminosity. The effect of underestimation or overestimation of the background systematic uncertainty can be seen in the curve of 30 fb^{-1}.

statistical significance for 5, 10% (dashed lines) as well as the estimated (full line) uncertainty for the background is also shown for 30 fb^{-1} of integrated luminosity.

11.2.8. Search for $\mathrm{A}^0/\mathrm{H}^0 \to \chi_2^0\chi_2^0 \to 4\ell + E_{\mathrm{T}}^{\mathrm{miss}}$ *channel in mSUGRA*

11.2.8.1. Introduction. In some regions of the SUSY parameter space, heavy neutral Higgs bosons can be searched for using their decay modes to supersymmetric particles. This is the case in particular in the difficult low and intermediate $\tan\beta$ region of the parameter space which is not accessible through the $\mathrm{A}^0/\mathrm{H}^0 \to \tau\tau$ decay channel as the coupling of the Higgs boson to taus is not sufficiently enhanced.

One of the most promising channel is the $\mathrm{A}^0/\mathrm{H}^0$ decay into a pair of next-to-lightest neutralinos, χ_2^0, followed by the decay $\chi_2^0 \to \ell^+\ell^-\chi_1^0$ (with $\ell = e, \mu$). This process results in a clean four leptons plus missing transverse energy final state:

$$\mathrm{A}^0/\mathrm{H}^0 \to \chi_2^0\chi_2^0 \to 4\ell + \mathrm{E}_{\mathrm{T}}^{\mathrm{miss}}.$$

There are two main categories of backgrounds to such process: SUSY and Standard Model backgrounds. In the SUSY category the dominant source of background is the production of leptons from the decays of squarks and gluinos which cascade to charginos and neutralinos. Unlike the neutralinos from the Higgs boson decay, the leptons in this case are produced in association with quarks and gluons. Therefore, the associated large hadronic activity can be used to suppress this type of background. An additional but smaller source of backgrounds come from the direct production of slepton or gaugino pairs via the Drell–Yan processes and the direct production of χ_2^0 pairs. The rejection of these backgrounds is more difficult, as the hadronic activity in these events is very small. In the Standard Model category, three processes which yield the same signature of 4 leptons in the final state contribute as backgrounds: ZZ^*/γ^*, $Zb\bar{b}$ and $t\bar{t}$.

Table 11.24. Chosen benchmark points.

Point	m_0 (GeV/c^2)	$m_{1/2}$ (GeV/c^2)	A_0 (GeV/c^2)	$\tan\beta$	sign(μ)
A	60	175	0	10	+
B	80	200	0	5	+
C	50	150	0	5	+

11.2.8.2. Analysis. The study is performed in the minimal Super Gravity constrained version of the MSSM (mSUGRA) [631]. To determine the regions where the signal has a sizeable branching ratio times cross section, a scan of the parameters space $(m_0, m_{1/2})$ for tan $\beta = 5, 10$, sign$(\mu) = +$ and $A_0 = 0$ is performed. Three benchmark points are defined for the evaluation of CMS sensitivity. The corresponding mSUGRA parameters are presented in Table 11.24.

The signal and SUSY background datasets are generated using ISASUGRA and PYTHIA. A pre-selection at generator level is applied, asking for $e^+e^-\mu^+\mu^-$ final state with e(μ) $p_T > 7(5)$ GeV/c and $|\eta| < 2.5$. The fast detector simulation is carried out using FAMOS.

The online selection of the events is a logical or of the dielectron and dimuon triggers. The offline reconstruction of electrons and muons is performed using FAMOS standard algorithms. Events are then analysed as follow:

- $e^+e^-\mu^+\mu^-$ final state is selected;
- the four leptons are required to be isolated;
- a jet veto is applied, requiring no jets with $E_T > 25$ GeV and $|\eta| < 5.0$;
- events must have E_T^{miss} and $p_{T(\ell\ell\ell\ell)}$ less than 80 GeV/c;
- a Z veto is imposed, *i.e.* events with a dilepton pair with invariant mass in the range $m_Z \pm 10$ GeV/c^2 are rejected;
- further optimisations are performed by introducing an upper limit to the dilepton invariant masses and by applying a cut on the four lepton invariant mass.

The signal acceptances w.r.t the production cross section times branching ratio are 6.3%, 5.1% and 2.5% respectively for point A, B and C, whereas the acceptances for SUSY backgrounds are 1.5×10^{-4}%, 3.6×10^{-4}% and 2.6×10^{-4}% respectively w.r.t. the total the SUSY production cross section.

11.2.8.3. Results. Figure 11.31 shows the invariant mass distribution of the four leptons for the 3 benchmarks points. Results are given for an integrated luminosity of 30 fb^{-1}.

Figure 11.32 shows the extrapolated 5σ-discovery regions in the $(m_0, m_{1/2})$ plane, for an integrated luminosity of 30 fb^{-1}. The values of the other mSUGRA parameters are $A_0 = 0$, $sign(\mu) = +$ and $\tan\beta = 5, 10$. The complex structure of the high significance region is mainly determined by the effective cross section of $A^0/H^0 \to \chi_2^0\chi_2^0 \to 4\ell + E_T^{miss}$. The A^0/H^0 could therefore be discovered through their decays to neutralino pairs in the region $150 < m_{1/2} < 250$ and $m_0 < 120$ for $\tan\beta = 10$ and in the region $150 < m_{1/2} < 250$ and $30 < m_0 < 120$ for $\tan\beta = 5$.

11.3. Discovery reach and measurement of MSSM parameters

11.3.1. Benchmark scenarios for MSSM Higgs boson searches

11.3.1.1. Why benchmarks — which benchmarks? The tree-level values for the CP-even Higgs bosons of the MSSM, M_h and M_H, are determined by $\tan\beta$, the CP-odd Higgs-boson

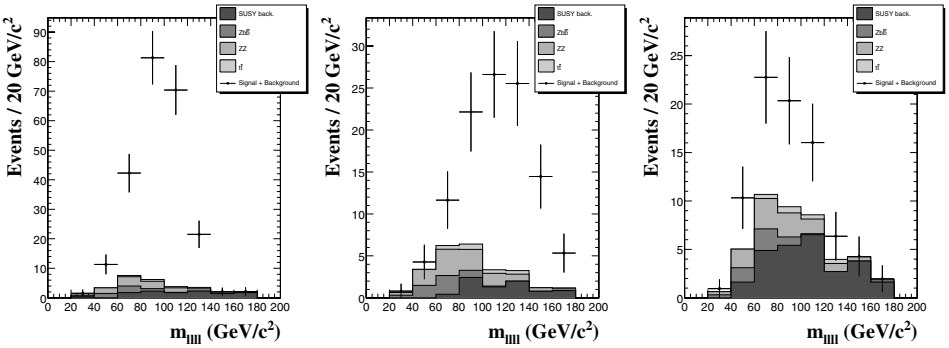

Figure 11.31. Four lepton invariant mass distributions for the 3 benchmark points. Distributions are shown for the signal+backgrounds (points) and for the contribution of each process (histograms).

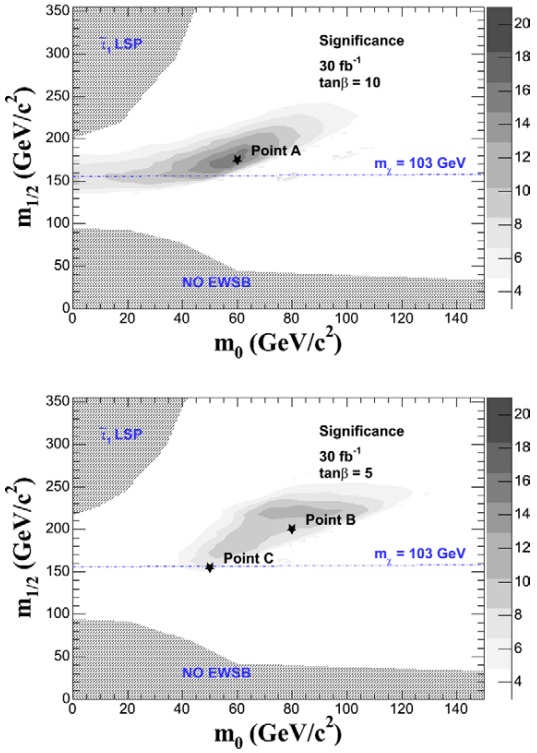

Figure 11.32. For integrated luminosity of $30\,\mathrm{fb}^{-1}$ the 5σ-discovery regions for $\mathrm{A}^0/\mathrm{H}^0 \to \chi_2^0\chi_2^0 \to 4\ell + \mathrm{E}_\mathrm{T}^\mathrm{miss}$ channel in the $(m_0, m_{1/2})$ plane for fixed $A_0 = 0$, $\mathrm{sign}(\mu) = +$ and $\tan\beta = 5, 10$.

mass M_A, and the Z boson mass M_Z. The mass of the charged Higgs boson, $M_{H^\pm}$, is given in terms of M_A and the W boson mass, M_W. Beyond the tree-level, the main correction to the Higgs boson masses stems from the $t/\tilde{t}$ sector, and for large values of $\tan\beta$ also from the $b/\tilde{b}$ sector, see Section 11.1. Sub-leading corrections come from all other sectors of the MSSM.

In this way the Higgs sector phenomenology is connected to the full spectrum of the MSSM via radiative corrections.

In the unconstrained version of the MSSM no particular SUSY breaking mechanism is assumed, but rather a parametrisation of all possible soft SUSY breaking terms is used. This leads to more than a hundred parameters (masses, mixing angles, phases) in this model in addition to the ones of the Standard Model. While a detailed scanning over the more-than-hundred-dimensional parameter space of the MSSM is clearly not practicable, even a sampling of three- or four-dimensional parameter space of certain SUSY-breaking models (such as mSUGRA, GMSB or AMSB) is beyond the present capabilities for phenomenological studies, in particular when it comes to simulating experimental signatures within the detectors. For this reason one often resorts to specific benchmark scenarios, i.e. one studies only specific parameter points [632,633] or samples of one- or two-dimensional parameter space [263,634,635], which exhibit specific characteristics of the MSSM parameter space. Benchmark scenarios of this kind are often used, for instance, for studying the performance of different experiments at the same collider. Similarly, detailed experimental simulations of MSSM particle production with identical parameters in the framework of different colliders can be very helpful for developing strategies for combining pieces of information obtained at different machines [5].

The question of which parameter choices are useful as benchmark scenarios depends on the purpose of the actual investigation. If one is interested, for instance, in setting exclusion limits on the SUSY parameter space from the non-observation of SUSY signals at the experiments performed up to now, it is useful to use a benchmark scenario which gives rise to "conservative" exclusion bounds. An example of a benchmark scenario of this kind is the $m_h^{\max}$-scenario [635] used for the Higgs search at LEP [566]. It gives rise to maximal values of the lightest CP-even Higgs-boson mass (for fixed values of the top-quark mass and the SUSY scale) and thus allows one to set conservative bounds on $\tan\beta$ and M_A [544]. Another application of benchmark scenarios is to study "typical" experimental signatures of SUSY models and to investigate the experimental sensitivities and the achievable experimental precisions for these cases. For this purpose it seems reasonable to choose "typical" (a notion which is of course difficult to define) and theoretically well motivated parameters of certain SUSY-breaking scenarios. Examples of this kind are the benchmark scenarios used so far for investigating SUSY searches at the LHC [632,633] and at the ILC [636]. As a further possible goal of benchmark scenarios, one can choose them so that they account for a wide variety of SUSY phenomenology. For this purpose, it can also be useful to consider "pathological" regions of parameter space or "worst-case" scenarios. Examples for this are the "small α_{eff} scenario" [635] for the Higgs search at LEP, for which the decay $h \to b\bar{b}$ or $h \to \tau^+\tau^-$ can be significantly suppressed.

A related issue concerning the definition of appropriate benchmarks is whether a benchmark scenario chosen for investigating physics at a certain experiment or for testing a certain sector of the theory should be compatible with additional information from other experiments (or concerning other sectors of the theory). This refers in particular to constraints from cosmology (by demanding that SUSY should give rise to an acceptable dark matter density [637–640]) and low-energy measurements such as the rate for $b \to s\gamma$ [641,642] and the anomalous magnetic moment of the muon, $(g-2)_\mu$ [643,644]. On the one hand, applying constraints of this kind gives rise to "more realistic" benchmark scenarios. On the other hand, one relies in this way on further assumptions (and has to take account of experimental and theoretical uncertainties related to these additional constraints), and it could eventually turn out that one has inappropriately narrowed down the range of possibilities by applying these constraints. This applies in particular if slight modifications of the model under

consideration are possible that have a minor impact on collider phenomenology but could significantly alter the bounds from cosmology and low-energy experiments. For instance, the presence of small flavour mixing terms in the SUSY Lagrangian could severely affect the prediction for BR($b \to s\gamma$), while allowing a small amount of R-parity violation in the model would strongly affect the constraints from dark matter relic abundance while leaving collider phenomenology essentially unchanged. The extent to which additional constraints of this kind should be applied to possible benchmark scenarios is related to the actual purpose of the benchmark scenario. For setting exclusion bounds in a particular sector (e.g. the Higgs sector) it seems preferable to apply constraints from this sector only.

11.3.1.2. The relevant MSSM parameters. Beyond the tree-level, the main correction to the Higgs boson masses and couplings comes from the $t/\tilde{t}$ sector, and for large values of $\tan\beta$ also from the $b/\tilde{b}$ sector. In order to fix our notations, we list the conventions for the inputs from the scalar top and scalar bottom sector of the MSSM: the mass matrices in the basis of the current eigenstates $\tilde{t}_L, \tilde{t}_R$ and $\tilde{b}_L, \tilde{b}_R$ are given by

$$\mathcal{M}^2_{\tilde{t}} = \begin{pmatrix} M^2_{\tilde{t}_L} + m_t^2 + \cos 2\beta \left(\frac{1}{2} - \frac{2}{3}s_W^2\right) M_Z^2 & m_t X_t \\ m_t X_t & M^2_{\tilde{t}_R} + m_t^2 + \frac{2}{3}\cos 2\beta s_W^2 M_Z^2 \end{pmatrix}, \tag{11.11}$$

$$\mathcal{M}^2_{\tilde{b}} = \begin{pmatrix} M^2_{\tilde{b}_L} + m_b^2 + \cos 2\beta \left(-\frac{1}{2} + \frac{1}{3}s_W^2\right) M_Z^2 & m_b X_b \\ m_b X_b & M^2_{\tilde{b}_R} + m_b^2 - \frac{1}{3}\cos 2\beta s_W^2 M_Z^2 \end{pmatrix}, \tag{11.12}$$

where

$$m_t X_t = m_t(A_t - \mu \cot\beta), \quad m_b X_b = m_b (A_b - \mu \tan\beta). \tag{11.13}$$

Here A_t denotes the trilinear Higgs-stop coupling, A_b denotes the Higgs-sbottom coupling, and μ is the Higgsino mass parameter.

SU(2) gauge invariance leads to the relation

$$M_{\tilde{t}_L} = M_{\tilde{b}_L}. \tag{11.14}$$

For the numerical evaluation, a convenient choice is

$$M_{\tilde{t}_L} = M_{\tilde{b}_L} = M_{\tilde{t}_R} = M_{\tilde{b}_R} =: M_{\mathrm{SUSY}}. \tag{11.15}$$

We furthermore use the short-hand notation

$$M_S^2 := M^2_{\mathrm{SUSY}} + m_t^2. \tag{11.16}$$

Accordingly, the most important parameters for the corrections in the Higgs sector are m_t, M_{SUSY}, X_t and X_b (or equivalently A_t and A_b), μ and $\tan\beta$. The Higgs sector observables furthermore depend on the SU(2) gaugino mass parameter, M_2. The other gaugino mass parameter, M_1, is usually fixed via the GUT relation

$$M_1 = \frac{5}{3}\frac{s_W^2}{c_W^2} M_2. \tag{11.17}$$

At the loop level also the gluino mass, $m_{\tilde{g}}$, enters the predictions for the Higgs-boson phenomenology.

It should be noted in this context that the results for Higgs boson sector observables have been obtained in different schemes. Most commonly these are the on-shell (OS) renormalisation scheme (in the Feynman-diagrammatic (FD) approach), and $\overline{\mathrm{MS}}$ scheme (for the renormalisation group (RG) approach) [645]. Owing to the different schemes used in the FD and the RG approach for the renormalisation in the scalar top sector, the parameters

X_t and M_{SUSY} are also scheme-dependent in the two approaches. This difference between the corresponding parameters has to be taken into account when defining the benchmark scenarios. In a simple approximation the relation between the parameters in the different schemes is at $\mathcal{O}(\alpha_s)$ given by [645]

$$M_S^{2,\overline{\mathrm{MS}}} \approx M_S^{2,\mathrm{OS}} - \frac{8}{3}\frac{\alpha_s}{\pi} M_S^2, \tag{11.18}$$

$$X_t^{\overline{\mathrm{MS}}} \approx X_t^{\mathrm{OS}} + \frac{\alpha_s}{3\pi} M_S \left(8 + 4\frac{X_t}{M_S} - 3\frac{X_t}{M_S}\log\left(\frac{m_t^2}{M_S^2}\right)\right). \tag{11.19}$$

At large $\tan\beta$ and large $|\mu|$ the corrections from the $b/\tilde{b}$ sector can become especially important. The leading effects are included in the effective Lagrangian formalism [563]. Numerically this is by far the dominant part of the contributions from the sbottom sector (see also Refs. [547,548]). The effective Lagrangian is given by

$$\mathcal{L} = \frac{g}{2M_W}\frac{\overline{m}_b}{1+\Delta_b}\Bigg[\tan\beta\; A\, i\, \bar{b}\gamma_5 b + \sqrt{2}\, V_{tb}\, \tan\beta\, H^+ \bar{t}_L b_R + \left(\frac{\sin\alpha}{\cos\beta} - \Delta_b \frac{\cos\alpha}{\sin\beta}\right) h \bar{b}_L b_R - \left(\frac{\cos\alpha}{\cos\beta} + \Delta_b \frac{\sin\alpha}{\sin\beta}\right) H \bar{b}_L b_R\Bigg] + \text{h.c.}. \tag{11.20}$$

Here $\overline{m}_b$ denotes the running bottom quark mass including SM QCD corrections. The pre-factor $1/(1+\Delta_b)$ in Eq. 11.20 arises from the resummation of the leading corrections to all orders. The function Δ_b consists of two main contributions, an $\mathcal{O}(\alpha_s)$ correction from a sbottom–gluino loop and an $\mathcal{O}(\alpha_t)$ correction from a stop–Higgsino loop. The explicit form of Δ_b in the limit of $M_S \gg m_t$ and $\tan\beta \gg 1$ reads [563]

$$\Delta_b = \frac{2\alpha_s}{3\pi} m_{\tilde{g}}\, \mu\, \tan\beta \times I(m_{\tilde{b}_1}, m_{\tilde{b}_2}, m_{\tilde{g}}) + \frac{\alpha_t}{4\pi} A_t\, \mu\, \tan\beta \times I(m_{\tilde{t}_1}, m_{\tilde{t}_2}, \mu). \tag{11.21}$$

The function I is given by

$$I(a,b,c) = \frac{1}{(a^2-b^2)(b^2-c^2)(a^2-c^2)}\left(a^2b^2\log\frac{a^2}{b^2} + b^2c^2\log\frac{b^2}{c^2} + c^2a^2\log\frac{c^2}{a^2}\right) \sim \frac{1}{\max(a^2,b^2,c^2)}. \tag{11.22}$$

It becomes obvious that the size and the sign of μ is especially relevant for this type of corrections.

11.3.1.3. The benchmark scenarios. Since at the tree-level the Higgs sector of the MSSM is governed by two parameters (in addition to M_Z and the SM gauge couplings), it seems reasonable to define benchmarks in which all SUSY parameters are fixed and only the two tree-level parameters, M_A and $\tan\beta$ are varied. For the search of the heavy MSSM Higgs bosons corrections from the $b/\tilde{b}$ sector can be especially relevant. In this case it is also appropriate to vary μ. We review the definition of the benchmark scenarios as defined in Refs. [263,635]. Another very important parameter is the top-quark mass. For sake of simplicity and to make different analyses readily comparable to each other a fixed value of $m_t = 175$ GeV can be used. Alternatively the current experimental value can be used as input.

The m_h^{max} scenario. This scenario was designed to obtained conservative $\tan\beta$ exclusion bounds [544] at LEP [566]. The parameters are chosen such that the maximum possible

Higgs-boson mass as a function of $\tan\beta$ is obtained (for fixed $M_{\rm SUSY}$, and M_A set to its maximal value, $M_A = 1$ TeV). The parameters are[48]:

$$\begin{aligned} &m_t = 175\,\text{GeV}, \quad M_{\rm SUSY} = 1\,\text{TeV}, \quad \mu = 200\,\text{GeV}, \quad M_2 = 200\,\text{GeV}, \\ &X_t^{\rm OS} = 2\,M_{\rm SUSY}\ \text{(FD calculation)}, \quad X_t^{\overline{\rm MS}} = \sqrt{6}\,M_{\rm SUSY}\ \text{(RG calculation)} \\ &A_b = A_t, \quad m_{\tilde g} = 0.8\,M_{\rm SUSY}. \end{aligned} \tag{11.23}$$

The no-mixing scenario. This benchmark scenario is the same as the $m_h^{\rm max}$ scenario, but with vanishing mixing in the $\tilde t$ sector and with a higher SUSY mass scale to avoid the LEP Higgs bounds [62,566],

$$\begin{aligned} &m_t = 175\,\text{GeV}, \quad M_{\rm SUSY} = 2\,\text{TeV}, \quad \mu = 200\,\text{GeV}, \quad M_2 = 200\,\text{GeV}, \\ &X_t = 0\ \text{(FD/RG calculation)}, \quad A_b = A_t, \quad m_{\tilde g} = 0.8\,M_{\rm SUSY}. \end{aligned} \tag{11.24}$$

The gluophobic Higgs scenario. In this scenario the main production cross section for the light Higgs boson at the LHC, $gg \to h$, is strongly suppressed. This can happen due to a cancellation between the top quark and the stop quark loops in the production vertex (see Ref. [502]). This cancellation is more effective for small $\tilde t$ masses and hence for relatively large values of the $\tilde t$ mixing parameter, X_t. The partial width of the most relevant decay mode, $\Gamma(h \to \gamma\gamma)$, is affected much less, since it is dominated by the W boson loop. The parameters are:

$$\begin{aligned} &m_t = 175\,\text{GeV}, \quad M_{\rm SUSY} = 350\,\text{GeV}, \quad \mu = 300\,\text{GeV}, \quad M_2 = 300\,\text{GeV}, \\ &X_t^{\rm OS} = -750\,\text{GeV}\ \text{(FD calculation)}, \quad X_t^{\overline{\rm MS}} = -770\,\text{GeV}\ \text{(RG calculation)}, \\ &A_b = A_t, \quad m_{\tilde g} = 500\,\text{GeV}. \end{aligned} \tag{11.25}$$

In the left plot of Fig. 11.33 we show $[\sigma \times \text{BR}]_{\rm MSSM}/[\sigma \times \text{BR}]_{\rm SM}$ for the channel $gg \to h \to \gamma\gamma$ in the $M_A - \tan\beta$-plane. This channel can be strongly suppressed over the whole parameter plane, rendering this detection channel difficult.

The small $\alpha_{\rm eff}$ scenario. Besides the channel $gg \to h \to \gamma\gamma$ at the LHC, other channels for light Higgs searches at the Tevatron and at the LHC rely on the decays $h \to \bar b b$ and $h \to \tau^+\tau^-$. If $\alpha_{\rm eff}$ is small, these two decay channels can be heavily suppressed in the MSSM due to the additional factor $-\sin\alpha_{\rm eff}/\cos\beta$ compared to the SM coupling. Such a suppression occurs for large $\tan\beta$ and not too large M_A for the following parameters:

$$\begin{aligned} &m_t = 175\,\text{GeV}, \quad M_{\rm SUSY} = 800\,\text{GeV}, \quad \mu = 2.5\,M_{\rm SUSY}, \quad M_2 = 500\,\text{GeV}, \\ &X_t^{\rm OS} = -1100\,\text{GeV}\ \text{(FD calculation)}, \quad X_t^{\overline{\rm MS}} = -1200\,\text{GeV}\ \text{(RG calculation)}, \\ &A_b = A_t, \quad m_{\tilde g} = 500\,\text{GeV}. \end{aligned} \tag{11.26}$$

In the right plot of Fig.11.33 we show $[\sigma \times \text{BR}]_{\rm MSSM}/[\sigma \times \text{BR}]_{\rm SM}$ for the channel $WW \to h \to \tau^+\tau^-$ in the $M_A - \tan\beta$-plane. Significant suppression occurs for large $\tan\beta$, $\tan\beta > 20$, and small to moderate M_A, $M_A < 400$ GeV. Thus, Higgs boson search via the WW fusion channel will be difficult in these parts of the parameter space.

11.3.1.4. Variation of μ. The most sensitive channels for detecting heavy MSSM Higgs bosons at the LHC are the channel $pp \to H/A + X$, $H/A \to \tau^+\tau^-$ (making use of different

[48] Better agreement with BR $(b \to s\gamma)$ constraints is obtained for the other sign of X_t (called the "constrained $m_h^{\rm max}$" scenario). However, this lowers the maximum M_h values by ~ 5 GeV.

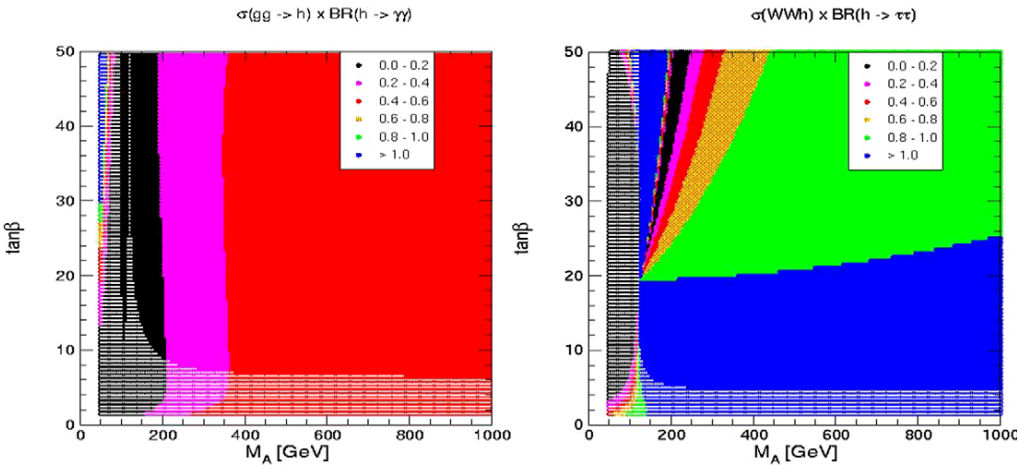

Figure 11.33. $[\sigma \times \mathrm{BR}]_{\mathrm{MSSM}}/[\sigma \times \mathrm{BR}]_{\mathrm{SM}}$ is shown for the channels $gg \to h \to \gamma\gamma$ in the gluophobic Higgs scenario (left plot) and $WW \to h \to \tau^+\tau^-$ in the small α_{eff} scenarios (right plot) in the $M_A - \tan\beta$-plane. The hatched area is excluded by LEP Higgs searches.

decay modes of the two τ leptons) and the channel $tH^{\pm}$, $H^{\pm} \to \tau\nu_{\tau}$ (for $M_{H^{\pm}} > m_t$). These channels show good prospects for $M_A \gg M_Z$ and large $\tan\beta$.

As discussed above, in this part of the parameter space the corrections from the $b/\tilde{b}$ sector can be very important and thus the size and the sign of μ can play a dominant role. This lead to the definition of an extension of the m_h^{max} and the no-mixing scenario by the following values of μ [263]

$$\mu = \pm 200, \pm 500, \pm 1000\,\mathrm{GeV}, \tag{11.27}$$

allowing both an enhancement and a suppression of the bottom Yukawa coupling and taking into account the limits from direct searches for charginos at LEP. It should be noted that the values $\mu = -500, -1000\,\mathrm{GeV}$ can lead to such a large enhancement of the bottom Yukawa coupling that a perturbative treatment is no longer possible in the region of very large values of $\tan\beta$. Some care is therefore necessary to assess up to which values of μ reliable results can be obtained.

A further variation of the discovery reach is caused by the decays of the heavy Higgs bosons into supersymmetric particles. For a given value of μ, the rates of these decay modes are strongly dependent on the particular values of the weak gaugino mass parameters M_2 and M_1. Since the Higgs couplings to neutralinos and charginos depend strongly on the admixture between Higgsino and gaugino states, the rate of these processes is strongly suppressed for large values of $|\mu| > 500$ GeV. In general, the effects of the decays $H/A \to \tilde{\chi}_i^0\tilde{\chi}_j^0$, $\tilde{\chi}_k^{\pm}\tilde{\chi}_l^{\mp}$ only play a role for $M_A > |\mu| + M_1$. Outside this range the dependence of the rates on μ is relatively weak.

11.3.2. Discovery reach in the $\mathrm{M_A} - \tan\beta$ *plane*

This section summarises the discovery reach in the M_{A}-$\tan\beta$ plane for the charged and the neutral MSSM Higgs bosons in the $\mathrm{m_h^{max}}$ scenario. The cross sections and branching ratios for the neutral Higgs bosons and the branching ratios for the charged Higgs boson were calculated with FeynHiggs 2.3.2 [142–144]. The next-to-leading order cross section for the

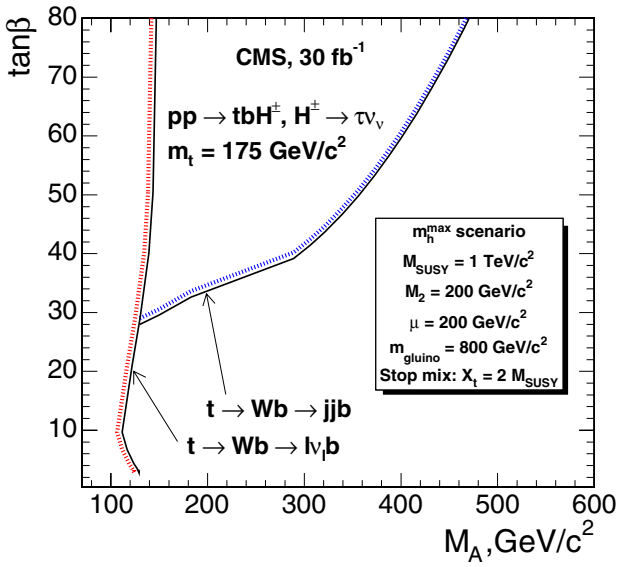

Figure 11.34. The 5σ discovery regions for the charged Higgs boson with the $\tau\nu$ decay mode in the m_h^{max} scenario.

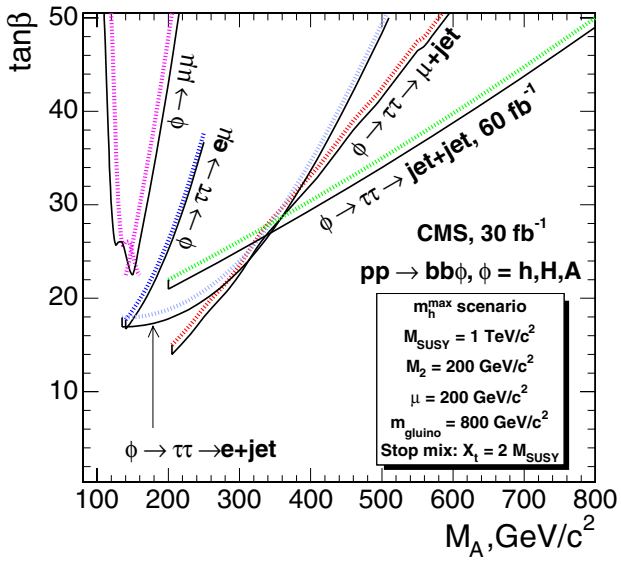

Figure 11.35. The 5σ discovery regions for the neutral Higgs bosons ϕ (ϕ = h, H, A) produced in the association with b quarks $pp \to b\bar{b}\phi$ with the $\phi \to \mu\mu$ and $\phi \to \tau\tau$ decay modes in the m_h^{max} scenario.

charged Higgs production was taken from Refs. [628], [597]. The NLO cross sections for the background processes were used, when available.

Figure 11.34 shows the 5σ discovery regions for the charged Higgs boson produced in the $pp \to tbH^{\pm}$ process with the $H^{\pm} \to \tau^{\pm}\nu_{\tau}$ ($\tau \to$ hadrons) decay mode. Figure 11.35

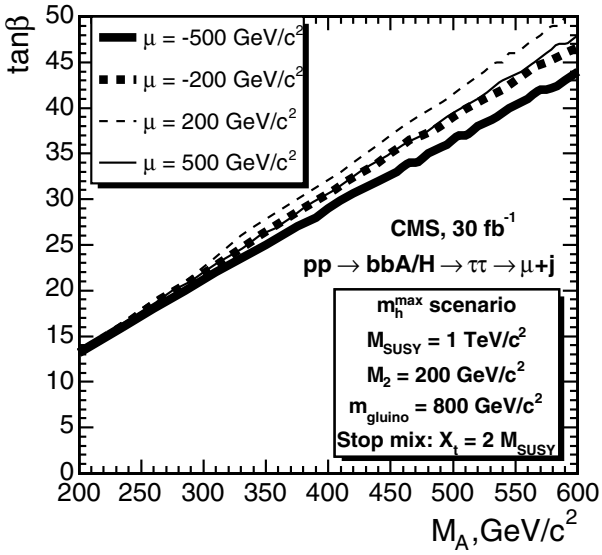

Figure 11.36. Variation of the 5σ discovery potential for the neutral Higgs bosons in the $\tau\tau \to \mu$+jet decay mode with μ in the m_h^{max} scenario.

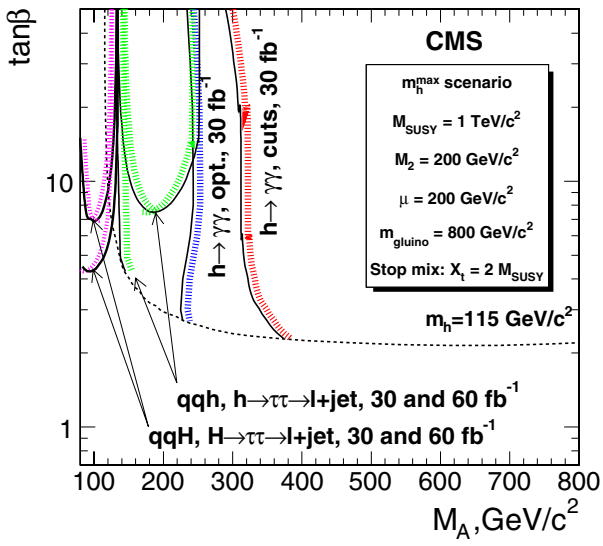

Figure 11.37. The 5σ discovery regions for the light, neutral Higgs boson h from the inclusive pp $\to$ h+X production with the h $\to \gamma\gamma$ decay and for the light and heavy scalar Higgs bosons, h and H, produced in the vector boson fusion qq $\to$ qqh(H) with the h(H) $\to \tau\tau \to \ell$+jet decay in the m_h^{max} scenario.

shows the 5σ discovery regions for the neutral Higgs boson ϕ ($\phi = $ h, H, A) produced in the association with b quarks pp $\to b\bar{b}\phi$ with the $\phi \to \mu\mu$ and $\phi \to \tau\tau$ decay modes. In both figures the discovery reach was evaluated in the m_h^{max} scenario with $\mu = 200\,\mathrm{GeV/c^2}$ (See Section 11.3.1).

The discovery reach was evaluated also in the extended m_h^{max} scenario (see Section 11.3.1.3 and [263]) with the values of $\mu = -200$ and $\pm 500\,\mathrm{GeV/c^2}$. The Fig. 11.36 presents the variation of the 5σ discovery potential for the neutral Higgs boson produced in the association with b quarks $pp \to b\bar{b}\phi$ with the $\phi \to \tau\tau \to \mu$+jet decay mode. The combination of the effects from supersymmetric radiative corrections and decay modes into supersymmetric particles gives rise to a rather complicated dependence of the discovery contour on μ. This results in a variation of the discovery region, especially for large M_A and large $\tan\beta$. For the positive values of μ the inclusion of the supersymmetric radiative corrections leads to a shift of the discovery region toward higher values of $\tan\beta$.

Figure 11.37 shows the 5σ discovery regions for the light, neutral Higgs boson h from the inclusive $pp \to h+X$ production with the $h \to \gamma\gamma$ decay and for the light and heavy scalar Higgs bosons, h and H, produced in the vector boson fusion $qq \to qqh(H)$ with the $h(H) \to \tau\tau \to \ell$+jet decay.

Chapter 12. Search for Higgs Boson in Non-SUSY Models

12.1. Scalar sector of 5D Randall–Sundrum model

The Randall–Sundrum model (RS) [94, 646] has recently received much attention because it could provide a solution to the hierarchy problem [565], by means of an exponential factor in a five dimensional nonfactorisable metric. In the simplest version the RS model is based on a five dimensional universe with two four-dimensional hypersurfaces (branes), located at the boundary of the fifth coordinate. By placing all the Standard Model fields on the visible brane all the mass terms, which are of the order of the Planck mass, are rescaled by the exponential factor, to a scale of the order of a TeV. The fluctuations in the metric in the fifth dimension are described in terms of a scalar field, the radion, which in general mixes with the Higgs boson. This scalar sector of the RS model is parameterised in terms of a dimensionless Higgs boson radion mixing parameter ξ, of the Higgs boson and radion masses m_h, m_ϕ and the vacuum expectation value of the radion field Λ_ϕ.

The phenomenology of Higgs boson and radion at LHC has been subject to several studies [647–652] concentrating mainly on Higgs and radion processes. The Higgs boson and radion detection is not guaranteed in all the parameter space region. The presence in the Higgs radion sector of trilinear terms opens the possibility of $\phi \to hh$ and $h \to \phi\phi$ decays. For example, for $m_h = 120\,\mathrm{GeV/c^2}$, $\Lambda_\phi = 5\,\mathrm{TeV/c^2}$ and $m_\phi \sim 250$–$350\,\mathrm{GeV/c^2}$ the BR($\phi \to hh$) ranges between 20 and 30%.

The CMS discovery potential is estimated for the decay of the radion in a pair of Higgs bosons, with $\gamma\gamma b\bar{b}$, $\tau\tau b\bar{b}$ and $b\bar{b}b\bar{b}$ final states and for an integrated luminosity of $30\,\mathrm{fb^{-1}}$. The study has been carried out for the radion mass of $300\,\mathrm{GeV/c^2}$ and the Higgs boson mass of $125\,\mathrm{GeV/c^2}$. The sensitivity was evaluated in the (ξ,Λ_ϕ) plane, with systematics uncertainties included.

A detailed description of the analysis can be found in [653]. A brief summary of the analysis and the results is presented below.

12.1.1. The $\phi \to hh$ analysis with the $\gamma\gamma b\bar{b}$ and $\tau\tau b\bar{b}$ final states

Signal events $gg \to \phi \to hh$ were generated with PYTHIA. The cross sections and branching ratios were evaluated using rescaled NLO cross sections for the SM Higgs boson and a modified HDECAY program. For the radion and a Higgs boson mass points considered ($m_h = 125\,\mathrm{GeV/c^2}$, $m_\phi = 300\,\mathrm{GeV/c^2}$) and for $\Lambda_\phi = 1\,\mathrm{TeV/c^2}$ the maximal cross section times branching ratio is 71 fb for $\gamma\gamma b\bar{b}$ final state. For the $\tau\tau b\bar{b}$ final state with the topology considered in the analysis, one τ lepton decaying leptonically and the other τ lepton decaying hadronically (producing a τ jet), the maximal cross section times branching ratio is 960 fb. This maximal cross section is reached for the radion mixing parameter $\xi = -0.35$.

For the $\gamma\gamma b\bar{b}$ final state the irreducible backgrounds $\gamma\gamma$jj (j = u, d, s, g) (generated with COMPHEP) and the $\gamma\gamma c\bar{c}$ and $\gamma\gamma b\bar{b}$ (generated with MADGRAPH) were studied. The reducible background from γ+three jets and four-jet processes was not evaluated directly, but assumed to be the same as in for the inclusive $h \to \gamma\gamma$ analysis [19], namely 40% of the total background after all selection. For the $\tau\tau b\bar{b}$ final state, the $t\bar{t}$, Z+jets, W+jets backgrounds (generated with PYTHIA) and the $b\bar{b}Z$ background (generated with COMPHEP) were studied.

The $\gamma\gamma b\bar{b}$ events were required to pass the Level-1 and HLT diphoton trigger. In the off-line analysis two photon candidates with $E_T^{\gamma 1,\gamma 2} > 40, 25\,\mathrm{GeV}$ were required to pass tracker cuts and calorimeter isolation cuts. Events with only two calorimeter jets of $E_T > 30\,\mathrm{GeV}$ and within $|\eta| < 2.4$ were selected. At least one of these jets must be tagged as a b-jet. Finally, the

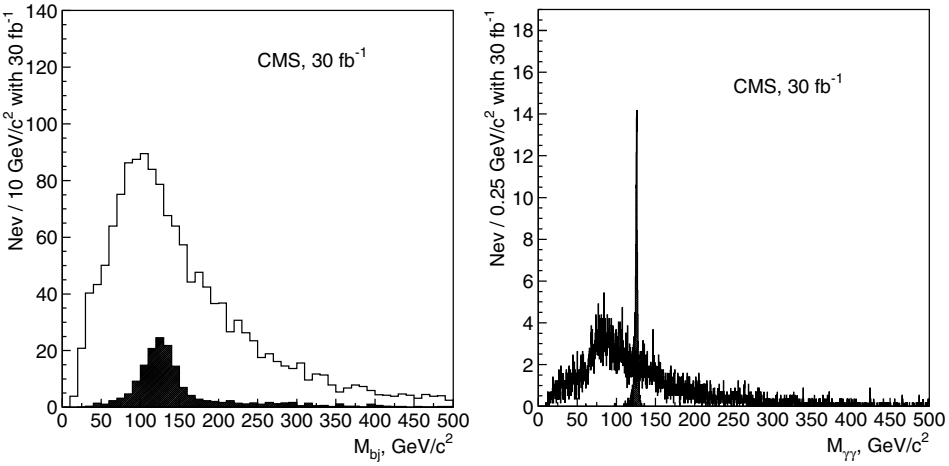

Figure 12.1. The dijet (left plot) and the diphoton (right plot) mass distribution for the background (open histogram) and the signal of $\phi \to hh \to \gamma\gamma b\bar{b}$ (full black histogram) after all selections except the mass window cuts with 30 fb^{-1}. The signal is shown for the maximal cross section times branching ratios point in (ξ $-\Lambda_\phi$) plane.

diphoton mass, $M_{\gamma\gamma}$, was required to be in a window of $\pm 2\,GeV/c^2$, the dijet mass, $M_{j\bar{b}}$, in a window of $\pm 30\,GeV/c$ and the diphoton-dijet mass, $M_{\gamma\gamma b\bar{b}}$, in a window $\pm 50\,GeV/c^2$ around the Higgs and Radion mass. Figure 12.1 shows the dijet (left plot) and the diphoton (right plot) mass distribution for the background (open histogram) and the signal of $\phi \to hh \to \gamma\gamma b\bar{b}$ (full, black histogram) after all selections except the mass window cuts, and for $30\,fb^{-1}$. The signal is shown for the maximal cross section times branching ratios point in (ξ-Λ_ϕ) plane. Figure 12.2 (left plot) shows the $M_{\gamma\gamma bj}$ distribution for the background (dashed histogram) and for the signal of $\phi \to hh \to \gamma\gamma b\bar{b}$ plus background (solid histogram) after all selections, and for $30\,fb^{-1}$.

The $\tau\tau b\bar{b}$ events were selected by the single electron and muon triggers and by the combined e-plus-τ-jet and the μ-plus-τ-jet triggers. In the off-line analysis a lepton and τ-jet identification was performed. The requirements on the jets were similar to the ones used in the $\gamma\gamma b\bar{b}$ analysis. In addition a cut of the transverse mass of the lepton and missing transverse momentum, $M_T^{\ell\nu} < 35\,GeV/c^2$ was applied to suppress the $t\bar{t}$ and W+jets backgrounds. The diτ-lepton mass was reconstructed using the missing transverse energy as described in Section 5.2.5. The significance of the discovery was calculated using expected number of the signal and background events after the mass window selections: $100 < M_{bj} < 150\,GeV/c^2$, $100 < M_{\tau\tau} < 160\,GeV/c^2$ and $280 < M_{\tau\tau bj} < 330\,GeV/c^2$. Figure 12.2 (right plot) shows the $M_{\tau\tau bj}$ distribution for the background (full, grey (yellow) histogram) and for the signal of $\phi \to hh \to \tau\tau b\bar{b}$ plus background (points with error bars) after all selections, for $30\,fb^{-1}$. Fitted curves for the background and the signal plus background are superimposed.

The four b-jet final state yields the highest rate for the signal. The maximal cross section times branching ratio at $\Lambda_\phi = 1\,TeV/c^2$ is 10.3 pb, which results in about 3.1×10^5 signal events for $30\,fb^{-1}$. The effective triggering and selection in the off-line analysis of these events is, however a big challenge due to the huge multi-jet background rate. In fact the remaining background is a few orders of magnitude larger than the signal in the relevant mass range. Techniques can be envisaged to normalise the background directly from a signal-free region and predict the number of background events in the signal region. In order to make a 3σ

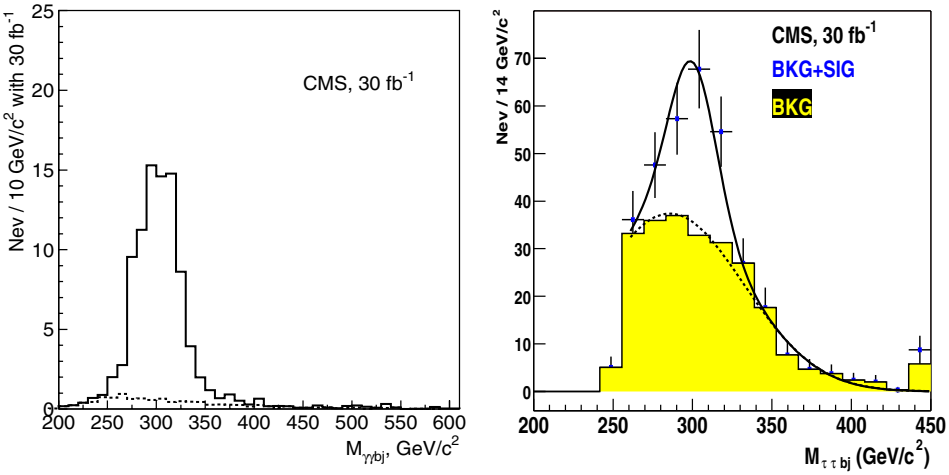

Figure 12.2. Left plot: the $M_{\gamma\gamma bj}$ distribution for the background (dashed histogram) and for the signal of $\phi \to hh \to \gamma\gamma b\bar{b}$ plus background (solid histogram) after all selections for 30 fb^{-1}. Right plot: the $M_{\tau\tau bj}$ distribution for the background (full grey (yellow) histogram) and for the signal of $\phi \to hh \to \tau\tau b\bar{b}$ plus background (black points with the error bars) after all selections for 30 fb^{-1}. The fitted curves for the background and signal plus background are superimposed. On both plots the signal is shown for the maximal cross section times branching ratios point in (ξ-Λ_ϕ).

discovery, such extrapolation needs to be performed with a precision of about 0.1%, making four b-jet channel essentially hopeless.

The background contribution to the $\gamma\gamma b\bar{b}$ final state can be determined directly from the $\gamma\gamma$-plus-two-jets data obtained after all selections, except the final mass window cuts on the $M_{\gamma\gamma}$, $M_{j\bar{b}}$ and $M_{\gamma\gamma b\bar{b}}$. The signal-to-background ratio is always less than 10% before the mass cuts are applied. The final cuts on the $M_{\gamma\gamma}$, $M_{j\bar{b}}$ and $M_{\gamma\gamma b\bar{b}}$ introduce a systematic uncertainty on the number of the background events expected after these cuts. This uncertainty is determined by the following factors: the energy scale uncertainty for the photons and jets, and the theoretical uncertainty of the shape of the mass distributions due to the scale and PDF uncertainties. Figure 12.3 (left plot) shows the 5σ discovery contours for the $\phi \to hh \to \gamma\gamma b\bar{b}$ channel for 30 fb^{-1}. The solid (dashed) contour shows the discovery region without (with) the effects of the systematic uncertainties.

For the $\tau\tau b\bar{b}$ final state the background uncertainty due to the experimental selections was estimated to be between 5% and 10% [653]. Figure 12.3 (right plot) shows the 5σ discovery contours for the $\phi \to hh \to \tau\tau b\bar{b}$ channel for 30 fb^{-1}. The two contours corresponds to the variation of the background NLO cross sections due to the scale uncertainty. The 5% experimental systematics on the background is taken into account.

12.2. Doubly charged Higgs boson pair production in the Littlest Higgs model

The main motivation of the Large Hadron Collider (LHC) experiments is to reveal the secrets of electroweak symmetry breaking. If the standard model (SM) Higgs boson will be discovered, the question arises what stabilises its mass against the Planck scale quadratically divergent radiative corrections. The canonical answer to this question is supersymmetry which implies very rich phenomenology of predicted sparticles in the future collider experiments.

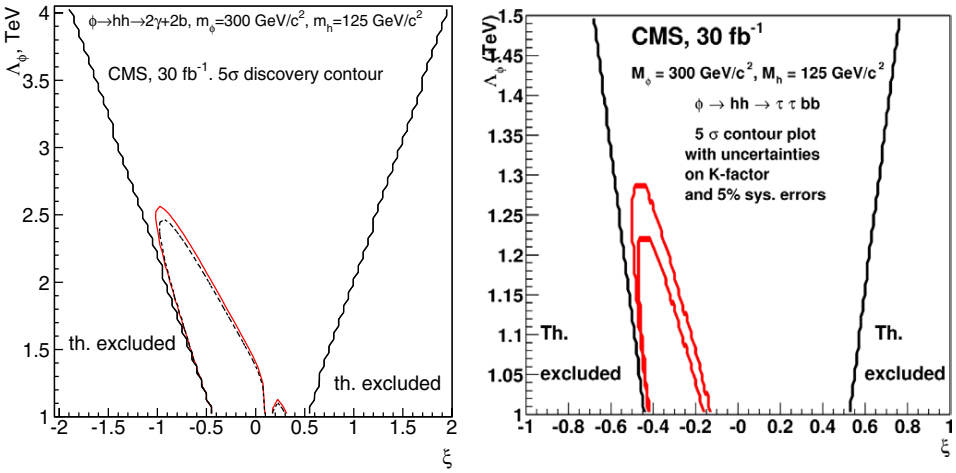

Figure 12.3. Left plot: the 5σ discovery contours for the $\phi \to \mathrm{hh} \to \gamma\gamma\mathrm{b\bar{b}}$ channel for $30\,\mathrm{fb}^{-1}$. The solid (dashed) contour shows the discovery region without (with) the effects of the systematic uncertainties (find more explanations in the text). Right plot: the 5σ discovery contours for the $\phi \to \mathrm{hh} \to \tau\tau\mathrm{b\bar{b}}$ channel for $30\,\mathrm{fb}^{-1}$. The two contours corresponds to the variation of the background NLO cross sections due to the scale uncertainty. The 5% experimental systematics on the background is taken into account (see text).

More recently another possibility of formulating the physics of electroweak symmetry breaking, called the little Higgs, was proposed [654–656]. In those models the SM Higgs boson is a pseudo Goldstone mode of a broken global symmetry and remains light, much lighter than the other new modes of the model which have masses of order the symmetry breaking scale $\mathcal{O}(1)$ TeV. In order to cancel one-loop quadratic divergences to the SM Higgs mass a new set of heavy gauge bosons W', Z' with the SM quantum numbers identical to WZ, and a vector like heavy quark pair T, $\bar{T}$ with charge 2/3 must be introduced. Notice that those fields are put in by hand in order to construct a model with the required properties. However, the minimal model based on the $SU(5)/SO(5)$ global symmetry, the so-called littlest Higgs model [657], has a firm prediction from the symmetry breaking pattern alone: the existence of another $\mathcal{O}(1)$ TeV pseudo Goldstone boson Δ with the $SU(2)_L \times U(1)_Y$ quantum numbers $\Delta \sim (3, 2)$.

Interestingly, the existence of triplet Higgs Δ might also be required to generate Majorana masses to the left-handed neutrinos [658]. Non-zero neutrino masses and mixing is presently the only experimentally verified signal of new physics beyond the SM. In the triplet neutrino mass mechanism [659] the neutrino mass matrix is generated via

$$(m_\nu)_{ij} = (Y_\Delta)_{ij} v_\Delta, \tag{12.1}$$

where $(Y_\Delta)_{ij}$ are the Majorana Yukawa couplings of the triplet to the lepton generations $i, j = e, \mu, \tau$ which are described by the Lagrangian

$$L = i\bar{\ell}^c_{Li}\tau_2 Y^{ij}_\Delta(\tau \cdot \Delta)\ell_{Lj} + \mathrm{h.c.}, \tag{12.2}$$

and v_Δ is the effective vacuum expectation value of the neutral component of the triplet induced via the explicit coupling of Δ to the SM Higgs doublet H as $\mu\Delta^0 H^0 H^0$. Here μ has a dimension of mass. In the concept of seesaw $\mu \sim M_\Delta$, and the smallness of neutrino masses is attributed to the very high scale of triplet mass M_Δ via the smallness of $v_\Delta = \mu v^2/M^2_\Delta$, where $v = 174$ GeV.

However, in the littlest Higgs model the triplet mass scale is $\mathcal{O}(1)$ TeV which alone cannot suppress v_Δ. Therefore in this model $\mu \ll M_\Delta$, which can be achieved, for example, via shining from extra dimensions as shown in ref. [660, 661] or if the triplet is related to the Dark Energy of the Universe [662]. In that case $v_\Delta \sim \mathcal{O}(0.1)$ eV while the Yukawa couplings Y_Δ can be large. For the normally hierarchical light neutrino masses neutrino data implies very small Δ decay branching fractions to electrons and $BR(\Delta^{++} \to \mu^+\mu^+) \approx BR(\Delta^{++} \to \tau^+\tau^+) \approx BR(\Delta^{++} \to \mu^+\tau^+) \approx 1/3$. We remind also that v_Δ contributes to the SM oblique corrections, and the precision data fit $\hat{T} < 2 \cdot 10^{-4}$ [663] sets an upper bound $v_\Delta \leqslant 1.2$ GeV on that parameter.

At LHC Δ^{++} can be produced singly and in pairs. The cross section of the single Δ^{++} production via the WW fusion process [664] $qq \to q'q'\Delta^{++}$ scales as $\sim v_\Delta^2$. In the context of the littlest Higgs model this process, followed by the decays $\Delta^{++} \to W^+W^+$, was studied in ref. [91, 665, 666]. The detailed ATLAS simulation of this channel shows [666] that in order to observe 1 TeV Δ^{++}, one must have $v_\Delta > 29$ GeV. This is in conflict with the precision physics bound $v_\Delta \leqslant 1.2$ GeV as well as with the neutrino data. Therefore the WW fusion channel is not experimentally promising for the discovery of very heavy doubly charged Higgs.

On the other hand, the Drell–Yan pair production process [664, 667] $pp \to \Delta^{++}\Delta^{--}$ is not suppressed by any small coupling and its cross section is known up to next to leading order [668] (possible additional contributions from new physics such as Z' are strongly suppressed for any practical purposes). Followed by the lepton number violating decays $\Delta^{\pm\pm} \to \ell^\pm\ell^\pm$, this process allows to reconstruct $\Delta^{\pm\pm}$ invariant mass from the same charged leptons rendering the SM background to be very small in the signal region. If one also assumes that neutrino masses come from the triplet Higgs interactions, one fixes the $\Delta^{\pm\pm}$ leptonic branching ratios. This allows to test neutrino mass models at LHC.

12.2.1. Search for the final state with four muons

12.2.1.1. Introduction. The doubly charged Higgs bosons $\Delta^{\pm\pm}$ pair-produced via the Drell–Yan process is investigated assuming a branching ratio of 100% into muons. This provides an almost background free channel.

12.2.1.2. Event generation. The signal events are generated using PYTHIA, with doubly charged Higgs bosons pair-produced through the Drell–Yan process. The Higgs bosons are forced to decay into muons. Datasets are produced for several values of the doubly charged Higgs boson mass, ranging from 100 to 800 GeV/c^2.

The leading order (LO) and the next-to-leading order (NLO) cross-sections [668] are shown for the signal as a function of the doubly charged Higgs boson mass in Fig. 12.4.

Important backgrounds for this channel with a four muon final state are:

- $t\bar{t} \to W^+W^-b\bar{b} \to 2\mu + 2\mu$ (generated with PYTHIA);
- $Zb\bar{b} \to 2\mu + 2\mu$ (generated with COMPHEP);
- $ZZ \to 2\mu + 2\mu$ (generated with COMPHEP);
- $ZZ \to 2\tau + 2\mu$ (generated with COMPHEP).

The ZZ production process includes γ^*. The contribution of background from $b\bar{b}$ production has also been investigated. The $b\bar{b}$ background is the QCD multi-jet background which yields the highest probability to fake events with multiple muons. It has been found that the $b\bar{b}$ background can be neglected after the online selection and a cut which requires four well-reconstructed muons with pseudorapidity $|\eta| < 2.1$ and transverse momentum $p_T >$ 8 GeV/c. The W bosons in the $t\bar{t}$ data sample are forced to decay into electrons, muons and taus. The tau leptons are forced to decay into electrons and muons. The Z boson in the $Z\bar{b}b$

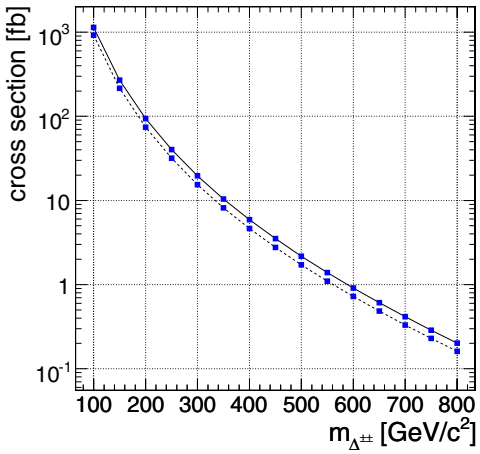

Figure 12.4. The leading order (LO) and the next-to-leading order (NLO) cross-section, for $H^{++}H^{--} \to 4\mu$.

sample is generated with $m_{Z/\gamma^*} > 5\,\mathrm{GeV/c^2}$ and is forced to decay into muons. The Z bosons in the ZZ samples are forced to decay into muons and the taus in the $ZZ \to 2\tau + 2\mu$ sample decay freely.

On all samples pre-selection cuts are applied at the generation level with the following requirements:

- Final state contains two positive and two negative muons.
- Transverse momentum $p_T(\mu) > 3\,\mathrm{GeVc}$ and pseudorapidity $|\eta(\mu)| < 2.4$ for all muons.

12.2.1.3. Event selection and reconstruction. The events are selected by dimuon trigger at Level 1 and the HLT. The p_T threshold for the dimuon HLT is 7 GeV/c. The Level 1 and HLT efficiency for the signal is >99% within uncertainties.

The muons are reconstructed by the Global Muon Reconstructor. At least 4 muons, with a $p_T > 8\,\mathrm{GeV/c}$ and $\eta \leqslant 2.1$, are required. The invariant mass of the doubly charged Higgs is reconstructed, by calculating the invariant mass of the two same charge muons with the highest p_T, after all cuts.

An event, where two or three muons are generated in one collision, and one or two in another, has also to be considered as background to our four muon signal. To suppress this background a vertex cut has been applied. For each muon in an event the impact point is determined. The impact point is the point of closest approach of the extrapolated muon trajectory to the nominal interaction point. The longitudinal distances Δz_{IPS} between the impact point states of all muons in one event are calculated. The biggest calculated Δz_{IPS} is required to be smaller than 0.05 cm. This is much smaller than the longitudinal size of the luminous region of the LHC beam of about 5 cm. So this cut rejects events with muons from different collision vertices with a probability of roughly 99%.

12.2.1.4. Results. Table 12.1 and Table 12.2 show the NLO production cross-section without any forced decay, the cross-section times branching ratio times pre-selection efficiency and the cross-section times branching ratio times efficiency after each stage of the online and offline event selection. Table 12.1 shows these values for each of the background samples.

Table 12.1. The NLO cross sections σ for background events with forced decay modes after each stage of the event selection. Errors are statistical only.

	$t\bar{t}$	$Z\bar{b}b$	$ZZ \to 4\mu$	$ZZ \to 2\mu 2\tau$
Pre-selection [fb]	232	289.8	87.4	1.63
Level-1 Trigger [fb]	232 ± 1	289 ± 1	87.3 ± 0.3	1.63 ± 0.02
High Level Trigger [fb]	149 ± 1	195 ± 1	69.7 ± 0.3	1.10 ± 0.01
4 μ reconstructed ($p_T > 8\,\text{GeV/c}, \lvert\eta\rvert < 2.1$) [fb]	45.1 ± 0.4	25.1 ± 0.3	18.5 ± 0.1	0.25 ± 0.01
Impact Point Cut [fb]	22.8 ± 0.3	13.1 ± 0.2	16.9 ± 0.1	0.22 ± 0.01

Table 12.2. Production cross sections (NLO) for signal events with $m_{H^{++}} = 300, 600, 800\,\text{GeV/c}^2$ and forced decay into four muons after each stage of the event selection. Errors are statistical only.

$\Delta^{\pm\pm}$ mass	$300\,\text{GeV/c}^2$	$600\,\text{GeV/c}^2$	$800\,\text{GeV/c}^2$
Production cross section(NLO) [fb]	19.6	0.909	0.201
Pre-selection [fb]	17.4±0.3	0.85 ± 0.02	0.190 ± 0.004
Level-1 Trigger [fb]	17.3 ± 0.3	0.85 ± 0.02	0.190 ± 0.004
High Level Trigger [fb]	17.1 ± 0.3	0.83 ± 0.02	0.188 ± 0.004
4 μ reconstructed ($p_T > 8\,\text{GeV/c}, \lvert\eta\rvert < 2.1$) [fd]	13.0 ± 0.2	0.70 ± 0.02	0.158 ± 0.003
Impact Point Cut [fd]	12.5 ± 0.2	0.67 ± 0.02	0.153 ± 0.003

Table 12.2 show these values for signal samples with doubly charged Higgs masses 300, 600 and $800\,\text{GeV/c}^2$.

Figure 12.5 shows the invariant mass spectrum of the reconstructed $\Delta^{\pm\pm}$ before and after the offline cuts, for $m(\Delta^{\pm\pm}) = 300\,\text{GeV/c}^2$ and for $m(\Delta^{\pm\pm}) = 600\,\text{GeV/c}^2$.

12.2.1.5. Statistical interpretation. To interpret the results, the CL_s method [508] is applied, which is based on log-likelihood ratios, calculated for all bins of the invariant mass distribution. CL_s is defined as ratio of the confidence levels for the signal and background hypotheses $CL_s = CL_{s+b}/CL_b$. CL_s can be understood as the probability of excluding an existing signal. The $1 - CL_b$ can be understood as the probability for the background distribution to fake a signal. For high doubly charged Higgs boson masses the amount of simulated background events goes to zero. Nevertheless, zero simulated background events do not necessarily mean zero background events in reality. To estimate the amount of background in this region, empty bins are filled for each background with upper limits to Poisson statistic. Zero background events are compatible with maximal three generated events. Therefore empty bins get filled for each background with three events times the scale factor for an integrated luminosity of $10\,\text{fb}^{-1}$. The left plot in Fig. 12.6 shows the $1 - CL_b$ values for different doubly charged Higgs boson masses. For a doubly charged Higgs Boson mass smaller than $650\,\text{GeV/c}^2$ the signal plus background expectation will exceed the background only expectation by more than 5σ. To claim a discovery, at least three signal events need to be detected. For a mass of $650\,\text{GeV/c}^2$ four detectable events remain after all cuts. The right plot in figure 12.6 shows the CL_s values for different doubly charged Higgs boson masses. If no signal can be detected for an integrated luminosity of $10\,\text{fb}^{-1}$ the existence of a doubly charged Higgs Boson in this decay channel can be excluded with 95% confidence up to a mass of $760\,\text{GeV/c}^2$. The ± 1 and ± 2-sigma bands in figure 12.6 are only for statistical errors.

12.2.1.6. Systematical uncertainties. The uncertainties on the exclusion limit resulting from systematical errors have yet to be studied in detail, once the detector is running.

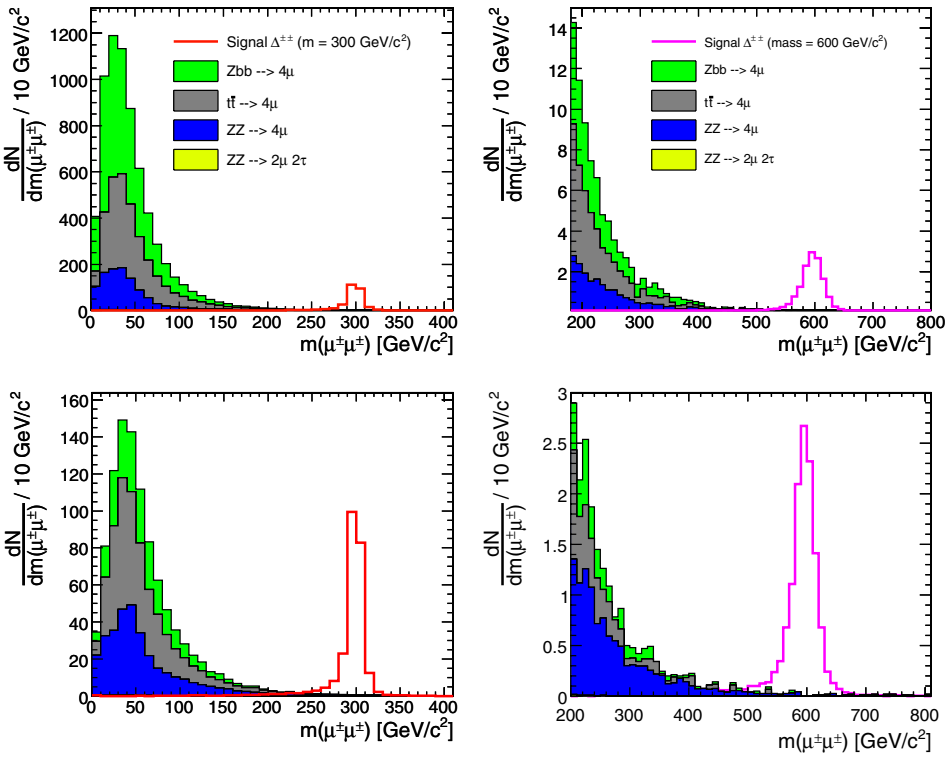

Figure 12.5. The reconstructed $\Delta^{\pm\pm}$ invariant mass after pre-selection and trigger selection (top) and after offline cuts (bottom).

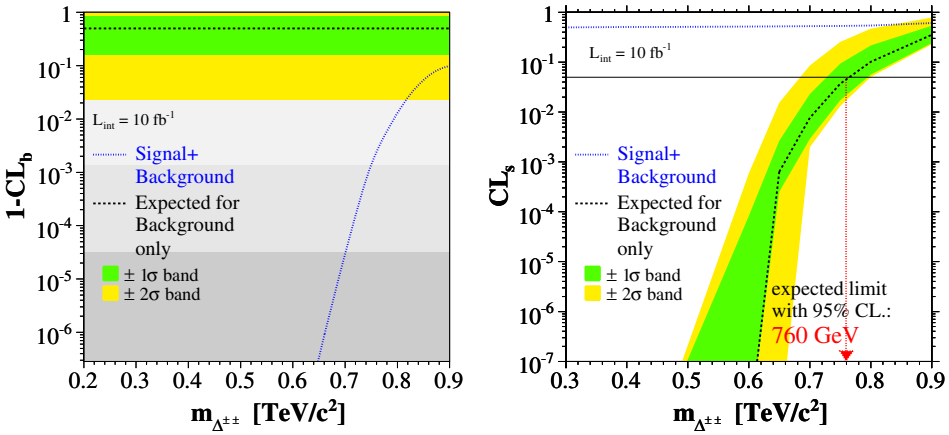

Figure 12.6. $1 - CL_b$ and CL_s as defined in the Log Likelihood Ratio Method after all selection cuts for an integrated luminosity of $10\,\mathrm{fb}^{-1}$.

The considered backgrounds are also backgrounds to the Standard Model $H \to ZZ \to 4\mu$ process. As this process is one of the benchmark processes of the future CMS detector, this backgrounds are studied in detail. The obtained total uncertainty on the background cross

Table 12.3. The NLO background processes cross sections used (in fb).

background	$t\bar{t} \to 4l$	$Z\, b\bar{b}$	ZZ	$t\bar{t}\, Z$
Cross section times BR	$88.4 \cdot 10^3$	$52.4 \cdot 10^3$	229.5	650

section is 1% to 6%. The uncertainty on signal cross section is 10% to 15%. The uncertainty on the luminosity $\mathcal{L}$ is $\sim 5\%$ for an integrated luminosity of $10\,\mathrm{fb}^{-1}$.

Using a background cross section uncertainty of 6%, a signal cross section uncertainty of 10% and a luminosity uncertainty of 5% the approximated uncertainties on the exclusion mass limit and on the discovery mass limit are:

$$\text{Exclusion Limit} = (760\ ^{+0.5}_{-2}(\text{bkg}) \pm 10(\text{signal}) \pm 4(\text{lumi}))\,\text{GeV/c}^2 \tag{12.3}$$

$$\text{Discovery Limit} = (650\ ^{+0.4}_{-0.3}(\text{bkg})\ ^{+3}_{-0.4}(\text{signal}) \pm 0.2(\text{lumi}))\,\text{GeV/c}^2. \tag{12.4}$$

12.2.2. Search for the final states with τ leptons

12.2.2.1. Introduction. In this section, we discuss the doubly charged Higgs boson pair-production via a Drell–Yan process and investigate decays which involve taus and muons. The branching ratios are assumed to be 1/3 for the following three channels: $\Delta^{\pm\pm} \to 2\mu^{\pm}$, $\Delta^{\pm\pm} \to \mu^{\pm}\tau^{\pm}$ and $\Delta^{\pm\pm} \to 2\tau^{\pm}$. The reasoning comes from recent neutrino mixing measurements. As the neutrino mixing matrix and doubly charged Higgs boson decays are directly related then the appropriate branchings can be determined.

12.2.2.2. Event generation. The doubly charged Higgs boson pair-production via Drell–Yan process is generated using PYTHIA. Datasets are produced with Higgs boson mass from $200\,\text{GeV/c}^2$ to $600\,\text{GeV/c}^2$. The taus from Higgs boson decays can decay both leptonically and hadronically while in analysis we only consider hadronic decays.

The backgrounds which were considered for this analysis are as follows:

- $t\bar{t} \to \mathrm{W^+W}\, b\bar{b}$ generated by PYTHIA, COMPHEP, ALPGEN, TOPREX and MADGRAPH with W boson decay $\mathrm{W} \to \ell\nu$ ($\ell = \mathrm{e}, \mu, \tau$) forced.
- $t\bar{t}\,\mathrm{Z} \to W^+W^-Z\, b\bar{b}$ generated with COMPHEP. The W and Z bosons are allowed to decay arbitrarily.
- $\mathrm{Zb\bar{b}}$ where the Z boson decays to muons and τ leptons, generated with COMPHEP.
- ZZ generated with PYTHIA, where the Z bosons are forced to decay leptonically (e, μ, τ). The contribution of γ^* is included with $\mathrm{m}_{\gamma^*} > 12\,\text{GeV/c}^2$.

The next-to-leading order (NLO) cross sections times branching ratios used for the backgrounds can be found in Table 12.3. The Monte Carlo statistics of the generated background exceed $30\,\mathrm{fb}^{-1}$ except $Zb\bar{b}$ background, where it is $8\,\mathrm{fb}^{-1}$. Therefore the results will be presented for an integrated luminosity of $10\,\mathrm{fb}^{-1}$.

12.2.2.3. Event selection and reconstruction. The events are triggered by the single muon trigger at Level 1 and HLT. After HLT the event is only used if it is possible to reconstruct the event primary vertex. If the primary vertex fails to be reconstructed the event is rejected.

The muons are reconstructed using Global Muon Reconstructor. The τ leptons are reconstructed using τ-jet candidates and missing transverse energy after selection cuts. The doubly charged Higgs boson invariant mass is reconstructed from the same charge lepton pairs after all selection cuts.

The selection cuts used on muons are:

- The transverse momentum must be higher than 50 GeV/c. For background events 80% of muons have p_T less than 50 GeV/c while for the signal with Higgs boson mass 200 GeV/c^2 it is 27% and for higher masses it reduces to around 10%.
- The distance to primary vertex in z-direction must not exceed 0.03 cm. It does not cut away any muons from the signal events but limits analysis to leptons coming from the same primary vertex.

The selection cuts used on τ jets are:

- For τ jets we consider τ decays which involve 1 or 3 charged tracks. We use τ-jet candidates which passed the τ-jet filtering algorithms described in [280]. Two isolation criteria are used. Either one or three charged tracks in the signal cone and no charged tracks in the isolation cone or two tracks in signal cone and exactly one charged track in the isolation cone.
- The maximal distance to the primary vertex in the z-direction of any charged track in the τ jet must not exceed 0.2 cm.
- The transverse energy of the hottest HCAL tower of the τ jet must be higher than 2 GeV. This cut eliminates 86% of all electrons taken as τ candidates and only removes 7.5% of real τ jets.
- The transverse energy of the τ jet candidate must exceed 50 GeV. It has been chosen to be the same as the cut used on muons.
- No muon track should be in a cone with $\Delta R = 0.3$ constructed around the τ-jet candidate. If there is, then the candidate is dropped. This eliminates false τ-jet candidates which are generated when a charged muon track passes the same region as photons or hadrons. With this cut only a few real τ jets are discarded however most of the false τ jets coming from this misidentification are rejected.

Missing transverse energy (E_T^{miss}) is reconstructed using calorimeter Type 1 E_T^{miss} (E_T^{miss} with the jet energy corrections) and p_T of muons.

Only events with at least four objects, muons or τ jets, are accepted. The possible final states are:

- $\Delta^{++}\Delta^{--} \rightarrow 4\mu$: this channel is investigated in the previous subsection.
- $\Delta^{++}\Delta^{--} \rightarrow 3\mu 1\tau$: this channel is easily reconstructible as there is only one neutrino and it goes the direction of the τ jet.
- $\Delta^{++}\Delta^{--} \rightarrow 2\mu 2\tau$: this channel can also be reconstructed using the assumption that the neutrinos go in the same directions as the τ jets.
- $\Delta^{++}\Delta^{--} \rightarrow 1\mu 3\tau$: this channel can be reconstructed only with very good E_T^{miss} resolution as it requires an additional assumption that the masses of the two reconstructed Higgs bosons are the same. However the reconstruction is very sensitive to E_T^{miss} accuracy and often the event has to be dropped due to negative τ-lepton energies.
- $\Delta^{++}\Delta^{--} \rightarrow 4\tau$: this channel can not be reconstructed (and triggered by the single muon trigger).

Once the event leptons are reconstructed, some additional selections are performed:

- Z boson veto: if the odd sign pairing gives an invariant mass of 91 ± 5 GeV/c^2 then these leptons are removed from further use.
- Same charge lepton pairs are reconstructed and only those reconstructed Higgs candidate pairs whose invariant mass difference is within 20% of each other are considered.

The reconstructed mass of doubly charged Higgs boson is shown on Figure 12.7 for the Higgs boson masses 200 and 500 GeV/c^2.

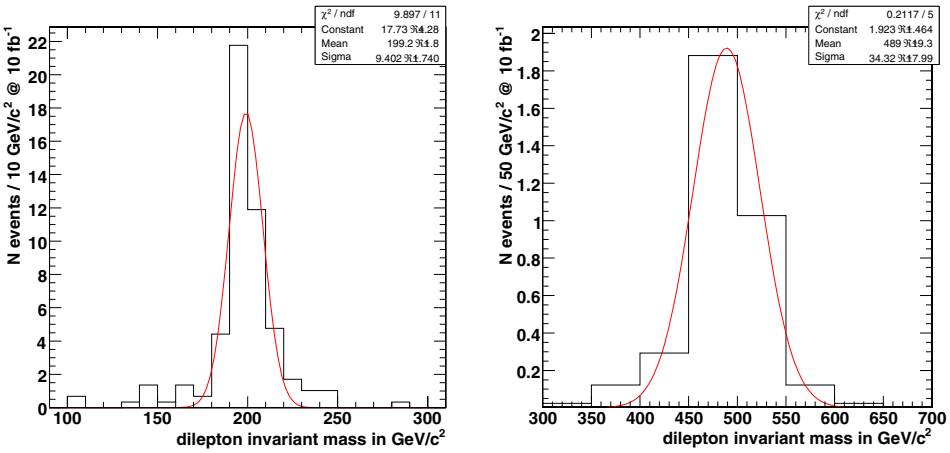

Figure 12.7. The reconstructed invariant mass for $M(\Delta^{\pm\pm}) = 200\,\mathrm{GeV/c^2}$ and $500\,\mathrm{GeV/c^2}$.

Table 12.4. The signal selection efficiencies for different $\Delta^{\pm\pm}$ masses. Total efficiency is the product of the single efficiencies.

$m_{\Delta}^{\pm\pm}$ ($\mathrm{GeV/c^2}$)	200	300	400	500	600
Level 1 and HLT	83.7%	86.0%	86.7%	85.8%	88.3%
Primary vertex	96.9%	98.5%	97.0%	97.5%	98.0%
4 leptons in final state	10.1%	17.2 %	23.6%	24.7%	26.7%
two pairs and at least one τ	44.9%	46.1%	41.7%	53.2%	52.9%
Mass difference	62.5%	77.2%	80.4%	74.3%	63.6%
Total signal efficiency	2.3%	5.1%	6.6%	8.1%	7.7%

12.2.2.4. Selection efficiencies. The upper limit of the signal selection efficiency is given by the fraction of events with $3\mu 1\tau, 2\mu 2\tau, 1\mu 3\tau$ ($\tau \rightarrow$ hadrons) topology relative to all possible final states with muons and τ leptons from decays of two Higgs bosons. Assuming the above mentioned branching ratios the upper limit is $\simeq 35\%$. The fraction of every selected topology is given below:

- $\Delta^{++}\Delta^{--} \rightarrow 3\mu 1\tau = 2/9$ events $\times\, 0.65 = 14.4\%$
- $\Delta^{++}\Delta^{--} \rightarrow 2\mu 2\tau = 3/9$ events $\times\, 0.65^2 = 14.1\%$
- $\Delta^{++}\Delta^{--} \rightarrow 1\mu 3\tau = 2/9$ events $\times\, 0.65^3 = 6.1\%$.

where 0.65 is the branching ratio of $\tau \rightarrow$ hadrons decays. Table 12.4 summarises the efficiencies of each selection (relative to the previous one) for the signal of different $\Delta^{\pm\pm}$ masses. The lepton selection efficiency and purity is shown in Table 12.5. Background efficiencies are shown in Table 12.6.

12.2.2.5. Systematic errors. At the integrated luminosity of $10\,\mathrm{fb^{-1}}$ the cuts implemented above result in an almost background free signal. For datasets with Monte Carlo statistics above $30\,\mathrm{fb^{-1}}$ giving zero Monte Carlo events after all selections ($t\bar{t}$, ZZ^*) we assume the background to be zero. For $t\bar{t}Z$ background where is one Monte Carlo event passing all cuts, which corresponds to 0.05 expected events when scaled with cross section and luminosity.

Table 12.5. Single muon and τ selection efficiencies and purity.

$m_{\Delta}^{\pm\pm}$ (GeV/c^2)	200	300	400	500	600
Single μ selection efficiency	70.7%	82.0%	86.1%	87.2%	89.2%
1 - purity of accepted muons:	0.1%	0.4%	0.8%	0.7%	1.0%
Single τ selection efficiency	36.6%	42.3%	50.6%	53.3%	53.3%
1 - purity of accepted τ jets:	2.2%	2.2%	4.2%	3.6%	3.2%

Table 12.6. Selection efficiencies for background. Total efficiency is the product of the single efficiencies.

Process	$t\bar{t}$	$t\bar{t}$ Z	ZZ	Zbb
Level 1 and HLT trigger	40.7%	20.3%	40.0%	42.1%
Primary vertex	99.3%	99.8%	96.7%	98.2%
4 leptons in final state	0.0015%	0.04 %	3.0%	0.0005%
two pairs and at least one τ	–	0.1%	–	–
Mass difference	–	100%	–	–
Total signal efficiency	–	0.0008%	–	–

For Z $b\bar{b}$ background where the Monte Carlo statistics corresponds to 8 fb^{-1} no events passed all cuts. The analysis was repeated with p_{T} cut on muon (τ jet) of 40 GeV/c, 30 GeV/c and 20 GeV/c, again with no events passing the cuts, which confirms the assumption that leptons coming from Z $b\bar{b}$ are too soft to produce a background. Considering the smallness of all backgrounds we assume no background at 10 fb^{-1} for the following analysis.

The systematic uncertainties used for the signal are the following:

- muon misidentification ($\Delta\mu$): 1% per muon;
- muon isolation ($\Delta\mu_{isol}$): 2% per event;
- τ jets identification ($\Delta\tau$): 9% per τ jet;
- luminosity ($\Delta\mathcal{L}$): 5%;
- PDF and scale ($\Delta\sigma$) 10% (theoretical uncertainty, it is not used for the signal cross section measurement with no background).

As the events are a mixture of different decay modes the total selection efficiency uncertainty ($\Delta\varepsilon_S$) is calculated per decay channel and then added together with the corresponding weights:

$$\Delta 3\mu 1\tau = \sqrt{3\Delta\mu^2 + \Delta\tau^2} = 8.2\%,$$

$$\Delta 2\mu 2\tau = \sqrt{2\Delta\mu^2 + 2\Delta\tau^2} = 11.4\%,$$

$$\Delta 1\mu 3\tau = \sqrt{\Delta\mu^2 + 3\Delta\tau^2} = 13.9\%,$$

giving

$$\Delta\varepsilon_S = \frac{144\Delta 3\mu 1\tau + 141\Delta 2\mu 2\tau + 61\Delta 1\mu 3\tau}{346} = 10.5\%.$$

The total systematic error for cross section measurement is then

$$\frac{\Delta\sigma}{\sigma} = \sqrt{\Delta\mu_{isol}{}^2 + \Delta\mathcal{L}^2 + \Delta\varepsilon_S{}^2} = 13\%.$$

Table12.7. Expected number of events, NLO cross section with expected statistical and systematic uncertainty of the cross section measurement at $10\,\text{fb}^{-1}$, and integrated luminosity needed for exclusion at 95% CL.

$m_{\Delta}^{\pm\pm}$ (GeV)	200	300	400	500
N_{ev} expected at $10\,\text{fb}^{-1}$	26	10	4	2
$\sigma_{NLO} \pm \text{stat} \pm \text{syst}$ (fb)	$93.9^{+19.3}_{-17.5} \pm 12.2$	$19.6^{+6.6}_{-5.6} \pm 2.5$	$5.9^{+3.4}_{-2.5} \pm 0.8$	$2.2^{+1.9}_{-1.3} \pm 0.3$
Luminosity for 95% CL exclusion, fb^{-1}	1.3	3.0	7.7	16.8

The statistical errors were evaluated constructing the shortest Bayesian confidence interval for the confidence level of 67% [669].

12.2.2.6. Results. The expected number of events at $10\,\text{fb}^{-1}$ and the NLO cross section with expected statistical and systematic uncertainty of the cross section measurement are given in Table 12.7. Table 12.7 shows also the integrated luminosity needed for exclusion at 95% CL.

Chapter 13. Supersymmetry

13.1. Introduction

This chapter presents the results of analyses by which evidence for supersymmetry could be obtained in CMS during the "low luminosity" period of the LHC. After a brief reminder of the main phenomenological features of SUSY in Section 13.2, Section 13.3 is devoted to the outline of the scope of present searches. The emphasis was not on a complete study of a specific point in the parameter space, but rather on covering all relevant signatures by which SUSY might be discovered. For this purpose, a set of test points have been defined, for which a full simulation of the CMS detector was performed, to serve as basis for the analyses. An algorithm allowing the separation of the sparticle decay chains, used in several analyses, is presented in Section 13.4. Sections 13.5 to 13.12 summarise the searches for SUSY and the reach as a function of luminosity, demonstrating that low mass supersymmetry can be discovered at the LHC with fairly low integrated luminosity for all these signatures in inclusive searches and show the projected reach at the end of the low luminosity run. They are followed by some exclusive studies, mass reconstruction in ditau final states (Section 13.13), tri-lepton final states from direct chargino/neutralino production (Section 13.14) and slepton pair production (Section 13.15). A possible violation of lepton number in $\tilde{\chi}_2^0$ decay is studied in Section 13.16. Section 13.18 contains some considerations on the robustness of the considered signatures in scenarios beyond mSUGRA, like for non-universal Higgs masses, and shows that the same signatures would still allow the discovery of supersymmetry. The chapter ends with our conclusion on the CMS reach.

13.2. Summary of supersymmetry

13.2.1. The MSSM

The Minimal Supersymmetry Model (MSSM) contains the minimal extension of the Standard Model (SM) particle content. Its gauge sector is fully determined by Supersymmetry. But the unknown mechanism for breaking Supersymmetry introduces a large number of free parameters [670] and makes this general model intractable. Therefore, several more constrained models have appeared in the literature. Below, we will focus on a version derived from Supergravity with minimal superpotential and Kähler potential, called mSUGRA, which guarantees universality of gaugino and scalar masses and of trilinear couplings at a high scale. Other SUSY breaking models, like Gauge Mediated Supersymmetry Breaking (GMSB) or Anomaly Mediated Supersymmetry Breaking (AMSB) have not been included here. R-parity breaking in SUSY is also not considered.

An earlier summary of the potentialities of the CMS experiment at LHC for the discovery of Supersymmetry has been published in 1998 [671]. The potential of the ATLAS experiment for the discovery of supersymmetry was analysed in [491].

13.2.2. mSUGRA parameters and spectrum

The mSUGRA model of supersymmetry is determined by 5 free parameters defined at the Grand Unification (GUT) scale. If it is assumed that the spontaneous gauge symmetry breaking is induced by radiative corrections, the absolute value of μ is determined from the Z^0 mass. The free parameters are then:

$$m_0\,,\ m_{1/2}\,,\ A_0\,,\ \tan\beta,\ \mathrm{sign}(\mu). \tag{13.1}$$

They are run down to the electroweak scale by Renormalisation Group Equations (RGE) from which the sparticle spectrum, decay branching ratios and production cross sections can be derived.

The gaugino mass parameters M_a at the electroweak scale are approximately:

$$\begin{aligned} M_3 \equiv M_{\tilde{g}} &\simeq 2.7 m_{1/2} \\ M_2(M_Z) &\simeq 0.8 m_{1/2} \\ M_1(M_Z) &\simeq 0.4 m_{1/2} \end{aligned} \tag{13.2}$$

The parameter M_3 determines the gluino mass (after QCD corrections). The masses of neutralinos $\tilde{\chi}_i^0$ ($i = 1$–4) and charginos $\tilde{\chi}_i^{\pm}(i = 1, 2)$ are obtained after diagonalising their mass matrices which are a function of M_1, M_2 and μ. In the mSUGRA framework, the lightest chargino and the two lightest neutralinos are dominantly gaugino-like with masses close to M_1 and M_2.

The sfermions of the first two generations have masses given approximately by:

$$\begin{aligned} m^2_{\tilde{u}_L} &\simeq m_0^2 + 5.0 m_{1/2}^2 + 0.35 cos2\beta M_Z^2 \\ m^2_{\tilde{d}_L} &\simeq m_0^2 + 5.0 m_{1/2}^2 - 0.42 cos2\beta M_Z^2 \\ m^2_{\tilde{u}_R} &\simeq m_0^2 + 4.5 m_{1/2}^2 + 0.15 cos2\beta M_Z^2 \\ m^2_{\tilde{d}_R} &\simeq m_0^2 + 4.4 m_{1/2}^2 - 0.07 cos2\beta M_Z^2 \\ m^2_{\tilde{e}_L} &\simeq m_0^2 + 0.49 m_{1/2}^2 - 0.27 cos2\beta M_Z^2 \\ m^2_{\tilde{\nu}} &\simeq m_0^2 + 0.49 m_{1/2}^2 + 0.50 cos2\beta M_Z^2 \\ m^2_{\tilde{e}_R} &\simeq m_0^2 + 0.15 m_{1/2}^2 - 0.23 cos2\beta M_Z^2 \end{aligned} \tag{13.3}$$

By comparing with the gluino mass, these relations show that the latter cannot be much larger than the squark mass:

$$M_{\tilde{g}} \lesssim 1.2 m_{\tilde{q}} \tag{13.4}$$

This relation (obtained for $m_0 = 0$) is not restricted to the mSUGRA case, as it depends primarily on the α_S contributions to the running down of the mass parameters from the GUT scale.

The masses of the third family scalars are more complicated as the contributions from Yukawa couplings can no longer be neglected and non-negligible off-diagonal elements between left and right states appear (they are proportional to the fermion masses).

13.3. Scope of present searches

13.3.1. Sparticle production and cascade decays

If we assume that Supersymmetry is discovered at the LHC, most likely from fully inclusive studies based on large missing energy and jets, it will be very important to investigate all the typical SUSY signatures to help pin down the underlying model.

If the squarks and/or gluinos are kinematically accessible at the LHC, they are expected to have large production rates. The cross sections for the production of a squark (excluding stop) or a gluino at the LHC are displayed in Fig. 13.1. The nearly diagonal lines delimit three regions:

- Region 1: in this region, the gluinos are heavier than any of the squarks. The decay chains of the produced sparticles are expected to be

$$\tilde{g} \to \tilde{q}\bar{q}, \tilde{q} \to q\chi. \tag{13.5}$$

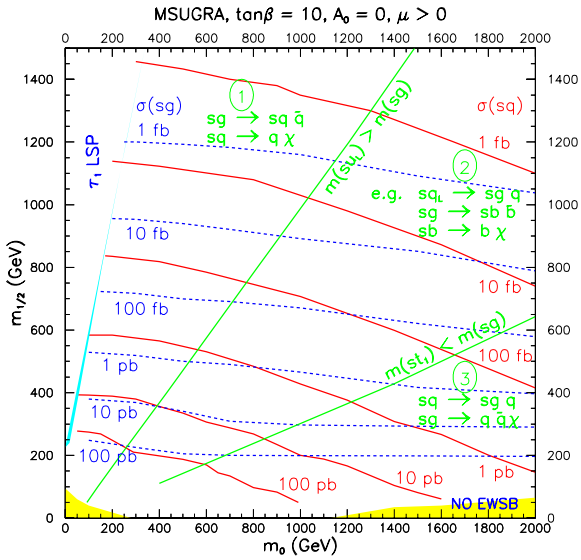

Figure 13.1. Regions of the m_0 versus $m_{1/2}$ plane showing the production cross-sections and with main squark and gluino decays.

- Region 2: in this region some squarks are heavier, other are lighter than the gluino. Hence, rather complicated decay chains are possible, for instance

$$\tilde{q}_L \to \tilde{g}q,\ \tilde{g} \to \tilde{b}\bar{b},\ \tilde{b} \to b\chi \tag{13.6}$$

  as the $\tilde{q}_L$ of the first two generations are expected to be among the heaviest squarks and the $\tilde{b}_1$ (and $\tilde{t}_1$) among the lightest.
- Region 3: in this region, the gluinos are lighter than any of the squarks. A typical decay chain is then

$$\tilde{q} \to \tilde{g}q,\ \tilde{g} \to q\bar{q}\chi \tag{13.7}$$

  where the gluino gives rise to a three-body decay mediated by a virtual squark.

They will cascade down to the LSP, here assumed to be stable. In mSUGRA, the lightest two neutralinos are $\tilde{\chi}_1^0$, which is dominantly bino-like, and $\tilde{\chi}_2^0$, which is dominantly wino-like. The $\tilde{q}_R$ then decays almost exclusively directly into $q\tilde{\chi}_1^0$. But the $\tilde{q}_L$ have usually a non-negligible branching ratio to decay via the $\tilde{\chi}_2^0$ or $\tilde{\chi}_1^\pm$. The decay of the $\tilde{\chi}_2^0$ will then provide an excellent signature for the events which can be observed in inclusive searches.

The main decay modes of the $\tilde{\chi}_2^0$, and hence the signatures, are

$$\tilde{\chi}_2^0 \to \tilde{l}l, \tag{13.8}$$

$$\tilde{\chi}_2^0 \to \tilde{\nu}\nu, \tag{13.9}$$

$$\tilde{\chi}_2^0 \to h^0\tilde{\chi}_1^0, \tag{13.10}$$

$$\tilde{\chi}_2^0 \to Z^0\tilde{\chi}_1^0, \tag{13.11}$$

$$\tilde{\chi}_2^0 \to l^+l^-\tilde{\chi}_1^0 \tag{13.12}$$

where the last decay is mediated by the exchange of an off-shell Z^0 or $\tilde{l}$. The first decay corresponds to a gauge interaction coupling a Wino to a slepton-lepton pair and dominates

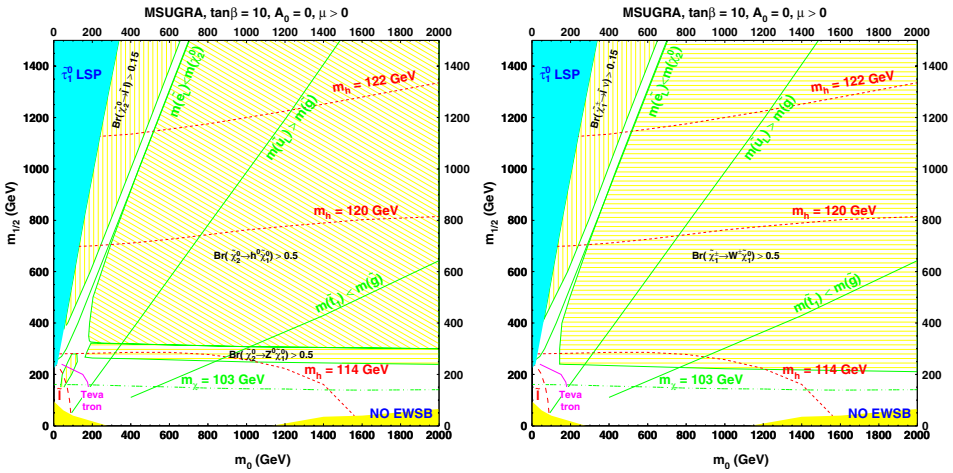

Figure 13.2. Regions of the m_0 versus $m_{1/2}$ plane with main χ_2^0 decays (left) and main decays of $\tilde{\chi}_1^{\pm}$ (right).

if it is kinematically allowed. When this decay is kinematically forbidden and $m_{1/2}$ is large enough, so that $m(\tilde{\chi}_2^0) - m(\tilde{\chi}_1^0) > m(h^0)$, the next preferred decay is to h^0. This corresponds to a gaugino-Higgsino transition and thus requires a non-zero Higgsino component in at least one of the two neutralinos. If also this decay is kinematically forbidden and the neutralino mass difference is sufficient, the $\tilde{\chi}_2^0$ decays to a Z^0 which is suppressed compared to the h^0 decay because it couples to the Higgsino component of both neutralinos. When also this decay is kinematically forbidden, direct three-body decays take place. The corresponding regions in the m_0 versus $m_{1/2}$ plane are illustrated for a mSUGRA case in Fig. 13.2 (left). The exact boundaries of the areas depend on the assumptions (mSUGRA) and on the value of $\tan\beta$ and the parameter A, but their existence is rather generic. It should be emphasised that the existence of these decay modes is a direct consequence of the gauge structure of the theory and is therefore independent of the model details. Their relative importance at a given SUSY point is, however, model dependent.

In addition to the decays via a $\tilde{\chi}_2^0$, a large fraction of squark decays will proceed via a $\tilde{\chi}_1^{\pm}$ decay, which may lead to

$$\tilde{\chi}_1^{\pm} \to \tilde{l}\nu, \tag{13.13}$$

$$\tilde{\chi}_1^{\pm} \to \tilde{\nu}l, \tag{13.14}$$

$$\tilde{\chi}_1^{\pm} \to W^{\pm}\tilde{\chi}_1^0, \tag{13.15}$$

$$\tilde{\chi}_1^{\pm} \to H^{\pm}\tilde{\chi}_1^0, \tag{13.16}$$

$$\tilde{\chi}_1^{\pm} \to l^{\pm}\nu\tilde{\chi}_1^0, \tag{13.17}$$

where the last decay is mediated by the exchange of an off-shell W, $\tilde{\nu}$ or $\tilde{l}$. The localisation of the chargino decay modes in the $(m_0, m_{1/2})$ plane is illustrated for a mSUGRA case in Fig. 13.2 (right).

Further constraints beyond the mSUGRA ones can be imposed, for example the compatibility with the measured relic density. These limit very severely the available parameter space. However, the lack of knowledge of the SUSY breaking mechanism

Table 13.1. mSUGRA parameter values for the test points. Masses are given in units of GeV/c^2.

Point	m_0	$m_{1/2}$	$\tan\beta$	sgn(μ)	A_0
LM1	60	250	10	+	0
LM2	185	350	35	+	0
LM3	330	240	20	+	0
LM4	210	285	10	+	0
LM5	230	360	10	+	0
LM6	85	400	10	+	0
LM7	3000	230	10	+	0
LM8	500	300	10	+	−300
LM9	1450	175	50	+	0
LM10	3000	500	10	+	0
HM1	180	850	10	+	0
HM2	350	800	35	+	0
HM3	700	800	10	+	0
HM4	1350	600	10	+	0

encourages the future experiments to prepare themselves to cope with the broadest possible spectrum of situations. Rather than restricting oneself to a very constrained model, it will be important to understand how to detect departures from the SM in a large variety of topologies and to investigate how to reconstruct the sparticle masses and other SUSY parameters. Of course, there is more information available in the events than just the end points, e.g. momentum asymmetries of the decay leptons, branching ratios and total cross section measurements. This additional information have so far not been used to a large extent.

13.3.2. Test points for mSUGRA

To cover the significantly different experimental signatures, a set of mSUGRA test points have been defined and will be used in the subsequent analyses. First, low mass (LM1 to LM9) test points were chosen to evaluate the sensitivity to SUSY signals in the early period of the LHC but above the Tevatron reach. Then, some high mass test points (HM1 to HM4) near the ultimate reach of the LHC were included.

Their parameters are defined in Table 13.1 and their position in the $(m_0, m_{1/2})$ plane is shown in Fig. 13.3. Points LM1, LM2 and LM6 are compatible with WMAP Cold Dark Matter limits in a strict mSUGRA scenario. The other points are not, but can be made compatible with CDM if universality of the Higgs mass parameters is abandoned (NUHM). Quoted branching ratios are from ISASUGRA7.69 [672] (lepton is e or μ). The post-WMAP benchmark points are found in [633], the NUHM points in [673] and the CMS DAQ TDR points in [76].

- **Point LM1:**
  - Same as post-WMAP benchmark point B′ and near DAQ TDR point 4.
  - $m(\tilde{g}) \geqslant m(\tilde{q})$, hence $\tilde{g} \to \tilde{q}q$ is dominant.
  - $B(\tilde{\chi}_2^0 \to \tilde{l}_R l) = 11.2\%$, $B(\tilde{\chi}_2^0 \to \tilde{\tau}_1 \tau) = 46\%$, $B(\tilde{\chi}_1^\pm \to \tilde{\nu}_l l) = 36\%$.
- **Point LM2:**
  - Almost identical to post-WMAP benchmark point I'.
  - $m(\tilde{g}) \geqslant m(\tilde{q})$, hence $\tilde{g} \to \tilde{q}q$ is dominant ($\tilde{b}_1 b$ is 25%).
  - $B(\tilde{\chi}_2^0 \to \tilde{\tau}_1 \tau) = 96\%$ $B(\tilde{\chi}_1^\pm \to \tilde{\tau}\nu) = 95\%$.

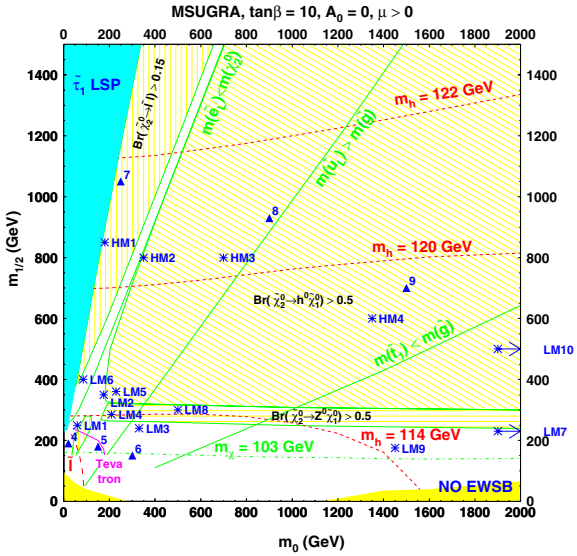

Figure 13.3. Position of the test points in the m_0 versus $m_{1/2}$ plane. The lines in this plane correspond to the assumptions that $\tan\beta = 10$, $A_0 = 0$ and $\mu > 0$. The shaded regions are excluded because either the $\tilde{\tau}_1$ would be the LSP or because there is not radiative electroweak symmetry breaking. The regions excluded by the LEP limit on the h^0 or the $\tilde{\chi}_1^{\pm}$ masses are delineated by dashed lines. The test CMS points are indicated by stars (LM7 and LM10 are outside the boundaries) and the points used in the CMS DAQ TDR by triangles. Also shown are the regions of interest for the decay of the $\tilde{\chi}_2^0$.

- **Point LM3:**
  - Same as NUHM point γ and near DAQ TDR point 6.
  - $m(\tilde{g}) < m(\tilde{q})$, hence $\tilde{g} \to \tilde{q}q$ is forbidden except $B(\tilde{g} \to \tilde{b}_{1,2}b) = 85\%$
  - $B(\tilde{\chi}_2^0 \to ll\tilde{\chi}_1^0) = 3.3\%$, $B(\tilde{\chi}_2^0 \to \tau\tau\tilde{\chi}_1^0) = 2.2\%$, $B(\tilde{\chi}_1^{\pm} \to W^{\pm}\tilde{\chi}_1^0) = 100\%$
- **Point LM4:**
  - Near NUHM point α in the on-shell Z^0 decay region
  - $m(\tilde{g}) \gtrsim m(\tilde{q})$, hence $\tilde{g} \to \tilde{q}q$ is dominant with $\tilde{g} \to \tilde{b}_1 b = 24\%$
  - $B(\tilde{\chi}_2^0 \to Z^0\tilde{\chi}_1^0) = 97\%$, $B(\tilde{\chi}_1^{\pm} \to W^{\pm}\tilde{\chi}_1^0) = 100\%$
- **Point LM5:**
  - In the h^0 decay region, same as NUHM point β.
  - $m(\tilde{g}) \gtrsim m(\tilde{q})$, hence $\tilde{g} \to \tilde{q}q$ is dominant with $B(\tilde{g} \to \tilde{b}_1 b) = 19.7\%$ and $B(\tilde{g} \to \tilde{t}_1 t) = 23.4\%$
  - $B(\tilde{\chi}_2^0 \to h^0\tilde{\chi}_1^0) = 85\%$, $B(\tilde{\chi}_2^0 \to Z^0\tilde{\chi}_1^0) = 11.5\%$, $B(\tilde{\chi}_1^{\pm} \to W^{\pm}\tilde{\chi}_1^0) = 97\%$
- **Point LM6:**
  - Same as post-WMAP benchmark point C′.
  - $m(\tilde{g}) \gtrsim m(\tilde{q})$, hence $\tilde{g} \to \tilde{q}q$ is dominant
  - $B(\tilde{\chi}_2^0 \to \tilde{l}_L l) = 10.8\%$, $B(\tilde{\chi}_2^0 \to \tilde{l}_R l) = 1.9\%$, $B(\tilde{\chi}_2^0 \to \tilde{\tau}_1\tau) = 14\%$, $B(\tilde{\chi}_1^{\pm} \to \tilde{\nu}_l l) = 44\%$
- **Point LM7:**
  - Very heavy squarks, outside reach, but light gluino.
  - $m(\tilde{g}) = 678\,\mathrm{GeV/c^2}$, hence $\tilde{g} \to$ 3-body is dominant

* $B(\tilde{\chi}_2^0 \to ll\tilde{\chi}_1^0) = 10\%$, $B(\tilde{\chi}_1^\pm \to \nu l\tilde{\chi}_1^0) = 33\%$
* EW chargino-neutralino production cross-section is about 73% of total.

- **Point LM8:**
  * Gluino lighter than squarks, except $\tilde{b}_1$ and $\tilde{t}_1$
  * $m(\tilde{g}) = 745$ GeV/c^2, $M(\tilde{t}_1) = 548$ GeV/c^2, $\tilde{g} \to \tilde{t}_1 t$ is dominant
  * $B(\tilde{g} \to \tilde{t}_1 t) = 81\%$, $B(\tilde{g} \to \tilde{b}_1 b) = 14\%$, $B(\tilde{q}_L \to q\tilde{\chi}_2^0) = 26-27\%$,
  * $B(\tilde{\chi}_2^0 \to Z^0\tilde{\chi}_1^0) = 100\%$, $B(\tilde{\chi}_1^\pm \to W^\pm\tilde{\chi}_1^0) = 100\%$
- **Point LM9:**
  * Heavy squarks, light gluino. Consistent with EGRET data on diffuse gamma ray spectrum, WMAP results on CDM and mSUGRA [674]. Similar to LM7.
  * $m(\tilde{g}) = 507$ GeV/c^2, hence $\tilde{g} \to$ 3-body is dominant
  * $B(\tilde{\chi}_2^0 \to ll\tilde{\chi}_1^0) = 6.5\%$, $B(\tilde{\chi}_1^\pm \to \nu l\tilde{\chi}_1^0) = 22\%$
- **Point LM10:**
  * Similar to LM7, but heavier gauginos.
  * Very heavy squarks, outside reach, but light gluino.
  * $m(\tilde{g}) = 1295$ GeV/c^2, hence $\tilde{g} \to$ 3-body is dominant
  * $B(\tilde{g} \to t\bar{t}\tilde{\chi}_4^0) = 11\%$, $B(\tilde{g} \to tb\tilde{\chi}_2^\pm) = 27\%$
- **Point HM1:**
  * $m(\tilde{g}) \geqslant m(\tilde{q})$, hence $\tilde{g} \to \tilde{q}q$ is dominant
  * $B(\tilde{g} \to \tilde{t}_1 t) = 25\%$, $B(\tilde{q}_L \to q\tilde{\chi}_2^0) = 32\%$,
    but $B(\tilde{t}_1 \to t\tilde{\chi}_2^0) = 6\%$, $B(\tilde{t}_1 \to t\tilde{\chi}_3^0) = 18\%$, $B(\tilde{t}_1 \to t\tilde{\chi}_4^0) = 9\%$,
  * $B(\tilde{\chi}_2^0 \to \tilde{l}_L l) = 27\%$, $B(\tilde{\chi}_2^0 \to \tilde{\tau}_1\tau) = 14\%$, $B(\tilde{\chi}_1^\pm \to \tilde{\nu}_l l) = 37\%$
- **Point HM2:**
  * $m(\tilde{g}) \geqslant m(\tilde{q})$, hence $\tilde{g} \to \tilde{q}q$ is dominant
  * $B(\tilde{g} \to \tilde{t}_1 t) = 25\%$, $B(\tilde{q}_L \to q\tilde{\chi}_2^0) = 32\%$,
    but $B(\tilde{t}_1 \to t\tilde{\chi}_2^0) = 6\%$, $B(\tilde{t}_1 \to t\tilde{\chi}_3^0) = 20\%$, $B(\tilde{t}_1 \to t\tilde{\chi}_4^0) = 9\%$,
  * $B(\tilde{\chi}_2^0 \to \tilde{\tau}_1\tau) = 78\%$, $B(\tilde{\chi}_1^\pm \to \tilde{\nu}\tau + \tilde{\tau}_1\nu) = 13+76\%$
- **Point HM3:**
  * $m(\tilde{g}) \geqslant m(\tilde{q})$, hence $\tilde{g} \to \tilde{q}q$ is dominant
  * $B(\tilde{g} \to \tilde{t}_1 t) = 52\%$, $B(\tilde{q}_L \to q\tilde{\chi}_2^0) = 32\%$,
    but $B(\tilde{t}_1 \to t\tilde{\chi}_2^0) = 5\%$, $B(\tilde{t}_1 \to t\tilde{\chi}_3^0) = 20\%$, $B(\tilde{t}_1 \to t\tilde{\chi}_4^0) = 11\%$,
  * $B(\tilde{\chi}_2^0 \to h^0\tilde{\chi}_1^0) = 94\%$, $B(\tilde{\chi}_1^\pm \to W^\pm\tilde{\chi}_1^0) = 100\%$
- **Point HM4:**
  * $m(\tilde{g}) < m(\tilde{q})$, hence $\tilde{q} \to \tilde{g}q$ is important
  * $B(\tilde{q}_L \to \tilde{g}q) = 43\%$, $B(\tilde{q}_R \to \tilde{g}q) = 77-93\%$, $B(\tilde{g} \to \tilde{t}_1 t) = 82\%$,
  * $B(\tilde{t}_1 \to t\tilde{\chi}_2^0) = 3\%$, $B(\tilde{t}_1 \to t\tilde{\chi}_3^0) = 22\%$, $B(\tilde{t}_1 \to t\tilde{\chi}_4^0) = 16\%$,
  * $B(\tilde{\chi}_2^0 \to h^0\tilde{\chi}_1^0) = 94\%$, $B(\tilde{\chi}_4^0 \to h^0\tilde{\chi}_2^0) = 30\%$, $B(\tilde{\chi}_1^\pm \to W^\pm\tilde{\chi}_1^0) = 100\%$

The cross sections for the test points are given at NLO and LO from PROSPINO1 in Table 13.2.

Table 13.2. Cross sections for the test points in pb at NLO (LO) from PROSPINO1.

Point	$M(\tilde{q})$	$M(\tilde{g})$	$\tilde{g}\tilde{g}$	$\tilde{g}\tilde{q}$	$\tilde{q}\bar{\tilde{q}}$	$\tilde{q}\tilde{q}$	Total
LM1	558.61	611.32	10.55	28.56	8.851	6.901	54.86
			(6.489)	(24.18)	(6.369)	(6.238)	(43.28)
LM2	778.86	833.87	1.443	4.950	1.405	1.608	9.41
			(0.829)	(3.980)	(1.013)	(1.447)	(7.27)
LM3	625.65	602.15	12.12	23.99	4.811	4.554	45.47
			(7.098)	(19.42)	(3.583)	(4.098)	(34.20)
LM4	660.54	695.05	4.756	13.26	3.631	3.459	25.11
			(2.839)	(10.91)	(2.598)	(3.082)	(19.43)
LM5	809.66	858.37	1.185	4.089	1.123	1.352	7.75
			(0.675)	(3.264)	(0.809)	(1.213)	(5.96)
LM6	859.93	939.79	0.629	2.560	0.768	0.986	4.94
			(0.352)	(2.031)	(0.559)	(0.896)	(3.84)
LM7	3004.3	677.65	6.749	0.042	0.000	0.000	6.79
			(3.796)	(0.028)	(0.000)	(0.000)	(3.82)
LM8	820.46	745.14	3.241	6.530	1.030	1.385	12.19
			(1.780)	(5.021)	(0.778)	(1.230)	(8.81)
LM9	1480.6	506.92	36.97	2.729	0.018	0.074	39.79
			(21.44)	(1.762)	(0.015)	(0.063)	(23.28)
LM10	3132.8	1294.8	0.071	0.005	0.000	0.000	0.076
			(0.037)	(0.004)	(0.000)	(0.000)	(0.041)
HM1	1721.4	1885.9	0.002	0.018	0.005	0.020	0.045
			(0.001)	(0.016)	(0.005)	(0.021)	(0.043)
HM2	1655.8	1785.4	0.003	0.027	0.008	0.027	0.065
			(0.002)	(0.024)	(0.007)	(0.028)	(0.061)
HM3	1762.1	1804.4	0.003	0.021	0.005	0.018	0.047
			(0.002)	(0.018)	(0.004)	(0.019)	(0.043)
HM4	1815.8	1433.9	0.026	0.056	0.003	0.017	0.102
			(0.014)	(0.043)	(0.003)	(0.017)	(0.077)

13.4. Hemisphere algorithm for separation of decay chains

13.4.1. Basic idea and goal

In the MSSM, the primary SUSY particles are heavy and tend to be produced with a large Q^2, whereas the transverse momentum of their decay products with respect to their initial direction is limited by the magnitude of their mass. Moreover, ignoring R_p violation, they are produced in pairs. It may, therefore, be possible to separate the two decay chains by reconstructing the two production directions (in 3D) and collecting the jets and leptons in two clusters according to their "closeness" to these axes. This procedure is inspired by the reconstruction of the thrust or sphericity axis in e^+e^- collisions, except that in hadron collisions two separate axes need to be introduced per event, as the laboratory frame does not coincide with the parton centre of mass frame. Moreover, the back-to-back orientation of the sparticles in the transverse plane cannot be used, as the invisible LSP disturbs significantly the direction of the observable particles.

In hadron colliders like the LHC, the large multiplicity of jets and leptons often lead to a large combinatorial background when trying to reconstruct peaks or to determine end points in effective mass distributions (to reconstruct sparticle masses). Provided the hemisphere algorithm has a large probability to assign correctly the jets to their parents, a reduction of a factor 2 to 4 can be expected in the combinatorial background.

The proposed algorithm consists of a recursive method going through the following steps:

- Starting off by computing two initial axes (called "seeds" below).
- Associating the objects (jets and leptons) to one of these axes according to a certain criterion (hemisphere association method).
- Recalculating the axes as the sum of the momenta of all the connected objects. In order to converge to a stable solution, the axes are only updated after a full iteration is performed.
- Iterating the association until no objects switch from one group to the other.

13.4.2. Seeding methods

Two seeding methods have been tested:

(1) The first axis is chosen as the direction of the highest momentum object and the second axis as the direction of the object with the largest $p \cdot \Delta R$ with respect to the first axis, where ΔR is defined as

$$\Delta R = \sqrt{\Delta\phi^2 + \Delta\eta^2}. \tag{13.18}$$

(2) The axes are chosen as the directions of the pair of objects which have the largest invariant mass.

13.4.3. Association methods

Three association methods are available. An object is assigned to a given axis $\vec{A}$ when:

(1) The scalar product $\vec{p} \cdot \vec{A}$ is maximum, which amounts to choosing the smallest angle
(2) The hemisphere squared masses are minimum, i.e. object k is associated to the hemisphere with mass m_i rather than m_j if $m_{ik}^2 + m_j^2 \leqslant m_i^2 + m_{jk}^2$. This is equivalent to the requirement

$$(E_i - p_i \cos\theta_{ik}) \leqslant (E_j - p_j \cos\theta_{jk}).$$

(3) The Lund distance measure is minimum, i.e.

$$(E_i - p_i \cos\theta_{ik}) \frac{E_i}{(E_i + E_k)^2} \leqslant (E_j - p_j \cos\theta_{jk}) \frac{E_j}{(E_j + E_k)^2}.$$

In order to converge to a stable solution, the axes are only updated after a full iteration is performed.

13.4.4. Results

The performance of the hemisphere assignment was tested on events with production of squarks and/or gluinos. Jets were reconstructed using the Iterative Cone method with $\Delta R = 0.5$ and calibrated with the "GammaJet" procedure. They were selected when $E_T > 30\,\text{GeV}$ and $|\eta| < 3.0$. The momentum vectors used were from the Monte carlo parton level objects which matched with the jets and/or leptons. Some of the CMS test points were used, namely LM1 (dilepton final states via $\tilde{l}_R$), LM5 (with decay of $\tilde{\chi}_2^0$ to $h \to b\bar{b}$) and LM9 (with dileptons from 3-body decays).

The efficiencies quoted below are the ratio between the correctly assigned MC objects and their total number. The correct hemisphere was chosen as the one for which

Table 13.3. Efficiencies for test point LM1.

Type of jet	all jets	quark jets	gluon jets	q from $\tilde{q}$	q from $\tilde{g}$
Seed 1, Assoc 1	79%	80%	74%	85%	69%
Seed 1, Assoc 2	80%	80%	77%	85%	72%
Seed 2, Assoc 2	81%	81%	78%	85%	72%
Seed 2, Assoc 3	81%	81%	79%	86%	73%

Table 13.4. Efficiencies for test points LM1, LM5 and LM9, using the methods Seed 2 and hemisphere association 3.

Point	all jets	quark jets	gluon jets	q from $\tilde{q}$	q from $\tilde{g}$
LM1	81%	81%	79%	86%	73%
LM5	77%	77%	74%	87%	70%
LM9	74%	75%	69%	–	76%

the axis matched most closely the original squark or gluino, after subtracting from it the unobserved $\tilde{\chi}_1^0$.

The efficiencies of various types of jets for the different algorithms at the test point LM1 are summarised in Table 13.3.

It is seen that all the algorithms behave nearly in the same way, with the combination (seed 1, hemisphere association 1) being slightly worse and (seed 2, hemisphere association 3) slightly better.

The efficiencies obtained for the different test points are listed in Table 13.4 for the different types of jets by using the (seed 2, hemisphere association 3) method. Note that at point LM9 the $\tilde{g}$ undergoes a direct 3-body decay, the $\tilde{q}$ being heavier than the $\tilde{g}$.

From these tests it can be concluded that quark jets from $\tilde{q}$ have a rather high efficiency, $\geqslant 85\%$, to be correctly assigned to a hemisphere, whereas the quark jets from a $\tilde{g}$ reach only $\gtrsim 70\%$. This reflects the fact that the latter jets are much softer, on average, than the jets from the $\tilde{q}$ decay.

The same procedure was also applied to leptons (e or μ). However, due to their small mass, the leptons barely "feel" the boost and are sent in any direction. The results were only slightly better than the expectation from random association. Some improvement could be obtained, e.g. for $\tilde{\chi}_2^0 \to e^+e^-\tilde{\chi}_1^0$, by treating the lepton pair as a single (massive) object. But this introduces some model dependence.

The power of the hemisphere separation can be further illustrated by the search for Higgs at point LM5. The reconstructed jets selected as above are identified as b-jets by a combined b-tagging method (see Vol. 1, Section 12.2.2) when the discriminant variable is > 1.5. The invariant mass of all combinations of two b-jets is displayed in Fig. 13.4 (left). The peak from $h^0 \to b\bar{b}$ is visible above a large combinatorial SUSY background, mostly due to the production of $\tilde{b}\tilde{b}$ and $\tilde{t}\tilde{t}$ (directly or from cascade decays). After applying the hemisphere separation method, the 2b invariant mass combinations are separated into the cases where both b-jets are in the same hemisphere (centre), with a clearly visible Higgs peak, and in opposite hemispheres (right), where almost no sign of Higgs remains. Note that these plots were obtained without selection cuts. This method has been used for the Higgs search in Section 13.10 and in other searches.

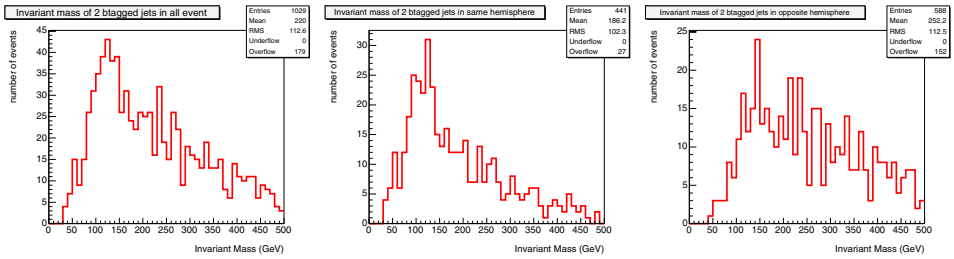

Figure 13.4. $b\bar{b}$ invariant mass distributions in h^0 production with mass $m_h = 116\,\text{GeV}$ for (left) all combinations, (centre) combinations in the same hemisphere, (right) combinations in opposite hemispheres.

13.5. Inclusive analysis with missing transverse energy and jets

The missing transverse energy plus multi-jets final state has been a canonical signature for SUSY searches. This study is a search for the production and decay of gluinos and scalar quarks in $\geqslant$3-jet events with large missing transverse energy. The large missing energy originates from the two LSPs in the final states of the squark and gluino decays. The three or more hadronic jets result from the hadronic decays of the squarks and/or gluinos. The full analysis is presented in section 4.2. The analysis uses the LM1 test-point at which squark and gluino production has a LO cross section of 49 pb. The major Standard Model background components include production of $Z+$ jets with the Z decaying invisibly, W+jets, top-anti-top pairs, dibosons, single top and QCD jets. The trigger path used is the missing energy plus jets both at Level-1 and at HLT.

13.5.1. Analysis path and results

Events that are accepted after clean-up pre-selection requirements, proceed through the analysis path if they have missing transverse energy $E_{\text{T}}^{\text{miss}} > 200\,\text{GeV}$ and at least three jets with $E_{\text{T}} \geqslant 30\,\text{GeV}$ within $|\eta| < 3$. In addition the leading jet is required to be within the central tracker fiducial volume *i.e.* $|\eta| < 1.7$. These requirements directly define the searched for signal signature. The rest of the analysis path is designed based on elimination of the major classes of backgrounds: the QCD production, top–anti-top pairs and the W /Z -QCD associated production. In Table 13.5 the path is shown with a remark indicating the reason and aim of each selection step.

A detailed explanation of the analysis path requirements and variables used is given in section 4.2. The global signal efficiency for the analysis is 13% while the signal to background ratio is ~ 26. The results are shown in Table 13.6 for $1\,\text{fb}^{-1}$.

In summary the major background components and their uncertainties are as follows:

- $t\bar{t}$ uncertainties: 7% $E_{\text{T}}^{\text{miss}}$ shape, 22% JES, 13% statistical;
- $Z \longrightarrow \nu\bar{\nu}+$jets, $W/Z+$jets: 5% Luminosity (direct candle normalisation to the data (*cf.* section 4.2);
- QCD: $E_{\text{T}}^{\text{miss}}$ 7% shape, 22% JES, 10% statistical.

The number of backgrounds events per background component and their uncertainties are tabulated in Table 13.7. Based on the Standard Model background estimates and their uncertainties, a 5σ observation of low mass SUSY at LM1 (gluino mass $600\,\text{GeV/c}^2$) is achievable with $\sim 6\,\text{pb}^{-1}$ in events with large missing energy plus multi-jets, using a

Table 13.5. The $E_{\mathrm{T}}^{\mathrm{miss}}$ + multi-jet SUSY search analysis path.

Requirement	Remark
Level 1	Level-1 trigger efficiency parametrisation
HLT, $E_{\mathrm{T}}^{\mathrm{miss}} > 200\,\mathrm{GeV}$	trigger/signal signature
primary vertex $\geqslant 1$	primary cleanup
$F_{em} \geqslant 0.175$, $F_{ch} \geqslant 0.1$	primary cleanup
$N_j \geqslant 3$, $\lvert\eta_d^{1j}\rvert < 1.7$	signal signature
$\delta\phi_{min}(E_{\mathrm{T}}^{\mathrm{miss}} - jet) \geqslant 0.3$ rad, $R1$, $R2 > 0.5$ rad,	
$\delta\phi(E_{\mathrm{T}}^{\mathrm{miss}} - j(2)) > 20^{\circ}$	QCD rejection
$Iso^{lead\,trk} = 0$	ILV (I) $W/Z/t\bar{t}$ rejection
$f_{em(j(1))}$, $f_{em(j(2))} < 0.9$	ILV (II), $W/Z/t\bar{t}$ rejection
$E_{\mathrm{T},j(1)} > 180\,\mathrm{GeV}$, $E_{\mathrm{T},j(2)} > 110\,\mathrm{GeV}$	signal/background optimisation
$H_{\mathrm{T}} \equiv E_{\mathrm{T}(2)} + E_{\mathrm{T}(3)} + E_{\mathrm{T}(4)} + E_{\mathrm{T}}^{\mathrm{miss}} > 500\,\mathrm{GeV}$	signal/background optimisation
SUSY LM1 signal efficiency 13%	

Table 13.6. Selected SUSY and Standard Model background events for 1 fb^{-1}.

Signal	$t\bar{t}$	single t	$Z(\rightarrow \nu\bar{\nu})$+ jets	$(W/Z, WW/ZZ/ZW)$ + jets	QCD
6319	53.9	2.6	48	33	107

Table 13.7. Standard Model background components and uncertainties for 1 fb^{-1}.

$t\bar{t}$, single top	$Z(\rightarrow \nu\bar{\nu})$+ jets	$(W/Z, WW/ZZ/ZW)$ + jets	QCD
56 ± 11(sys) ± 7.5(stat)	48 ± 3.5 (all)	33 ± 2.5 (all)	107 ± 25(sys) ± 10(stat)

significance computed with ScPf, defined in Appendix A.1. After $\sim 1.5\,\mathrm{fb}^{-1}$ the W/Z+jets backgrounds, including the invisible decays of the Z boson which constitutes a large irreducible background component, can be reliably normalised using the $Z \rightarrow \mu\mu$ and $Z \rightarrow ee$ + multi-jet data candle. The comparison of the signal, total background estimated and its components for the $M_{eff} \equiv E_{\mathrm{T}(1)} + E_{\mathrm{T}(2)} + E_{\mathrm{T}(3)} + E_{\mathrm{T}(4)} + E_{\mathrm{T}}^{\mathrm{miss}}$ can be found in section 4.2.

To perform the 5 σ reach scan (Fig. 13.5) in the mSUGRA parameter space, the HM1 test point is used as optimisation reference and the $E_{\mathrm{T}}^{\mathrm{miss}}$ and H_{T} requirements are raised to 600 GeV and 1500 GeV correspondingly. The analysis efficiency for HM1 is ~12% while the total Standard Model background for 1 fb^{-1} is 4.36 events with a total uncertainty of 7% . The background composition is 67% Z invisible decays, 19% QCD jets and 14% W/Z+jets.

13.6. Inclusive muons with jets and missing transverse energy

We study the production and decay of new particles in mSUGRA via inclusive final states including muons, high p_{T} jets, and large missing transverse energy. Requiring at least one muon provides a relatively clean experimental signature (complementing searches involving only inclusive jets and missing energy), however requires a well-understood trigger shortly after the LHC start-up. In this work [675], the fully simulated and reconstructed LM1 mSUGRA point is taken as the benchmark for selection optimisation and study of systematic effects. Even though the study was performed within the context of mSUGRA, this method is not specific to the mSUGRA framework and should apply equally well in other contexts.

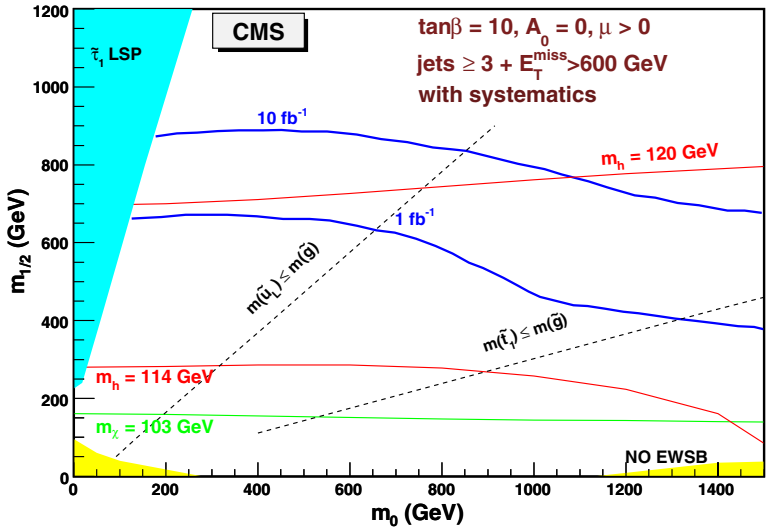

Figure 13.5. 5 σ reach for 1 and 10 fb^{-1} using multi-jets and missing transverse energy final state.

The strategy employed in this analysis is to optimise a set of selection cuts based on an objective function which provides a reasonable estimate of the significance to exclude the Standard Model null-hypothesis while explicitly including systematic uncertainties (thus avoiding regions of phase space which are prone to systematics). This work uses a Genetic Algorithm (GARCON [63]) for the optimisation of cuts.

13.6.1. Signal selection and backgrounds considered

Because this work is an inclusive study of mSUGRA signatures involving at least one muon accompanied by multiple jets and large $E_{\text{T}}^{\text{miss}}$, several Standard Model processes contribute as sources of background and must be taken into account. Accordingly, the main backgrounds studied in this analysis correspond to QCD dijet (2.8 million events with $0 < \hat{p}_{\text{T}} < 4\,\text{TeV/c}$), top ($t\bar{t}$) production (3.3 million events), electroweak single-boson production (4.4 million events with $0 < \hat{p}_{\text{T}} < 4.4\,\text{TeV/c}$) and electroweak dibosons production (1.2 million events). All backgrounds used in this work are fully simulated and reconstructed. This work uses only leading order cross-sections, consistently for both signal and all backgrounds. Considering NLO k-factors for the signal and background processes do not change the final results significantly.

The CMS trigger system is described in [76], and the current working trigger menu is described in Appendix E. This work uses an event sample which is triggered by either of two HLT triggers: the inclusive isolated single-muon trigger or the isolated dimuon trigger.

The following quality criteria are applied to muons and jets. The leading muon is required to have a transverse momentum above $p_{\text{T}} = 30\,\text{GeV/c}$ which ensures that the muon candidate is reconstructed with good efficiency, well above the trigger thresholds. Further, the leading muon is required to be isolated with less than 10 GeV of calorimeter energy within a cone of radius $R = 0.3$, reducing the effects due to fake muons, whilst preserving reasonable efficiency for signal acceptance. Finally, the three leading jets must each have an E_{T} of at least 50 GeV which guarantees that jets are reconstructed with good efficiency.

Table 13.8. Total number of selected events (for $10\,\text{fb}^{-1}$) and significance ("Signif.") with systematic uncertainties (but excluding uncertainties due to finite Monte Carlo simulation statistics and higher order QCD effects). "SM" represents the total of all Standard Model backgrounds considered.

Sample(s)	Events	Signif.	Sample	Events	Signif.	Sample	Events	Signif.
SM	2.54	–	LM4	246	29.2	LM6	277	31.6
LM1	311	34.0	LM5	165	22.9	HM1	13	5.0

The genetic algorithm GARCON [63] used for the optimisation of cuts results in: $E_{\text{T}}^{\text{miss}} > 130\,\text{GeV}$, $E_{\text{T}}^{\text{j1}} > 440\,\text{GeV}$, $E_{\text{T}}^{\text{j2}} > 440\,\text{GeV}$, $|\eta^{\text{j1}}| < 1.9$, $|\eta^{\text{j2}}| < 1.5$, $|\eta^{\text{j3}}| < 3$, $\cos\left[\Delta\phi(\text{j1},\text{j2})\right] < 0.2$, $-0.95 < \cos\left[\Delta\phi(E_{\text{T}}^{\text{miss}},\text{j1})\right] < 0.3$, $\cos\left[\Delta\phi(E_{\text{T}}^{\text{miss}},\text{j2})\right] < 0.85$. Assuming $10\,\text{fb}^{-1}$ of collected data, this set of cuts would expect to select a total of 2.54 background events from the Standard Model and 311 signal events from the mSUGRA LM1 benchmark signal point.

13.6.2. Results for 10 fb^{-1} using full detector simulation and reconstruction

After all selection cuts have been applied, several effects contribute as systematic uncertainties, including: jet energy scale (10%), jet energy resolution (5%), luminosity measurement (5%), and full GEANT simulation versus fast simulation differences (5%), used to determine the analysis reach in mSUGRA parameters in Section 13.6.3). Since this analysis is performed consistently at leading order, the inclusion of higher order effects involving ISR/FSR is not taken into account. A generator-level comparison of the parton shower method for inclusive $t\bar{t}$ used by PYTHIA [69] with the matrix element calculation for $t\bar{t}+1$jet from COMPHEP [355] suggests a $\approx 10\%$ enhancement in the acceptance of $t\bar{t}+1$jet events (generated via the matrix element method) compared with inclusive $t\bar{t}$. When combined with other expected effects – such as underlying event (5%), pile-up (5%), and parton distribution functions (5%) – a total theoretical systematic uncertainty of $\sim 13\%$ is estimated. The dominant uncertainty (32%) arises from an inability to precisely predict the number of background events, due to finite Monte Carlo simulation statistics. We note that by the time $10\,\text{fb}^{-1}$ of data is collected, many of the contributing background processes will be measured from real data, thereby reducing this uncertainty. If one includes the uncertainty due to finite Monte Carlo simulation statistics, the total systematic uncertainty for this work is 37%. Neglecting Monte Carlo simulation statistics, as well as higher order QCD effects, the total systematic uncertainty for this work is 19%.

Table 13.8 shows the main results of this study. For the fully simulated low mass mSUGRA point LM1, and assuming $10\,\text{fb}^{-1}$ of data, this work selects an expected 311 signal events (with an efficiency of 0.074%) compared with 2.54 expected background events, comprised of $t\bar{t}$ (0.73 events), $W+$ jets (1.56 events), and $Z+$ jets (0.24 events). The separation of signal from background for the different low mass mSUGRA points range in values from 23 to 34 in significance, including systematic uncertainties (but excluding uncertainties related to the limited number of simulated events). Such large values of significance merely indicate that the low mass mSUGRA region will either have been discovered or excluded, long before $10\,\text{fb}^{-1}$ of data is collected. We note that shortly after the LHC start-up, the systematic understanding of the CMS detector is expected to be quite different than what is presented in this work, which assumes $\mathcal{L} = 10\,\text{fb}^{-1}$. Nevertheless, if one assumes a similar systematic understanding and extrapolates the results of this work to early running, the expected

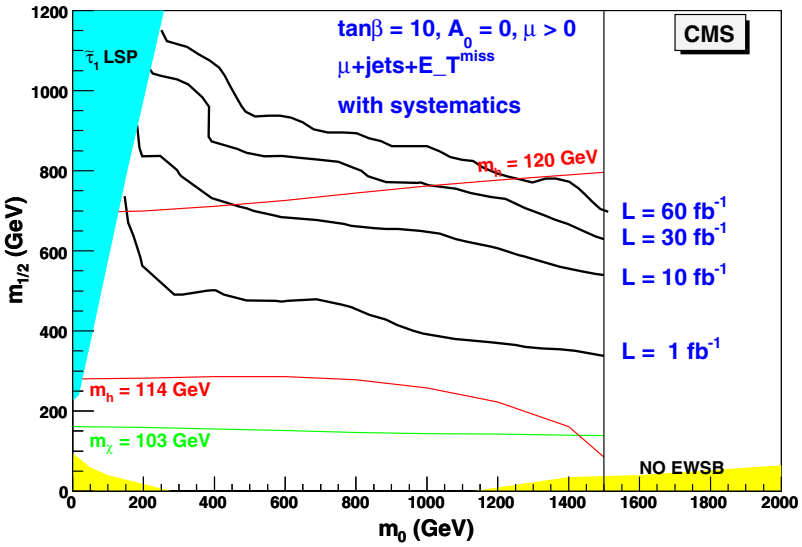

Figure 13.6. CMS discovery reach contours in the m_0–$m_{1/2}$ plane using inclusive muons with jets and missing energy for 10 fb^{-1} (lower contour), 30 fb^{-1} (middle contour), and 60 fb^{-1} (upper contour) including systematics.

luminosity required to discover the LM1 mSUGRA study point would be O(0.1) fb^{-1}. Hence, low mass SUSY is a prime candidate for possible discovery during the very early running of the LHC.

13.6.3. CMS Reach using inclusive muons with jets and missing energy

Since CMS will have either discovered or excluded the lower mass region well in advance of the time required to collect 10 fb^{-1} of data, the selection cuts for 30 fb^{-1} and 60 fb^{-1} are re-optimised using GARCON to select the HM1 mSUGRA point: $E_{\mathrm{T}}^{\mathrm{miss}} > 210\,\mathrm{GeV}$, $E_{\mathrm{T}}^{\mathrm{j1}} > 730\,\mathrm{GeV}$, $E_{\mathrm{T}}^{\mathrm{j2}} > 730\,\mathrm{GeV}$, $\cos\left[\Delta\phi(\mathrm{j1},\mathrm{j2})\right] < 0.95$, $\cos\left[\Delta\phi(\mathrm{E_T^{miss}},\mathrm{j1})\right] < -0.2$, $\cos\left[\Delta\phi(\mathrm{E_T^{miss}},\mathrm{j2})\right] < 0.95$. To estimate the reach for 30 fb^{-1} and 60 fb^{-1}, this same cut-set is applied in both cases and results in an estimated Standard Model background yield of $N_{\mathrm{B}} = 0.25$ for 30 fb^{-1}, and $N_{\mathrm{B}} = 0.49$ for 60 fb^{-1}. In both cases the uncertainty on the background levels is $\approx 71\%$, primarily due to a limited number of simulated events; if one neglects that uncertainty, the systematic uncertainty is $\approx 19\%$.

Fast simulation and reconstruction was also performed in order to scan the plane of universal scalar (m_0) and gaugino ($m_{1/2}$) masses for fixed mSUGRA parameters: $\tan\beta = 10$, $\mu > 0$ and $A_0 = 0$. Points were generated on a coarse grid with $\Delta m_0 = 100\,\mathrm{GeV/c^2}$ and $\Delta m_{1/2} = 100\,\mathrm{GeV/c^2}$, starting from the point $m_0 = 100\,\mathrm{GeV}$, $m_{1/2} = 100\,\mathrm{GeV}$. Figure 13.6 shows the discovery reach of this analysis (contours correspond to a significance value of 5), plotted in the mSUGRA m_0–$m_{1/2}$ plane. Assuming 10 fb^{-1} of data, CMS can observe SUSY mass scales of over $\approx 1.5\,\mathrm{TeV/c^2}$; assuming 30 fb^{-1} of integrated luminosity, several of the high mass CMS SUSY benchmark points become interesting for possible discovery; and, assuming 60 fb^{-1} of integrated luminosity, CMS is able to reach in this channel SUSY mass scales of up to $\approx 2\,\mathrm{TeV/c^2}$.

13.7. Inclusive analyses with same sign dimuons

The topology of two same sign isolated muons, high p_T jets, and large missing transverse energy is interesting as it allows for an efficient suppression of the Standard Model backgrounds, and at the same time allows much of the mSUGRA signal to be retained. Like-sign leptons can result from several signal processes because the gluino, being a Majorana particle, has equal probability of yielding either a positively or a negatively charged lepton in its decay chain. Squark production is another important source of like-sign dileptons, since the squark charge tends to be determined by the valence quarks in the proton-proton collision. The same-sign muon topology provides a clean experimental signature and has the extra advantage of an anticipated efficient and well-understood dimuon trigger soon after LHC start-up. Even though this study [676] is performed within the context of mSUGRA, this method is not specific to the mSUGRA framework.

The genetic algorithm GARCON [63] is used to determine the optimal set of cuts for each mSUGRA benchmark point. An interval for each physics cut-parameter is then defined corresponding to its minimal cut value and the maximum cut value, determined over all different optimal mSUGRA benchmark point cut-sets. The interval for each cut-parameter is then coarsely binned and the significance systematically calculated for each possible cut combination within this reduced sub-space.

13.7.1. Signal selection and backgrounds

Because this work is an inclusive study of mSUGRA signatures involving at least two like-sign muons accompanied by multiple jets and large missing transverse energy, several Standard Model processes contribute as sources of background and must be taken into account. Accordingly, the main backgrounds studied in this analysis correspond to QCD dijet (2.8 million fully simulated events with $0 < \hat{p}_T < 4\,\text{TeV/c}$), top ($t\bar{t}$) production (3.3 million fully simulated events), electro-weak single boson production (4.4 million fully simulated events with $0 < \hat{p}_T < 4.4\,\text{TeV/c}$) and electro-weak dibosons production (1.2 million fully simulated events). This work uses only leading order cross-sections, consistently for both signal and all backgrounds.

The dimuon HLT trigger (98% efficient) is required for this analysis. The following selection criteria are applied to muons and jets. The two leading muons are required to be of the same sign and to each have a transverse momentum above 10 GeV/c, ensuring that the muon candidate is reconstructed with good efficiency, above the symmetric thresholds of 7 GeV/c in the dimuon trigger. Also this analysis requires at least three jets in the event, all of which are required to have $E_T > 50\,\text{GeV}$.

In order to select the particular SUSY diagrams responsible for prompt same-sign dimuons, we apply the following criteria. Each reconstructed muon is required to be separated by at least $\Delta R \geqslant 0.01$ from the other muons. The muon track fit is required to have $\chi^2_\mu \leqslant 3$ and the number of hits associated with the muon must be at least 13. Each muon is required to be isolated, both with respect to the tracker and calorimeter. A combined isolation parameter is used to account for correlations between the tracker (`IsoByTk`) and calorimeter (`IsoByCalo`) isolation variables, $\texttt{Iso} = \texttt{IsoByTk} + 0.75 \times \texttt{IsoByCalo}$, with $\texttt{Iso}_{\mu 1} \leqslant 10\,\text{GeV}$, $\texttt{Iso}_{\mu 2} \leqslant 6\,\text{GeV}$.

In addition to *a priori* requiring three jets in the event, the cut-set maximising the significance (with GARCON) to discover the lowest significant fully simulated mSUGRA test point is then chosen as the final optimal cut-set: $E_T^{j1} > 175\,\text{GeV}$, $E_T^{j2} > 130$ GeV, $E_T^{j3} > 55$ GeV, $E_T^{\text{miss}} > 200\,\text{GeV}$.

Table 13.9. Total number of selected events (for $\mathcal{L} = 10\,\text{fb}^{-1}$) and significance ("Signif.") with systematic uncertainties. "SM" represents the total of all Standard Model backgrounds considered.

Sample(s)	Events	Signif.	Sample	Events	Signif.	Sample	Events	Signif.
SM	1.5	–	LM5	61	14.0	LM10	4	2.2
LM1	341	>37.0	LM6	140	22.3	HM1	4	2.2
LM2	94	17.6	LM7	82	16.3	HM2	2	1.1
LM4	90	17.2	LM8	294	35.9			

13.7.2. Results for full detector simulated mSUGRA samples

After all selection cuts have been applied the main systematic uncertainty is due to the absolute jet energy scale, which is estimated to be 15% after $10\,\text{fb}^{-1}$. In addition, jet energy resolution (10%), muon identification efficiency and fake rate (negligible), luminosity (5%), theory (10%; cross sections, showering, ISR/FSR, etc.) and full simulation versus fast simulation (5%, used to determine the analysis reach in mSUGRA parameters in Section 13.7.3) have been evaluated. Since this analysis is performed consistently at leading order, the inclusion of higher order effects involving ISR/FSR is not taken into account. A generator-level comparison of the parton shower method for inclusive $t\bar{t}$ used by PYTHIA [69] with the matrix element calculation for $t\bar{t}+1$jet from COMPHEP [355] suggests a $\approx 10\%$ enhancement in the acceptance of $t\bar{t}+1$jet events (generated via the matrix element method) compared with inclusive $t\bar{t}$. The total systematic uncertainty on the number of background events is 24%.

Table 13.9 shows the main results of this study. For the fully simulated low mass mSUGRA point LM1, assuming $10\,\text{fb}^{-1}$ of data, this work selects an expected 341 signal events (with an efficiency of 0.081%) compared with 1.5 expected background events (comprised of $t\bar{t}$). For other fully simulated low mass mSUGRA points (excluding LM10) and an integrated luminosity $10\,\text{fb}^{-1}$ of data, the selection cuts (collectively optimised over all benchmark points) achieve a separation of signal from background with a statistical significance of between 16σ and greater than 37σ, including systematic uncertainties. Such a large significance merely indicates that the low mass mSUGRA region will either have been discovered or excluded, long before $10\,\text{fb}^{-1}$ of data is collected. Hence, low mass SUSY is a prime candidate for possible discovery during the very early running of the LHC. The discovery of high mass SUSY, represented by the fully simulated HM1 and HM2 points, is more difficult and requires more than $10\,\text{fb}^{-1}$ of data.

13.7.3. CMS inclusive reach

Fast simulation and reconstruction was also performed in order to scan the plane of universal scalar (m_0) and gaugino ($m_{1/2}$) masses for fixed mSUGRA parameters: $\tan\beta = 10$, $\mu > 0$ and $A_0 = 0$. Points were generated on a coarse grid with $\Delta m_0 = 100\,\text{GeV/c}^2$ and $\Delta m_{1/2} = 100\,\text{GeV/c}^2$, starting from the point $m_0 = 100\,\text{GeV/c}^2$, $m_{1/2} = 100\,\text{GeV/c}^2$.

The 5σ reach of this analysis, including systematic uncertainties, for different integrated luminosities and assuming no re-optimisation of the selection cuts is shown on Fig. 13.7. By the time CMS collects integrated luminosity $30\,\text{fb}^{-1}$, the high mass point HM1 becomes interesting for possible discovery. For comparison, $\mathcal{L} = 1\,\text{fb}^{-1}$ and $\mathcal{L} = 100\,\text{fb}^{-1}$ are also shown in the figure. Clearly, the systematics for $\mathcal{L} = 1\,\text{fb}^{-1}$ will be higher than that assumed in this work, nevertheless these results strongly suggest (provided systematics can be brought

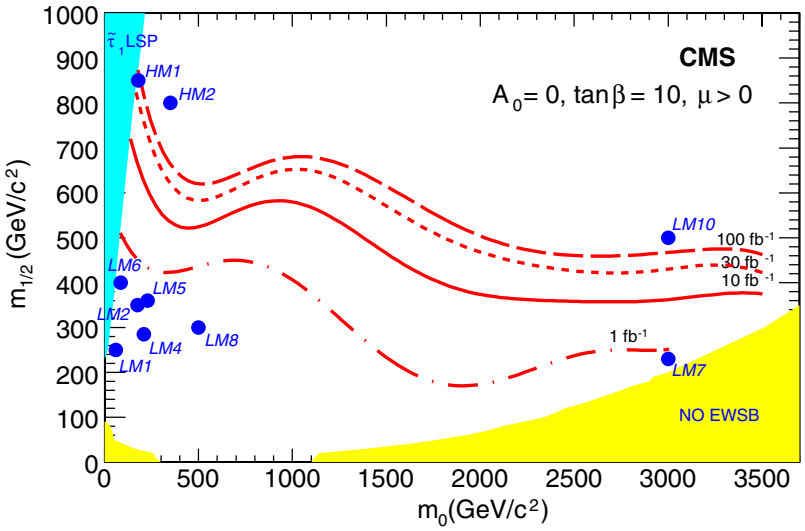

Figure 13.7. CMS reach contours (systematic uncertainties included) in the $(m_0, m_{1/2})$ plane for SUSY processes involving two prompt same-sign muons for $\mathcal{L} = 1\,\text{fb}^{-1}$ (dot-dashed line), $\mathcal{L} = 10\,\text{fb}^{-1}$ (solid line), $\mathcal{L} = 30\,\text{fb}^{-1}$ (short dashed line) $\mathcal{L} = 100\,\text{fb}^{-1}$ (dashed line). The other mSUGRA parameters are fixed to $\tan\beta = 10$, $\mu > 0$ and $A_0 = 0$. Points corresponding to the full detector simulation and reconstruction are also shown (solid circles).

under control) that most of the low mass mSUGRA points are well within reach of CMS during the early running of the LHC.

13.8. Inclusive analyses with opposite sign dileptons

Final states with opposite sign dileptons, originating from the decay $\tilde{\chi}_2^0 \to \tilde{l}_R l \to l^+ l^- \tilde{\chi}_1^0$ in the cascade decays of squarks and gluinos provide a clean signature of SUSY with isolated leptons, high p_T jets and missing transverse energy [677]. In addition, the dilepton invariant mass distribution for this decay is expected to have a triangular shape with a sharp upper edge, which renders this signature striking and useful for further characterisation of SUSY.

13.8.1. Signal selection and backgrounds

The analysis is performed at the LM1 mSUGRA test-point using GEANT-based detailed simulation of the CMS detector [8] and reconstruction [10]. The fast CMS simulation and reconstruction [11] is used to evaluate the discovery reach in the mSUGRA parameter space.

Signal events were generated by ISAJET 7.69 interfaced to PYTHIA 6.225 at the test point LM1, where the NLO cross section at NLO is about 52 pb, dominated by the production of $\tilde{q}\tilde{g}$, $\tilde{g}\tilde{g}$ and $\tilde{q}\bar{\tilde{q}}$. The gluino is the heaviest particle and decays to $\tilde{q}q$. While right squarks decay almost directly to the LSP, due to the bino-like nature of the $\tilde{\chi}_1^0$ at Point LM1, left-handed squarks decay to $\tilde{\chi}_2^0$ with a branching ratio $\sim 30\%$.

The SM backgrounds studied consist of $t\bar{t}$, W+ jets, Z+ jets, WW+ jets, ZZ+ jets, Zbb (with leptonic decays of the Z boson), Drell–Yan leptonic events and QCD dijet production processes.

Table 13.10. Cross section at NLO, selection efficiencies and number of events surviving cuts for signal and background processes.

Process	σ (pb)	Ev. analysed	ε	N_{ev} in 1 fb $^{-1}$
SUSY (LM1)	52	478 k	0.016	853
$t\bar{t}$	830	913 k	$1.9 \cdot 10^{-4}$	155
WW+ jets	188	197 k	$1.4 \cdot 10^{-4}$	26
Z+ jets	$5 \cdot 10^3$	606 k	$4.8 \cdot 10^{-6}$	24
DY $\rightarrow 2\mu$	$3.97 \cdot 10^3$	916 k	$< 1.1 \cdot 10^{-6}$	< 4
DY $\rightarrow 2\tau$	$3.97 \cdot 10^3$	514 k	$1.1 \cdot 10^{-6}$	4.5
$Zbb \rightarrow llbb(l = e, \mu, \tau)$ $P^T_{hat} > 60$ GeV/c	57.4	621 k	$8.4 \cdot 10^{-5}$	4.83
$t\bar{t}b\bar{b}$	3.3	50 k	$9.8 \cdot 10^{-4}$	3.2
ZZ+ jets	11	37k	$2.4 \cdot 10^{-4}$	2.7
W+ jets	$1.5 \cdot 10^5$	1765k	$6.7 \cdot 10^{-9}$	1

The SUSY final state studied contains at least two high-p_T isolated leptons, at least two high-p_T jets and large missing transverse energy. The event selection path includes the following requirements:

- the Level-1 and HLT path that requires a single isolated lepton (muon or electron);
- at least two same-flavour opposite-sign (SFOS) isolated leptons (e or μ) with $p_T \geqslant 10$ GeV/c and $\Delta R_{ll} \geqslant 0.2$ and 0.15 for ee and $\mu\mu$, respectively where ΔR_{ll} is the distance of the two leptons in the $\eta - \phi$ space;
- $E_T^{miss} > 200$ GeV;
- at least two jets with $p_T \geqslant 100$ and $\geqslant 60$ GeV/c within $|\eta| < 3$.

The isolation of the leptons is obtained requiring the sum of p_T of the tracks in a cone of $\Delta R = 0.25$ around the lepton track to be less than 5 GeV/c. The E_T^{miss} is computed from the vectorial sum of the jets and leptons.

These selection criteria result in 853 signal events (which correspond to 913 dilepton pairs) for a luminosity of 1 fb^{-1}. The Standard Model background consists of 155 $t\bar{t}$ events, 26 events from WW + jets and 24 events from Z + jets (Table 13.10). All other backgrounds have been found to be negligible and amount in total to at most 20 events.

13.8.2. Results for point LM1

The dilepton invariant mass distribution for 1 fb^{-1} is displayed in Fig. 13.8 showing a clear dilepton edge structure.

The presence of two SFOS leptons can also be due to other processes. Two leptons can result from independent leptonic decays, for example from two charginos or two W's. In that case the final state contains as many SFOS leptons as different-flavour opposite-sign (DFOS) ones and with identical distributions. The background to the SFOS contribution is removed by subtracting the DFOS events, which leads to the dilepton mass distribution of Figure 13.9. The $t\bar{t}$ and WW + jets backgrounds are also strongly reduced by the flavour subtraction. The resulting dilepton invariant mass distribution is fitted using a triangular function smeared (for resolution effects) with a Gaussian to extract the end-point related to the kinematics of the decay $\tilde{\chi}_2^0 \rightarrow \tilde{l}_R l \rightarrow l^+ l^- \tilde{\chi}_1^0$. The value obtained from 1 fb^{-1} of integrated luminosity is:

$$M_{ll}^{max} = 80.42 \pm 0.48 \text{ GeV/c}^2 \tag{13.19}$$

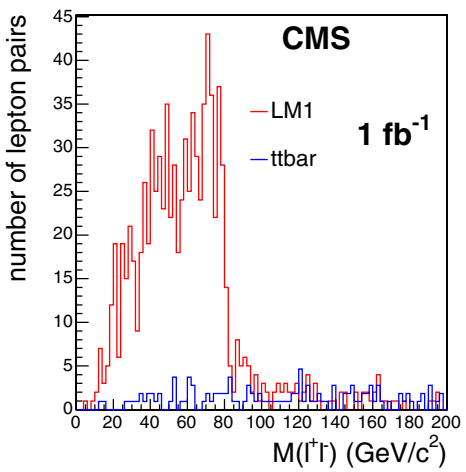

Figure 13.8. Invariant mass distribution of $\mu^+\mu^- + e^+e^-$ and $\mu^\pm e^\mp$ pairs at LM1 for 1 fb^{-1} luminosity. The contribution from the $t\bar{t}$ background is also shown.

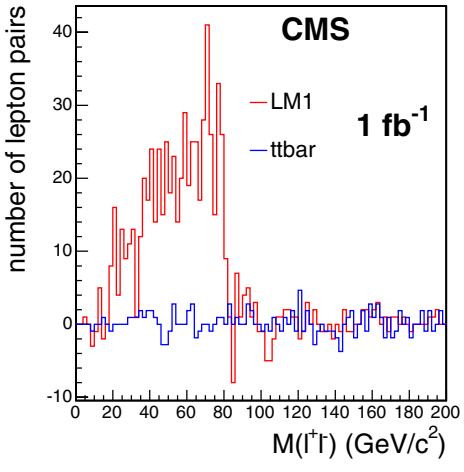

Figure 13.9. Invariant mass distribution of $\mu^+\mu^- + e^+e^-$ and $\mu^\pm e^\mp$ pairs at point LM1 for 1 fb^{-1} luminosity after subtracting $e^+\mu^-$ and μ^+e^- pairs. The contribution from the $t\bar{t}$ background is also shown.

to be compared to the expected value of 81.04 GeV/c^2 for the masses $m(\tilde{\chi}_1^0) = 95$, $m(\tilde{\chi}_2^0) = 180$ and $m(\tilde{l}_R) = 119$ GeV/c^2. The signal-to-background ratio at point LM1 is 4.1, the total signal efficiency is 1.6% and the background composition is 69% of total ttbar, 11.6% of total WW + jets, 10% Z + jets, 3% DY, 2% Zbb, 1% ttbb, 1% ZZ + jets, fractions the others. The total efficiency for the QCD background is too low to be directly calculated, and is then estimated through a factorisation, considering separately the effects due to the single selection cuts. Although the number of surviving QCD events is expected to be negligible, a residual QCD background is still possible, which will be measured using the real data. A statistical significance of 5 sigma, calculated using S_{cP} defined in Appendix A.1, is achieved with 14 pb^{-1} of integrated luminosity. At this luminosity 12.8 signal events are expected with 3.1 Standard Model background events. Therefore this signature is a strong probe for early discovery of low mass supersymmetry.

Systematic uncertainties have been evaluated under the assumption that control data are used for the Standard Model processes. Hence no uncertainties on the theory cross sections, showering, ISR/FSR, are taken into account. The main systematic uncertainty considered is due to the absolute jet energy scale. A $\simeq 7\%$ uncertainty on the jet energy scale for 1 fb^{-1} of data is used while this is expected to be $\simeq 2\%$ after 10 fb^{-1}. After applying the selection cuts this leads to a $\simeq 20\%$ systematic uncertainty on the $t\bar{t}$ background and to a $\simeq 8\%$ systematic uncertainty on the SUSY signal. The electron energy scale uncertainty, expected to be 0.25%, leads to a systematic uncertainty of less than 1% on the background, and less than 0.1% on the signal. The total considered systematic uncertainty on the Standard Model background is 20% at low luminosity, 5% at high luminosity. The effect on the signal of the Tracker and Muon System misalignment in the first months of LHC run has also been evaluated. The number of selected dimuon (dielectron) pairs is lowered by about 30% (10%) while the total signal selection efficiency is decreased by about 20%. The measurement of the distribution end-point is affected by about 1 GeV/c^2. The effect of the electron energy scale uncertainty on the dilepton measurement gives a systematic uncertainty of about 0.15 GeV/c^2.

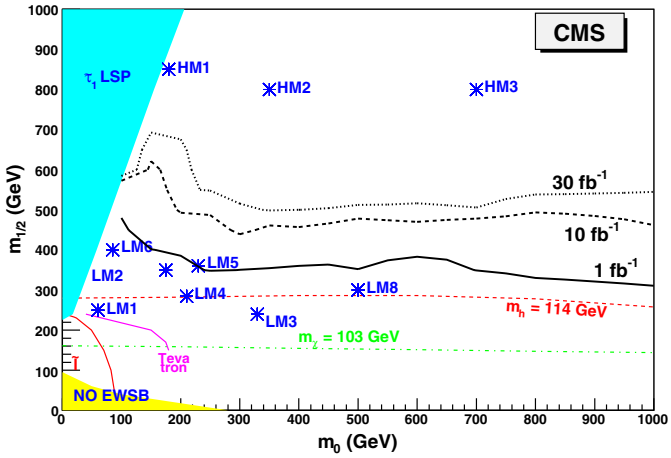

Figure 13.10. 5σ discovery reach for the dilepton final state, assuming $\tan\beta = 10$, $A = 0$, $\mu > 0$ and 1, 10, 30 fb^{-1} integrated luminosity (statistical uncertainties only).

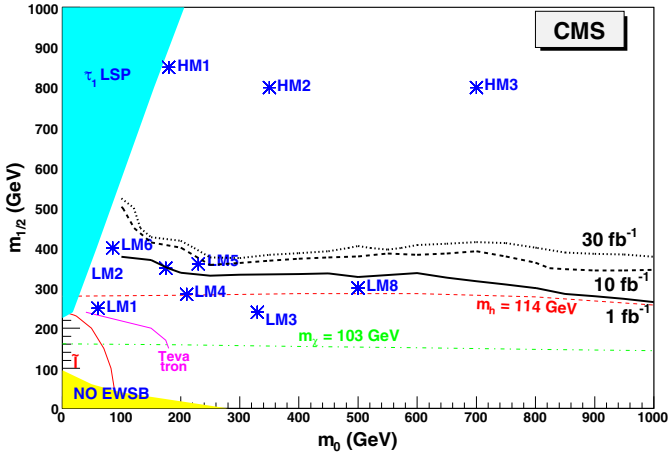

Figure 13.11. 5σ discovery reach for $\tan\beta = 10$ taking into account background systematic uncertainties.

Taking into account the systematic uncertainties on the Standard Model backgrounds expected after the first 1 fb^{-1} of data, the 5 sigma discovery can be achieved with 17 pb^{-1} of integrated luminosity.

13.8.3. CMS inclusive reach

Using the discussed selection path a scan was performed over the mSUGRA parameters in the $(m_0, m_{1/2})$ plane for $\tan\beta = 10$, $A = 0$, $\mu > 0$ to determine the 5 σ discovery reach. The observability of the signal over the Standard Model background uses the dilepton estimates before flavour subtraction. The results of the survey are shown for integrated luminosities of 1, 10 and 30 fb^{-1} in Figs. 13.10 and 13.11. It is notable that most of the low mass test-points can be discovered with about 1 fb^{-1}.

13.9. Inclusive analyses with ditaus

In this section, $\tilde{\tau}$ production through the $\tilde{\chi}_2^0$ decays in $\tilde{q}$ or $\tilde{g}$ cascades is investigated. The $\tilde{\tau}$ is produced through $\tilde{\chi}_2^0 \to \tau^{\pm}\tilde{\tau}^{\mp}$, which further decays to $\tau\tilde{\chi}_1^0$ leaving a final state with two taus of opposite sign. The branching fraction of $\tilde{\tau}$ production through $\tilde{\chi}_2^0$ varying with mSUGRA parameters, the analysis is first carried out at large $\tan\beta$, at the LM2 test point, which parameters are given in Section 13.3.2, where the $\tilde{\chi}_2^0$ is predicted to decay 95% of the time into $\tau^{\pm}\tilde{\tau}^{\mp}$. Results are then generalised to any choice of mSUGRA parameters.

This section studies the opportunity of discovering such a model in the first years of data taking of LHC, with integrated luminosities as low as $0.1\,\text{fb}^{-1}$ and up to $10\,\text{fb}^{-1}$. The possibility of measuring the SUSY mass spectra associated to this cascade decay (in particular $\tilde{\chi}_2^0$, $\tilde{\chi}_1^0$ and $\tilde{\tau}$ masses) is investigated in Section 13.13.

13.9.1. Event selection and background studies

For this analysis, 93.5k events (corresponding to an integrated luminosity of $12.6\,\text{fb}^{-1}$) were generated at the LM2 test point using ISASUGRA. Those events were further passed through the full simulation of the CMS detector [8] then digitised and reconstructed [10]. The same procedure was applied to the Monte Carlo samples used as SM background in this analysis. However, in some cases, where large statistics were required, the fast simulation program [11] was used. All Monte Carlo samples used in this analysis are produced with leading order Parton Distribution Functions.

Physics processes responsible for W and Z production and $t\bar{t}$ which final states may contain several taus and jets are considered as potential background sources. In addition, because of its huge cross section ($1.3 \cdot 10^{-4}$ mb) QCD jet production is also considered. The latter can also represent an important source of fake taus as well as fake missing transverse energy ($E_{\text{T}}^{\text{miss}}$) due to imprecision in jet energy measurement.

13.9.1.1. Event selection using all reconstructed taus. In this analysis [678], only events passing the JETMET level1 and HLT triggers are accepted. The event selection is then carried out using only the $E_{\text{T}}^{\text{miss}}$, the reconstructed taus and jets. In order to increase the sensitivity of the selection both tau's decaying hadronically and leptonically are considered in this section.

The mSUGRA events are selected with the following requirement:

- $E_{\text{T}}^{\text{miss}}$ larger than 150 GeV.
  This cut removes a large fraction of Standard Model physics background.
- At least two tau candidates are required.
- At least two jets with $E_{\text{T}} > 150\,\text{GeV}$.
  This requirement is very aggressive on the LM2 events, however it allows to remove most of the Standard Model background.
- ΔR between any pair of tau's should be smaller than two.

This cut makes use of the fact that in $\tilde{\chi}_2^0$ decays, taus belonging to a same cascade decay will be produced relatively close to each other while in Standard Model physics processes taus as well as Supersymmetric physics processes such as chargino production (producing one tau in each cascade) tend to be produced in opposite direction. This cut also reduces the amount of wrong pairing.

Both theoretical and experimental systematic uncertainties are considered in this analysis. The theoretical systematic uncertainty is estimated for the signal according to standard CMS guidelines and involves changing the PDF [351] and varying generator parameters governing

both hard process and fragmentation. Each variation leads to the generation of a new LM2 sample which is then simulated and reconstructed using FAMOS and analysed in the same way as the main signal samples. Variations in the number of selected events are then taken as systematic uncertainty. The relative theoretical systematic uncertainty on the signal was found to be 12%. The experimental systematic uncertainties are coming from the Jet energy scale, the $E_{\mathrm{T}}^{\mathrm{miss}}$ and the tau-jet energy scale. These uncertainties are estimated following standard CMS procedure, see appendix B, by varying the jet and tau energies by an amount corresponding to their respective energy scales and redoing the analysis. The uncertainty on $E_{\mathrm{T}}^{\mathrm{miss}}$ is estimated in a similar way by varying the energy of the jets used to estimate $E_{\mathrm{T}}^{\mathrm{miss}}$ within their energy scale. The experimental systematic uncertainty affect the selection of signal events by 11% for low integrated luminosities (smaller than $1\,\mathrm{fb}^{-1}$) but for large integrated luminosities the systematic effect is less than 3.2%. The experimental systematic uncertainty on the background is 30% for integrated luminosities smaller than $1\,\mathrm{fb}^{-1}$ and 11% for larger integrated luminosities.

At $12.67\,\mathrm{fb}^{-1}$, $N_s = 2735 \pm 273(\mathrm{sys}) \pm 52(\mathrm{stat})$ events from the signal and $N_{bkg} = 938 \pm 103(\mathrm{sys}) \pm 114(\mathrm{stat})$ events from the background survive the selection. 50% of the remaining background is coming from QCD, 39% from $t\bar{t}$ and 11% from W+jets.

To this selection corresponds a ratio signal over background $S/B = 2.9$. The global efficiency of the selection of the signal is around 3% (of which 88% are SUSY events with at least two taus), while only 0.001% of the background remains after selection. Using S_{cL} significance, defined in Appendix A.1, it is possible to estimate that a 5σ discovery can be achieved with only $0.07\,\mathrm{fb}^{-1}$. Using S_{cP} significance [679], which takes into account systematic uncertainties on the background, a 5σ discovery can be expected with a luminosity of $0.125\,\mathrm{fb}^{-1}$.

13.9.1.2. Event selection using only reconstructed taus decaying hadronically. If only taus decaying hadronically are used in the selection described in 13.9.1.1, both signal and backgrounds are affected differently.

At $12.67\,\mathrm{fb}^{-1}$, $N_s = 1447 \pm 144(\mathrm{sys}) \pm 38(\mathrm{stat})$ events from the signal and $N_{bkg} = 543 \pm 60(\mathrm{sys}) \pm 112(\mathrm{stat})$ events from the background survive the selection. 70% of the remaining background is coming from QCD, 20% from $t\bar{t}$ and 10% from W + jets. To this selection corresponds a ratio signal over background $S/B = 2.6$. The global efficiency of the selection of the signal is around 1.5% (of which 88% are SUSY events with at least two taus), while only 0.0006% of the background remains after selection. This time, using S_{cL} a 5σ discovery is achieved with only $0.14\,\mathrm{fb}^{-1}$. Using S_{cP} significance [679], which takes into account systematic uncertainties on the background, a 5σ discovery can be expected with a luminosity of $0.26\,\mathrm{fb}^{-1}$.

13.9.2. Discovery potential of mSUGRA with ditaus final states

A scan of the mSUGRA $(m_0, m_{1/2})$ parameters plane is performed in order to delimit the mSUGRA parameter region where SUSY could be discovered with this analysis. Because the analysis focuses on ditau final states and since the respective branching ratio to ditaus and to other leptons from SUSY may vary by large amounts in the mSUGRA parameter space, allowing large contamination from leptons into ditaus final states the scan is performed using only hadronic tau decays as described in section 13.9.1.2.

This scan is achieved by generating many mSUGRA samples varying m_0 and $m_{1/2}$ values so that the entire region of the plane $(m_0, m_{1/2})$ below $m_0 < 1500\,\mathrm{GeV}$ and $m_{1/2} < 800\,\mathrm{GeV}$ is covered. The samples were generated with ISASUGRA 7.69 then simulated and reconstructed

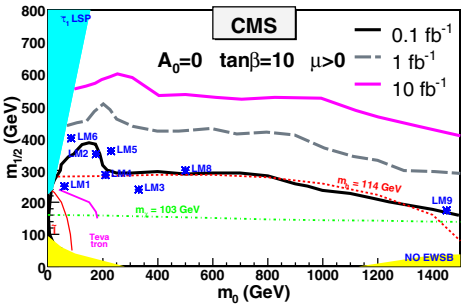

Figure 13.12. Inclusive ditau analysis discovery potential for mSUGRA between 0.1 and 30 fb^{-1} for $\tan\beta = 10$ including only statistical uncertainties.

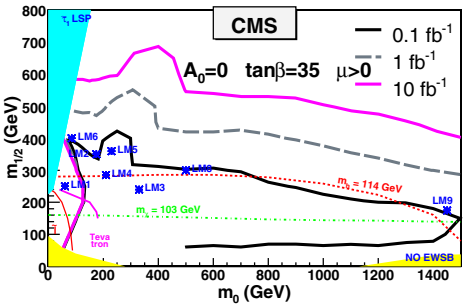

Figure 13.13. Inclusive ditau analysis discovery potential for mSUGRA between 0.1 and 30 fb^{-1} for $\tan\beta = 35$ including only statistical uncertainties.

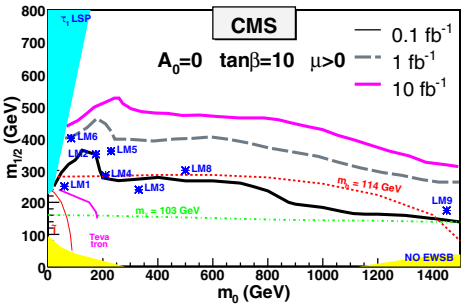

Figure 13.14. Inclusive ditau analysis discovery potential for mSUGRA between 0.1 and 30 fb^{-1} for $\tan\beta = 10$ where both statistical and systematic uncertainties are taken into account.

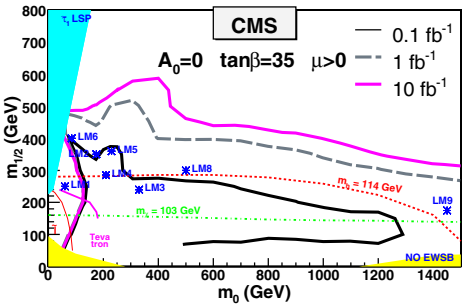

Figure 13.15. Inclusive ditau analysis discovery potential for mSUGRA between 0.1 and 30 fb^{-1} for $\tan\beta = 35$ where both statistical and systematic uncertainties are taken into account.

with FAMOS and analysed in the same way as the LM2 sample. The resulting number of events surviving the selection were used to estimate the significance at each point of the mSUGRA parameter plane. Two types of significance are estimated here, S_{cL} which accounts only for statistical uncertainties and S_{cp} which accounts for both statistical and systematics effects on the background. The resulting 5σ contours over the mSUGRA $(m_0, m_{1/2})$ parameter plane obtained with S_{cl} for several integrated luminosities between 0.1 and 30 fb^{-1} are shown in Figs. 13.12 and 13.13 for $\tan\beta = 10$ and $\tan\beta = 35$, respectively. Results obtained with S_{cp} are shown in Figs. 13.14 and 13.15. The region where a 5σ discovery is possible is somewhat shrunk, especially for the very early measurement at 0.1 fb^{-1} as a precise knowledge of the jet energy scale and of the measurement of the $E_{\text{T}}^{\text{miss}}$ will still be limited. However, a large region is accessible with larger integrated luminosities.

13.10. Inclusive analyses with Higgs

This section describes the potential of the CMS experiment to discover a light supersymmetric Higgs boson (h^0) produced at the end of a cascade of supersymmetric particles starting with the strong production of squarks ($\tilde{q}$) and gluinos ($\tilde{g}$). Because of the cascade production mechanism, the events can be efficiently triggered using inclusive SUSY triggers such as jet $+E_{\text{T}}^{\text{miss}}$, and the dominant $h^0 \to b\bar{b}$ decay mode of the Higgs boson can be exploited.

This analysis focuses on a full CMS detector simulation [8] and event reconstruction [10] at the mSUGRA point LM5, defined in Section 13.3.2. The total SUSY cross section at this parameter point is about 7.75 pb at NLO.

All SUSY channels leading to a light Higgs boson in the final state have been taken into account. The signal events are characterised by at least two b-tagged jets, an important missing transverse energy ($E_{\mathrm{T}}^{\mathrm{miss}}$) and multiple hard jets. This signature allows to suppress the majority of the $b\bar{b}$ background due to SM processes (mainly top pair production $t\bar{t}$, $W^{\pm}$+jets, Z^0+jets).

13.10.1. Signal selection and backgrounds

This analysis has been developed based on the CMS reconstruction. The two main algorithms used for the signal reconstruction are the jet reconstruction algorithm (the Iterative cone algorithm with a cone size of 0.5 radians and the GammaJet calibration) and the b-tagging algorithm (Combined b-tagging algorithm, see the PTDR Volume 1, Section 12.2).

A first rejection of the Standard Model backgrounds happens at the online trigger stage. The Level-1 and the High Level Trigger (HLT) efficiencies for the signal and background have been evaluated. The trigger path used for this analysis consists of the Level-1 and HLT Jet + $E_{\mathrm{T}}^{\mathrm{miss}}$ stream. This particular trigger is already an important tool in rejecting Standard Model backgrounds, for example it rejects 96% of the $t\bar{t}$ background while keeping 79% of the signal events.

In order to further remove the SM background events and reduce the SUSY background, a number of offline selection cuts are applied: a minimal number of four jets with a transverse energy above 30 GeV is required, of which at least two are b-tagged with high quality (i.e. a b-tag discriminator greater than 1.5).

The mean b-tagging efficiency is found to be 50% with a mistagging rate of about 1.6%, for u, d, s quarks and gluons, and 12% for c quarks. The mean b jet energy originating from the Higgs decay is approximately 70 GeV, corresponding to a b-tagging efficiency of about 50% at this energy. This means that approximately 25% of the signal events will pass the double b-tag criterion.

Other variables have been identified in order to improve the signal over background ratio, in particular for the most problematic $t\bar{t}$ background: the $E_{\mathrm{T}}^{\mathrm{miss}}$, the first, second and third highest jet P_t. The selection requires a $E_{\mathrm{T}}^{\mathrm{miss}} > 200$ GeV, the highest jet p_t in the event > 200 GeV/c, the second highest jet p_t in event > 150 GeV/c, the third highest jet p_t in event > 50 GeV/c.

Next, in order to select the b-jet pair coming from the Higgs decay, two methods are used. First, the Hemisphere separation technique (see section 13.4) is applied to identify two groups of jets in the detector, each group associated with an initial squark and/or gluino cascade. After that, the b-jet pairing is done only in each of these groups separately, reducing the number of possible combinations by a large factor. In addition, as the Higgs is relatively heavy, its decay products have an important boost leading to a small angle $\Delta R = \sqrt{\Delta\eta^2 + \Delta\phi^2}$ between the two b jets. Therefore, in case of multiple possible combinations inside one hemisphere, the pair with the smallest ΔR value within $\Delta R < 1.5$ is chosen. This procedure gives an efficiency of around 40% and strongly suppresses the combinatorial background.

The full selection chain leads to a signal efficiency of about 8% for all SUSY channels yielding a Higgs. The global rejection factor for $t\bar{t}$ events, including the rejection made by the Jet + $E_{\mathrm{T}}^{\mathrm{miss}}$ trigger, is close to $4.6 \cdot 10^4$. No Z + jets, W + jets nor QCD events from the full simulation samples pass the previously described series of cuts, hence the only remaining background is from $t\bar{t}$. The resulting SUSY signal over SM background ratio is >70. 61%

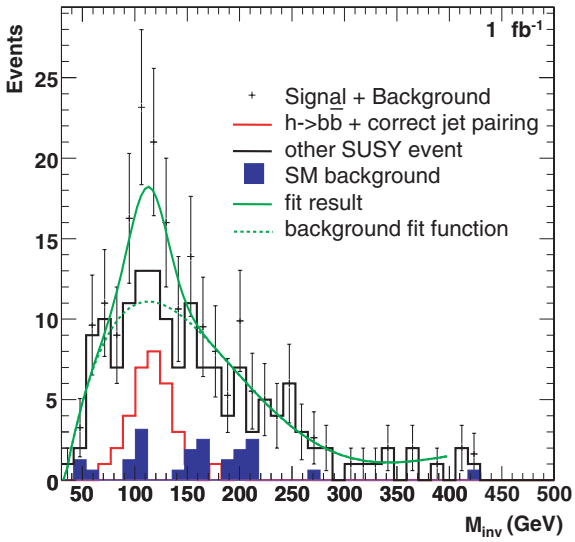

Figure 13.16. Invariant mass distribution of $b\bar{b}$ jets for the search of Higgs final states with 1 fb^{-1}.

of the SUSY signal comes from events with a true h^0, but only part of those have the correct b-jet pairing with both jets from the h^0.

13.10.2. Results at LM5 and systematics

The resulting invariant mass distribution, after the selection cuts described above, is shown in Fig. 13.16. The plot corresponds to the expected statistics equivalent to 1 fb^{-1} of integrated luminosity. A peak around 116 GeV/c^2 is visible. The main background is due to the remaining SUSY background events and some $t\bar{t}$ events.

A fit was performed representing the background by a fifth order polynomial and approximating the Higgs signal by a Gaussian. The r.m.s of the Gaussian has been fixed to 18 GeV, which is the Higgs mass resolution estimated using the Monte Carlo truth. In real data, this number will be determined from studying b-rich samples such as $t\bar{t}$. The results of the fit for the equivalent of 1 fb^{-1} of data are the following: the Higgs mass is found to be (112.9 ± 6.6) GeV/c^2 (for a generated mass of 116 GeV/c^2) and the fraction of signal in the distribution is evaluated to be 0.28 ± 0.08. The significance S_{CL}, directly extracted from the fraction of signal in the histogram, is found to be 4.5. A significance of 5 should be achieved with approximately 1.5 fb^{-1} luminosity.

For 1 fb^{-1}, the jet energy scale and $E_{\mathrm{T}}^{\mathrm{miss}}$ uncertainties have been estimated assuming a linear evolution from $\pm 15\%$ to $\pm 5\%$ for low energy jets (below 50 GeV) and then fixed at $\pm 5\%$ for higher energy jets. As the $E_{\mathrm{T}}^{\mathrm{miss}}$ is computed from the jets, a correction on the jet energy is automatically propagated to its estimation. The effects are about 15% on the SUSY event selection and 17% on the $t\bar{t}$ event rejection respectively. The impact on the Higgs mass measurement have been estimated to be ± 7.5 GeV/c^2; on the signal fraction, the effect is ± 0.04.

Another systematic uncertainty is introduced by the misalignment of the tracker. Both the short and long term misalignment scenarios have been investigated. The short term misalignment corresponds to a displacement of the tracker (strips/pixels) = (100 μm/10 μm), while the long term misalignment takes the following shift of the tracker (strips/pixels) = (20μ m/10 μm) into account. The misalignment of the tracker reduces the

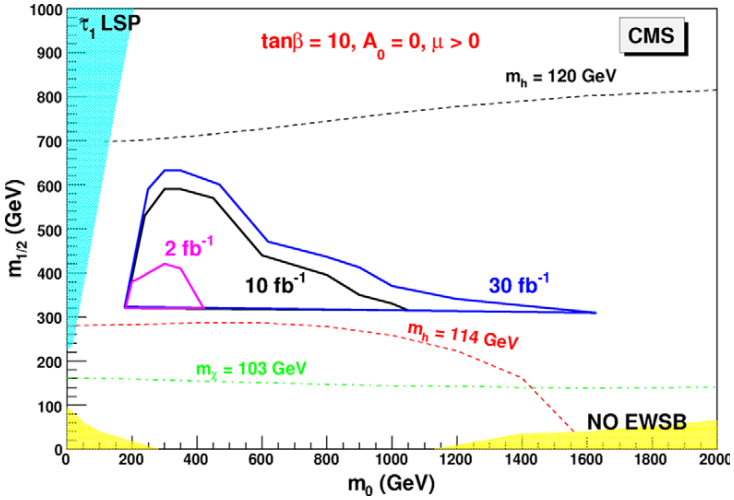

Figure 13.17. Higgs discovery reach in SUSY cascades for 2, 10 and 30 fb^{-1}.

track reconstruction resolution, which results in a reduced b-tagging efficiency and which in its turn causes a reduced signal event selection efficiency. The long term misalignment scenario results in a drop of the signal selection efficiency of (∼10%) compared to the case of an aligned detector; for the short term misalignment case, the reduction is (∼17%). No effect on the position/width of the Higgs mass peak was observed.

Finally, the systematics due to the choice of the background fit function has been estimated to be small (by changing the background function to a third, fourth, sixth or a seventh order polynomial): ±0.3 GeV/c^2 on the Higgs mass and ±0.01 on the signal fraction.

The final result including all the previously discussed systematics for 1 fb^{-1} of integrated luminosity is then 112.9 ± 6.6 (stat) ±7.5 (syst) GeV/c^2 for the Higgs mass and 0.28 ± 0.08 (stat) ± 0.04 (syst) for the signal fraction.

13.10.3. CMS reach for inclusive Higgs production

After establishing the visibility of the signal for the LM5 point, a scan was performed in the $(m_0, m_{1/2})$ plane in order to determine the region where a 5σ discovery could be made with 2, 10 and 30 fb^{-1}.

First, an effective cross section ($\sigma \times BR(h0)$) was used (calculated with PROSPINO and ISASUGRA) to obtain an estimate of the reach. Using this first estimate, 40 points were chosen for which the full spectrum was calculated and a fast simulation was performed with FAMOS [11]. The same selection criteria as for LM5 point were applied, and the number of Higgs signal and background events was determined. Given that the background is dominated by SUSY events, the signal and background are similarly affected by the systematic uncertainties and the effect on the significance is small. The same significance definition (S_{CL}) was used in order to determine the 5-sigma contours. Comparing the ORCA/FAMOS results at LM5, the significances obtained with both programs were found to agree well.

The result of the scan is displayed in the reach plot in Fig. 13.17. Although for 1 fb^{-1} the sensitivity remains below 5σ, everywhere a sizeable region of the $(m_0, m_{1/2})$ plane, up to 1100 (1600) GeV in m_0 and 600 (650) GeV in $m_{1/2}$, can be covered with 10 (30) fb^{-1}. With 2 fb^{-1} of integrated luminosity, a small region of the plane can already be probed. The plot assumes $\tan\beta = 10$, $A_0 = 0$, and a positive sign of μ.

Table 13.11. Number of events for signal ($\tilde{\chi}_2^0 \to Z^0 + \tilde{\chi}_1^0,\ Z^0 \to e^+e^-, \mu^+\mu^-$) and background before and after selection criteria for 10 fb^{-1}. The numbers below Zj specify the range of partonic p_T in GeV/c.

	LM4 with $\tilde{\chi}_2^0$	LM4 no $\tilde{\chi}_2^0$	ZZj	ZWj	WWj	$t\bar{t}$	Zj 85–250
σ NLO (pb)	0.664	17.4	15.5	51.5	270	830	116.7
10 fb^{-1}							
total events	6640	173.8 K	155 K	515 K	2.7 M	8.3 M	1.17 M
L1+HLT	6032	81.7 K	12.6 K	24.4 K	174 K	973 K	462 K
OS leptons	4489	7147	9124	14.7 K	26.3 K	268 K	331 K
M_{ll}	3773	804	6999	11.5 K	2406	23.1 K	249 K
E_T^{miss}	1420	306	32	24	70	149	44
$\Delta\phi_{ll}$	1289	264	31	22	47	61	35

13.11. Inclusive SUSY search with Z^0

13.11.1. Topology of the signal

SUSY processes leading to final states with Z^0 can be detected in CMS using the Z^0 decays into same flavour opposite sign (SFOS) lepton pairs. The detection of SUSY in the mSUGRA framework through the decay $\tilde{\chi}_2^0 \to Z^0 + \tilde{\chi}_1^0$ is the scope of this study. The mSUGRA test-point LM4 with the parameters described in Section 13.3 is chosen. The $\tilde{\chi}_2^0$ is produced mainly through the cascade decays of gluinos ($M_{\tilde{g}} = 695$ GeV) and squarks (mainly the $\tilde{b}_1$ with $M_{\tilde{b}_1} = 601$ GeV). The decays of the second neutralino to Z^0 have a large branching ratio ($\sim$100%). The signal events are characterised by large missing E_T (due to the undetectable LSP) and the SFOS lepton pair from Z^0. The analysis details can be found in [680].

The main Standard Model backgrounds originate from the production of one or more Z^0 bosons in association with jets as well as $t\bar{t}$. In addition SUSY events contain dileptons that do not originate from the above neutralino decay chain and large missing transverse energy. These events are considered as signal for SUSY detection but as background for the $\tilde{\chi}_2^0$ detection. The following backgrounds were considered in this study: dibosons ($ZZ + j$, $ZW + j$, $WW + j$), inclusive top ($t\bar{t}$) and Z+ jets. The signal events were generated interfacing ISAJET 7.69 with PYTHIA. Unless otherwise stated all events are fully simulated and analysed using the CMS full detector simulation [8] and reconstruction [10] packages. The next to leading order (NLO) cross sections of the relevant processes are shown in Table 13.11.

13.11.2. Event selection

The following requirements are imposed in order to efficiently select the signal and reject the background events. All criteria were chosen so that the final SUSY search significance estimator S_{c1} [102, 681] for 10 fb^{-1} integrated luminosity is maximised. Very similar requirements maximise also significance estimator S_{L2} [102] used in the case of 1 fb^{-1} integrated luminosity. The effect of the selection requirements on the signal and on each background sample separately can be seen in Table 13.11 for 10 fb^{-1} integrated luminosity.

- Events are required to pass the HLT dielectron or dimuon triggers.
- An e^+e^- or $\mu^+\mu^-$ pair with lepton $p_T > 17$ GeV for electrons and $p_T > 7$ GeV for muons (as per L1 trigger requirements). Each lepton is required to be within $|\eta| < 2.4$.
- The SFOS lepton pair invariant mass is required to be consistent with the Z^0 mass, i.e. 81 GeV $< M_{ll} <$ 96.5 GeV. The reconstructed masses for the e^+e^- and the $\mu^+\mu^-$ pairs and

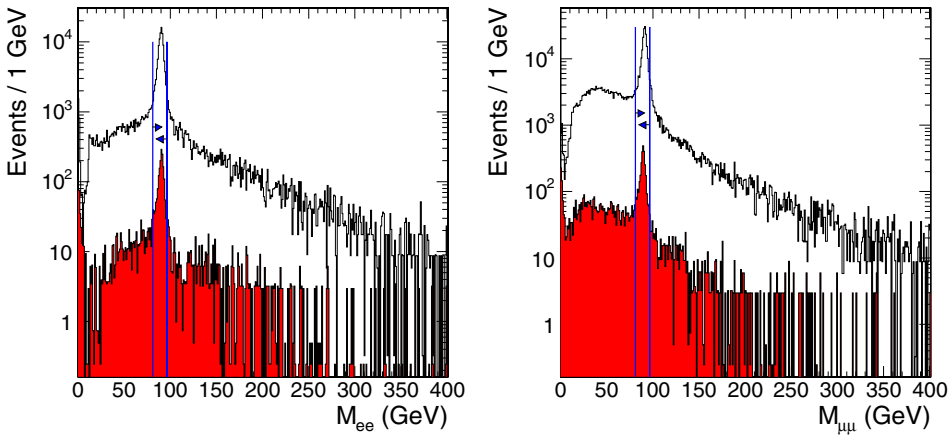

Figure 13.18. Reconstructed masses for (left) e^+e^- and (right) $\mu^+\mu^-$ pairs for the background and for the signal (shaded) events. SUSY events not involving $\tilde{\chi}_2^0$ are considered signal. The vertical lines denote the imposed mass requirement.

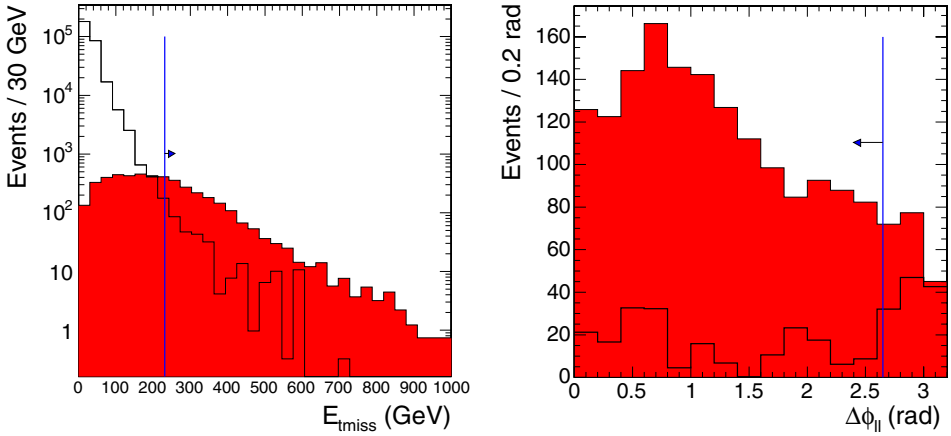

Figure 13.19. $E_{\mathrm{T}}^{\mathrm{miss}}$ (left) and $\Delta\phi$ between the two leptons (right) for background (black line) and signal (shaded) events. SUSY events not involving $\tilde{\chi}_2^0$ are considered signal. The vertical lines denote the $E_{\mathrm{T}}^{\mathrm{miss}}$ and $\Delta\phi$ requirements.

the mass requirements are shown in Figs. 13.18 (left) and (right) respectively. This cut reduces backgrounds not involving a Z^0 ($t\bar{t}$, WW+j) and the sample of SUSY events not involving $\tilde{\chi}_2^0$.

- The missing transverse energy $E_{\mathrm{T}}^{\mathrm{miss}}$ is required to be greater 230 GeV. This requirement reduces all backgrounds as seen in Fig. 13.19 (left). It allows, however, for enough signal and background events in order to maintain good statistics both for 1 fb^{-1} and for 10 fb^{-1} integrated luminosity.
- The angle $\Delta\phi$ between the two leptons of the lepton pair that reconstructs the mass of Z^0 is required to be less than 2.65 rad. The $\Delta\phi$ distribution is shown in Fig. 13.19 (right) for signal and background. This requirement targets the remainder of the $t\bar{t}$ and the WW + j backgrounds that survived the $E_{\mathrm{T}}^{\mathrm{miss}}$ requirement.

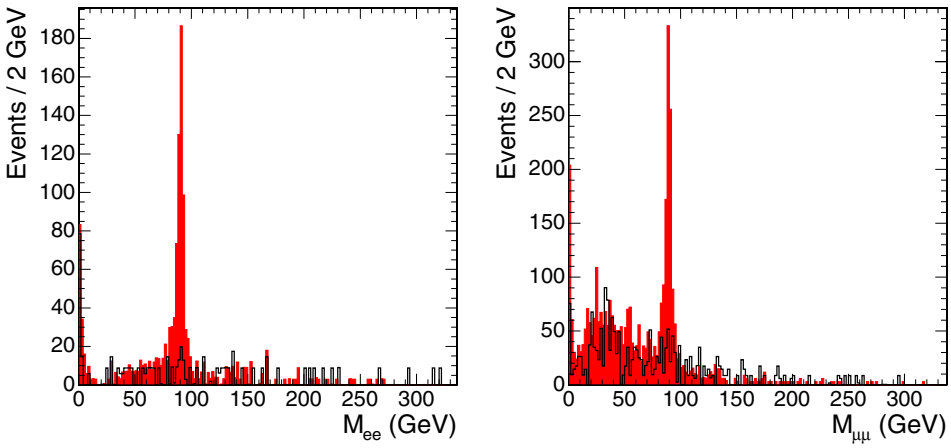

Figure 13.20. Reconstructed masses for (left) e^+e^- and (right) $\mu^+\mu^-$ pairs for the background and for the signal (shaded) events after the cut on $E_{\mathrm{T}}^{\mathrm{miss}}$. SUSY events not involving $\tilde{\chi}_2^0$ are considered signal.

13.11.3. Results and systematic uncertainties

The reconstructed masses for the e^+e^- and the $\mu^+\mu^-$ pairs without the Z^0 mass cut but after the cut on $E_{\mathrm{T}}^{\mathrm{miss}}$ are shown in Fig. 13.20 (left) and (right) respectively. A clear Z^0 peak from the signal is observed.

After the application of the above criteria and for 10 fb^{-1} integrated luminosity we have 1553 SUSY events and 196.5 Standard Model background events in the Z^0 window. This gives a signal over background ratio of 8 and inside the signal events 83% originate from a $\tilde{\chi}_2^0$ decay. The total efficiency for Z^0 events from a $\tilde{\chi}_2^0$ decay is 19.4%. The background is composed of 31% $t\bar{t}$, 24% WW, 18% Zj, 16% ZZ and 11% ZW.

The significance based on statistical uncertainties only has been evaluated by means of S_{cL}, defined in Appendix A.1. A significance of 5σ would be reached after 0.06 fb^{-1} if systematic effects were negligible.

When LHC will start running many uncertainties will be controlled from data. In this analysis relevant uncertainties are the lepton P_t resolution and the $E_{\mathrm{T}}^{\mathrm{miss}}$ uncertainty. The lepton P_t resolution ($\sim$3%) introduces an uncertainty of 2.7% in the number of background events. The dominant systematic, however, is the $E_{\mathrm{T}}^{\mathrm{miss}}$ energy scale uncertainty which is estimated to $\sim$5% and which introduces a 20% uncertainty in the number of background events, nearly independent of the background channel. The significance was recomputed after including the systematic uncertainties using S_{c12s} (see Appendix A.1), which increases the required integrated luminosity for a 5σ discovery to $\sim$0.1 fb^{-1}.

13.11.4. CMS reach for inclusive Z^0 search

A scan was performed over the mSUGRA $m_0, m_{1/2}$ parameter space in order to determine the range over which the above analysis can reveal new physics. The test points were taken at high density in the area where the Z^0 has high production cross section (especially due to the decay $\tilde{\chi}_2^0 \to Z^0 + \tilde{\chi}_1^0$). This is an almost horizontal band in the $m_0 - m_{1/2}$ plane between $m_{1/2} \sim 240\,\mathrm{GeV/c^2}$ and $m_{1/2} \sim 340\,\mathrm{GeV/c^2}$. Points were also taken at higher and lower $m_{1/2}$ values, because there is an excess of lepton pairs created due to SUSY processes. These may have invariant mass close to the Z^0 mass and pass analysis cuts assisting in the detection

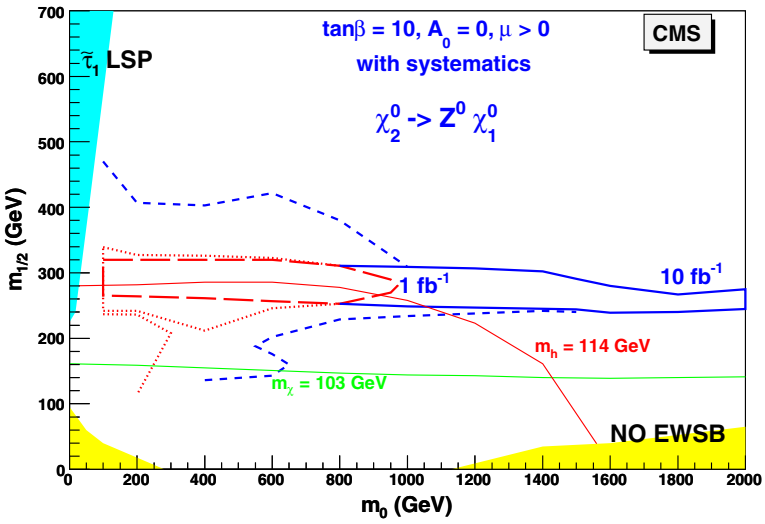

Figure 13.21. The 5σ significance contours of final states with Z^0 for 1 fb^{-1} (dashed line) and 10 fb^{-1} (full line) integrated luminosities, taking into account systematic uncertainties, in the region where the $\tilde{\chi}_2^0 \to Z^0\tilde{\chi}_1^0$ decay takes place. Also indicated as dotted and short dashed lines are the extensions at higher and lower $m_{1/2}$ where the Z^0 is off-shell.

of SUSY. For each point 2000 events were produced with an OS lepton pair close to the Z^0 mass. The events were generated interfacing ISAJET 7.69 with PYTHIA 6.227 and they were simulated, reconstructed and analysed using the FAMOS fast simulation package [11]. Systematic uncertainties were taken into account. The 5σ significance contour is shown for integrated luminosities of 1 fb^{-1} and 10 fb^{-1} in Fig. 13.21.

13.12. Inclusive analyses with top

The supersymmetric partner of the top quark in most of the supersymmetric scenarios is the lightest squark. Finding evidence of its existence can be a clear signature for supersymmetry. In the main part of the allowed m_0–$m_{1/2}$ plane, the stop can decay to a top plus a neutralino. This neutralino can be either the LSP ($\tilde{\chi}_1^0$) or a heavier neutralino which decays in turn to a LSP which appears as missing transverse energy ($E_{\mathrm{T}}^{\mathrm{miss}}$). Hence in the final state there is at least a top quark plus large $E_{\mathrm{T}}^{\mathrm{miss}}$.

The search for top was tuned on test point LM1, where the stop decays according to

$$\tilde{t}_1 \to t\tilde{\chi}_2^0 \to tl\tilde{l}_R \to tll\tilde{\chi}_1^0 \tag{13.20}$$

giving rise to a final state which also contains two leptons. Although this analysis consists primarily in a search for an excess of top quarks from any SUSY origin with respect to its SM production, it was also optimised for the selection of events where the top results from the production of $\tilde{t}$.

13.12.1. Top quark and lepton reconstruction and identification

Electrons and muons are requested to have $p_{\mathrm{T}} \geqslant 5\,\mathrm{GeV/c}$ and $\eta \leqslant 2.5$.

Electrons are separated from jets by requiring that the ratio of energy deposited in the HCAL to the ECAL $\leqslant 0.1$, the absolute difference in η between the electromagnetic cluster

in the ECAL and the associated track $\Delta\eta \leqslant 0.006$ and the energy weighted spread of the electron shower in η be $\sigma_{\eta\eta} \leqslant 0.015$.

Leptons were required to be isolated, namely that the ratio of p_{T} of the lepton to the p_{T} sum of other particles inside a cone of size $\Delta R = 0.1$ around the lepton track be greater than 2. Jets were reconstructed from ECAL and HCAL towers using an Iterative cone algorithm with cone size $\Delta R = 0.5$ and were selected if their uncalibrated transverse energy $E_{\mathrm{T}} \geqslant 30\,\mathrm{GeV}$ in the acceptance of $\eta \leqslant 2.5$. Their energy was calibrated using corrections from photon-jet balancing studies presented in Vol. 1 Section 11.6.3.

In this analysis only hadronic decays of the top quark were considered. A kinematic fit with constraints is utilised to find the best combination of jets to make the top quark. Since the purpose of this analysis is not to measure the top quark mass, its known value was used to constrain the invariant mass of the system of three jets. Among these three jets, one and only one must be tagged as a b-jet and the other two were constrained to be consistent with a hadronically decaying W. The fit then consisted in minimising the χ^2 as a function of the three jet energies and imposing the top and W mass constraints. The solution was obtained by an iterative method based on Lagrange multipliers. As several combinations may lead to a convergent fit for a given event, only the combination with the best χ^2 was kept, with the additional requirement that its χ^2 probability was greater than 0.1.

13.12.2. Signal selection and backgrounds

All events were fully simulated [8], digitised with low luminosity pileup and reconstructed [10].

The signal events consisted of an inclusive SUSY sample at the test point LM1 (see Section 13.3.2), where the total cross section at NLO is about 52 pb. Top quarks are found in the decay of $\tilde{t}$, but other important sources exist, e.g. $\tilde{b} \to t\tilde{\chi}_1^{\pm}$. At an integrated luminosity of $1\,\mathrm{fb}^{-1}$, the total SUSY production amounts to 52000 events, out of which 8375 contain a top quark.

The main backgrounds, generated with PYTHIA 6.225 [69], consist of $t\bar{t}$, $WW + jets$, $WZ + jets$ and QCD. In addition, single top generated with TOPREX 4.11 [44] and $W + jets$ generated with ALPGEN V2.0 [161] were considered.

The selection of SUSY events containing a top quark was based on the following criteria:

- L1T: every event must pass the first level of the Trigger (L1T) cuts corresponding to "Jet/Met" (a jet with $E_{\mathrm{T}} > 88$ and $E_{\mathrm{T}}^{\mathrm{miss}} > 46$ GeV/c).
- HLT: events were required to pass High level Trigger (HLT) cuts (a jet with $E_{\mathrm{T}} > 180$ and $E_{\mathrm{T}}^{\mathrm{miss}} > 123\,\mathrm{GeV}$).
- $\geqslant 4$ jets with $E_{\mathrm{T}}^{raw} \geqslant 30\,\mathrm{GeV}$ and $\eta \leqslant 2.5$.
- $\geqslant 1$ b-jet with $E_{\mathrm{T}}^{raw} \geqslant 30\,\mathrm{GeV}$ and $\eta \leqslant 2.5$.
- $E_{\mathrm{T}}^{\mathrm{miss}} \geqslant 150\,\mathrm{GeV}$ to suppress $t\bar{t}$ and other SM backgrounds.
- a convergent fit with $P(\chi^2) \geqslant 0.1$.
- $\Delta\Phi$ between the fitted top and $E_{\mathrm{T}}^{\mathrm{miss}} \leqslant 2.6$ rad to suppress semi-leptonic $t\bar{t}$ events.
- $\geqslant 1$ isolated lepton (e or μ) with $p_{\mathrm{T}} \geqslant 5\,\mathrm{GeV}$ and $\eta \leqslant 2.5$ to suppress QCD background.

These criteria were simultaneously optimised to reject SM backgrounds and to maximise the ratio of events with a top quark at generator level, called SUSY(with top), to events without top at generator level, called SUSY(no top).

The effect of the cuts is shown in Table 13.12. As a result of the selection, the signal events remaining for a $1\,\mathrm{fb}^{-1}$ luminosity consist of 38 events SUSY(with top) and 17 events

Table 13.12. Effect of different cuts on different samples. In every row, the number of the remaining events after that cut is shown. "No.of.used.events" shows the number of events used in this analysis, "NEve(Nor.xsec)1 fb^{-1}" is the same number after normalising to the cross section times 1 fb^{-1} and "wT/noT" means $\frac{SUSY(withTop)}{SUSY(noTop)}$.

cut	SUSY (withTop)	SUSY (noTop)	ttInc	WW	ZW	Single t	wT/noT
x-sec(pb) NLO	52	830	269.91	51.5	250	-	
No.of.used.events	494261	1674500	305000	70000	100000	-	
NEve(Nor.xsec)1 fb^{-1}	8375	43625	830000	269910	51500	250000	0.19
L1T (Jet/Met)	6269	33582	75806	18498	598	10875	0.19
HLT (Jet/Met)	5070	29427	14430	4733	142	1750	0.17
MET $\geqslant$ 150 GeV	4183	25677	4930	2312	99	653	0.16
$n_{bj} \geqslant 1$	3457	14388	3718	792	32	355	0.24
$n_j^{b\ or\ light} \geqslant 4$	1789	4576	769	25	0	33	0.39
A convergent Fit	1335	3062	557	12	0	28	0.44
χ^2 probability >0.1	105	69	56	0	0	5	1.52
$\Delta\phi$ <2.6	79	52	12	0	0	5	1.51
$n_l > 0$	38	17	5	0	0	0	2.19

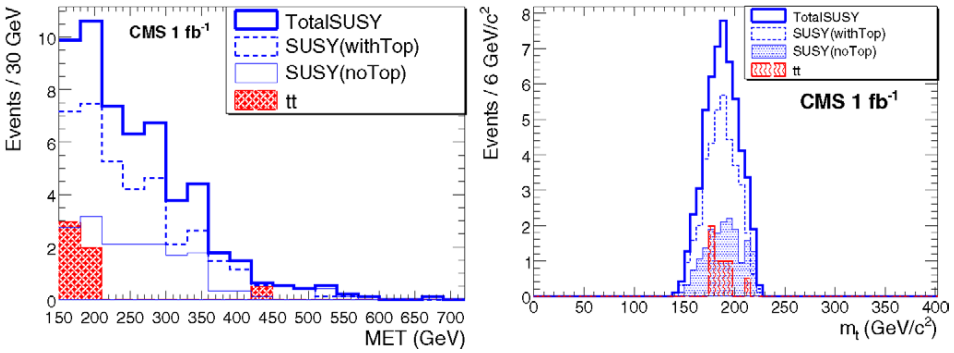

Figure 13.22. (left) Distributions of $E_{\mathrm{T}}^{\mathrm{miss}}$ and (right) fitted top mass after all selection criteria are applied.

SUSY(no top). The remaining backgrounds are 5 events from $t\bar{t}$. The resulting distributions of $E_{\mathrm{T}}^{\mathrm{miss}}$ and of the fitted top mass are displayed in Fig. 13.22.

13.12.3. Results at point LM1

The significance of a discovery was computed from statistical uncertainties only using the formula of S_{c12}, defined in Appendix A.1, where the number of signal events, S, is the sum of SUSY(with top) and SUSY(no top) and B represents the sum of all SM backgrounds. Using this formula, the integrated luminosity required to make a discovery at point LM1 with a significance of 5 amounts to $\sim$210 pb^{-1}.

Many systematic uncertainties (cross section, showering, ISR/FSR, ...) will be rendered very small by using real data. The main uncertainties remaining will be the absolute jet energy scale (estimated to 5% for jets and MET in 1 fb^{-1}), which leads to 5.1% from jets and 18.3% from MET in the $t\bar{t}$ sample and the b-tagging efficiency estimated to 8% for 1 fb^{-1}. Adding them in quadrature yields a total systematic uncertainty of 21%, considered common to all backgrounds. It is seen that this remains negligible compared to the statistical uncertainty.

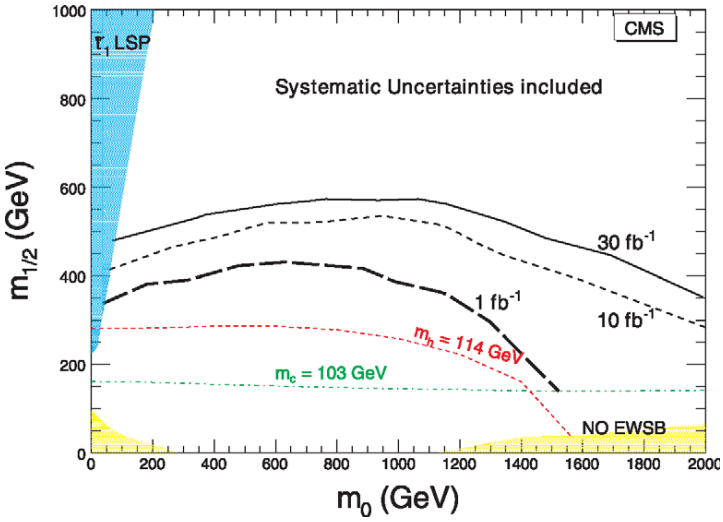

Figure 13.23. The 5σ reach in $m_0, m_{1/2}$ plane with 1, 10 and 30 fb^{-1} obtained for final states with a top quark.

13.12.4. CMS reach for inclusive top search

The CMS fast simulation, FAMOS, was used to find the reach of CMS in this channel in $m_0, m_{1/2}$ plane. In total 36 points have been tried. The ntuples were generated by using the CMS-official ISAPYTHIA. The NLO cross sections were derived by PROSPINO [682].

Figure 13.23 shows the 5σ reach in $m_0, m_{1/2}$ plane with 1, 10 and 30 fb^{-1}.

13.13. Mass determination in final states with ditaus

In this section the determination of the sparticle masses using invariant mass distributions in the ditau final state is investigated. The selection of the events is the same as presented in Section 13.9.

13.13.1. Extraction of mSUGRA mass spectra from the measurement of the end points of invariant mass distributions

Using the kinematics of the successive two body decays in $\tilde{q} \to q\tilde{\chi}_2^0 \to q\tau\tilde{\tau} \to q\tau\tau\tilde{\chi}_1^0$, it is possible to express the mass of the sparticles involved in that cascade as a fully resolved system of equations which depends only on the end-point of the invariant mass distributions obtained by combining the leptons and quark-jets observed in the final state.

However, the tau-lepton always decays, producing at least one undetected neutrino. Therefore, instead of observing a triangle-shaped distribution like for the dilepton invariant mass distribution of chapter 13.8, where the end-point coincides with the maximum of the distribution, the absence of the neutrino smears the resulting mass distribution to lower values. Even though the end-point of the distribution remains unchanged, it now lies at the tail of a gaussian-like distribution.

The $\tilde{\chi}_2^0$ cascade always produces a pair of opposite charge τ's, therefore signal samples are obtained by combining opposite charge tau pairs to the two most energetic jets of the event. In 75% of the cases the quark produced by the decay of the $\tilde{q}$ to $\tilde{\chi}_2^0$ is among these

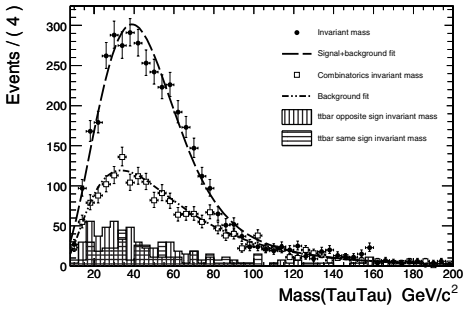

Figure 13.24. Ditau invariant mass distribution.

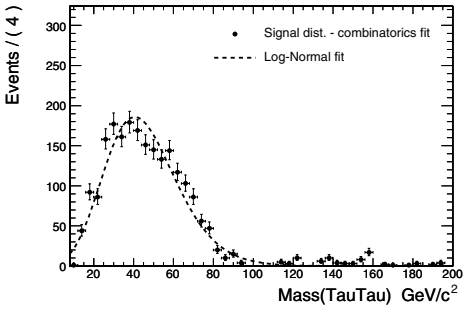

Figure 13.25. Difference between ditau invariant mass distribution and combinatorics fit together with log-normal fit.

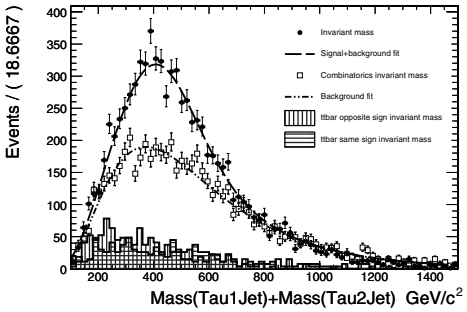

Figure 13.26. τ_1Jet + τ_2Jet invariant mass distribution.

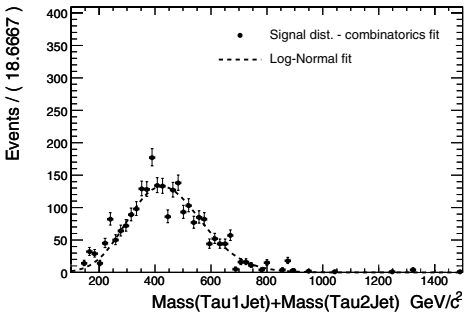

Figure 13.27. Difference between τ_1Jet + τ_2Jet invariant mass distribution and combinatorics fit together with log-normal fit.

two jets, due to the fact that the $\tilde{q}$ is much heavier than the $\tilde{\chi}_2^0$. This large number of tau's and jets is responsible for a high combinatorial background. A good description of this combinatorial background, in particular of its tail, is essential for extracting the true end-points. The combinatorial background in the opposite sign invariant ditau mass is estimated by taking same sign tau pairs. The combinatorial background from the jets is estimated by combining all tau pairs to a jet taken among the 2 most energetic jets of a previous event selected randomly to insure that the jet and tau's are uncorrelated.

Five invariant mass and their associated combinatorial background distributions are then obtained: $M(\tau\tau)$, $M(\tau\tau\text{Jet})$, $M(\tau_1 Jet)$, $M(\tau_2 Jet)$ and $M(\tau_1\text{Jet}) + M(\tau_2\text{Jet})$. ($\tau_1$ is defined as the one which maximises the invariant mass formed by its association with a jet, $M(\tau_1 Jet) > M(\tau_2 Jet)$).

The distributions of combinatorial background are first fitted. Then, the resulting fit parameters are used together with a Log-normal distribution, which gives a good description of the tail of the true distributions, to fit the distributions of the signal. Since it is possible to express the log-normal distribution as a function of the end-point, the end-point can be extracted directly from the fit.

The ditau invariant mass and $M(\tau_1\text{Jet}) + M(\tau_2\text{Jet})$ are fitted first (Figs 13.24–13.27). The three other invariant mass distributions are built using only candidates found to have values for the two previous distributions below the measured end-points. Then, they are fitted using the same procedure. The sparticle masses are evaluated by solving the system of four equations giving the end-points as a function of the sparticle mass [683].

Table 13.13. End-point obtained with the lognormal fit together with sparticle masses measured with the end-point technique for LM2 for integrated luminosities around 40 fb^{-1}.

End-points (GeV)	case 1 (GeV)	case 2 (GeV)
$m(\tau_1\tau_2)^{\max} = 95 \pm 3$	$M(\tilde{\chi}_1^0) = 213 \pm 14$	$M(\tilde{\chi}_1^0) = 147 \pm 23$
$m(\tau_1 Q)^{\max} = 559 \pm 11$	$M(\tilde{\chi}_2^0) = 337 \pm 17$	$M(\tilde{\chi}_2^0) = 265 \pm 10$
$m(\tau_2 Q)^{\max} = 298 \pm 7$	$M(\tilde{\tau}) = 310 \pm 17$	$M(\tilde{\tau}) = 165 \pm 10$
$m(\tau_1\tau_2 Q)^{\max} = 596 \pm 12$	$M(\tilde{q}) = 839 \pm 19$	$M(\tilde{q}) = 763 \pm 33$
$E_5^{meas} = 780 \pm 20$	$E_5^{calc} = 815 \pm 26$	$E_5^{calc} = 765 \pm 30$

Table 13.14. sparticle masses measured with end-point method for LM2 together with theoretical value.

	LM2 benchmark point	
	measured	theory
$M(\tilde{\chi}_1^0)$ (GeV)	$147 \pm 23(\text{stat}) \pm 19(\text{sys})$	138.2
$M(\tilde{\chi}_2^0)$ (GeV)	$265 \pm 10(\text{stat}) \pm 25(\text{sys})$	265.5
$M(\tilde{\tau})$ (GeV)	$165 \pm 10(\text{stat}) \pm 20(\text{sys})$	153.9
$M(\tilde{q})$ (GeV)	$763 \pm 33(\text{stat}) \pm 58(\text{sys})$	753–783 (light $\tilde{q}$)

When several solutions are possible for the SUSY mass spectrum (as it is the case here, where two valid solutions exist), the choice is made by comparing the measured $M(\tau_1\text{Jet}) + M(\tau_2\text{Jet})$ end-point value, E_5, to the one computed from the sparticle masses found by solving the systems of equations.

The most probable mass hypothesis is then chosen as the one for which E_5 computed for each mass spectrum is the closest to the measured one. The measured end-point was found to be 780±20 GeV while the calculations for the mass hierarchy in case 1 and case 2 yield to 815±26 GeV and 765±30 GeV respectively (Table 13.14). The second hypothesis, which corresponds to the correct LM2 mass hierarchy, gives a result compatible with the measured end-point value.

Three main systematic uncertainties are considered, the jet energy scale and tau-jet energy scale as well as systematics uncertainties arising from the extraction procedure.

Results obtained are shown in Table 13.14 for 40 fb^{-1}, together with LM2 generated sparticle masses. They are found to be in good agreement with the theoretical values. Using a 40 fb^{-1} LM2 sample, it is possible to measure the SUSY mass spectra and in particular $\tilde{\tau}$ mass with a precision of 30 GeV.

13.14. Direct $\chi_2^0\chi_1^\pm$ production in tri-leptons

The exclusive tri-lepton final state appears in $pp \to \tilde{\chi}_2^0\tilde{\chi}_1^\pm$ channel with subsequent three body decays of the second neutralino, $\tilde{\chi}_2^0 \to \tilde{\chi}_1^0 ll$, and chargino, $\tilde{\chi}_1^\pm \to \tilde{\chi}_1^0 W^* \to \tilde{\chi}_1^0 l\nu$; or via sleptons in two body decay, $\tilde{\chi}_2^0 \to l\tilde{l} \to l\tilde{\chi}_1^0 l$, and $\tilde{\chi}_1^\pm \to l\tilde{\nu} \to l\tilde{\chi}_1^0\nu$, $\tilde{\chi}_1^\pm \to \nu\tilde{l} \to \nu\tilde{\chi}_1^0 l$. The final signatures are two Opposite-Sign Same-Flavour (SFOS) leptons (e, μ) from the neutralino $\tilde{\chi}_2^0$ decay plus any lepton from the chargino $\tilde{\chi}_1^\pm$. Jets are expected to be only due to gluon state radiation or pile up events. In spite of the escaping $\tilde{\chi}_1^0$, the $E_{\text{T}}^{\text{miss}}$ is relatively small at low $m_{1/2}$ and is comparable with the one of SM backgrounds, especially for three body decays at large m_0. The invariant mass of the SFOS dileptons exhibits a particular shape with a kinematic end point M_{ll}^{max} that depends upon the event topology, see section 13.3.

13.14.1. Datasets

The tri-lepton cross section σ_{3l} was calculated with ISAJET (7.69) and PYTHIA (6.225 CTEQ5L) at LO, the K_{NLO} factor calculated with PROSPINO is in the range of 1.30–1.25 (for $m_{\tilde{\chi}_2^0} = 150-300\,\mathrm{GeV/c^2}$) [684]. The σ_{3l} drops rapidly with the neutralino mass $m_{\tilde{\chi}_2^0} \sim 0.8 m_{1/2}$, $\sigma_{3l} \sim m_{1/2}^{-4}$. This study is restricted to the low $m_{1/2}$ region, where σ_{3l} contributes, for instance, $\sim 0.5\%$ to the total SUSY cross section at $m_0 > 1000\,\mathrm{GeV/c^2}$. The three body decays are dominant in this m_0, $m_{1/2}$ region, except for $m_0 < 150\,\mathrm{GeV/c^2}$ and $\tan\beta \leqslant 20$. The kinematic end point in the invariant mass is approximately $M_{ll}^{max} \sim 0.42^* m_{1/2} - 18.4$ $\mathrm{GeV/c^2}$ (at $m_0 \sim 1000\,\mathrm{GeV/c^2}$), thus moving into the Z-peak region at $m_{1/2} > 250\,\mathrm{GeV/c^2}$ where the SM background is high. Among the CMS benchmark points in this region, LM9 ($m_{1/2} = 175$, $m_0 = 1450$, $\tan\beta = 50$, $A_0 = 0$) has the largest cross section, ~ 3700 events are produced for $30\,\mathrm{fb}^{-1}$, and it was used as a reference.

13.14.2. Backgrounds and trigger path

The main background results from the Drell–Yan, Z + jets, $t\bar{t} \to WbWb$, ZW, ZZ, Wt+jets, WW+jets, W+jets and inclusive SUSY channels. For all backgrounds, except ZW and ZZ, some leptons originate from jets, mostly $b \to l + j$. The background events were produced with PYTHIA (ALPGEN and TOPREX are also used) and their cross section corrected to NLO. The Z and W bosons are forced to decay leptonically to e, μ, $\tau \to e$, μ. The DY and Z+jets cross section is large ($\sigma_{DY,Zj} \sim 10\,\mathrm{nb}$) and events were preselected by requiring three leptons with $p_T > 5\,\mathrm{GeV/c}$ and $|\eta| < 2.4$ at the generator level. The full data samples of $30\,\mathrm{fb}^{-1}$ for the LM9 test point and backgrounds are simulated with the CMS fast simulations (FAMOS) validated with smaller statistics samples produced with the full GEANT based simulation (OSCAR, ORCA). Low luminosity pile-up was included.

All events were required to pass Level-1 and HLT triggers. The main trigger paths for LM9 are the dimuons (74%) and dielectrons (25%). The trigger efficiency is 86% at Level-1 and 91% at HLT for LM9 and is increasing for larger $m_{1/2}$ where the leptons become harder. In the off-line selection, at least three isolated leptons in $|\eta| < 2.4$ and $P_T^{\mu,e} > 10\,\mathrm{GeV/c}$ are required for each event. The leptons are reconstructed using standard reconstruction algorithms. Electrons and muons are required to be isolated, *i.e.* other tracks may only contribute up to $\sum P_T$ of $1.5\,\mathrm{GeV/c}$ inside a cone of $\Delta R < 0.3$. Moreover, for muons the energy deposit in calorimeters should be $E_T < 5\,\mathrm{GeV}$ in a cone of $\Delta R < 0.3$. In addition, electron candidates are required to satisfy quality criteria based on a likelihood function, > 0.65. The muons and electrons reconstruction efficiencies in ORCA are found to be 78% ($P_T^{\mu} > 5\,\mathrm{GeV/c}$) and 66% ($P_T^{e} > 10\,\mathrm{GeV/c}$) respectively. The jets are reconstructed using an iterative cone algorithm with the seed energies $E_T^{seed} > 0.5\,\mathrm{GeV}$ in a cone $\Delta R < 0.5$.The E_T^{miss} was reconstructed from the calorimeter towers. Since the E_T^{miss} for the signal events is relatively small and its reconstruction at low energy scale is limited by the E_T resolution, a E_T^{miss} requirement is not as efficient as in other SUSY channels.

13.14.3. Analysis path

The reconstructed events are selected in two steps. First, sequential cuts are applied: 1) No central jets with corrected energy $E_T > 30\,\mathrm{GeV}$ in $|\eta| < 2.4$, 2) Two SFOS isolated leptons (e, μ) in $|\eta| < 2.4$ with $P_T^{\mu} > 10\,\mathrm{GeV/c}$, $P_T^{e} > 17\,\mathrm{GeV/c}$ and the dilepton invariant mass below the Z peak $M_{ll} < 75\,\mathrm{GeV/c^2}$. 3) The third lepton is with $P_T^{\mu,e} > 10\,\mathrm{GeV/c}$ in $|\eta| < 2.4$. The evolution of statistics and the efficiencies of the selection cuts are presented in Table 13.15.

Table 13.15. Evolution of signal and background statistics with the cuts as expected for 30 fb^{-1}. The last column gives the results of a neural network selection applied after the sequential cuts.

channel	N_{ev} 30 fb^{-1} ($\sigma \times BR$ [pb])	L1+HLT	No Jets	2 SFOS+l SFOS $M_{ll} < 75$ GeV/c^2	NN_{LM9}
LM1	2640 (0.088)	1544 (58%)	864 (56%)	70 (8%)	17 (24%)
LM7	1540 (0.051)	1250 (82%)	738 (59%)	91 (12%)	57 (62%)
LM9	3700 (0.125)	2896 (78%)	1740 (60%)	239 (14%)	158 (68%)
SUSY	$4{\cdot}10^5$ ($13.1\ ^{NLO}$)	$2.5{\cdot}10^5$ (63%)	$1.8{\cdot}10^4$ (7%)	34 (0.2%)	22 (65%)
ZW	$5{\cdot}10^4$ ($1.68\ ^{NLO}$)	$3.6{\cdot}10^4$ (73%)	$1.9{\cdot}10^4$ (53%)	173 (1%)	44 (25%)
ZZ	$4.8{\cdot}10^3$ ($0.16\ ^{NLO}$)	$3.5{\cdot}10^3$ (73%)	$1.7{\cdot}10^3$ (48%)	38 (2.3%)	15 (39%)
$t\bar{t}$	$2.6{\cdot}10^6$ ($88\ ^{NLO}$)	$1.8{\cdot}10^6$ (70%)	$1.3{\cdot}10^5$ (7%)	239 (0.2%)	89 (37%)
Z+jets(3l)	$4.6{\cdot}10^5$ ($15.4\ ^{LO}$)	$3.7{\cdot}10^5$ (80.5%)	$9.8{\cdot}10^4$ (26.5%)	504 (0.5%)	129 (26%)
DY(3l)	$4.5 \cdot 10^5$ ($15.1\ ^{LO}$)	$3.2{\cdot}10^5$ (71%)	$1.4{\cdot}10^5$ (44%)	670 (0.5%)	131 (20%)
$Zb\bar{b}$(3l)	$8.4{\cdot}10^4$ ($2.8\ ^{LO}$)	$7.3{\cdot}10^4$ (87%)	$1.5{\cdot}10^4$ (20%)	69 (0.6%)	18 (26%)
Wt+jets	$3{\cdot}10^5$ ($10\ ^{NLO}$)	$2.1{\cdot}10^5$ (70%)	$3.9{\cdot}10^4$ (18.5%)	52 (0.1%)	20 (38%)
WW+jets	$6{\cdot}10^5$ ($19.8\ ^{LO}$)	$3.8{\cdot}10^5$ (63%)	$1.9{\cdot}10^4$ (50%)	7 (0.04%)	2 (29%)
Tot. bkg	$\sim 4.9{\cdot}10^6$			1786	470 (26%)

In a second step the background suppression is improved with a Neural Network (NN). Five networks for DY, Z+jets, $t\bar{t}$, ZW and ZZ backgrounds are trained on the LM9 signal sample using the following variables: $P_T^{1,2,3}$, $\sum P_T$, M_{ll}, P_T^{2l} (transverse momentum of two SFOS leptons), $A = \frac{P_T^1 - P_T^2}{P_T^1 + P_T^2}$, Θ_{ll} (angle between two SFOS leptons), Φ_{ll} (angle in transverse plane), E_T^{miss}, N_{jets} (number of jets passing the jets veto), E_t^{hj} (of the highest E_T jet), η_{hj} (rapidity of the highest jet). The selection cuts on the NN outputs were optimised for the maximum significance at LM9 with the genetic algorithm GARCON [63]. The efficiency of the NN selection is also shown in Table 13.15.

13.14.4. Results at LM9 and systematics

After the selection based on cuts the S_{cp} significance calculated for all SFOS pair combination is 6.1 at point LM9 for an integrated luminosity of 30 fb^{-1}. The NN improves the S_{cp} for all SFOS combinations to 7.8.

In addition to the real tri-lepton final state, leptons can be produced in the detector volume from $\pi^{\pm}$, $K^{\pm}$ decays, bremsstrahlung, punch-through or faked by jets. The rate per event of such fake leptons was estimated individually for each background by matching the reconstructed lepton with the generated one and is $\sim 10^{-4}$ for electrons and $\sim 10^{-5}$ for muons. The expected fake leptons substantially increase the background, especially for the preselected channels like DY or Z + jets, by $\sim 221 \pm 48$ events and $\sim 31 \pm 16$ events respectively for the tri-muon final state where the fake rate is smaller. The S_{cP} significance defined in Appendix A.1 including fakes but without other systematic uncertainties for all SFOS combinations and for the tri-muon state at LM9 is 6.5 and 5.1 respectively.

The reconstruction uncertainties related to the jet energy scale (5%) and the lepton momentum resolution (2%) contribute 1% to the uncertainties on the background. The average theoretical uncertainty from the PDFs, calculated with the LHPDF subsets using the re-weighting technique for each background channel, amounts to 1.7%. These uncertainties reduce the significances to 5.8 and 4.8 for the all SFOS pairs and for the tri-muon final state, respectively. However the largest uncertainties are coming from the Monte Carlo statistical

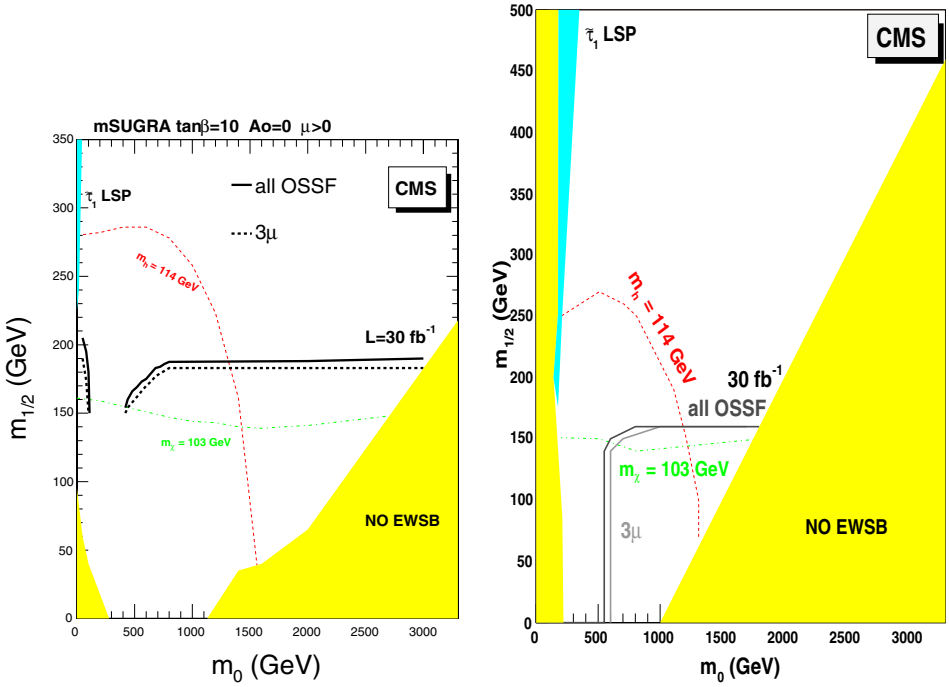

Figure 13.28. Discovery reach of tri-lepton from the $pp \to \tilde{\chi}_2^0 \tilde{\chi}_1^\pm$ production at $\mathcal{L}_{int}$=30 fb^{-1} for all SFOS lepton combinations (dashed) and for the tri-muon final state (solid) including systematic uncertainties from reconstruction, for (left) tan $\beta = 10$ and (right) tan $\beta = 50$.

errors in the fake rate estimation which contribute $\sim$7% to the background uncertainties rendering the signal hardly observable, $S_c p \sim 3.3$. These fake rate uncertainties can be reduced with larger simulation samples.

In summary, for the tri-lepton mSUGRA study presented here, the final signal to background ratio is 0.23, the total signal efficiency is 4.4% and the background composition is 28% Drell–Yan, 27% Z + jets, 19% $t\bar{t}$, 9% WZ, and 17% ZZ, WW, SUSY, W+ jets and QCD. The total considered theoretical and reconstruction systematic uncertainties on the Standard Model background is 2.2%. The Monte Carlo statistics systematic errors in the fake rates increases this to 7.5%.

13.14.5. CMS reach for the tri-lepton final state

Figure 13.28 shows the 5σ discovery reach in m_0 and $m_{1/2}$ plane at $L_{int} = 30\,\text{fb}^{-1}$ for all SFOS combinations and for the tri-muon final state including the systematic uncertainties due to the reconstruction. The signal can be observed at large $m_0 > 1000\,\text{GeV/c}^2$ in a narrow band below $m_{1/2} < 180\,\text{GeV/c}^2$. At low $m_0 < 100\,\text{GeV/c}^2$ the two body decays are visible although a better optimisation is possible in this region, see Sections 13.8 and 13.15. The tri-lepton final state from direct neutralino-chargino production is complementary to the inclusive SFOS dilepton search and provides an additional verification for the leptonic decays of the neutralino at low $m_{1/2}$.

13.15. Production of $\tilde{l}\tilde{l}$

The aim of this section is the study of the possibility of detecting sleptons. Note the previous related papers where the sleptons detection was studied at the level of a toy detector [685–689].

13.15.1. Simulation details

ISASUSY 7.69 [672] was used for the calculation of coupling constants and cross sections in the leading order approximation for SUSY processes. For the calculation of the next-to-leading order corrections to the SUSY cross sections the PROSPINO code [682] was used. Cross sections of the background events were calculated with PYTHIA 6.227 [69] and COMPHEP 4.2pl [355]. For considered backgrounds the NLO corrections are known and they were used. Official datasets (DST) production was used for the study of CMS test point LM1 and backgrounds ($t\bar{t}$, ZZ, WW, Wt, Z $b\bar{b}$, DY2e, DY2τ). For WZ, DY2μ and W + jet backgrounds the events were generated with PYTHIA 6.227. The detector simulation and hits production were made with full CMS simulation [8], digitised and reconstructed [10]. The DY2μ and W + jet backgrounds were simulated with fast simulation [11].

Jets were reconstruction using an iterative cone algorithm with cone size 0.5 and their energy corrected with the GammaJet calibration.

The events are required to pass the Global Level 1 Trigger (L1) and the High Level Trigger (HLT). The events have to pass at least one of the following triggers: single electron, double electron, single muon, double muon.

The CMS fast simulation code was used for the determination of the sleptons discovery plot.

13.15.2. Sleptons production and decays

When sleptons are heavy relative to $\tilde{\chi}_1^{\pm}$, $\tilde{\chi}_2^0$, they are produced significantly at the LHC through the Drell–Yan mechanism (direct sleptons production), via $q\bar{q}$ annihilation with neutral or charged boson exchange in the s-channel, namely, $pp \to \tilde{l}_L\tilde{l}_L, \tilde{l}_R\tilde{l}_R, \tilde{\nu}\tilde{\nu}, \tilde{\nu}\tilde{l}, \tilde{l}_L\tilde{l}_R$. The left sleptons decay to charginos and neutralinos via the following (kinematically accessible) decays:

$$\tilde{l}_L^{\pm} \to l^{\pm} + \tilde{\chi}_{1,2}^0 , \tag{13.21}$$

$$\tilde{l}_L^{\pm} \to \nu_l + \tilde{\chi}_1^{\pm} , \tag{13.22}$$

$$\tilde{\nu} \to \nu_l + \tilde{\chi}_{1,2}^0 , \tag{13.23}$$

$$\tilde{\nu} \to l^{\pm} + \tilde{\chi}_1^{\pm} . \tag{13.24}$$

For right sleptons only decays to neutralino are possible and they decay mainly to LSP:

$$\tilde{l}_R^{\pm} \to l^{\pm} + \tilde{\chi}_1^0 . \tag{13.25}$$

If sleptons are light relative to $\tilde{\chi}_1^{\pm}$, $\tilde{\chi}_2^0$, they can be abundantly produced, besides the Drell–Yan mechanism, also from chargino and neutralino decays $\tilde{\chi}_1^{\pm}$, $\tilde{\chi}_2^0$ (indirect production), equations (13.8), (13.9), (13.13) and (13.14).

13.15.3. Signature and backgrounds

The slepton production and decays described previously lead to the signature with the simplest event topology: *two leptons* $+E_{\mathrm{T}}^{\mathrm{miss}} + jet\ veto$. This signature arises for both direct and indirect slepton pair production. In the case of indirectly produced sleptons not only the event topology with two leptons but with single, three and four leptons is possible. Besides, indirect slepton production from decays of squarks and gluino through charginos, neutralinos can lead to an event topology *two leptons* $+E_{\mathrm{T}}^{\mathrm{miss}} + (n \geqslant 1)\ jets$.

The cut set close to the optimal one is the following:

(a) for leptons:
- p_{T} - cut on leptons ($p_{\mathrm{T}}^{lept} > 20\,\mathrm{GeV/c}$, $|\eta| < 2.4$) and lepton isolation within $\Delta R < 0.3$ cone containing calorimeter cells and tracker;
- effective mass of two opposite-sign and the same-flavour leptons is outside ($M_Z - 15\,\mathrm{GeV}$, $M_Z + 10\,\mathrm{GeV}$) interval;
- $\Phi(l^+l^-) < 140^\circ$ cut on angle between two leptons;

(b) for $E_{\mathrm{T}}^{\mathrm{miss}}$:
- $E_{\mathrm{T}}^{\mathrm{miss}} > 135\,\mathrm{GeV}$ cut on missing E_{T};
- $\Phi(E_{\mathrm{T}}^{\mathrm{miss}}, ll) > 170^\circ$ cut on relative azimuthal angle between dilepton and $E_{\mathrm{T}}^{\mathrm{miss}}$;

(c) for jets:
- jet veto cut: $N_{jet} = 0$ for a $E_{\mathrm{T}}^{jet} > 30\,\mathrm{GeV}$ (corrected jets) threshold in the pseudorapidity interval $|\eta| < 4.5$.

The Standard Model (SM) backgrounds are: $\mathrm{t\bar{t}}$, WW, WZ, ZZ, Wt, $\mathrm{Zb\bar{b}}$, DY, W + jet. The main contributions come from WW and $\mathrm{t\bar{t}}$ backgrounds. There are also internal SUSY backgrounds which arise from $\tilde{q}\tilde{q}$, $\tilde{g}\tilde{g}$ and $\tilde{q}\tilde{g}$ productions and subsequent cascade decays with jets outside the acceptance or below the threshold. Note that when we are interested in new physics discovery we have to compare the calculated number of SM background events N_{SMbg} with new physics signal events $N_{new\ physics} = N_{slept} + N_{SUSYbg}$, so SUSY background events increase the discovery potential of new physics.

13.15.4. Results

For the point LM1 with the used set of cuts for the integral luminosity $\mathcal{L} = 10\,\mathrm{fb}^{-1}$ the number of signal events (direct sleptons plus sleptons from chargino/neutralino decays) is $N_S = 60$, whereas the number of SUSY background events is $N_{SUSYbg} = 4$ and the number of SM background events is $N_{SMbg} = 41$. The total signal efficiency is 1.16×10^{-4} and the background composition is 1.32×10^{-6} of the total ttbar, 1.37×10^{-5} of the total WW, 4×10^{-6} of the total WZ, 4.4×10^{-5} of the total ZZ, 8.1×10^{-6} of the total Wt, 0 of the total Zbb, DY, W + jet.

The SUSY background is rather small compared to the signal, so we can assume $N_S = N_{direct\ sleptons} + N_{chargino/neutralino} + N_{SUSYbg} = 64$. It corresponds to the significances $S_{c12} = 7.7$ and $S_{cL} = 8.3$, defined in Appendix A.1.

Taking into account the systematic uncertainty of 23% related with in exact knowledge of backgrounds leads to the decrease of significance S_{c12} from 7.7 to 4.3.

The ratio of the numbers of background events from two different channels $N(e^+e^- + \mu^+\mu^-)/N(e^\pm\mu^\mp)$=1.37 will be used to keep the backgrounds under control.

The CMS discovery plot for $two\ leptons + E_{\mathrm{T}}^{\mathrm{miss}} + jet\ veto$ signature is presented in Fig. 13.29.

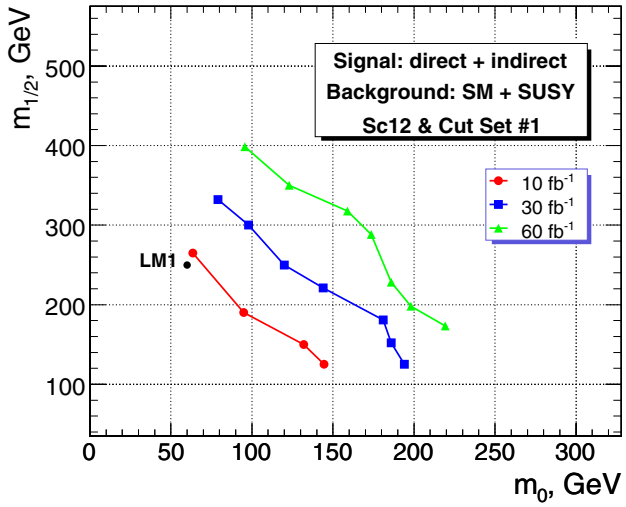

Figure 13.29. Discovery plot ($\tan\beta = 10$, sign(μ) = +, $A = 0$) for final states with l^+l^-, missing transverse energy and a jet veto.

13.16. Lepton flavour violation in neutralino decay

The aim of this section is the study of the possibility to detect SUSY and Lepton Flavour Violation (LFV) using the $e^{\pm}\mu^{\mp} + E_{\mathrm{T}}^{\mathrm{miss}}$ signature.

13.16.1. Signal selection and backgrounds

The simulation details of this study could be found in the Section 13.15.

The SUSY production $pp \to \tilde{q}\tilde{q}', \tilde{g}\tilde{g}, \tilde{q}\tilde{g}$ with subsequent decays leads to the event topology $e^{\pm}\mu^{\mp} + E_{\mathrm{T}}^{\mathrm{miss}}$. In the MSSM with lepton flavour conserving neutralino decays into leptons $\tilde{\chi}^0_{2,3,4} \to l^+l^-\tilde{\chi}^0_1$ do not contribute to this signature and contribute only to $l^+l^- + E_{\mathrm{T}}^{\mathrm{miss}}$ signature (here $l = e$ or μ). The main backgrounds which contribute to the $e^{\pm}\mu^{\mp}$ events are: $\mathrm{t\bar{t}}$, ZZ, WW, WZ, Wt, $\mathrm{Zb\bar{b}}$, DY2τ, Z+jet. It has been found that $\mathrm{t\bar{t}}$ background is the biggest one and it gives more than 50% contribution to the total background.

Our set of cuts is the following:

- p_{T} - cut on leptons ($p_{\mathrm{T}}^{lept} > 20\,\mathrm{GeV/c}$, $|\eta| < 2.4$) and lepton isolation within $\Delta R < 0.3$ cone.
- $E_{\mathrm{T}}^{\mathrm{miss}} > 300\,\mathrm{GeV}$ cut on missing E_{T}.

13.16.2. Results at CMS test points and reach

For integrated luminosity $\mathcal{L} = 10\,\mathrm{fb}^{-1}$ the number of background events is $N_B = 93$. The results for this luminosity are presented in Table 13.16. At point LM1 the signal over background ratio is 3 and the signal efficiency is 6×10^{-4}. The background composition is 9.5×10^{-6} of the total ttbar, 3.4×10^{-6} of the total WW, 4×10^{-6} of the total WZ, 3.2×10^{-6} of the total Wt, 2.2×10^{-6} of the total Z + jet, 0 of the total ZZ, $\mathrm{Zb\bar{b}}$, DY2τ.

The CMS discovery plot for the $e^{\pm}\mu^{\mp} + E_{\mathrm{T}}^{\mathrm{miss}}$ signature is presented in Fig. 13.30.

In the MSSM the off-diagonal components of the slepton mass terms violate lepton flavour conservation. As it was shown in Refs. [690–692] it is possible to look for lepton

Table 13.16. Number of signal events and significances S_{c12} [50] and S_{cL} [100, 102], defined in Appendix A.1, for $\mathcal{L} = 10\,\text{fb}^{-1}$.

Point	N events	S_{c12}	S_{cL}
LM1	329	21.8	24.9
LM2	94	8.1	8.6
LM3	402	25.2	29.2
LM4	301	20.4	23.1
LM5	91	7.8	8.3
LM6	222	16.2	18.0
LM7	14	1.4	1.4
LM8	234	16.9	18.8
LM9	137	11.0	11.9

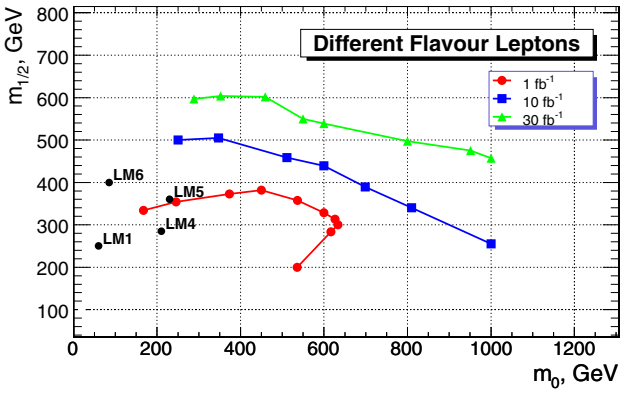

Figure 13.30. Discovery plot ($\tan\beta = 10$, $\text{sign}(\mu) = +$, $A = 0$) for the luminosities $\mathcal{L} = 1$, 10, $30\,\text{fb}^{-1}$ for the $e^{\pm}\mu^{\mp} + E_{\text{T}}^{\text{miss}}$ signature.

flavour violation at supercolliders through the production and decays of the sleptons. For the LFV at the LHC one of the most promising processes is the LFV decay of the second neutralino [693, 694] $\tilde{\chi}_2^0 \to \tilde{l}l \to \tilde{\chi}_1^0\, ll'$, where the non zero off-diagonal component of the slepton mass matrix leads to the different flavours for the leptons in the final state. By using the above mode, LFV in $\tilde{e} - \tilde{\mu}$ mixing has been investigated in Refs. [693, 694] at a parton model level for a toy detector. In this section we study the perspectives of the LFV detection in CMS on the base of full simulation of both signal and background is studied. To be specific, we study the point LM1. We assume that the LFV is due to nonzero mixing of right-handed smuon and selectron. The signal of the LFV $\tilde{\chi}_2^0$ decay is two opposite-sign leptons ($e^+\mu^-$ or $e^-\mu^+$) in the final state with the characteristic edge structure. In the limit of lepton flavour conservation, the process $\tilde{\chi}_2^0 \to \tilde{l}l \to ll\tilde{\chi}_1^0$ has the edge structure for the distribution of the lepton-pair invariant mass m_{ll} and the edge mass m_{ll}^{max} is expressed by the slepton mass $m_{\tilde{l}}$ and the neutralino masses $m_{\tilde{\chi}_{1,2}^0}$ as follows:

$$(m_{ll}^{max})^2 = m_{\tilde{\chi}_2^0}^2 \left(1 - \frac{m_{\tilde{l}}^2}{m_{\tilde{\chi}_2^0}^2}\right)\left(1 - \frac{m_{\tilde{\chi}_1^0}^2}{m_{\tilde{l}}^2}\right). \tag{13.26}$$

The SUSY background for the LFV comes from uncorrelated leptons from different squark or gluino decay chains. The SM background comes mainly from

$$t\bar{t} \to bWbW \to blbl'\nu\nu'. \tag{13.27}$$

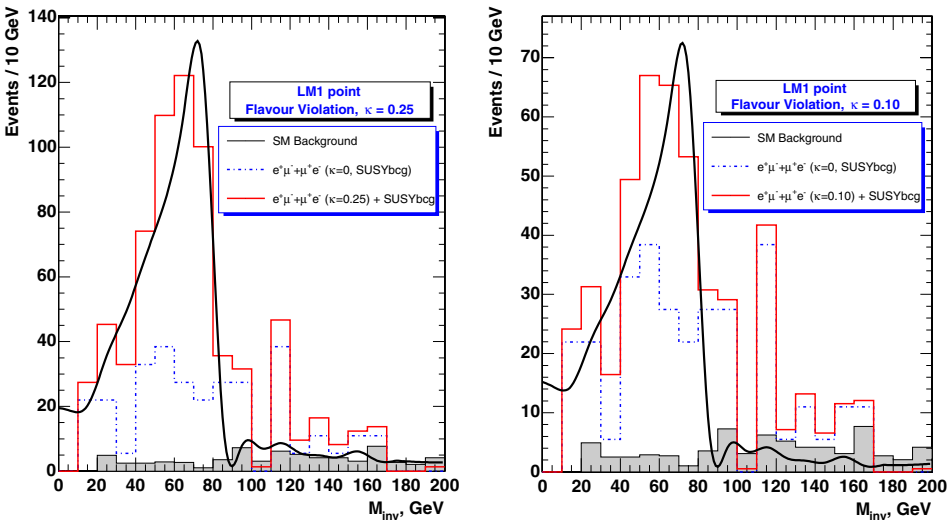

Figure 13.31. The distribution of dilepton invariant mass after selection of two isolated $e^{\pm}\mu^{\mp}$ leptons with $p_{\mathrm{T}}^{lept} > 20\,\mathrm{GeV/c}$ and $E_{\mathrm{T}}^{\mathrm{miss}} > 300\,\mathrm{GeV}$ for flavour violation parameter $k = 0.25$ (left) and $k = 0.1$ (right). The superimposed curves are fits to the invariant mass distribution for the case of 100% LFV.

The Drell–Yan background from $pp \to \tau\tau \to e\mu \ldots$ is negligible. It should be stressed that for the signature with $e^{\pm}\mu^{\mp}$ in the absence of the LFV we do not have the edge structure for the distribution on the invariant mass $m_{inv}(e^{\pm}\mu^{\mp})$. As the result of the LFV the edge structure for $e^{\pm}\mu^{\mp}$ events arises too. Therefore the signature of the LFV is the existence of an edge structure in the $e^{\pm}\mu^{\mp}$ distribution. The rate for a flavour violating decay is

$$Br(\tilde{\chi}_2^0 \to e^{\pm}\mu^{\mp}\tilde{\chi}_1^0) = \kappa\, Br(\tilde{\chi}_2^0 \to e^+e^-\tilde{\chi}_1^0, \mu^+\mu^-\tilde{\chi}_1^0), \tag{13.28}$$

where

$$Br(\tilde{\chi}_2^0 \to e^+e^-\tilde{\chi}_1^0, \mu^+\mu^-\tilde{\chi}_1^0) = Br(\tilde{\chi}_2^0 \to e^+e^-\tilde{\chi}_1^0) + Br(\tilde{\chi}_2^0 \to \mu^+\mu^-\tilde{\chi}_1^0), \tag{13.29}$$

$$\kappa = 2x \sin^2\theta \cos^2\theta, \tag{13.30}$$

$$x = \frac{\Delta m^2_{\tilde{e}\tilde{\mu}}}{\Delta m^2_{\tilde{e}\tilde{\mu}} + \Gamma^2}, \tag{13.31}$$

$$Br(\tilde{\chi}_2^0 \to e^{\pm}\mu^{\mp}) = Br(\tilde{\chi}_2^0 \to e^+\mu^-) + Br(\tilde{\chi}_2^0 \to e^-\mu^+). \tag{13.32}$$

Here θ is the mixing angle between $\tilde{e}_R$ and $\tilde{\mu}_R$ and Γ is the sleptons decay width. The parameter x is the measure of the quantum interference effect. There are some limits on $\tilde{e} - \tilde{\mu}$ mass splitting from lepton flavour violating processes but they are not very strong.

For $\kappa = 0.25$, $\kappa = 0.1$ the distributions of the number of $e^{\pm}\mu^{\mp}$ events on the invariant mass $m_{inv}(e^{\pm}\mu^{\mp})$ (see Figure 13.31) clearly demonstrates the existence of the edge structure [695], i.e. the existence of the lepton flavour violation in neutralino decays. It appears that for the point LM1 the use of an additional cut

$$m_{inv}(e^{\pm}\mu^{\mp}) < 85\,\mathrm{GeV} \tag{13.33}$$

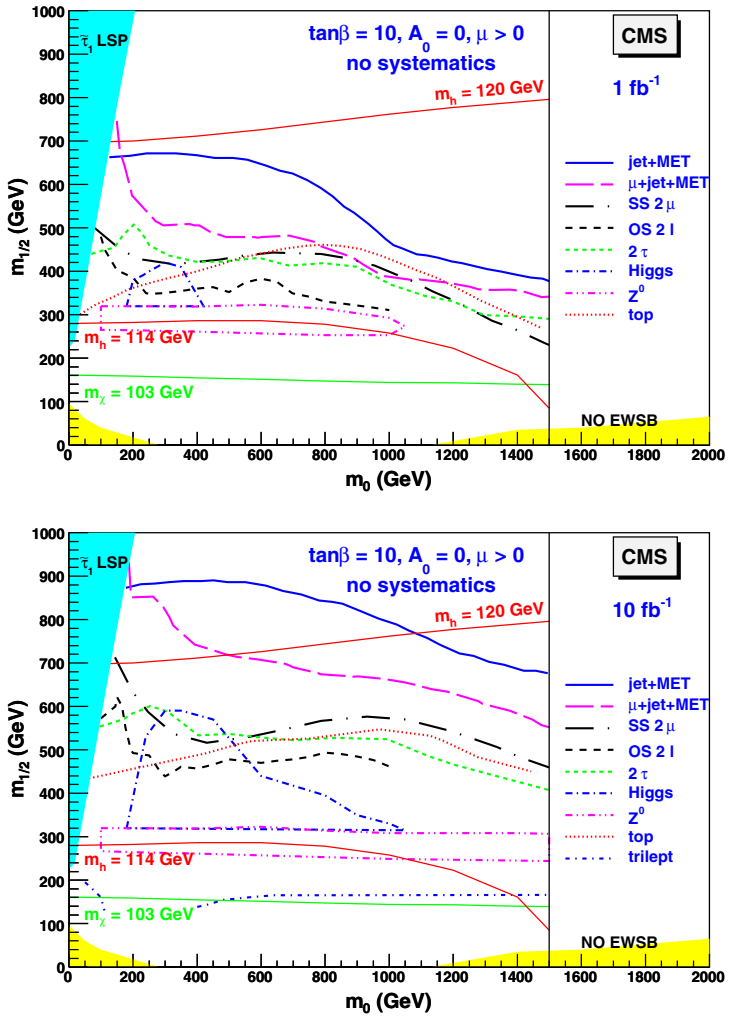

Figure 13.32. Regions of the m_0 versus $m_{1/2}$ plane showing CMS the reach when only statistical uncertainties are taken into account. (Top) for 1 fb^{-1} integrated luminosity, except the Higgs case which assumes 2 fb^{-1}. (Bottom) for 10 fb^{-1}.

reduces both the SM and SUSY backgrounds and increases the discovery potential in the LFV search. For the point LM1 we found that in the assumption of exact knowledge of the background (both the SM and SUSY backgrounds) for the integrated luminosity $\mathcal{L} = 10\,\text{fb}^{-1}$ it would be possible to detect LFV at 5σ level in $\tilde{\chi}_2^0$ decays for $\kappa \geqslant 0.04$.

13.17. Summary of the reach with inclusive analyses

13.17.1. Summary of the mSUGRA studies

In previous sections, several characteristic topologies (or signatures) for MSSM were studied and it was shown that many are already detectable with rather low integrated luminosity

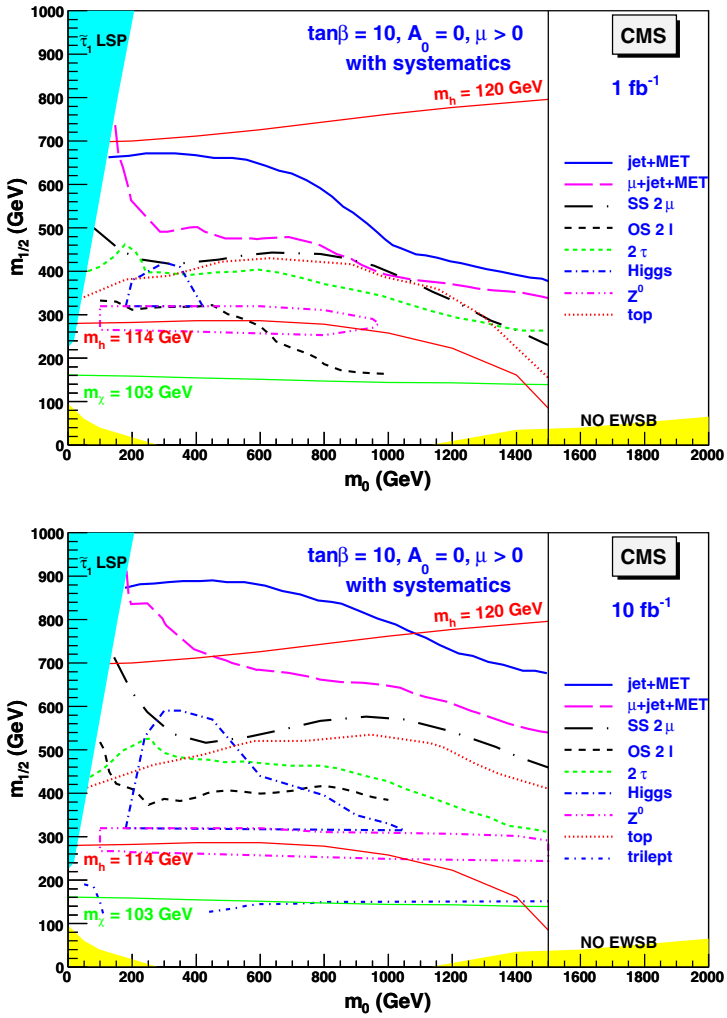

Figure 13.33. Regions of the m_0 versus $m_{1/2}$ plane showing CMS the reach when systematic uncertainties are included. (Top) for 1 fb^{-1} integrated luminosity, except the Higgs case which assumes 2 fb^{-1}. (Bottom) for 10 fb^{-1}.

(few years of LHC running) over a sizeable part of the parameter space, extending well beyond the Tevatron reach.

The curves in Fig. 13.32 summarise the reach estimated for the various topologies of the preceding sections for integrated luminosities of 1 and 10 fb^{-1} when only statistical uncertainties are taken into account. The same results are shown in Fig. 13.33 when systematic uncertainties are included. It is seen that the systematic uncertainties do not degrade the reach very much for integrated luminosities up to 10 fb^{-1}. It should be noted that the analyses have not been reoptimised for the inclusion of systematics nor for higher masses which could be reached with higher luminosity. Moreover, the reach will be further improved by the addition of topologies with electrons, which are presently missing for the muon + jet + MET and same sign dimuon searches.

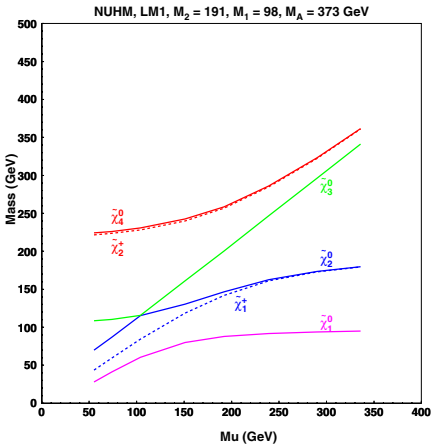

Figure 13.34. Variation of the chargino and neutralino masses as a function of μ for the CMS test point LM1.

The best reach is obtained with the most inclusive channels, the jets + MET and muons + jet + MET. The range of gluino and squark masses up to about 1.5 TeV can be probed with an integrated luminosity of only 1 fb^{-1} and is extended to about 2 TeV with 10 fb^{-1}. Moreover, a large part of the area is covered by several search topologies. The simultaneous observation of a signal in various topologies will help unravel the underlying physics. Examples are the triangular dilepton mass distribution, the observation of the Z^0 or the h^0 in less inclusive channels, which provide a hint that their origin may be the decay of a $\tilde{\chi}_2^0$. If discovered, yet more exclusive analyses should then allow a more quantitative study, e.g. the reconstruction of the sparticle masses and cross section measurements of relevant sub-processes and their ratios.

13.18. Look beyond mSUGRA

13.18.1. Non-universal Higgs masses

It was emphasised in Section 13.3 that the signatures of SUSY with a stable LSP result from the fundamental Supersymmetry gauge couplings, together with the composition of the lightest charginos and neutralinos. As all previous analyses were based on mSUGRA, it is interesting to verify their robustness when relaxing some of the assumptions which might affect the signal observability. As full generality, including giving up all universality assumptions, would lead to an intractable model, a choice needs to be made. Here, a mild extension is considered whereby the two Higgsino mass parameters at the GUT scale are no longer supposed to be degenerate with the other scalar masses, which is sometimes called the Non Universal Higgs Masses (NUHM [696]) scenario. This scenario is conveniently parameterised in terms of two low scale parameters, the mass of the CP-odd Higgs (m_A) and the parameter μ. More specifically, we will analyse the effect of lowering the value of μ compared to its mSUGRA value on the observability of the signatures, as this modifies the composition of the charginos and neutralinos as a function of the gaugino and Higgsino fields. For simplicity, m_A is kept at a fixed value. As exemplified in Fig. 13.34 for the test point LM1, lowering μ also lowers the gaugino masses and in particular their splittings, which affect the

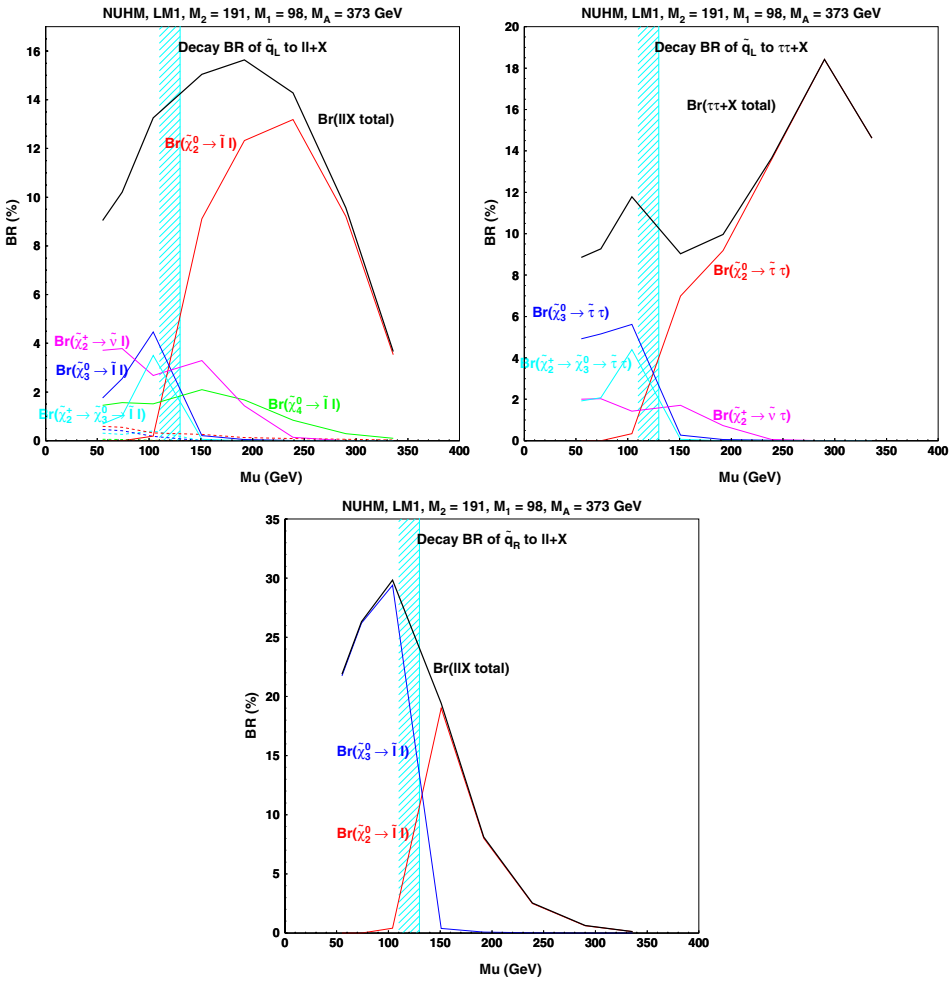

Figure 13.35. Decay branching ratios as a function of μ for $\tilde{q}_L$ into ll and $\tau\tau$ and for $\tilde{q}_R$ into ll at the test point LM1.

branching ratios through phase space effects (a similar behaviour is observed for the other test points). The $\tilde{q}$ and $\tilde{l}$ spectra are almost unaffected. As for low values of μ the lightest chargino becomes lighter than the exclusion from LEP, $m_(\tilde{\chi}_1^{\pm}) \geqslant 103$ GeV, this region is excluded and is indicated on Fig. 13.35 by a grey (blue) shaded strip.

13.18.1.1. Signatures at point LM1. The test point LM1 was studied above for its detectability in cascade decays via a $\tilde{\chi}_2^0$ into $\tilde{l}_R l$. Figure 13.35 shows the variation of some branching ratios from the value of μ near the region where radiative electroweak symmetry breaking is not possible up to its value in mSUGRA.

It is seen that by lowering μ, $B(\tilde{q}_L \to q\tilde{\chi}_2^0 \to q\tilde{l}_R l)$ first increases (due to closing the competing decay to $\tilde{\nu}\nu$), then decreases when the $\tilde{\chi}_2^0$ becomes Higgsino-like, but it remains considerably larger than its mSUGRA value for all values of μ down to the LEP limit. In

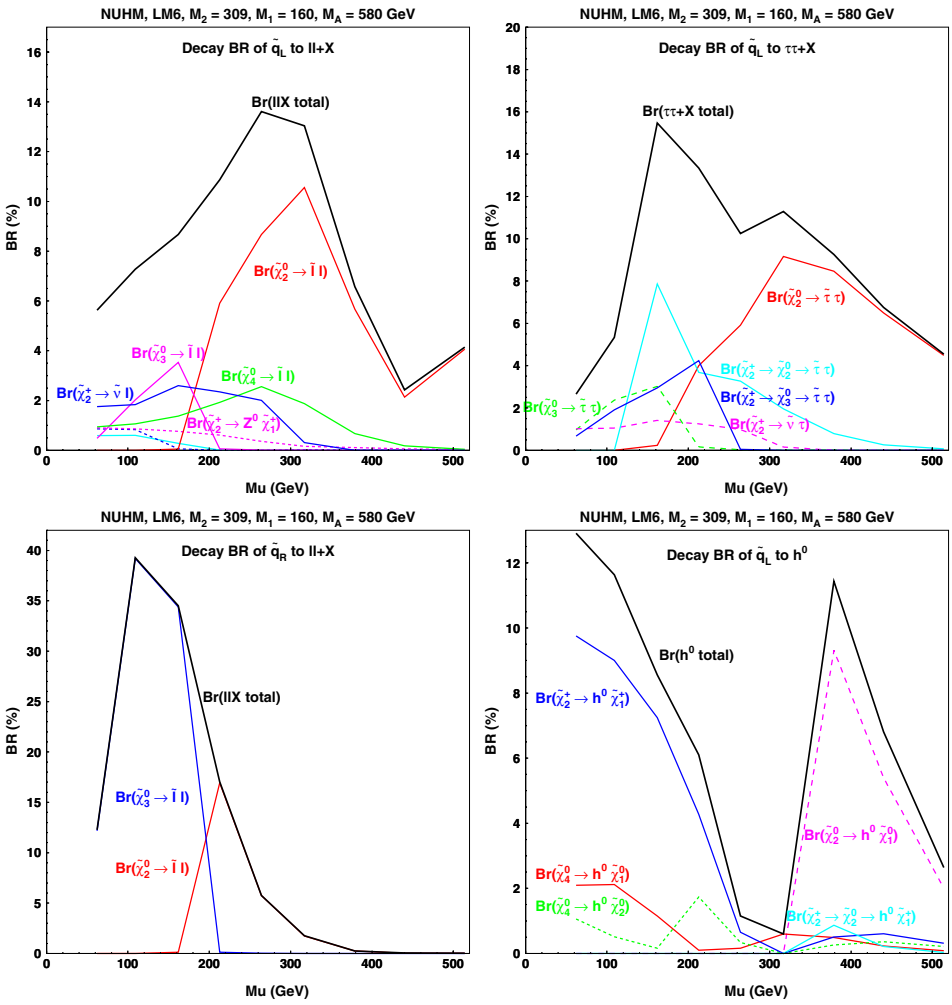

Figure 13.36. Decay branching ratios as a function of μ for $\tilde{q}_L$ into ll, $\tau\tau$ and h^0 and for $\tilde{q}_R$ into ll at the test point LM6.

addition, some new channels open up, like the decay via $\tilde{\chi}_4^0$ into left and right sleptons and the decay via a $\tilde{\chi}_2^\pm \to \tilde{\nu}_l \bar{l}$ followed by $\tilde{\nu}_l \to \tilde{\chi}_1^\pm l$ (the $\tilde{\chi}_4^0$ and $\tilde{\chi}_2^\pm$ become more Wino-like). Other decays via $\tilde{\chi}_3^0$ might also contribute, but only in the region excluded by LEP.

The branching for the decay to $\tilde{\tau}\tau$ shows qualitatively the same behaviour, but is larger than its mSUGRA value in only a small region of μ. Also here a small contribution from the decay $\tilde{\chi}_2^\pm \to \tilde{\nu}\tau$ is present at small μ.

It is interesting to note that, although for mSUGRA the $\tilde{q}_R$ decays exclusively directly to the LSP, it may have for lower μ a non negligible branching ratio to $\tilde{\chi}_2^0$ and also contributes to the dilepton signature.

Finally, there is a non-zero branching ratio for the $\tilde{q}_L$ to the light Higgs via the $\tilde{\chi}_2^\pm$ or $\tilde{\chi}_4^0$ (not shown), but it remains below 1% over the whole range of μ above the LEP limit and will be difficult to detect.

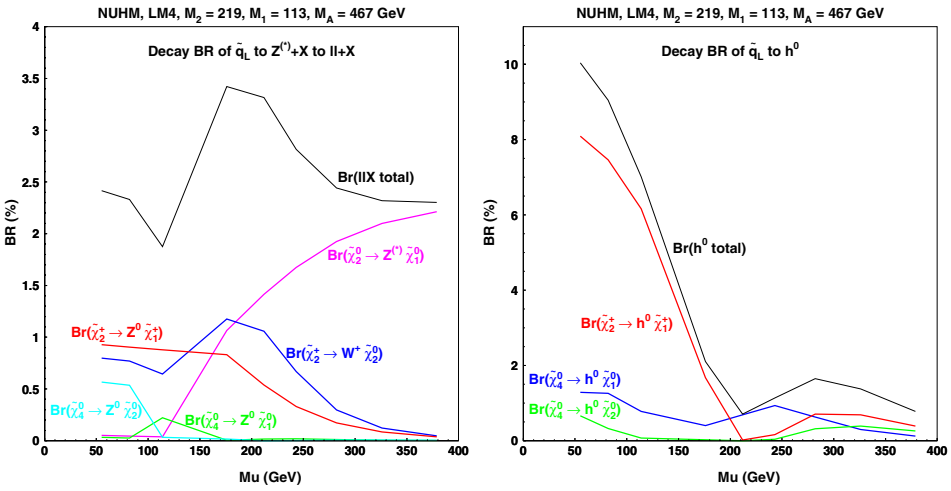

Figure 13.37. Decay branching ratios as a function of μ for $\tilde{q}_L$ into ll and h^0 at the test point LM4.

13.18.1.2. Signatures at point LM6. The test point LM6 has many features in common with LM1, but the $\tilde{\chi}_2^0$ decays mainly to $\tilde{l}_L l$ with a small admixture of $\tilde{l}_R l$. Moreover the decay $\tilde{\chi}_2^0 \to h^0 \tilde{\chi}_1^0$ is kinematically allowed, although suppressed due to the strong gaugino dominance in the $\tilde{\chi}_1^0$ and $\tilde{\chi}_2^0$. The variation of the branching ratios as a function of μ is displayed in Fig. 13.36.

The cascade decays of $\tilde{q}_L$ to $\tilde{l}l$ and $\tilde{\tau}\tau$ via $\tilde{\chi}_2^0$ show grossly the same behaviour as for LM1, with an increase at intermediate values of μ followed by a decrease at low μ. Again, the contributions from other charginos and neutralinos are non negligible near the LEP exclusion limit. Also $\tilde{q}_R$ decays contribute to the dilepton signal via $\tilde{\chi}_2^0$ and $\tilde{\chi}_3^0$ intermediate states.

A distinctive feature of LM6 is its production of final states with h^0. The $\tilde{q}_L$ branching ratio via $\tilde{\chi}_2^0 \to h^0 \tilde{\chi}_1^0$, which is only 2% for mSUGRA increases drastically for lower μ due to the increased Higgsino components in $\tilde{\chi}_1^0$ and $\tilde{\chi}_2^0$, then it drops as the decay becomes kinematically forbidden. After a gap where the branching ratio is below 1%, a strong increase is again visible for lower μ from the cascade dominated by $\tilde{\chi}_1^\pm \to h_0 \tilde{\chi}_1^\pm$ down to the LEP limit. Such an effect is not observed at LM1 due to the smaller spacing of the masses.

13.18.1.3. Signatures at point LM4. Point LM4 was chosen for its characteristic decay of $\tilde{\chi}_2^0$ into $Z^0 \tilde{\chi}_1^0$. Figure 13.37 shows the variation of the branching ratios as a function of μ.

As the decay $\tilde{\chi}_2^0 \to Z^0 \tilde{\chi}_1^0$ requires Higgsino components in both the $\tilde{\chi}_1^0$ and $\tilde{\chi}_2^0$, its branching ratio remains above 90% for all values of μ allowed by the LEP limit. The branching ratio of the $\tilde{q}_L$ into $Z^{(+)}$ via a $\tilde{\chi}_2^0$ decreases mainly due to the decrease of $B(\tilde{q}_L \to q \tilde{\chi}_2^0)$ (the $\tilde{\chi}_2^0$ becomes less gaugino-like). This loss is, however, compensated by the contributions from cascades via $\tilde{\chi}_2^\pm \to W \tilde{\chi}_2^0$ and $\tilde{\chi}_2^\pm \to Z^0 \tilde{\chi}_1^\pm$ and the overall effect is a net increase of the branching ratio of the $\tilde{q}_L$ to final states with a Z^0.

For low values of μ there is also a contribution to h^0 final states via the decay $\tilde{\chi}_2^\pm \to h^0 \tilde{\chi}_1^\pm$, but it remains small above the limit imposed by LEP.

13.18.1.4. Signatures at point LM5. At point LM5, the main signature for mSUGRA is provided by the cascade via $\tilde{\chi}_2^0 \to h^0 \tilde{\chi}_1^0$. The variation of the branching ratios with μ are shown in Fig. 13.38.

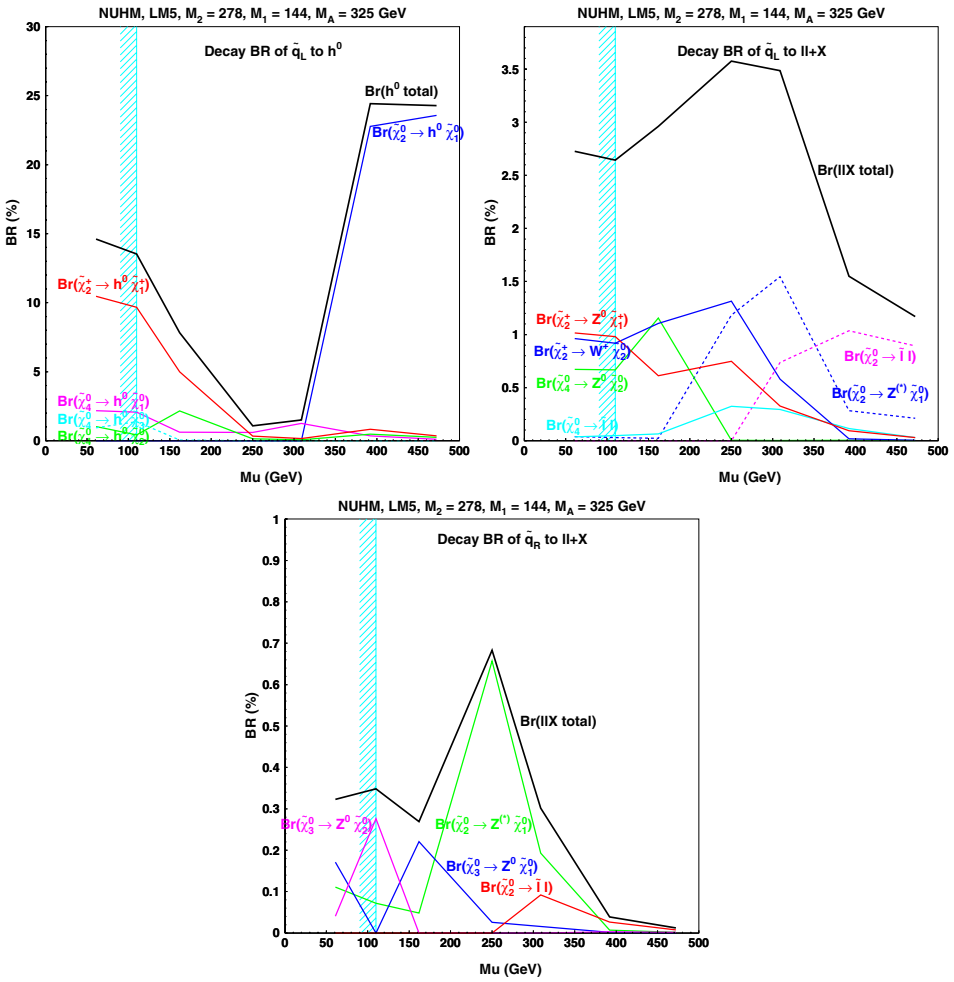

Figure 13.38. Decay branching ratios as a function of μ for $\tilde{q}_L$ into h^0 and ll and for $\tilde{q}_R$ into ll at the test point LM5.

The sharp drop in the branching ratio of $\tilde{\chi}_2^0$ to h^0 below the mSUGRA value of μ results from the decrease in the mass splitting between $\tilde{\chi}_2^0$ and $\tilde{\chi}_1^0$ which suppresses the decay to h^0. For lower values of μ, final states with h^0 are again produced mainly via the $\tilde{\chi}_2^{\pm} \to h^0 \tilde{\chi}_1^{\pm}$. In between these two decay chains, a narrow gap is left where the Higgs branching ratio is less than 2% and hence very difficult to detect.

It is seen that this loss of sensitivity to Higgs final states is to some extent compensated by an increase of the dilepton final states in the region of the gap. The cascade decays of both $\tilde{q}_L$ and $\tilde{q}_R$ contribute in this region, the main contributions being through $\tilde{\chi}_2^0 \to Z^* \tilde{\chi}_1^0$, $\tilde{\chi}_2^{\pm} \to Z^0 \tilde{\chi}_1^{\pm}$ and $\tilde{\chi}_2^{\pm} \to W \tilde{\chi}_2^0$. It gives a branching ratio of up to 3.5% for the dilepton decay of $\tilde{q}_L$ and less than 1% for $\tilde{q}_R$ and hence should be detectable. However, the mixture of intermediate states leading to the dileptons will make the sparticle mass reconstruction very challenging.

13.18.1.5. Conclusion. It can be concluded that the same flavour dilepton signatures originating from the decay of $\tilde{l}l$ or Z^* are quite robust with respect to the chargino and neutralino composition. Lowering μ with respect to its mSUGRA value, a sizeable increase of the branching ratio is even observed for the test points LM1, LM4 and LM6. The h^0 signature at point LM5 is less robust and a region with low branching ratio exists at intermediate values of μ. It is compensated by an increase of dilepton final states. It may be noted that the loss of $\tilde{\chi}_2^0$ decay to h^0 is due to the reduction of the $\tilde{\chi}_2^0$ and $\tilde{\chi}_1^0$ mass splitting. It is therefore a consequence of the low mass spectrum chosen and should disappear at larger values of $m_{1/2}$. Another feature of the NUHM scenario is that for small μ the cascades from $\tilde{q}_R$ also contribute to the signatures, unlike the mSUGRA case. Moreover the signatures at low to intermediate μ tend to be produced by several intermediate neutralino and chargino states. This points to the difficulty of identifying which sparticles are at the origin of the observed end points in the effective mass distributions.

Chapter 14. Extra Dimensions and New Vector Boson High Mass States

14.1. Introduction

The theoretical and phenomenological landscape of beyond the standard model searches extends to a multitude of exotic tendencies today in collider physics. Most are conceived within one kind or another of extra dimensions and supersymmetric scenarios. The strict or loose dualities between different frameworks for physics "beyond the Standard Model" have a direct experimental consequence: the final states and signatures of the models are very similar. This renders the characterisation of an excess or a deviation a fine and probably long challenge. To mention a couple of examples: the question "is it extra dimensions (e.g. UED/ TeV) or is it SUSY?" or "is it a Randall–Sundrum graviton mode or a Z′" is not going to be answered immediately when the excess is observed. The results from all the collider data to date, together with the as yet unobserved Higgs and including the data on the neutrino masses and the composition of the universe, impose a wide program of searches that the LHC experiments are preparing for.

In the present chapter and as well as the "alternatives" chapter that follows, a series of searches is presented with signatures (corresponding to models) as indicated below:

- Dilepton, dijet, diphoton resonances
  - ∗ using ee, $\mu\mu$, $\gamma\gamma$, dijets
  - ∗ searching for Z' (leptons, jets), RS Extra Dimensions (leptons, photons, jets), Z_{KK} in TeV^{-1} (electrons) (can also be interpreted in the context of Little Higgs models)
- Dilepton, dijet continuum modification
  - ∗ using $\mu\mu$, dijets
  - ∗ searching for ADD graviton exchange (dimuons), contact interactions (dimuons, dijets)
- Dilepton + dijets
  - ∗ using ee, $\mu\mu$ + dijets
  - ∗ searching for heavy neutrino from right-handed W (can also be interpreted in the context of leptoquark searches)
- Single photon + missing E_{T}
  - ∗ using γ + missing $\mathrm{E_T}$
  - ∗ searching for ADD direct graviton emission (can also be interpreted in the context of GMSB gravitino-type searches)
- Single lepton + missing E_{T}
  - ∗ using μ + missing $\mathrm{E_T}$
  - ∗ searching for W' (can also be interpreted in the context of little Higgs or W_{KK} excitation in TeV^{-1} models)
- Multilepton + multijet
  - ∗ using top, W and Z reconstruction and constraints
  - ∗ searching for technicolour, littlest Higgs (can also be interpreted in the context of leptoquark searches)
- Same-sign dileptons
  - ∗ using ee, $\mu\mu$, $e\mu$
  - ∗ searching for same-sign top (can be interpreted in the context of technicolour, charged Higgs or SUSY searches)

- High multiplicity/sphericity
  - searching for microscopic black holes in large extra dimensions scenarios

Although not included here, a number of searches are being developed for signatures that involve heavy highly-ionising charged particles and split-SUSY type R-hadrons as well as low P_T multi-lepton signatures in UED scenarios. Strategies are being developed to extract the Standard Model backgrounds from data and control its systematic uncertainties. Fake rates are being estimated as possible while machine and cosmic ray induced backgrounds are not included although methods to suppress them are being developed.

14.1.1. Models with heavy vector bosons

Additional heavy neutral gauge bosons (Z') are predicted in many superstring-inspired [87, 88] and grand unified theories (GUTs) [89], as well as in dynamical symmetry breaking [90] and "little Higgs" [91] models. There are no reliable theoretical predictions, however, of the Z' mass scale. Current lower limits on the Z' mass are (depending on the model) of the order of 600–900 $\mathrm{GeV/c^2}$ [54]. The mass region up to about 1 $\mathrm{TeV/c^2}$ is expected to be explored at Run II at the Tevatron [92, 93]. The LHC offers the opportunity to search for Z' bosons in a mass range significantly larger than 1 $\mathrm{TeV/c^2}$. In the Z' studies presented here (Sections 14.3 and 14.2) six models which are frequently discussed and whose properties are representative of a broad class of extra gauge bosons are used:

- Z_{SSM} within the Sequential Standard Model (SSM), which has the same couplings as the Standard Model Z^0.
- Z_ψ, $Z\eta$ and Z_χ, arising in E_6 and SO(10) GUT groups with couplings to quarks and leptons as derived in Refs. [96, 97].
- Z_{LRM} and Z_{ALRM}, arising in the framework of the so-called "left–right" [98] and "alternative left–right" [92, 93] models with couplings as derived in Ref. [92, 93], with the choice of $g_R = g_L$.

The W' search presented in Section 14.4 uses a reference model by Altarelli [697], in which the W' is a heavy copy of the W, with the very same left-handed fermionic couplings (including CKM matrix elements), while there is no interaction with the Standard Model gauge bosons or with other heavy gauge bosons such as a Z'.

14.1.2. Arkani-Hamed–Dimopoulos–Dvali (ADD) models

ADD refers to the class of models which incorporate the large extra dimensions scenario of Arkani-Hamed, Dvali, and Dimopoulos [698]. These were the first extra dimensions models in which the compactified dimensions can be of macroscopic size, consistent with all current measurements, and they are referred to as "large extra dimensions" models. In the most basic version, n extra spatial dimensions are compactified on a torus with common circumference R, and a brane is introduced which extends only in the three infinite spatial directions. Strictly speaking, the brane should have a very small tension (energy per unit volume) in order that it does not significantly warp the extra dimensional space. It is assumed that all standard model fields extend only in the brane. This can be considered as a toy version of what happens in string theory, where chiral gauge theories similar to the standard model are confined to reasonably simple brane configurations in reasonably simple string compactifications [699].

A consequence of these assumptions is that the effective 4d Planck scale is related to the underlying fundamental Planck scale of the $4+n$-dimensional theory and to the volume of

the compactified space. This relation follows from Gauss' law, or by dimensional analysis

$$M_{\text{Planck}}^2 = M_*^{2+n}\, R^n, \tag{14.1}$$

where M_{Planck}^2 is defined by Newton's constant: $M_{\text{Planck}} = 1/\sqrt{G_N} = 1.2 \times 10^{19}\,\text{GeV/c}^2$. M_*^{2+n} is defined as the gravitational coupling which appears in the $4+n$-dimensional version of the Einstein–Hilbert action. It is the quantum gravity scale of the higher dimensional theory.

If M_{Planck}, M^* and $1/R$ are all of the same order, as is usually assumed in string theory, this relation is not very interesting. But it is plausible and experimentally allowed that M^* is equal to some completely different scale. Taking $M^* \sim 1\,\text{TeV/c}^2$ [700] the hierarchy problem of the standard model is translated from an ultraviolet problem to an infrared one. Note that if there is any interface with string theory, ADD-like models must arise from string ground states in which the string scale (and thus the ultraviolet cutoff for gravity) is also in the TeV range. This is difficult to achieve but has been studied in [701].

The ADD scenario renders observations of quantum gravity at the LHC possible. In such models only the graviton, and possibly some non-SM exotics like the right-handed neutrino, probe the full bulk space. There is a Kaluza–Klein (KK) tower of graviton modes, where the massless mode is the standard 4d graviton, and the other KK modes are massive spin 2 particles which also couple to SM matter with gravitational strength.

Whereas bremsstrahlung of ordinary gravitons is a completely negligible effect at colliders, the total cross section to produce *some* massive KK graviton is volume enhanced, and effectively suppressed only by powers of M^* and not M_{Planck}. From Eq. (14.1) it follows:

$$\sigma \sim \frac{1}{M_{\text{Planck}}^2}(E\,R)^n \sim \frac{1}{M_*^2}(E\,M_*)^n, \tag{14.2}$$

where E is the characteristic energy of the subprocess.

For graviton phenomenology it is useful to replace the ADD parameter M^* by other rescaled parameters. The two most useful choices are taken from the work of Giudice, Rattazzi and Wells (GRZ) [702], and Han, Lykken and Zhang (HLZ) [703]:

$$M_*^{n+2} = \frac{S_{n-1}}{(2\pi)^n} M_s^{n+2}\,, \tag{14.3}$$

$$M_*^{n+2} = \frac{8\pi}{(2\pi)^n} M_D^{n+2}\,, \tag{14.4}$$

where M_s is the HLZ scale, M_D is the GRW scale, and S_{n-1} is the surface area of a unit n-sphere:

$$S_{n-1} = \frac{2\pi^{n/2}}{\Gamma(n/2)}\,. \tag{14.5}$$

Both notations are equivalent. To obtain a complete dictionary between ADD, GRZ and HLZ, one also needs to relate the ADD parameter R to those used by the other authors: $R = R_{\text{HLZ}} = 2\pi\, R_{GRW}$, and take note of the different notations for Newton's constant:

$$\kappa^2 = 16\pi\, G_N \text{ (HLZ)}; \quad \overline{\text{M}}_{\text{P}}^2 = \frac{1}{8\pi\,\text{G}_{\text{N}}} \text{ (GRW)}\,. \tag{14.6}$$

A Kaluza–Klein graviton mode has a mass specified by an n-vector of integers $\vec{k}$:

$$m^2(\vec{k}) = \frac{\vec{k}^2}{R_{\text{GRW}}^2}\,. \tag{14.7}$$

Let $r = |\vec{k}|$. Then for large r (as is often the relevant case for ADD phenomenology) the number of KK graviton states of a given polarisation with $r \leqslant r_{\max}$ is given by the integral

$$S_{n-1} \int_0^{r_{\max}} dr\, r^{n-1} = \frac{1}{n} S_{n-1}\, r_{\max}^n = \int_0^{m_{\max}} \rho(m)\, dm, \tag{14.8}$$

where the KK density of states is

$$\rho(m) = \frac{m^{n-1}}{G_N M_s^{n+2}}. \tag{14.9}$$

M_s is the natural scaling parameter for KK graviton production. The density of states formulation can be applied to a much more general class of models than ADD, and can also include graviton wavefunction factors when the extra dimensions are not flat.

Consider an on-shell production of a KK graviton from a pp or collision. To leading order this is a $2 \to 2$ process with two massless partons in the initial state, plus a massive KK graviton and a massless parton in the final state. Let p_1, p_2 denote the 4-momenta of the initial state partons, p_3 the 4-momentum of the graviton, and p_4 the 4-momentum of the outgoing parton. The total cross section for any particular variety of partonic subprocess has the form

$$\sigma(1+2 \to \mathrm{KK}+4) = \int dx_1 dx_2\, f_1(x_1, \hat{s})\, f_2(x_2, \hat{s}) \int d\hat{t} \int_0^{\sqrt{\hat{s}}} dm\, \rho(m)\, \frac{d\sigma_m}{d\hat{t}}(\hat{s}, \hat{t}), \tag{14.10}$$

where $f_1(x_1, \hat{s})$, $f_2(x_2, \hat{s})$ are the parton distribution functions (PDFs) for the initial state partons, $\hat{s} = x_1 x_2 s = (p_1 + p_2)^2$ is the square of the total centre of mass (cm) energy of the subprocess, and $\hat{t} = (p_1 - p_3)^2$ is the usual Mandelstam invariant. The formulae for $d\sigma_m/d\hat{t}$, the differential subprocess cross sections for KK gravitons of mass m, are given in [702].

14.1.2.1. Graviton production above the cutoff. At the LHC, proton–proton collisions will probe a distribution of partonic subprocess energies $\sqrt{\hat{s}}$. This creates a problem for the consistent analysis of missing energy signatures in the framework of ADD models. These models are simple low energy effective theories which are only valid for $\sqrt{\hat{s}}$ below some cutoff. This cutoff is at most $2M^*$, and could be a factor of a few smaller if the ultraviolet completion of the model is weakly coupled string theory [704]. The same is true for the Lykken–Randall model [705], which is a low energy description of gravity in a single infinite warped extra dimension, valid up to a cutoff $\sim M^*$. It is inconsistent to use either type of model to describe LHC collisions with subprocess energies greater than the cutoff.

This problem was first noted by the authors of [702], who suggested replacing the ADD graviton density of states $\rho(m)$ by $\rho(m)\theta(\sqrt{\hat{s}} - M_D)$, where θ is a step function. This introduces a systematic theory error into the analysis. The size of this error is very sensitive to the values of M_D and n. For initial LHC data sets, we will be probing the lower range of M_D values, beginning at the current $\simeq 1\,\mathrm{TeV/c^2}$ bounds from Tevatron and LEP. This increases the theory systematic from the cutoff for any fixed n. For fixed M_D, the theory systematic increases rapidly for increasing n. For $n = 2$, the theory uncertainty in the total cross section remains below about 20% even for M_D approaching $1\,\mathrm{TeV/c^2}$.[49] For $n = 6$ and above, the effect of the cutoff is enormous for modest values of M_D, because the rapid rise in the graviton density of states is not compensated by the rapid falloff of the pdfs. The theory error for the total cross section in this case can be as large as an order of magnitude.

[49] To avoid strong astrophysical constraints, $n = 2$ ADD models also require an *ad hoc* infrared cutoff, truncating the massive graviton spectrum for masses below about 20 MeV. This has a negligible effect on LHC analysis.

The resolution of this problem depends upon whether or not there is a signal in the missing energy channels (we will not discuss the related problems which arise in channels affected by virtual graviton exchanges). If there is a signal, the optimal procedure is to measure the observables $d^2\sigma/dp_T d\eta$ as accurately as possible, perhaps at more than one collider energy as suggested in [706, 707]. No theory systematic should be included in these analyses. Instead, one should use the data to find the best fit form for $\rho(m, \sqrt{\hat{s}})$. Simple trial forms can be obtained, for example, from multiplying the ADD density of states by the form factors obtained in models with strings [704, 708, 709] or branes [710]. For the lower range of M_D values, the sensitivity to n suggested in [706, 707] will tend to be washed out. This is not a bad outcome, since it is a result of convolving the n dependence with the effects of strings, branes or other new physics. Thus the theory systematic is replaced by likelihood fits to theories of Planck scale physics.

More problematic is the case where there is no graviton signal in a given data set. Since in this case we are trying to set a limit, we need an estimate of the theory systematic. The simplest possibility is to implement the GRW cutoff defined above, and estimate the theory error by varying the cutoff. For ADD with $n \geqslant 6$, one expects to obtain no lower bound at all on M_D, as noted in [702].

14.1.3. Virtual graviton exchange

The second class of collider signals for large extra dimensions is that of virtual graviton exchange[702, 711] in $2 \to 2$ scattering. This leads to deviations in cross sections and asymmetries in Standard Model processes with difermion final states. It may also give rise to new production processes which are not present at tree-level in the Standard Model, such as $gg \to \ell^+\ell^-$. The signature is similar to that expected in composite theories and provides a good experimental tool for searching for large extra dimensions for the case $\sqrt{s} < M_D$.

Graviton exchange is governed by the effective Lagrangian

$$\mathcal{L} = i\frac{4\lambda}{M_H^4} T_{\mu\nu} T^{\mu\nu} + \text{h.c.} \tag{14.11}$$

The amplitude is proportional to the sum over the propagators for the graviton KK tower which may be converted to an integral over the density of KK states. However, in this case, there is no specific cut-off associated with the process kinematics and the integral is divergent for $n > 1$. This introduces a sensitivity to the unknown ultraviolet physics which appears at the fundamental scale. This integral needs to be regulated and several approaches have been proposed: (i) a naive cut-off scheme [702, 711], (ii) brane fluctuations [710], or (iii) the inclusion of full weakly coupled TeV-scale string theory in the scattering process [704, 708]. The most model independent approach which does not make any assumptions as to the nature of the new physics appearing at the fundamental scale is that of the naive cut-off. Here, the cut-off is set to $M_H \neq M_D$; the exact relationship between M_H and M_D is not calculable without knowledge of the full theory. The parameter $\lambda = \pm 1$ is also usually incorporated in direct analogy with the standard parametrisation for contact interactions [123] and accounts for uncertainties associated with the ultraviolet physics. The substitution

$$\mathcal{M} \sim \frac{i^2\pi}{M_{\text{Pl}}^2} \sum_{\vec{n}=1}^{\infty} \frac{1}{s - m_{\vec{n}}^2} \to \frac{\lambda}{M_H^4} \tag{14.12}$$

is then performed in the matrix element for s-channel KK graviton exchange with corresponding replacements for t- and u-channel scattering. As above, the Planck scale suppression is removed and superseded by powers of $M_H \sim \text{TeV/c}^2$.

The resulting angular distributions for fermion pair production are quartic in $\cos\theta$ and thus provide a unique signal for spin-2 exchange.

The experimental analyses also make use of the cut-off approach. Using virtual Kaluza–Klein graviton exchange in reactions with diphoton, dibosons and dilepton final states, ($G_n \to \gamma\gamma$, VV, $\ell\ell$), the LEP and Tevatron experiments exclude exchange scales up to $\sim 1.1\,\mathrm{TeV/c^2}$.

In the dimuon studies presented here (14.3.2) with $1\,\mathrm{fb}^{-1}$ a 5-sigma effect from the virtual contributions of ADD gravitons to Drell–Yan process is observable for effective fundamental Planck scale of 4.0 TeV and for $n = 6$ extra dimensions.

14.1.4. Inverse TeV sized extra dimensions

The possibility of TeV $^{-1}$-sized extra dimensions naturally arises in braneworld theories [700]. By themselves, they do not allow for a reformulation of the hierarchy problem, but they may be incorporated into a larger structure in which this problem is solved. In these scenarios, the Standard Model fields are phenomenologically allowed to propagate in the bulk. This presents a wide variety of choices for model building: (i) all, or only some, of the Standard Model gauge fields exist in the bulk; (ii) the Higgs field may lie on the brane or in the bulk; (iii) the Standard Model fermions may be confined to the brane or to specific locales in the extra dimension. The phenomenological consequences of this scenario strongly depend on the location of the fermion fields. Unless otherwise noted, our discussion assumes that all of the Standard Model gauge fields propagate in the bulk.

The masses of the excitation states in the gauge boson KK towers depend on where the Higgs boson is located. If the Higgs field propagates in the bulk, the zero-mode state of the Higgs KK tower receives a vacuum expectation value (vev) which is responsible for the spontaneous breaking of the electroweak gauge symmetry. In this case, the resulting mass matrix for the states in the gauge boson KK towers is diagonal and the excitation masses are shifted by the mass of the gauge zero-mode, which corresponds to the Standard Model gauge field, giving

$$m_{\vec{n}} = (m_0^2 + \vec{n}\cdot\vec{n}/R_c^2)^{1/2} \tag{14.13}$$

where $\vec{n} = (n_1, n_2, \ldots)$ labels the KK excitation levels. However, if the Higgs is confined to the brane, its vev induces mixing, amongst the gauge KK states of order $(m_0 R_c)^2$. The KK mass matrix must then be diagonalised in order to determine the excitation masses. For the case of 1 extra TeV $^{-1}$-sized dimension, the coupling strength of the gauge KK states to the Standard Model fermions on the brane is $\sqrt{2}g$, where g is the corresponding Standard Model gauge coupling.

In the case where the Standard Model fermions are rigidly fixed to the brane, they do not feel the effects of the additional dimensions. For models in this class, precision electroweak data place strong constraints on the mass of the first gauge KK excitation. Contributions to electroweak observables arise from the virtual exchange of gauge KK states and a summation over the contributions from the entire KK tower must be performed. For $D > 5$, this sum is divergent. In the full higher dimensional theory, some new, as of yet unknown, physics would regularise this sum and render it finite. An example of this is given by the possibility that the brane is flexible or non-rigid, which has the effect of exponentially damping the sum over KK states. Due to our present lack of knowledge of the full underlying theory, the KK sum is usually terminated by an explicit cut-off, which provides a naive estimate of the magnitude of the effects.

Since the $D = 5$ theory is finite, it is the scenario that is most often discussed and is sometimes referred to as the 5-dimensional Standard Model (5DSM). In this case, a global

fit to the precision electroweak data including the contributions from KK gauge interactions yields $m_1 \sim R_c^{-1} \gtrsim 4\,\mathrm{TeV/c^2}$. In addition, the KK contributions to the precision observables allow for the mass of the Higgs boson to be somewhat heavier than the value obtained in the Standard Model global fit. Given the constraint on R_c from the precision data set, the gauge KK contributions to the anomalous magnetic moment of the muon are small. The first gauge KK state can be produced as a resonance at the LHC in the Drell–Yan channel provided $m_1 \lesssim 6\,\mathrm{TeV/c^2}$. In the studies presented here using the Z_{KK} in the dielectron channel a 5-sigma reach for $m_1 \sim R_c^{-1} \sim 4.97\,\mathrm{TeV/c^2}$ is obtained with $10\,\mathrm{fb}^{-1}$.

In the scenario where the Standard Model fermions are localised at specific points in the extra TeV^{-1}-sized dimensions, the fermions have narrow gaussian-like wave functions in the extra dimensions with width much smaller than R_c^{-1}. The placement of the different fermions at distinct locations in the additional dimensions, along with the narrowness of their wavefunctions, can then naturally suppress operators mediating dangerous processes such as proton decay. The exchange of gauge KK states in $2 \to 2$ scattering processes involving initial and final state fermions is sensitive to the placement of the fermions and can be used to perform a cartography of the localised fermions, i.e., measure the wavefunctions and locations of the fermions. At very large energies, it is possible that the cross section for such scattering will tend rapidly to zero since the fermions' wavefunctions will not overlap and hence they may completely miss each other in the extra dimensions.

14.1.5. Randall–Sundrum (RS) models

Randall–Sundrum refers to a class of scenarios, also known as warped extra dimensions models, originated by Lisa Randall and Raman Sundrum [94, 646]. In these scenarios there is one extra spatial dimension, and the five-dimensional geometry is "warped" by the presence of one or more branes. The branes extend infinitely in the usual three spatial dimensions, but are sufficiently thin in the warped direction that their profiles are well-approximated by delta functions in the energy regime of interest. If we ignore fluctuations of the branes, we can always choose a "Gaussian Normal" coordinate system, such that the fifth dimension is labelled y and the usual 4d spacetime by x^μ. The action for such a theory contains, at a minimum, a 5d bulk gravity piece and 4d brane pieces. The bulk piece has the 5d Einstein–Hilbert action with gravitational coupling M^3, and a 5d cosmological constant Λ. The brane pieces are proportional to the brane tensions V_i, which may be positive or negative. These act as sources for 5d gravity, contributing to the 5d stress-energy terms proportional to

$$\sum_i V_i \delta(y - y_i) \tag{14.14}$$

where the y_i are the positions of the branes. Combined with a negative Λ, this results in a curved geometry, with a 5d metric of the form:

$$\begin{aligned} &g_{\mu\nu}(x^\rho, y) = a^2(y)\, \tilde{g}_{\mu\nu}(x^\rho)\,, \\ &g_{\mu y} = 0\,, \quad g_{yy} = 1\,, \end{aligned} \tag{14.15}$$

where $a(y)$ is called the warp factor, $\tilde{g}$ is a 4d metric, and we have made a useful choice of coordinates. Warping refers to the fact that a 4d distance d_0 measured at $y = y_0$ is related to an analogous 4d distance d_1 measured at $y = y_1$ by $a(y_0)d_0 = a(y_1)d_1$. Thus in Randall–Sundrum scenarios 4d length, time, energy and mass scales vary with y.

Most collider physics phenomenology done with warped extra dimensions so far is based upon one very specific model, the original simple scenario called RSI. In this model the extra dimension is compactified to a circle of circumference $2L$, and then further orbifolded by identifying points related by $y \to -y$. The fifth dimension then consists of two periodically

identified mirror copies of a curved 5d space extending from $y = 0$ to $y = L$. It is assumed that there is a brane at $y = 0$, with positive tension V_0; it is known as the Planck brane – strong gravity resides on that brane. There is another brane at $y = L$, with negative tension V_L, known as the TeV brane–the entire 4d universe is confined to the TeV brane.

Randall and Sundrum showed that, for a tuned choice of input parameters $V_0 = -V_L = -M^2\Lambda$, the 5d Einstein equations have a simple warped solution on $0 < y < L$ with metric:

$$g_{\mu\nu}(x^\rho, y) = \mathrm{e}^{-2ky}\,\eta_{\mu\nu}\,,$$
$$g_{\mu y} = 0\,, \quad g_{yy} = 1\,, \tag{14.16}$$

where $\eta_{\mu\nu}$ is the 4d flat Minkowski metric, and $k = \sqrt{-\Lambda}$. Away from the branes, the 5d curvature is constant and negative; it is thus equivalent locally to AdS_5, with the anti-de Sitter radius of curvature given by $1/k$. At the locations of the branes the curvature is discontinuous, due to the fact that the branes are delta function sources for curvature.

The RSI model is completely described by three parameters: k, M, and L. Restricting the scenario to a low energy effective description implies considering $k, 1/L \ll M$. In fact in RSI it is assumed that k is merely parametrically small compared to the 5d Planck scale M, i.e. $k \sim M/10$. The effective 4d Planck scale, which is the same as the coupling of the graviton zero mode, is given by dimensional truncation:

$$M^2_{\mathrm{Planck}} = \frac{M^3}{2k}\left(1 - \mathrm{e}^{-2kL}\right). \tag{14.17}$$

Then, within an order of magnitude, $M \sim k \sim M_{\mathrm{Planck}}$. In RSI the distance L is fixed by requiring that $a(L)M_{\mathrm{Planck}} \simeq 1$ TeV, thus $kL \sim 30$. This is *not* a large extra dimension: its inverse size is comparable to the grand unification scale.

Since the standard model fields live on the TeV brane as in ADD models, the phenomenology of RSI is concerned with the effects of the massive KK modes of the graviton. These modes as measured on the TeV brane have their mass splittings of the order of a TeV, and have TeV suppressed couplings to the standard model fields. In RSI, the Standard Model is replaced at the TeV scale by a new effective theory in which gravity is still very weak, but there are exotic heavy spin-two particles.

At the LHC the KK gravitons of RSI would be seen as difermion or dibosons resonances, since (unlike the KK gravitons of ADD) the coupling of each KK mode is only TeV suppressed [712]. The width of these resonances is controlled by the ratio $c = k/M$; the resonances become more narrow as the coupling parameter $c = k/M$ is reduced, as shown in Fig. 14.1.

The studies presented here focus on dilepton and diphoton final states while results using dijets can be found in Section 14.4.1. Note that due to the spin-2 nature of the graviton its branching ratio to diphotons is roughly twice that of a single dilepton channel.

14.2. High mass dielectron final states

This section presents the CMS experiment discovery potential for new heavy resonances, decaying into an electron pair. The $\mathrm{e^+e^-}$ decay channel provides a clean signature in the CMS detector. The presence of a heavy particle would be detected in CMS by the observation of a resonance peak in the dielectron mass spectrum over the Drell–Yan process ($\mathrm{pp} \to \gamma/\mathrm{Z} \to \mathrm{e^+e^-}$) which constitutes the main Standard Model background.

Heavy resonances with mass above 1 TeV/$\mathrm{c^2}$ are predicted by several models beyond the Standard Model. Three models are considered here: Kaluza–Klein (KK) excitations of a Z boson (TeV^{-1} model, see Section 14.1.4) and KK excitation of a graviton (Randall–Sundrum

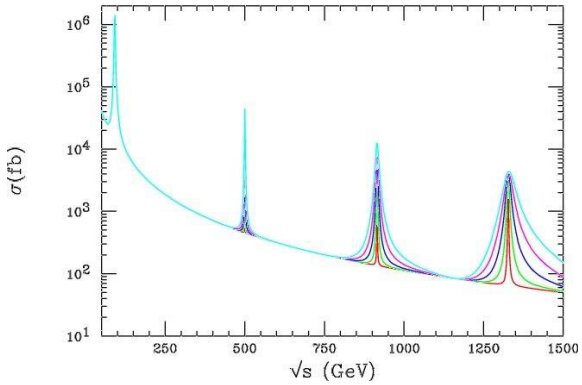

Figure 14.1. The cross section for $e^+e^- \to \mu^+\mu^-$ including the exchange of KK gravitons in the RSI model. The narrowest resonances correspond to $k/M = 0.05$, the widest to $k/M = 0.14$. (Taken from Ref. [713].)

(RS) model, see Section 14.1.5), both predicted in extra dimensions models, and neutral heavy Z' boson predicted by Grand Unified Theories (GUT) (see Section 14.1.1). For the Z' bosons, 6 models are studied, as for the $Z' \to \mu^+\mu^-$ channel [100] that is discussed in Section 14.3.

Details of the analyses presented in this section can be found in [714] and [715].

14.2.1. Event selection and correction

Two electrons are required for this analysis. They are reconstructed as super-clusters (SC) in the ECAL calorimeter in the barrel and the endcap regions [716]. For endcap SC, the energy loss in the preshower detector is taken into account. The two SC with highest energies are selected as the electron candidates.

Reducible backgrounds (like QCD jets and γ-jets) are suppressed by applying the following requirements:

- The ratio of the HCAL to ECAL energy deposits is required to be $H/E < 10\ \%$.
- The two SC must be isolated: the total additional transverse energy in a cone of radius $0.1 < \Delta R < 0.5$ is required to be below 2% of the SC transverse energy (where $\Delta R = \sqrt{\Delta\eta^2 + \Delta\phi^2}$).
- To identify electrons and reject neutral particles, a track is requested to be associated for each electron candidate. If a track is associated with only one of these SC, the event is however kept if it contains a third SC with $E > 300\,\text{GeV}$ with an associated track and satisfying the H/E and isolation cuts described above.

The selected events are then corrected for the following effects:

- Saturation correction. For very energetic electrons and photons, saturation occurs in the ECAL electronics because of the limited dynamical range of the Multi-Gain-Pre-Amplifier. The saturation threshold has been established to be at 1.7 TeV in crystals of the barrel and 3.0 TeV in the endcaps. A correction method (for barrel only) has been developed using the energy deposit in crystals surrounding the saturated crystal. The correction allows the energy deposits of clusters suffering from saturation to be estimated with a resolution of about 7% [717].

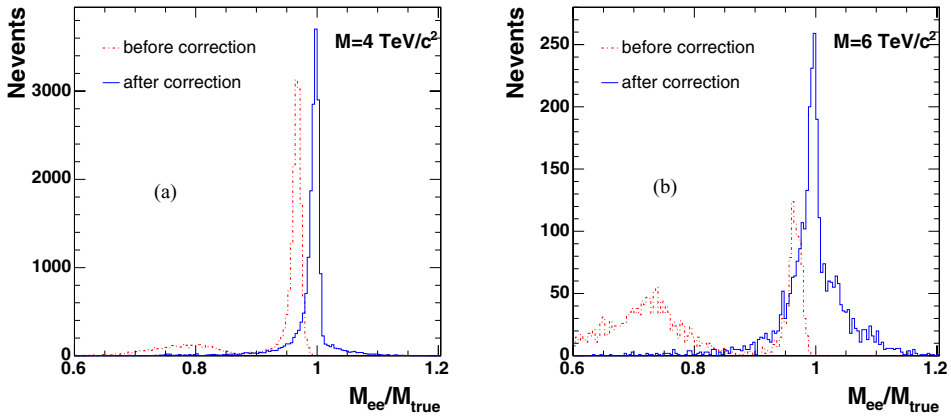

Figure 14.2. Ratio M_{ee}/M_{true} before and after corrections for KK Z boson production, for $M = 4\,\mathrm{TeV/c^2}$ (a) and $M = 6\,\mathrm{TeV/c^2}$ (b).

- Energy correction. The ECAL measured electron energy after preshower, HCAL and saturation corrections, is smaller than the generated energy. Dedicated energy correction factors for very energetic electrons have been determined using calibration files. These factors depend on both energy, η and whether saturation occurs or not. The resolution on the corrected SC energy is 0.6% at $E = 1000\,\mathrm{GeV}$.
- z-vertex distribution. The measurement in η takes into account the knowledge of the z-vertex position.
- FSR recovery. Hard photon emission from Final State Radiation can induce the detection in the event of a third energetic SC If a SC with $E > 300\,\mathrm{GeV}$ satisfying the H/E and isolation cuts is observed very close to the SC of the electron candidates ($\Delta R < 0.1$), this additional SC is associated to the corresponding electron.

14.2.2. Mass peak distributions

The resonance mass is reconstructed from the energies and angles of the 2 electron candidates, after the selection cuts and energy corrections mentioned above. Figures 14.2a and 14.2b show the ratio of the reconstructed and the true masses, M_{ee}/M_{true}, before and after energy corrections for KK Z production with $M = 4$ and $6\,\mathrm{TeV/c^2}$, respectively. The peaks at low values of M_{ee}/M_{true} correspond to events with saturated ECAL electronics. The final resolution on the resonance mass is around 0.6% for events with no saturation, and 7% in case of saturation.

Figure 14.3a presents the signal and the Drell–Yan background for KK Z boson production with $M = 4\,\mathrm{TeV/c^2}$; Fig. 14.3b for Z' boson production with $M = 1.5\,\mathrm{TeV/c^2}$; Fig. 14.3c for graviton production with $M = 1.5\,\mathrm{TeV/c^2}$ and coupling parameter, defined in Section 14.1.5, $c = 0.01$.

14.2.3. Discovery potential of CMS

The discovery potential of a new physics resonance is determined using the likelihood estimator S_{cL} (defined in Appendix A.1) based on event counting, suited for small event samples. The discovery limit is defined by $S_{cL} > 5$.

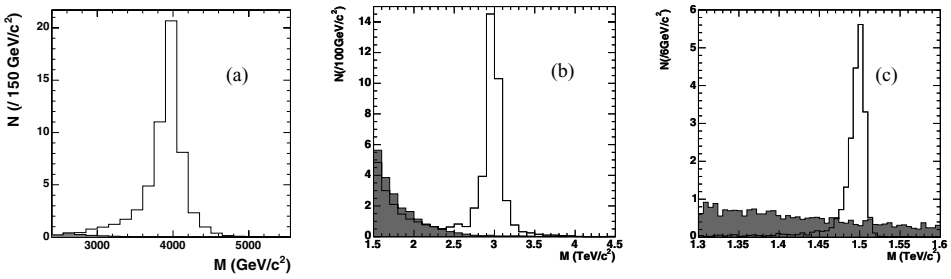

Figure 14.3. Resonance signal (white histograms) and Drell–Yan background (shaded histograms) for KK Z boson production with $M = 4.0\,\mathrm{TeV/c^2}$ (a), SSM Z' boson production with $M = 3.0\,\mathrm{TeV/c^2}$ (b), and graviton production with $M = 1.5\,\mathrm{TeV/c^2}$, coupling parameter $c = 0.01$ (c), for an integrated luminosity of $30\,\mathrm{fb^{-1}}$.

Table 14.1. Number of events for resonant signal, N_s, and for Drell–Yan background, N_b, and corresponding significances S_{cL} for an integrated luminosity of $30\,\mathrm{fb^{-1}}$. The masses M and the mass windows M_w are in $\mathrm{TeV/c^2}$.

	KK Z		G, $c = 0.01$	G, $c = 0.1$	SSM Z'	
M	4.0	6.0	1.5	3.5	1.0	5.0
M_w	3.5–4.5	5.0–6.7	1.47–1.52	3.30–3.65	0.92–1.07	4.18–5.81
N_s	50.6	1.05	18.8	7.30	72020	0.58
N_b	0.13	0.005	4.16	0.121	85.5	0.025
S	22.5	3.0	6.39	6.83	225	1.63

The number of signal and background events, N_s and N_b, computed for a given mass window around the peak, are presented in Table 14.1 for the three models, together with the corresponding significance, for an integrated luminosity of $30\,\mathrm{fb^{-1}}$.

The 5σ discovery limits as a function of mass are given in Fig. 14.4a and Fig. 14.4b, for KK Z boson production and Z' production (for the 6 considered models), respectively. In the graviton case, the 5σ discovery plane as a function of the coupling parameter c and the resonance mass is given in Fig. 14.4c.

For KK Z bosons, a 5σ discovery can be achieved for a resonance mass up to $M = 4.97\,\mathrm{TeV/c^2}$ for an integrated luminosity of $10\,\mathrm{fb^{-1}}$, $M = 5.53\,\mathrm{TeV/c^2}$ for $30\,\mathrm{fb^{-1}}$ and $M = 5.88\,\mathrm{TeV/c^2}$ for $60\,\mathrm{fb^{-1}}$. For gravitons, with an integrated luminosity of $30\,\mathrm{fb^{-1}}$, a 5σ discovery can be extracted for masses up to $1.64\,\mathrm{TeV/c^2}$ for $c = 0.01$ and up to $3.81\,\mathrm{TeV/c^2}$ for $c = 0.1$. For Z' boson production, with an integrated luminosity of $30\,\mathrm{fb^{-1}}$, a 5σ discovery can be extracted for masses up to $3.31\,\mathrm{TeV/c^2}$ for model ψ and up to $4.27\,\mathrm{TeV/c^2}$ for model ARLM. The 5σ discovery limits on the resonance masses for 10, 30 and $60\,\mathrm{fb^{-1}}$ are summarised in Table 14.2.

For KK Z boson production, the luminosities needed for a five σ discovery are 1.5, 4.0, 10.8, 29.4, and $81.4\,\mathrm{fb^{-1}}$ for $M = 4.0, 4.5, 5.0, 5.5$ and $6.0\,\mathrm{TeV/c^2}$, respectively; for SSM Z' boson production, they are 0.015, 3.0 and $260\,\mathrm{fb^{-1}}$ for $M = 1, 3$ and $5\,\mathrm{TeV/c^2}$; for graviton production, most of the interesting region of the (mass, coupling) plane is already covered with $10\,\mathrm{fb^{-1}}$.

For KK Z and Z' production, a K factor of 1 was conservatively taken for both the signal and the Drell–Yan background, since heavy Z production interferes with Z/γ Drell–Yan production. For the graviton analysis, as little interference is present with the Standard Model

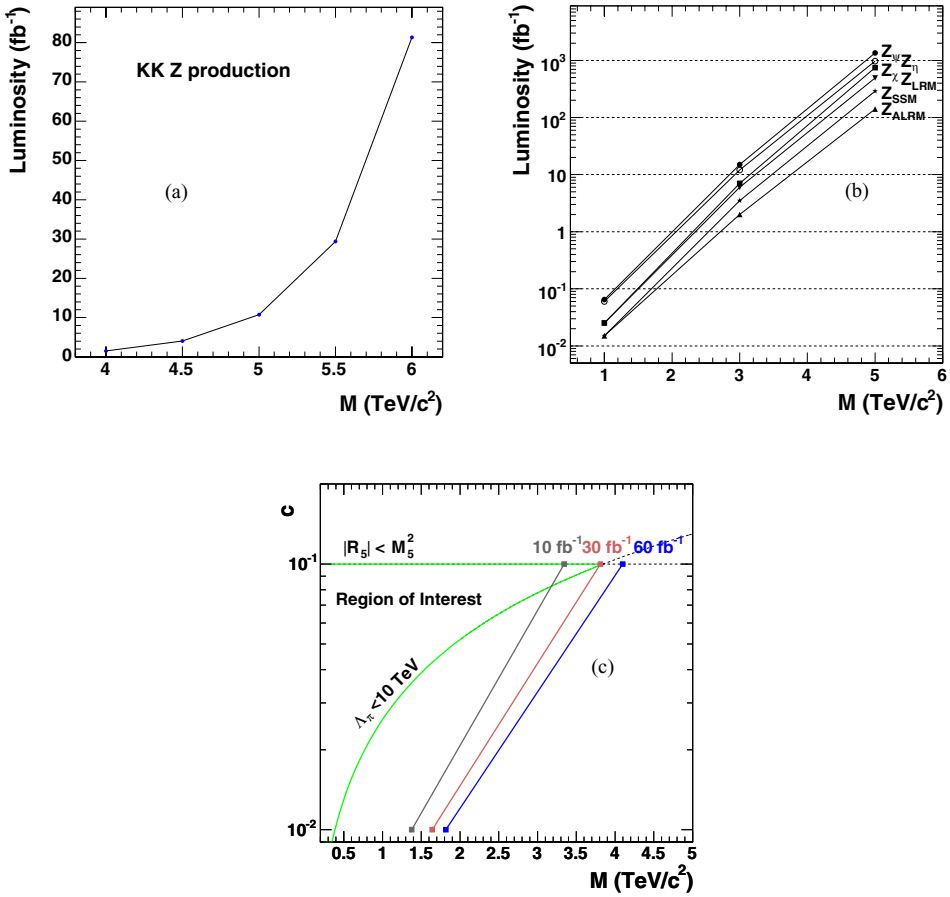

Figure 14.4. Five σ discovery limit as a function of the resonance mass for KK Z boson production (a), for the 6 Z' models (b); five σ discovery plane for graviton production as a function of the coupling parameter c and the graviton mass (c).

Table 14.2. The 5σ discovery limit on the resonance mass (given in TeV/c^2) for the three models, for an integrated luminosity of 10, 30 and 60 fb^{-1}.

Model	Luminosity (fb^{-1})		
	10	30	60
KK Z	4.97	5.53	5.88
G ($c = 0.01$)	1.38	1.64	1.82
G ($c = 0.1$)	3.34	3.81	4.10
Z' (ψ)	2.85	3.31	3.62
Z' (ALRM)	3.76	4.27	4.60

processes, a K factor of 1.0 is used for the signal and of 1.3 for the Drell–Yan background, in order to take into account the higher order terms in the cross section. The latter number comes from the CDF analysis [718] and is compatible with the K factor obtained from theoretical computations [348].

14.2.4. Systematic uncertainties

The uncertainty coming from the choice of the parton distribution function (PDF) was investigated using the set of 20 positive and 20 negative errors, of the CETQ6.1M "best fit" parametrisation [12, 719, 720]. For each event, a weight factor is computed according to the x_1, x_2, and Q^2 variables, for each of the 40 PDF errors, in the case of graviton production with $M = 1.5\,\mathrm{TeV/c^2}$ ($c = 0.01$) and $M = 3.5\,\mathrm{TeV/c^2}$ ($c = 0.1$). The uncertainties on the PDF modify the number of signal events by a factor 1.20 (positive deviations) and 0.86 (negative deviations) for $M = 1.5\,\mathrm{TeV/c^2}$ ($c = 0.01$). The corresponding numbers for $M = 3.5\,\mathrm{TeV/c^2}$ ($c = 0.1$) are 1.47 and 0.78. For the Drell–Yan background, the re-weighting effects on the numbers of events are 1.07 and 0.94 for masses around $1.5\,\mathrm{TeV/c^2}$, and 1.19 and 0.88 for masses around $3.5\,\mathrm{TeV/c^2}$. For an integrated luminosity of $30\,\mathrm{fb^{-1}}$, the significances with the "best fit" and with the positive/negative deviations are equal respectively to 6.40 and 7.25/5.78 for $M = 1.5\,\mathrm{TeV/c^2}$, and to 6.83 and 8.54/5.93 for $M = 3.5\,\mathrm{TeV/c^2}$. The main effect of the variation comes from the gluon-fusion contribution to the graviton production cross section. A lower dependence is observed for the KK Z and Z' channels, which are produced by quark-anti-quark annihilation. For KK Z boson production at $M = 4\,\mathrm{TeV/c^2}$ with an integrated luminosity of $30\,\mathrm{fb^{-1}}$, the significances with the "best fit" and with the positive/negative errors are equal respectively to 22.5 and 23.3/21.9.

Changing to 1 the value of the K factor of the Drell–Yan background for RS graviton production increases the significance from 6.39 to 6.87 ($M = 1.5\,\mathrm{TeV/c^2}$, $c = 0.01$) and from 6.83 to 7.09 ($M = 3.5\,\mathrm{TeV/c^2}$, $c = 0.1$). The discovery limits increase respectively from 1.64 to $1.68\,\mathrm{TeV/c^2}$ and from 3.81 to $3.84\,\mathrm{TeV/c^2}$.

The data themselves will be used to estimate and cross-check the Drell–Yan background at very high energy. For resonance discovery, the number of events in the side-bands of the resonance and their mass dependence will be used to estimate the number of background events under the resonance peak, provided there is enough data in the side-bands. In this approach, the uncertainties on the background cross-sections, the PDF and the luminosity measurement are highly reduced.

14.2.5. Identification of new particles

Once a resonance is found, information will be gained on its characterisation from the study of other decay channels, like $\gamma\gamma$ (see Section 14.6), of angular distributions and of asymmetries, in view of the spin determination (see also Section 14.3).

As an example, RS gravitons with spin 2 can be distinguished from the Standard Model background and Z' bosons with spin 1 using the distribution of the $\cos\theta^*$ variable, computed as the cosine of the polar angle between the electron and the boost direction of the heavy particle in the latter rest frame. In addition to the cuts defined above, the electron and positron candidates are requested to have opposite charges, in order to identify the electron, from which the $\cos\theta^*$ variable is computed.

The $\cos\theta^*$ distributions for graviton production with $M = 1.25\,\mathrm{TeV/c^2}$, $c = 0.01$ and $M = 2.5\,\mathrm{TeV/c^2}$, $c = 0.1$, are presented in Fig. 14.5, for an integrated luminosity of $100\,\mathrm{fb^{-1}}$. The error bars represent the corresponding statistical uncertainties, applied to the signal distribution obtained from a large statistics simulation. The spin-2 hypothesis is compared to the spin-1 hypothesis (dashed red curve in the figures), formed by the Drell–Yan production (Figs. 14.5a and 14.5b) or the ALRM Z' production (Figs. 14.5c and 14.5d). For graviton production, the expected background is included in the $\cos\theta^*$ distributions.

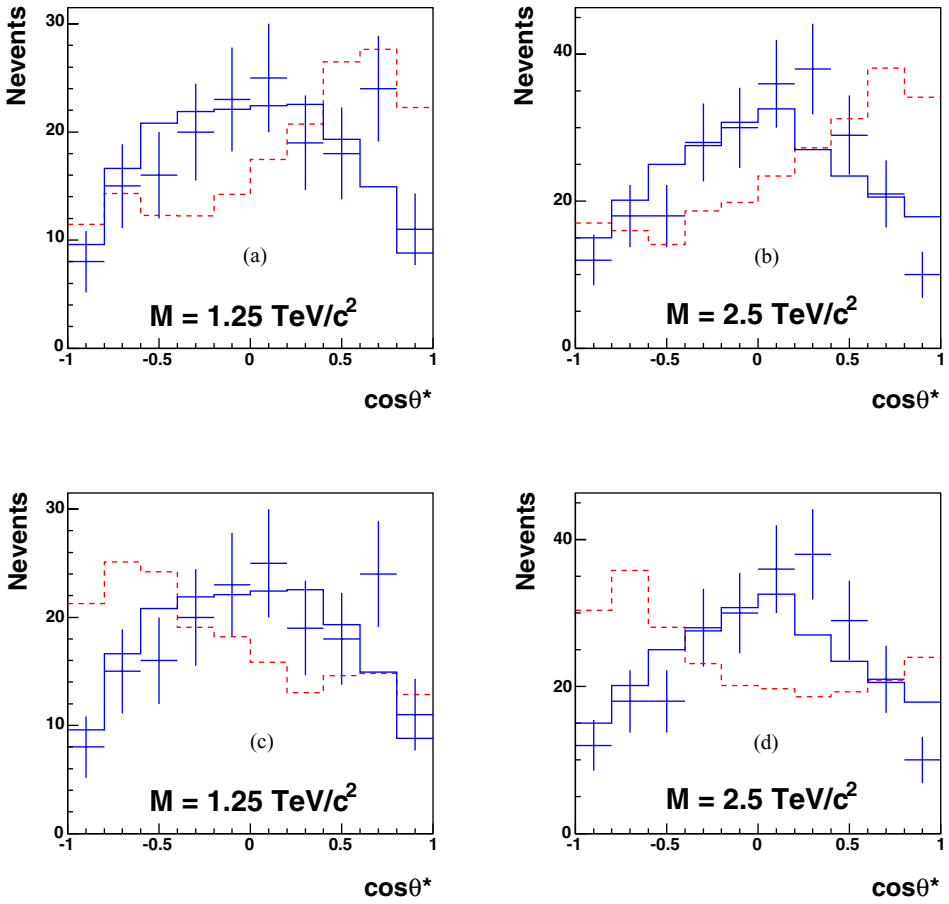

Figure 14.5. Distributions of $\cos\theta^*$ for graviton production (full blue curves) and for Drell–Yan production (dashed red curves) normalised to the signal, for $M = 1.25\,\mathrm{TeV/c^2}$ (a) and $2.5\,\mathrm{TeV/c^2}$ (b), and for Z' boson (ALRM model) (dashed red curves), normalised to the signal, for $M = 1.25\,\mathrm{TeV/c^2}$ (c) and $2.5\,\mathrm{TeV/c^2}$ (d), with an integrated luminosity of $100\,\mathrm{fb}^{-1}$. The error bars represent the "1-experiment" distribution for the graviton production. The expected background is included in the $\cos\theta^*$ distributions.

The spin 2 nature of RS gravitons can be determined in contrast to the Drell–Yan production or the Z' boson production for an integrated luminosity of $100\,\mathrm{fb}^{-1}$ up to $1.25\,\mathrm{TeV/c^2}$ for $c = 0.01$ and $2.5\,\mathrm{TeV/c^2}$ for $c = 0.1$.

14.3. High mass dimuon final states

Many scenarios beyond the Standard Model are expected to manifest themselves through modifications in the mass spectrum of high-mass dimuon pairs. The potential of the CMS experiment to discover dimuon decays of a new heavy neutral gauge boson, Z′, is discussed in Section 3.3.4; the discovery reach for a representative set of Z′ models was found to be in the range between 2.9 and $3.8\,\mathrm{TeV/c^2}$ for an integrated luminosity of $10\,\mathrm{fb}^{-1}$. In this section, we discuss the observability of $\mu^+\mu^-$ final states predicted in two classes of

large extra dimensions models, RS and ADD. While the RS scenario gives rise to relatively narrow resonances, the ADD model is expected to be observed via non-resonant modifications of the dimuon spectrum; therefore, these two searches require somewhat different experimental approaches. The search for compositeness in the dimuon channel is described in Section 15.2.

Once a new physics is discovered, observables other than dimuon invariant mass can be used to determine the theoretical framework to which it belongs. The measurement of the forward-backward asymmetries of leptonic decay products has long been known as a powerful tool to identify Z′; some aspects of such a measurement at the LHC are discussed in Section 3.3.5. Spin discrimination of new heavy resonances based on an unbinned likelihood ratio statistic incorporating the angles of the decay products is described in Section 3.3.6.

14.3.1. The Randall–Sundrum model in the dimuon channel

We consider the range of RS1 graviton masses in the range $1 < m < 4\,\mathrm{TeV/c^2}$ and the dimensionless coupling constant in the expected theoretical range $0.01 \leqslant c \leqslant 0.1$ [721]. A full simulation with PYTHIA [69] version 6.227 and with the GEANT4-based CMS program [8] and reconstruction with the CMS full-reconstruction package [10], including pile-up of minimum-bias collisions is carried out. We derive both the CMS discovery potential for Randall–Sundrum gravitons and the performance of spin determination in this channel (see details in Ref. [117]). The non-reducible backgrounds are the Drell–Yan process, vector boson pair production ZZ, WZ, WW, $t\bar{t}$ production, etc. In the SM the expected leading-order cross section of the Drell–Yan process dominates the other contributions (see the Section 9.2 for details). The trigger simulation is based on the reconstruction package, using the on-line reconstruction algorithm. We require the single or double muon trigger, no requirement for calorimeter isolation of high-p_{T} muons is made. The total trigger + reconstruction efficiency varies between 95% and 90% for dimuons in the mass range $1 < m < 4\,\mathrm{TeV/c^2}$. Only the events which passed both the Level-1 and HLT cuts are selected. Note that the trigger efficiency is significantly decreased after applying of the calorimeter isolation cuts (down to 15%). This drop is caused by electromagnetic showers accompanying high-energy muons. In the following, no cuts on calorimeter isolation of muon tracks are applied at the HLT level.

14.3.1.1. The Randall–Sundrum model discovery potential. The significance estimators used for studying the discovery potential of the RS1 model were S_{cP}, S_{cL} and S_L, defined in Appendix A.1 (see discussion of S_L in Section 3.3.4.1).

Figure 14.6a shows the integrated luminosity required for a 5σ discovery as a function of the dimuon mass. The results for different values of integrated luminosity are summarised in Table 14.3 and Fig. 14.6b. The CMS experiment can observe a RS1 graviton with mass up to $2.3\,\mathrm{TeV/c^2}$ with an integrated luminosity of $\int L\,dt = 1\,\mathrm{fb^{-1}}$ if the coupling c is equal to 0.1. For $c = 0.01$ the mass reach does not exceed $1.9\,\mathrm{TeV/c^2}$, even for the asymptotic regime of LHC operation with $\int \mathcal{L}\,dt = 300\,\mathrm{fb^{-1}}$. The asymptotic reach limit for $c = 0.1$ is $4.5\,\mathrm{TeV/c^2}$.

A combined analysis [721] in the RS1 scenario shows that the value of the coupling constant c is strongly restricted (Fig. 14.6b) due to the theoretical constraints to assure that the model does not introduce a new hierarchy (the scale parameter $\Lambda_\pi = M_{Pl}e^{kL} < 10\,\mathrm{TeV/c^2}$ with the symbols defined in Section 14.1.5). The direct comparison of results on a mass reach region for c with the data of the Fig. 14.6 shows that a luminosity of $100\,\mathrm{fb^{-1}}$ is needed to test the RS1 model everywhere in (c – M_{grav}) space of model parameters. However, these conclusions are not definitive since the initial theoretical constraints are quite arbitrary.

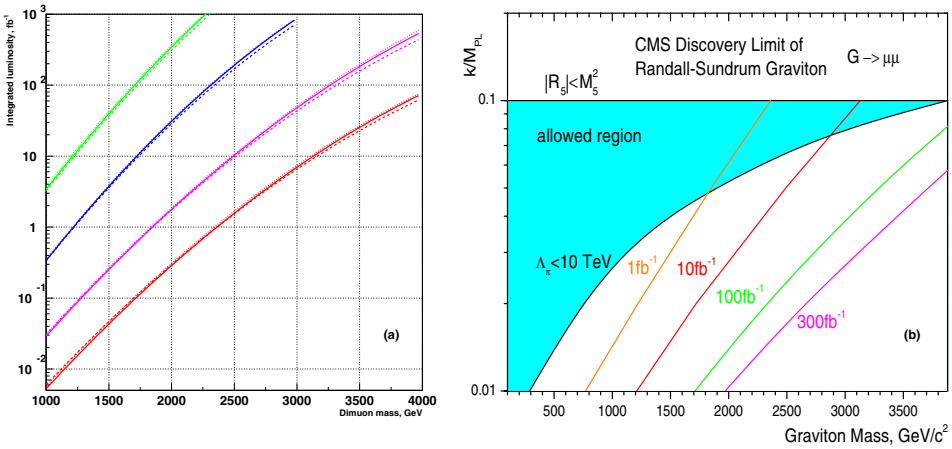

Figure 14.6. (a) Discovery limit for RS1 graviton with $\mu^+\mu^-$ decay mode for different values of RS1 coupling constant $c = 0.01, 0.02, 0.05$ and 0.1 (from top to bottom). Used discovery limit $S > 5$ for the S_{cP} estimator (solid lines), S_L (dashed lines), S_{cL} (dotted lines). (b) Reach of the CMS experiment as a function of the coupling parameter c and the graviton mass for various values of integrated luminosity. The left part of each curve is the region where significance exceeds 5σ.

Table 14.3. CMS discovery potential invariant mass reach (in TeV) to observe the RS1 graviton in $\mu^+\mu^-$ channel.

Coupling constant c	Estimator	1 fb^{-1}	10 fb^{-1}	100 fb^{-1}	300 fb^{-1}
	S_{cP}	0.75	1.20	1.69	1.95
0.01	S_{cL}	0.77	1.21	1.71	1.97
	S_L	0.78	1.23	1.73	1.99
	S_{cP}	1.21	1.72	2.30	2.63
0.02	S_{cL}	1.22	1.72	2.31	2.64
	S_L	1.22	1.74	2.34	2.68
	S_{cP}	1.83	2.48	3.24	3.67
0.05	S_{cL}	1.85	2.49	3.26	3.71
	S_L	1.85	2.51	3.31	3.79
	S_{cP}	2.34	3.11	4.12	4.52
0.1	S_{cL}	2.36	3.13	4.14	4.54
	S_L	2.36	3.16	4.23	4.73

14.3.1.2. Systematic uncertainties. The results taking into account the systematic uncertainties are shown in Fig. 14.7. The expected effects of misalignment are considered in two misalignment scenarios: the First Data and the Long Term scenarios [99], which correspond to different stages of the alignment corrections for the positions of the tracker and muon chambers. The current estimate is that the transition to the Long Term scenario can be achieved at an integrated luminosity of about 1 fb^{-1} [86]. In contrast to Fig. 14.6 which assumed a K-factor equal to unity, a K-factor of $K = 1.30 \pm 0.05$ is used both for the RS1 signal and Drell–Yan background. Additional variations due to EW corrections, hard-scale and PDF uncertainties have been considered, the details being found in Ref. [117].

14.3.1.3. Spin discrimination in angular analysis. A study of muon angular distributions allows a discrimination between the hypotheses of Graviton (spin-2 particle) and Z' (spin-1 particle) – see the discussion and the results in Section 3.3.6.

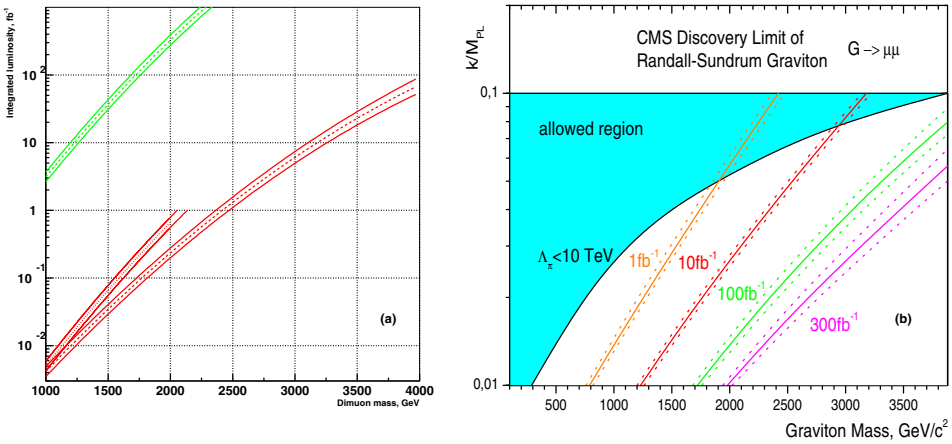

Figure 14.7. (a) Discovery limit for coupling constants $c = 0.01, 0.1$ (upper and lower curves, respectively) after taking into account the systematic uncertainties including misalignment in two scenarios: the curves ending at integrated luminosity of $1\,\text{fb}^{-1}$ correspond the First Data misalignment scenario, the other ones correspond to the Long Term scenario. The ranges show the expected variations due to the systematic uncertainties. (b) The ranges of the expected variations due to the systematic uncertainties for the mass reach of the CMS experiment.

14.3.2. The ADD model in the dimuon channel

We consider the fundamental Planck scale of the ADD model in the range of $3.0 < M_S < 10.0\,\text{TeV/c}^2$ and numbers of extra dimensions in the range of $3 \leqslant n \leqslant 6$ [698]. The contribution of KK-modes of ADD gravitons to the Drell–Yan processes is computed using the leading-order matrix element [722] which was implemented in STAGEN generator collection as external matrix element in PYTHIA [69] version 6.227. A full simulation [8] of the CMS detector and reconstruction [10], without a pile-up of minimum-bias collision is performed to derive the CMS discovery potential for ADD virtual gravitons (see details in Ref. [723]). The non-reducible backgrounds are the Drell–Yan process, vector boson pair production ZZ, WZ, WW, $t\bar{t}$ production, etc. In the SM the expected leading-order cross section of the Drell–Yan process dominates the other contributions (see Section 9.2 for details). The trigger simulation is realised in the reconstruction package, using the on-line reconstruction algorithm. A single or double muon trigger is required, but no requirement for calorimeter isolation of high-p_T muons is made. The total trigger + reconstruction efficiency varies between 70% and 90% for dimuons dependent on the model parameters. Only the events which passed both the Level-1 and HLT cuts are selected.

14.3.2.1. The ADD discovery limit. The CMS discovery potential was estimated using as significance S_{cP} and S_{cL}, defined in Appendix A.1. The computed significance values for the ideal detector as a function of a fundamental theory scale, M_S, are presented in Fig. 41.8 for integrated luminosities of 0.1, 1.0, 10, 100, 300, $1000\,\text{fb}^{-1}$. The main observations are:

- $\int \mathcal{L}\text{d}t = 1\,\text{fb}^{-1}$, even a low luminosity regime allows us to measure the effect from the virtual contributions of ADD gravitons to Drell–Yan process for an effective fundamental Planck scale up to 4.0 TeV for the most unfavourable case with $n = 6$. For a scenario where the number of extra dimensions is $n = 3$ the reach limit is extended to 5.8 TeV.
- $\int \mathcal{L}\text{d}t = 10\,\text{fb}^{-1}$, M_S values of 4.8 and 7.2 TeV can be reached for $n = 3$ and $n = 6$ respectively.

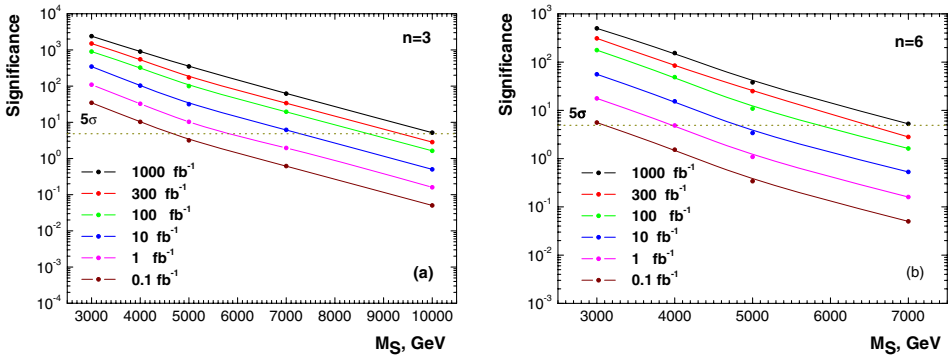

Figure 14.8. Significance as a function of M_S for (a) $n = 3$ and (b) $n = 6$.

- $\int \mathcal{L} dt = 100\,\text{fb}^{-1}$, for LHC operation in a high luminosity regime allow the observation of the ADD signal at $5.8 \div 8.7$ TeV of model scale dependent on a number of extra dimensions.
- $\int \mathcal{L} dt = 300\,\text{fb}^{-1}$, in the asymptotic regime the CMS sensitivity to fundamental Planck scale is increased to values of $6.5 \div 9.3$ TeV.

14.3.2.2. Systematics. The results taking into account the systematical uncertainties with the S_{cP} estimator are shown in Fig. 14.8. To take into account the misalignment effect two scenario of misalignment were considered during reconstruction procedure: *First Data* scenario [99] for 0.1 and $1.0\,\text{fb}^{-1}$ and *Long Term* scenario [99] for 10, 100, 300, $1000\,\text{fb}^{-1}$. The K-factor of $K = 1.30 \pm 0.05$ is used both for ADD signal and Drell–Yan background. Additional variations due to hard-scale and PDF uncertainties as well as trigger and selection uncertainties have been considered, the details being given in Ref. [723].

14.4. High energy single lepton final states

14.4.1. Introduction

Several theoretical models predict, in addition to the well known electroweak vector bosons γ, W, Z, further heavy gauge bosons. These additional particles are postulated for example in Left–Right Symmetric Models [724–727], based on the gauge group $\text{SU(3)}_\text{C} \times \text{SU(2)}_\text{L} \times \text{SU(2)}_\text{R} \times \text{U(1)}_{\text{B}-\text{L}}$ (B, L: baryon-, lepton-number) in theories predicting a substructure of the known "elementary particles", and in Little Higgs Models [91].

Here we investigate the detection capabilities for a hypothetical heavy partner of the W, a charged spin-1 boson W'. We do not assume one of the specific models mentioned above, but derive the W' properties from the Reference Model by Altarelli [697], which has been used in several earlier experiments, so that the resulting limits can be compared easily. In this Reference Model the W' is a carbon copy of the W, with the very same left-handed fermionic couplings (including CKM matrix elements), while there is no interaction with the Standard Model gauge bosons or with other heavy gauge bosons as a Z'. Thus the W' decay modes and corresponding branching fractions are similar to those for the W, with the notable exception of the $\text{t}\bar{\text{b}}$ channel, which opens for W' masses beyond 180 GeV.

In hadron collisions W' bosons can be created through $q\bar{q}$ annihilation, in analogy to W production. Previous searches for the Reference W' at LEP and at the Tevatron give rise to lower bounds approaching 1 TeV [728].

This analysis is based on the decay $W' \to \mu\nu$, with a branching ratio of roughly 10%. The resulting signature of a high energy muon accompanied by missing energy allows an easy separation of signal and background reactions. More details are found in [729].

14.4.2. Data samples

For this study we assume an integrated luminosity of $10\,\text{fb}^{-1}$ and an average instantaneous luminosity of $\mathcal{L} = 2 \times 10^{33}\,\text{cm}^{-2}\,\text{s}^{-1}$ corresponding to an average pile-up of 3.5 pp-collisions per bunch crossing.

Reference Model W' events decaying into muon and neutrino have been generated with PYTHIA v6.227 [69], based on the leading order cross section and the parton density functions CTEQ 5L (leading order) [719]. In total about 300 000 events have been produced for W' masses between 1 TeV and 8 TeV. The product of LO cross section and branching fraction varies between 3.0×10^3 fb (1 TeV) and 3.3×10^{-4} fb (8 TeV), to be compared with 1.7×10^7 fb for Standard Model W production and muonic decay. The detector response was simulated with the full CMS simulation [8] and reconstruction [10] software. Both the signal events and the following background samples were analysed: $\text{W} \to \mu\nu$, $Z \to \mu\mu$, WW inclusive, ZZ inclusive, ZW inclusive, $t\bar{t}$ inclusive. These data sets have been produced in the CMS Data Challenge 2004. On average 3.5 minimum bias reactions have been overlaid to each event.

14.4.3. Event selection and analysis

Events have been preselected requiring at least one globally reconstructed muon which pass the trigger criteria.

The final cuts to select $W' \to \mu\nu$ candidate events are:

- muon quality: at least 13 hits along the global track, $\chi^2/N_{dof} < 50$ for the fit;
- single muon requirement;
- muon isolation: no additional track ($p_\text{T} > 0.8\,\text{GeV}$) within a cone of size $\Delta R = 0.17$.

These cuts have been chosen to maximise the signal/background ratio.

For the selected events the transverse mass

$$M_\text{T} = \sqrt{2 p_{\text{T}_\mu} E_\text{T}^\text{miss} (1 - \cos \Delta\phi_{\mu, E_\text{T}^\text{miss}})}$$

is calculated from the muon transverse momentum p_{T_μ}, the missing energy component in the transverse plane E_T^miss and the angular $\Delta\phi_{\mu, E_\text{T}^\text{miss}}$ between both in this plane. Figure 14.9 shows the resulting distribution for signal (1 and 5 TeV) and background events. The W' boson distributions show a Jacobian peak which is spread out for large M_T due to the detector resolution. It can be seen immediately, that a 1 TeV boson can be discovered or excluded easily, while for higher masses a statistical analysis is needed to quantify the sensitivity.

14.4.4. Discovery and exclusion potential

To interpret the results, the CL_s method [508] is applied, which is based on the likelihood ratios, calculated for all bins of the M_T distribution. CL_s is defined as ratio of the confidence levels for the signal and background hypotheses, $\text{CL}_\text{s} = \text{CL}_{\text{s+b}}/\text{CL}_\text{b}$.

Figure 14.10 shows, that for an integrated luminosity of $10\,\text{fb}^{-1}$, a limit of 4.7 TeV at the 95% CL is reachable, if no signal is present in the CMS data. Both the expected discovery and exclusion limits are displayed in Fig. 14.11 as a function of integrated luminosity and W' mass. To investigate the sensitivity to the signal and background cross sections, they have been varied in a wide range; relative changes by factors of 2 and 10, respectively, lead to a lowering of the accessible mass range by about 0.5 TeV in the worst case.

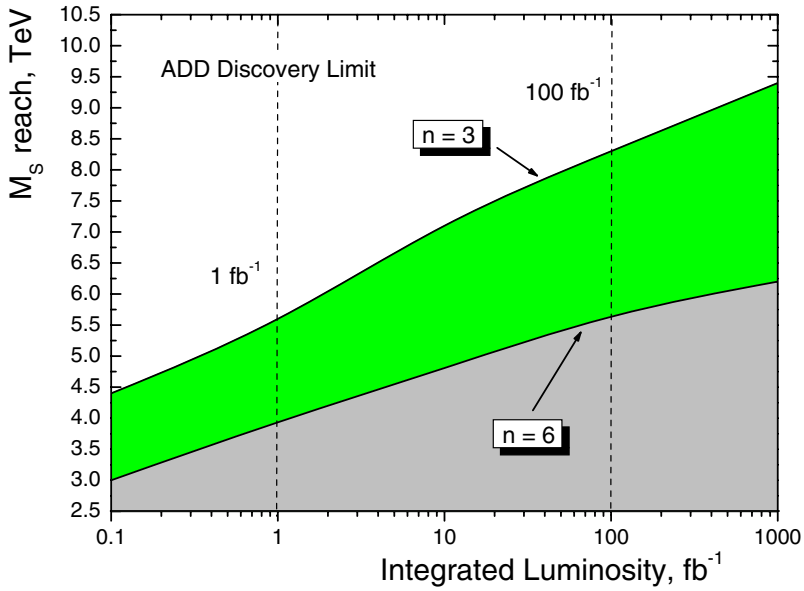

Figure 14.9. 5σ limit on M_S for the number of extra dimensions $n = 3$ and 6.

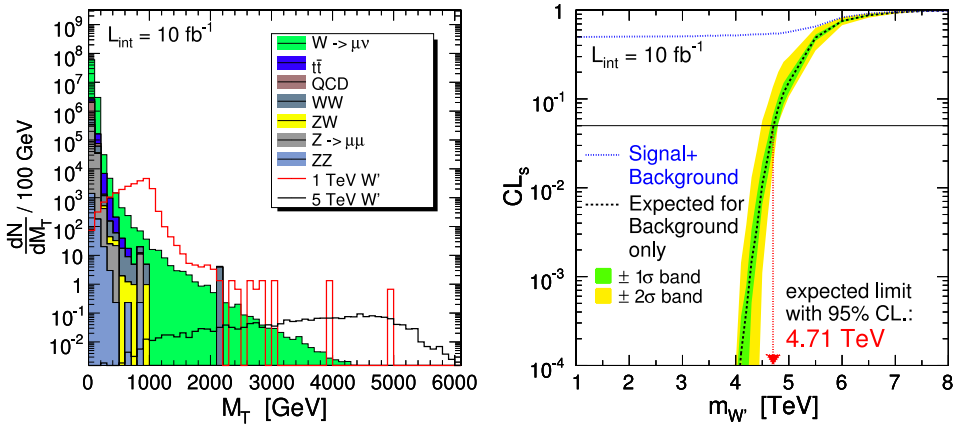

Figure 14.10. (Left) transverse invariant mass spectrum of signal (1 and 5 TeV, non-stacked) and background (stacked) after applying the selection cuts. (Right) result of the CL_s-method: with an integrated luminosity of 10 fb^{-1}. Reference W' bosons can be excluded up to a mass of 4.7 TeV.

14.4.5. Systematic uncertainties

The uncertainties arising from an imperfect knowledge of the PDFs at LHC energies and the error from the hard scale parameters have been investigated by using the Les Houches Accord PDFs [95] and varying the hard scale, respectively. The relative errors on the cross-section of the signal are listed in Table 14.4. The error on the background is comparable to that of the W' at the corresponding invariant mass.

The steep falling invariant mass distribution especially of the W background holds a potential danger for the detection of W' bosons: if only a small fraction of these events is

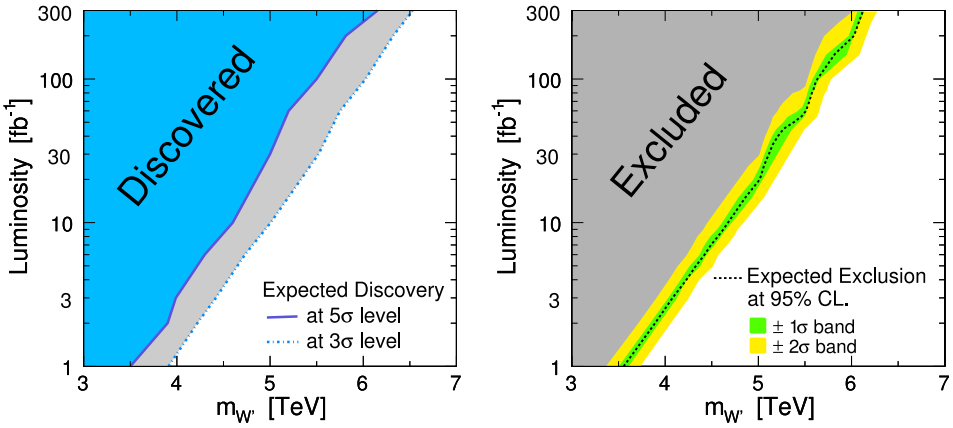

Figure 14.11. The plots show which integrated luminosity is needed to discover (left) or exclude (right) W' bosons of a certain mass.

Table 14.4. Relative systematic uncertainties in percent, arising from an imperfect theoretical knowledge (parton density functions, hard scale) and the expected luminosity error for an integrated luminosity of 10 fb^{-1}.

	Systematic Uncertainties				
Type	1 TeV W'	2 TeV W'	3 TeV W'	4 TeV W'	5 TeV W'
PDF $\Delta\sigma/\sigma$	$^{+3.6}_{-4.3}$	$^{+6.8}_{-5.9}$	$^{+6.2}_{-8.3}$	$^{+17.1}_{-10.6}$	$^{+33.7}_{-18.9}$
Hard Scale $\Delta\sigma/\sigma$	$^{+4.1}_{-4.1}$	$^{+7.5}_{-6.9}$	$^{+10.4}_{-9.2}$	$^{+13.1}_{-10.3}$	$^{+14.8}_{-12.7}$
Luminosity $\Delta\mathcal{L}/\mathcal{L}$	$\pm5\%$	$\pm5\%$	$\pm5\%$	$\pm5\%$	$\pm5\%$

reconstructed with a by far too large mass, which might result from a mis-measured muon momentum, the detection of a W' becomes extremely difficult. Such a behaviour would be visible in non-gaussian tails for example in the p_{T} resolution distribution. Using a large sample of a W events it could be demonstrated, that the alignment precision expected after an integrated luminosity of 10 fb^{-1} has only a small influence on the non-gaussian tails of the muon p_{T} resolution distribution.

The luminosity uncertainty at the considered integrated luminosity of 10 fb^{-1} is expected to be 5%, while other experimental errors (neutron background, dead detector components, etc.) are expected to be negligible.

14.4.6. Summary

For an integrated luminosity of 10 fb^{-1}, W' bosons of the Reference Model can be discovered or excluded up to a mass of 4.5–5 TeV, from an analysis of the muonic decay mode.

14.5. High mass dijet final states

14.5.1. Dijet resonances and contact interactions

Dijet resonances and contact interactions are the two major signals of new physics with dijets. Dijet resonances are direct and compelling observations of a new physical object at a mass M, requiring an incoming parton-parton collision energy equal to the mass. Contact interactions

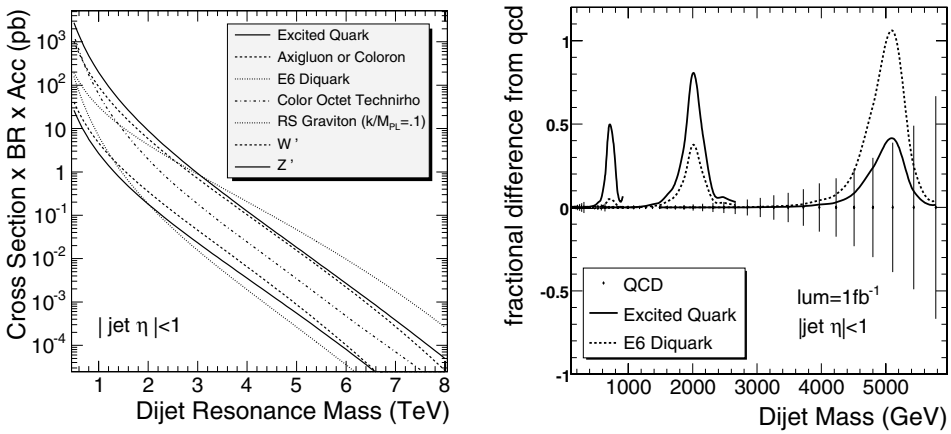

Figure 14.12. (Left) The total cross section times branching ratio times acceptance for dijet resonances from eight different models (see text). (Right) For resonance masses of 0.7, 2.0, and 5.0 TeV/c^2, the fractional difference between an excited quark (solid curve) or an E6 diquark (dashed curve) and the QCD dijet background is compared to the QCD statistical errors (vertical lines).

(discussed in Section 15.3) are indirect observations of an energy scale of new physics, Λ, which can be significantly larger than the available collision energy. Resonances are clear signals but contact interactions are often observed first.

14.5.2. Dijet resonance search

We search for processes producing narrow resonances, X, decaying to dijets: $pp \to X \to$ jet + jet (inclusive) [730]. Our experimental motivation is that LHC is a parton-parton collider, and resonances made from partons must decay to the same partons giving two jets in the final state. The theoretical motivation is broad, since there are many models that predict narrow dijet resonances.

14.5.2.1. Dijet resonance models. In Fig. 14.12 we show the cross section times branching ratio times acceptance calculated to lowest order for eight benchmark models. Here we introduce them in order of descending cross section at low mass. Excited states of composite quarks [731] are strongly produced giving large cross sections ($qg \to q^*$). Axigluons (A) [732] or colorons (C) [733] from an additional colour interaction are also strongly produced, but require an anti-quark in the initial state ($q\bar{q} \to A$ or C) slightly reducing the cross section compared to excited quarks. Diquarks [734] from superstring inspired E_6 grand unified models are produced with electromagnetic coupling from the valence quarks of the proton ($ud \to D$). The cross section for E_6 diquarks at high mass is the largest of all the models considered, because at high parton momentum the probability of finding a quark in the proton is significantly larger than the probability of finding a gluon or anti-quark. Colour octet technirhos [735] from topcolour-assisted technicolour are produced for either gluons or quark-anti-quark pairs in the initial state through a vector-dominance model of mixing between the gluon and the technirho ($q\bar{q}, gg \to g \to \rho_{\mathrm{T8}}$). Randall–Sundrum gravitons [94] from a model of large extra dimensions are produced with a significant cross section at masses below 1 TeV/c^2 primarily from gluons in the initial state ($q\bar{q}, gg \to G$). Heavy W bosons [736] inspired by left-right symmetric grand unified models have electroweak couplings and

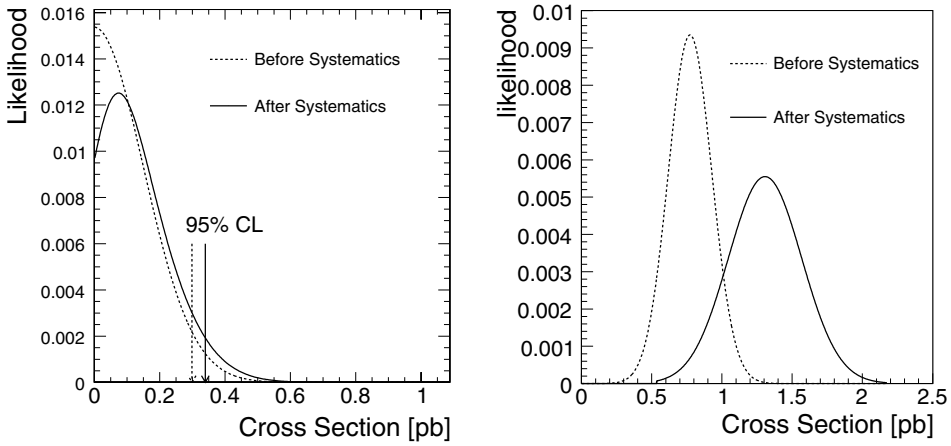

Figure 14.13. Likelihoods for observing a narrow dijet resonance of mass 2 TeV/c^2 in a 1 fb^{-1} data sample that contains only QCD background (left) and a data sample that also contains a resonance with a significance of 5σ (right) are shown with statistical uncertainties only (dashed) and including systematics (solid).

require anti-quarks for their production ($q_1\bar{q}_2 \to W'$) giving small cross sections. Heavy Z bosons [736] inspired by grand-unified models are widely anticipated by theorists, but they are weakly produced, and require an anti-quark in the initial state ($q\bar{q} \to Z'$), so their production cross section is around the lowest of the models considered. Lower limits from CDF [120] and D0 [121] on the mass of these models range from 0.4 to 1.0 TeV/c^2.

14.5.2.2. Dijet resonance sensitivity estimates. The signal and background dijet mass distributions for narrow resonances were presented in Section 4.1.4. In Fig. 14.12 we demonstrate the size of the signal for excited quarks and E_6 diquarks compared to the QCD background and it's statistical uncertainty. It is clear that we will be sensitive to such large signals for strongly produced dijet resonances. Here we quantify our sensitivity to any model of narrow dijet resonances. In Fig. 14.13 we show examples of likelihoods for excluding or observing a narrow resonance signal on a QCD background as a function of the signal cross section. In the case where the observed sample is QCD only, the signal likelihood peaks around zero cross section, and the 95% CL excluded signal cross section is shown. In the case where the observed sample is QCD plus a resonance signal, we have varied the signal size until the Gaussian distributed likelihood is 5σ above zero. In Fig. 14.13 we have included estimates of our systematic uncertainties. For a resonance mass of 0.7 (5.0) TeV/c^2 the systematic uncertainty on the observable signal cross section due to the jet energy uncertainty in the background rate is 15% (25%), the uncertainty due to jet resolution in the resonance shape is 10% (10%), the uncertainty due to radiation's affect on the resonance shape is 10% (25%), and the uncertainty due to luminosity is 10% (10%). For resonance masses just above the dijet mass thresholds where the trigger prescale decreases, there is an additional systematic uncertainty from the jet energy uncertainty. Systematic uncertainties have a greater effect on discovery than exclusion, because exclusions occur at a smaller signal cross section and are dominated by statistical uncertainties.

Figure 14.14 demonstrates that the 95% CL exclusion and 5σ discovery signal cross sections, including statistical uncertainties only, have reasonable values when compared to the size of the QCD statistical errors. Also in Fig. 14.13 we present the resonance cross

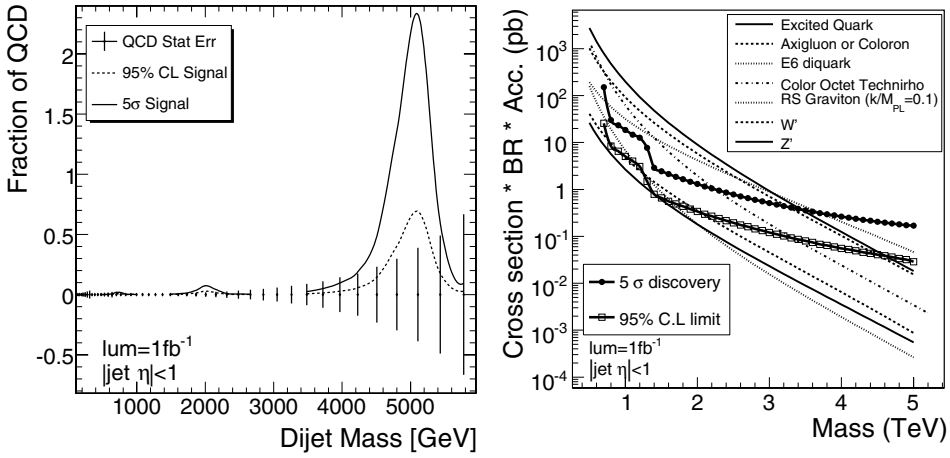

Figure 14.14. (Left) For resonances of mass 0.7, 2.0 and 5.0 TeV/c^2, the rate as a fraction of QCD that CMS expects to exclude (dashed) or discover (solid) including statistical uncertainties only. (Right) The resonance cross section that CMS expects to exclude (boxes) or discover (circles), including systematic uncertainties, is compared to the cross section for eight resonance models.

Table 14.5. Sensitivity to dijet resonances with 100 pb^{-1}, 1 fb^{-1} and 10 fb^{-1}. For each resonance model, we show the range of masses we expect to be able to exclude at a confidence level of 95% or greater, and the range of masses we expect to be able to discover with a significance of 5σ or greater. All estimates are with both statistical and systematic uncertainties.

Resonance Model	95% CL Excluded Mass (TeV/c^2)			5σ Discovered Mass (TeV/c^2)		
	100 pb^{-1}	1 fb^{-1}	10 fb^{-1}	100 pb^{-1}	1 fb^{-1}	10 fb^{-1}
Excited Quark	0.7–3.6	0.7–4.6	0.7–5.4	0.7–2.5	0.7–3.4	0.7–4.4
Axigluon or Colouron	0.7–3.5	0.7–4.5	0.7–5.3	0.7–2.2	0.7–3.3	0.7–4.3
E_6 diquarks	0.7–4.0	0.7–5.4	0.7–6.1	0.8–2.0	0.8–3.7	0.8–5.1
Colour Octet Technirho	0.7–2.4	0.7–3.3	0.7–4.3	0.7–1.5	0.7–2.2	0.7–3.1
Randall–Sundrum	0.7–1.1	0.7–1.1	0.7–1.1			
Graviton		1.3–1.6	1.3–1.6	N/A	N/A	N/A
			2.1–2.3			
W′	0.8–0.9	0.8–0.9	0.8–1.0	N/A	N/A	N/A
		1.3–2.0	1.3–3.2			
Z′	N/A	N/A	2.1–2.5	N/A	N/A	N/A

section values for jet $|\eta| < 1$ that CMS can expect to exclude at 95% CL or discover at 5σ significance for an integrated luminosity of 1 fb^{-1}. These can be compared with the cross section of any model of narrow dijet resonances, and here we compare with our benchmark models. From Fig. 14.14 we can read off the mass limits or discoveries that are possible with 1 fb^{-1} of data, which are listed in Table 14.5 along with the results of repeating the same analysis for 100 pb^{-1} and 10 fb^{-1}. The resonances that are produced via the colour interaction (excited quarks, axigluons, colorons and colour octet technirhos) or from the valence quarks of each proton (E_6 diquarks) have large cross sections and can be discovered up to a mass of a few TeV. A single search for resonances in the dijet mass distribution provides CMS with a sensitive test of many different models of the widely anticipated New Physics at the TeV scale.

14.6. High mass diphoton final states

14.6.1. Introduction

The study of the Randall–Sundrum (RS) graviton decaying into the two photons is particularly interesting as the detection of such few $\mathrm{TeV/c^2}$ mass resonance in such channel together with its observation in the dilepton channel will sign a RS graviton, distinguishing it from a Z′ production. The model is governed by two parameters: the graviton mass M and its coupling to Standard Model particles c, the latter being related to the natural width of the resonance.

14.6.2. Event generation and kinematics pre-selection

The search for the $\mathrm{G} \to \gamma\gamma$ signal at LHC is affected by four types of backgrounds:

- The prompt diphoton production from the quark annihilation and gluon fusion diagrams, which provides an intrinsic or 'irreducible' background.
- The γ + jets production consisting of two parts: i) prompt photon from hard interaction + the second photon coming from the outgoing quark due to final state radiation and ii) prompt photon from hard interaction + the decay of a neutral hadron (mostly isolated π^0) in a jet, which could fake a real photon.
- The background from QCD hadronic jets, where electromagnetic energy deposits result from the decay of neutral hadrons (especially isolated π^0s) in both jets.
- Drell–Yan process with e^+e^- in a final state which could mimic photons when correspondent electron tracks will not be assigned to the superclusters during the reconstruction.

Generator-level pre-selection and parameters used for QCD and bremsstrahlung backgrounds is described in [737].

14.6.3. Offline selection and analysis

The requirements for the analysis were as follows:

1 Two super-clusters (SCs) with $E_\mathrm{T} > 150\,\mathrm{GeV}$ and two HLT trigger bits triggered at the same time: 2p (two photons) and r2p (two photons relaxed).
2 Calorimeter isolation criteria: for each SC the energy in a cone of $\Delta R = 0.5$ (excluding SC itself) should be $< 0.02 E_\mathrm{T}(SC)$
3 $E(HCAL)/E(ECAL) < 0.05$
4 Tracker isolation: the sum of the energy of all tracks in a cone $\Delta R = 0.5$ around the SC should be $< 0.01 E_\mathrm{T}(SC)$
5 Photon energy corrections are done in a simple way so far:
   - For E1 energy $< 1.7\,\mathrm{TeV}$, only a simple energy dependent part of correction is applied (just a shift of the peak).
   - For E1 energy $> 1.7\,\mathrm{TeV}$, the MGPA saturation correction (1d) was applied (see and [738]).

14.6.4. K-factors

To produce the final results and to calculate the expected statistical significance for RS-1 graviton search recently calculated next-to-leading order corrections (K factors) to the cross sections of different types of background are used: $\mathrm{K} = 1.5$ for quark annihilation [26], $\mathrm{K} = 1.2$ for gluon fusion [29], $\mathrm{K} = 1$ for the γ + hadronic jets [29] and $\mathrm{K} = 1$ for QCD jets. For signal, a conservative $\mathrm{K} = 1$ value is taken.

Table 14.6. Number of events passed through the analysis cuts defined above for $M_G = 1.5\,\mathrm{TeV/c^2}$, $c = 0.01$ and $\mathcal{L} = 30\,\mathrm{fb^{-1}}$. Leading column is non-saturated events, all saturated events, passed through the analysis, were added in brackets, where applied.

	signal	Born (K = 1.5)	Box (K = 1.2)	Brem (K = 1)	QCD (K = 1)	DY (K = 1)
trigger + 2SC	28.9	8.6	0.10	29.2	798.7	4.3
+ EM isolation	24.5	5.5	0.08	20.3	361.8	3.5
+ HCAL/ECAL	24.3	5.4	0.08	4.4	12.8	3.5
+ tracker isolation	17.6	4.2(+0.2)	0.05	0.17	0.0	0.0

Table 14.7. Number of events passed through the analysis cuts defined above for $M_G = 3.5\,\mathrm{TeV/c^2}$, $c = 0.1$ and $\mathcal{L} = 30\,\mathrm{fb^{-1}}$. Leading column is non-saturated events, all saturated events, passed through the analysis, were added in brackets, where applied.

	signal	Born (K = 1.5)	Box (K = 1.2)	Brem (K = 1)	QCD (K = 1)	DY (K = 1)
trigger + 2SC	11.6	0.20	$4.4 * 10^{-4}$	0.78	821.9	0.10
+ EM isolation	10.8	0.14	$3.6 * 10^{-4}$	0.32	164.4	0.095
+ HCAL/ECAL	10.6	0.13	$3.4 * 10^{-4}$	0.016	0.0	0.095
+ tracker isolation	8.9(+1.0)	0.10(+0.02)	$2.7(+0.24) * 10^{-4}$	$1.7 * 10^{-3}$	0.0	$7.2 * 10^{-4}$

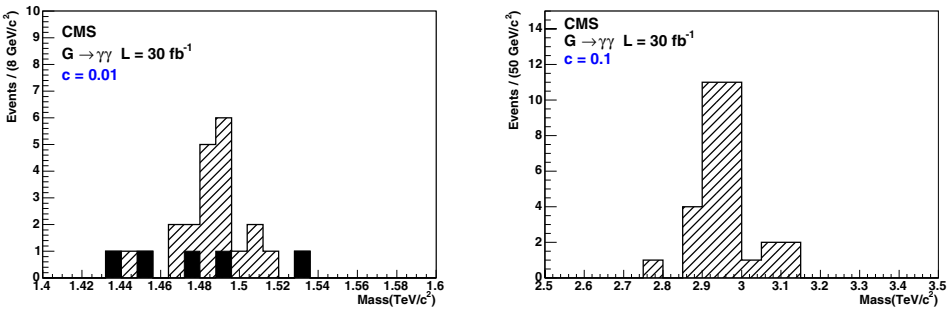

Figure 14.15. Number of events passing all cuts for ($1.5\,\mathrm{TeV/c^2}$, 0.01) (left) and ($3.0\,\mathrm{TeV/c^2}$,0.1) (right) RSI gravitons for $30\,\mathrm{fb^{-1}}$ integrated luminosity.

14.6.5. Results

The numbers of events passing the analysis cuts described above, for the signal and for the backgrounds, are presented in Table 14.6 ($1.5\,\mathrm{TeV/c^2}$, 0.01) and in Table 14.7 ($3.5\,\mathrm{TeV/c^2}$, 0.1).

Figure 14.15 shows the number of events satisfying all cuts for both signal and backgrounds for the cases ($1.5\,\mathrm{TeV/c^2}$, 0.01) and ($3.0\,\mathrm{TeV/c^2}$, 0.1) after $30\,\mathrm{fb^{-1}}$ luminosity. The results for one year low luminosity of $10\,\mathrm{fb^{-1}}$ are presented in Fig. 14.16.

Taking into account the K-factors described above, the number of events for signal and background and the significance S_{cL} (defined in Appendix A.1) for $c = 0.01$ and $c = 0.1$ are shown respectively in Tables 14.8 and 14.9 for an integrated luminosity of $30\,\mathrm{fb^{-1}}$.

The significance as a function of the graviton mass (M_G) for integrated luminosities of $10\,\mathrm{fb^{-1}}$, $30\,\mathrm{fb^{-1}}$ and $60\,\mathrm{fb^{-1}}$ are displayed in Fig. 14.17.

The discovery region in the plane of the coupling parameter c and the graviton mass is shown in Fig. 14.18.

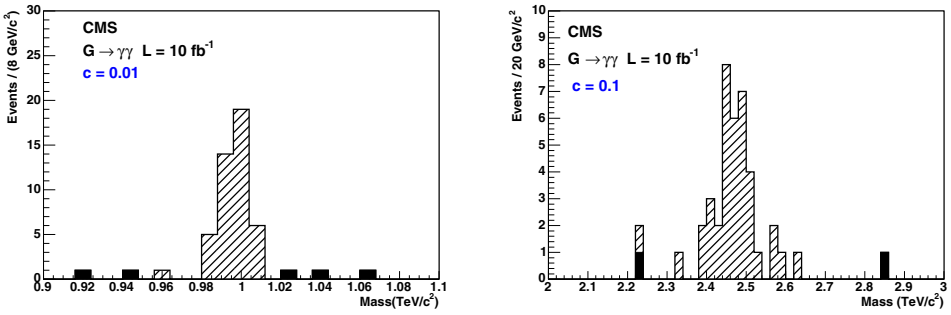

Figure 14.16. Number of events passing all cuts for ($1.0\,\mathrm{TeV/c^2}$, 0.01) (left) and ($2.5\,\mathrm{TeV/c^2}$,0.1) (right) RS-1 gravitons for $10\,\mathrm{fb}^{-1}$ integrated luminosity.

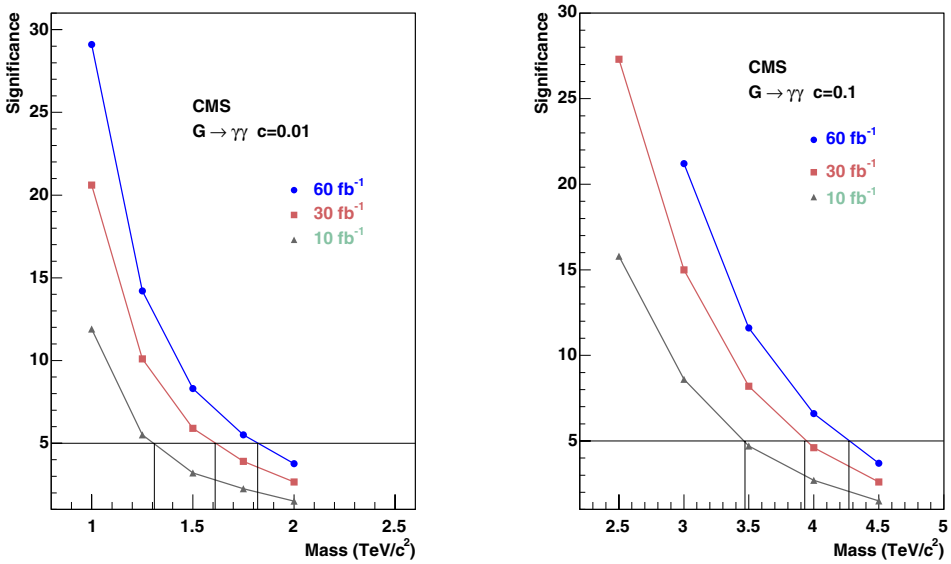

Figure 14.17. Significance as a function of the graviton mass for $10\,\mathrm{fb}^{-1}$, $30\,\mathrm{fb}^{-1}$ and $60\,\mathrm{fb}^{-1}$ integrated luminosities, with c = 0.01 (left) and c = 0.1 (right).

Table 14.8. Significance for $c = 0.01$ and $\mathcal{L} = 30\,\mathrm{fb}^{-1}$.

	$M_G = 1.0$ TeV/c^2	$M_G = 1.25$ TeV/c^2	$M_G = 1.5$ TeV/c^2	$M_G = 1.75$ TeV/c^2	$M_G = 2.0$ TeV/c^2
N_s	135.8	44.0	17.6	7.3	3.9
N_{bkg}	15.0	8.8	4.6	1.8	1.2
Significance	20.6	10.1	5.9	3.9	2.6

Table 14.9. Significance for $c = 0.1$ and $\mathcal{L} = 30\,\mathrm{fb}^{-1}$.

	$M_G = 2.5$ TeV/c^2	$M_G = 3.0$ TeV/c^2	$M_G = 3.5$ TeV/c^2	$M_G = 4.0$ TeV/c^2	$M_G = 4.5$ TeV/c^2
N_s	103.8	31.6	9.9	3.44	1.11
N_{bkg}	1.11	0.35	0.13	0.06	0.02
Significance	27.3	15.0	8.2	4.6	2.6

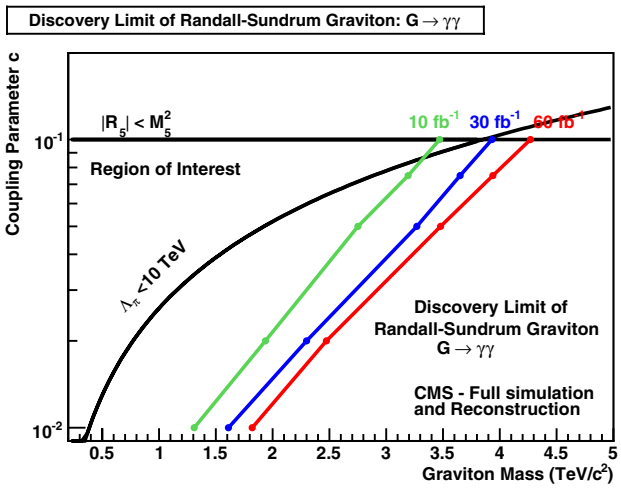

Figure 14.18. Reach of the CMS experiment in the search for the Randall–Sundrum graviton decaying into diphoton channel as a function of the coupling parameter c and the graviton mass for $10\,\text{fb}^{-1}$, $30\,\text{fb}^{-1}$ and $60\,\text{fb}^{-1}$. The left part of each curve is the region where the significance exceeds 5σ.

Table 14.10. Hard scale confidence limits uncertainties for $30\,\text{fb}^{-1}$.

	$4\hat{s}$	$0.25\hat{s}$
$c = 0.01$	$-62\,\text{GeV/c}^2$	$+56\,\text{GeV/c}^2$
$c = 0.1$	$-47\,\text{GeV/c}^2$	$+42\,\text{GeV/c}^2$

The discovery region for $60\,\text{fb}^{-1}$ extends to $M_G = 1.82\,\text{TeV/c}^2$ if $c = 0.01$ and to $M_G = 4.27\,\text{TeV/c}^2$ if $c = 0.1$. For $30\,\text{fb}^{-1}$ it is $M_G = 1.61\,\text{TeV/c}^2$ if $c = 0.01$ and $M_G = 3.95\,\text{TeV/c}^2$ if $c = 0.1$. For $10\,\text{fb}^{-1}$ it reaches to $M_G = 1.31\,\text{TeV/c}^2$ if $c = 0.01$ and $M_G = 3.47\,\text{TeV/c}^2$ if $c = 0.1$.

14.6.6. Systematic uncertainties for 30 fb^{-1}

Several systematic uncertainties and their effect on the mass reach have been evaluated for an integrated luminosity of $30\,\text{fb}^{-1}$. The effect of hard scale uncertainties is given in Table 14.10, computed by multiplying and dividing the scale $\hat{s}$ by a factor 2. The uncertainties from the pdfs, computed with LHAPDF, amount for $c = 0.01$ to $-55\,\text{GeV/c}^2$ and for $c = 0.1$ to $-152\,\text{GeV/c}^2$. There is another source of uncertainties due to the fact, that we have used K-factor = 1.5 for the Born process, while the most recent measurements at the Tevatron pointed to a K-factor closer to 2 [739]. The effect of such a change on the mass reach is $-50\,\text{GeV/c}^2$ for $c = 0.01$ and $-30\,\text{GeV/c}^2$ for $c = 0.1$.

14.7. Single γ final state with E_T^{miss} from extra dimensions

14.7.1. Topology of single-photon final states

An introduction to the signals involving direct graviton emission in ADD type of extra dimensions frameworks is given is Section 14.3.2. The topology of single photon events can

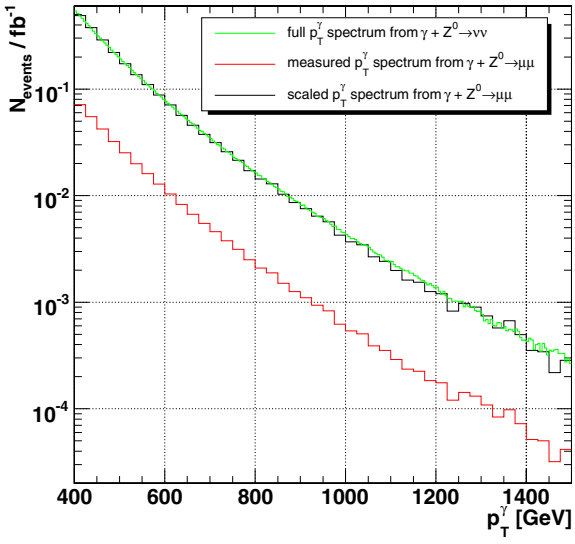

Figure 14.19. Number of expected p_T^γ events per 25 GeV bin at 1 fb^{-1} from measured γ+$Z^0 \to \mu^+\mu^-$ events before and after transformation compared with the generator distribution for γ+$Z^0 \to \nu_i\bar{\nu}_i$ – the transformed muon distribution models the $\nu_i\bar{\nu}_i$ spectrum well.

be identified by:

- a single high p_T photon in the central η region;
- high missing p_T back-to-back to the photon in the azimuthal plane with a similar p_T distribution.

These characteristics are not strongly dependent on the ADD model parameters. The details of this analysis can be found in [740].

14.7.2. Backgrounds from the Standard Model

All signal and background samples used in the following were simulated using the CMS fast detector simulation [11]. Fully simulated reference samples were generated for the signal and the largest irreducible background, $Z^0\gamma \to \nu\bar{\nu}+\gamma$. A detailed comparison of the resolution, efficiency and purity of all reconstructed objects used in this analysis to the GEANT-based CMS simulation confirmed that the fast simulation provides a very good approximation of the expected detector response. All samples were consistently generated using a generator level cut in PYTHIA $\hat{p}_T > 400$ GeV. The backgrounds considered in the study are, $Z^0\gamma \to \nu\bar{\nu}+\gamma$, $W^\pm \to \ell\nu$ where ℓ is electron, muon or tau, $W^\pm\gamma \to e\nu+\gamma$ γ+Jets, QCD, di γ and Z^0 + jets. For the main background, a normalisation method from measured data is developed employing the reconstructed leptonic decays of the Z^0 into muon and electron pairs.

The detector acceptance for selecting the leptons is parameterised using a two-dimensional function $\alpha(p_T^\gamma, \eta_\gamma)$. Figure 14.19 shows the measured and the p_T^γ spectrum from γ+$Z^0 \to \mu^+\mu^-$ after the (acceptance $\times$ efficiency) parameterisation is applied, in comparison with the generator spectrum for γ+$Z^0 \to \nu_i\bar{\nu}_i$ events. For $p_T^\gamma > 100$ GeV/c there is 1170 $Z^0 \to \mu^+\mu^-/e^+e^-$ events expected after all selection cuts for 30 fb^{-1}. These can be used as the candle sample that provides a direct normalisation of the γ+$Z^0 \to \nu_i\bar{\nu}_i$ with a statistical precision of 3%.

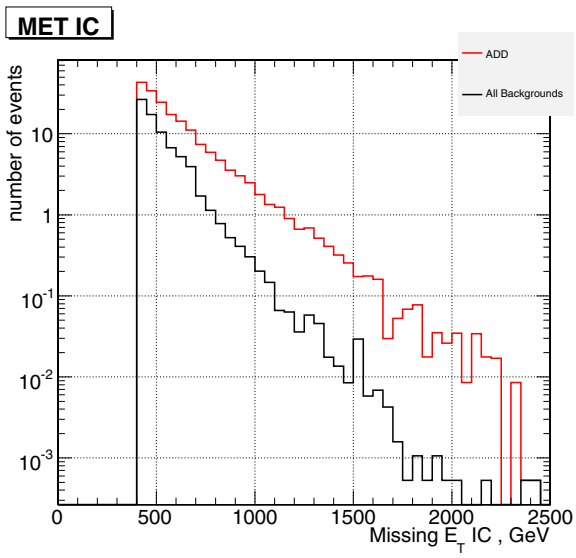

Figure 14.20. Spectrum of the missing E_{T} for all backgrounds (black histogram) and for an example signal sample ($M_{\mathrm{D}} = 2.5\,\mathrm{TeV}, n = 2$). The number of events corresponds to an integrated luminosity of $30\,\mathrm{fb}^{-1}$.

14.7.3. Event selection

The main trigger path for the selection of signal and background events will be the single photon trigger, both at the Level-1 and the HLT. Presently the single photon trigger has a HLT level threshold of 80 GeV, which is far below the selection cut for events with isolated photons above 400 GeV used here. Hence the expected trigger efficiency is close to 100% and its efficiency can be monitored from data with a $E_{\mathrm{T}}^{\mathrm{miss}}$ trigger which will have a threshold in the range of 200–300 GeV, well below the acceptance of the bulk of the signal. Both the topological characteristic and the necessity to reduce the Standard Model background lead to the following selection criteria:

- At least a $E_{\mathrm{T}}^{\mathrm{miss}} > 400\,\mathrm{GeV}$ is required and the photon p_{T} has to be above 400 GeV.
- $|\eta|$ of the photon < 2.4.
- $\Delta\phi(E_{\mathrm{T}}^{\mathrm{miss}}, \gamma) > 2.5$.
- A track veto for high p_{T} tracks $> 40\,\mathrm{GeV}$ is applied. This is a powerful criterion to reduce all backgrounds containing high-energetic charged particles (such as $e^{\pm}$, $\mu^{\pm}$, jets).
- An Isolated Photon Likelihood criterion is applied to remove residual background from hard photon emission from jets as well as fake photons from jets.

Figure 14.20 shows the missing transverse energy spectra for events surviving the selection path for both the signal and the backgrounds. As expected the $Z^0\gamma$ is by far the most dominant component of the background, followed by $W^{\pm}\gamma$ while the contributions of the other Standard Model backgrounds are small. For all ADD cross section the hard truncation approach is used (see Section 14.1), i.e. events with $M_G < M_D$ are rejected.

14.7.4. Systematic uncertainties and discovery potential

We consider an uncertainty of 2% for the measurement of the photon p_{T}^{γ} in the electromagnetic calorimeter and an uncertainty of 5% for the $E_{\mathrm{T}}^{\mathrm{miss}}$ measurement. The

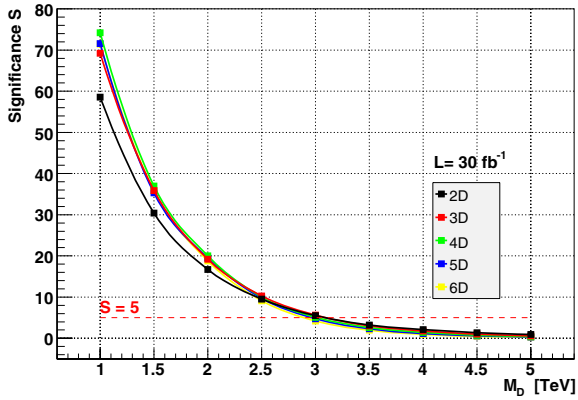

Figure 14.21. Expected significances as function of M_{D} for different number n of extra dimensions.

resulting decrease of the significance is 1.0% and 1.6% respectively. For the main background the systematics can be reduced to the luminosity measurement using the Z^0 candle calibration method. It can thus be measured with a precision of 3% after 30 fb^{-1}. The 5σ discovery reach is achievable for M_D <2.5 $\mathrm{TeV/c^2}$ and all values of extra dimensions while for $M_D <$ 3 $\mathrm{TeV/c^2}$ 5σ reach is achievable for n between 2 and 4. Figure 14.21 shows the expected significances as function of M_{D}.

14.8. Black holes

14.8.1. Introduction to higher-dimensional black holes

One of the consequences of large extra dimensions is the possibility to produce microscopic black hole (BH) at LHC energies. Such a BH formed in a (4+n)-dimensional space-time has a Schwarzschild radius

$$r_{s(4+n)} = \frac{1}{\sqrt{\pi}\, M_{(4+n)}} \left(\frac{M_{BH}}{M_{(4+n)}} \left(\frac{8\Gamma((n+3)/2)}{n+2} \right) \right)^{1/(n+1)} \tag{14.18}$$

where $M_{(4+n)}$ is the reduced Planck scale and n is the number of large extra dimensions [741]. A high energy collision of two partons can result in the formation of a BH when the impact parameter is smaller than $r_{s(4+n)}$. In the semi-classical approach the BH cross section is given by $\sigma(M_{\mathrm{BH}}) = \pi r^2_{s(4+n)}$ at the parton level. If for low masses $M_{(4+n)}$, i.e. around 2 TeV, the BH production cross sections at the LHC is in the pb range.

Once produced, these BHs are expected to decay thermally via Hawking radiation [742]. The Hawking temperature for a BH in 4 + n dimensions is [743]

$$T_{(4+n)} \sim M_{(4+n)} (M_{(4+n)}/M_{\mathrm{BH}})^{1/(n+1)}. \tag{14.19}$$

These BHs have a very short lifetime typically of $\sim 10^{-27}$ seconds.

BH events are expected to evaporate democratically by emission of all particle types that exist in nature, independent of their spin, charge, quantum numbers or interaction properties. Therefore they can be a source of new particles. BH physics at the LHC can provide the possibility of probing quantum gravity in the lab.

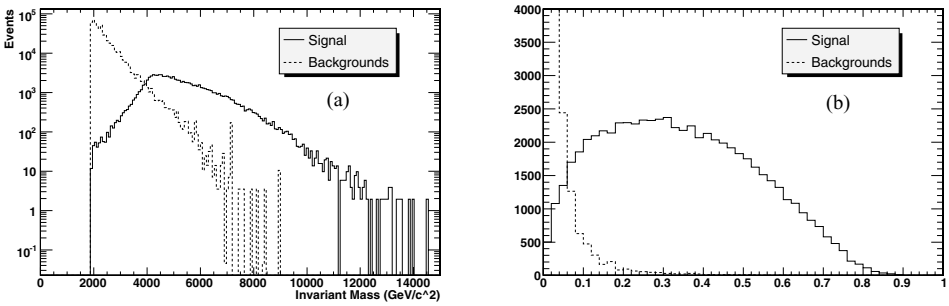

Figure 14.22. (a) Reconstructed invariant mass distribution and (b) event sphericity for black hole and standard model background events.

14.8.2. Analysis selection path and results

Black hole event samples were produced using the CHARYBDIS event generator [744]. As a benchmark the case which is analysed has the following parameters: a) $2\,\mathrm{TeV/c^2}$ effective Planck scale, b) $4\,\mathrm{TeV/c^2}$ minimum and $14\,\mathrm{TeV/c^2}$ maximum black hole mass c) 3 extra dimensions. Time evolution during Hawking radiation and gray body effects are included. The detector response was simulated by us using the CMS fast simulation (FAMOS, version 1.4.0) after validation against the detailed CMS GEANT-based simulation. The Standard Model backgrounds taken into account include QCD jets, top production and boson plus jet production. The invariant mass of all final state objects (electrons, photons, jets and muons) in the event is found to be correlated with the input black hole mass. In addition since the black hole formation can only occur if $M_{\mathrm{BH}} > M_{(4+n)}$, the event invariant mass can indicate the effective Planck scale $M_{(4+n)}$. In the benchmark scenario the invariant mass is required to be greater than $2\,\mathrm{TeV/c^2}$. BH events are characterised by a high multiplicity of the final state particles, which increase as a function of the BH mass (and decreases as a function of Hawking temperature). In particular the ratio of jets to leptons is found to be 5 to 1. In this study with a simple jet and lepton multiplicity counting the jet/lepton ratio is formed. The average value of this ratio is found to be 4.5. The thermal nature of Hawking radiation requires the distribution of BH remnants to be spherical as shown and a sphericity of 0.28 is required which eliminates drastically the Standard Model backgrounds. The invariant mass distribution and sphericity for the signal and background events is shown in Fig. 14.22.

Events are counted when the total sum of the P_{T} of all reconstructed objects plus the missing transverse energy is larger than 2500 GeV. A study of the Level-1 and HLT trigger path shows that the 4 jet trigger has a 93% efficiency for the signal events and is used in the analysis.

The event selection criteria applied to the reconstructed events and the efficiencies of the requirements are listed in Table 14.11.

The minimum integrated luminosity needed for 5σ significance and for the benchmark point is $\sim 2\,\mathrm{pb^{-1}}$. A survey of the parameter space using 25 points shows that for effective Planck scale of 2–3 TeV, minimum black hole mass up to 4 TeV and 2–6 extra dimensions the 5 sigma significance can be obtained with luminosity between fraction of $\mathrm{pb^{-1}}$ and 100's of $\mathrm{pb^{-1}}$. For effective Planck scale of 4 TeV a few $\mathrm{fb^{-1}}$ is needed for discovery. To account for the systematic uncertainties in the number of signal events, the effect of PDF distribution on cross section is calculated using the CTEQ6 NLO PDF set with the help of LHAPDF interface. PDF uncertainties for the chosen benchmark point is found to be $^{+24.2\%}_{-9.07\%}$. Using these uncertainties, the error in significance calculation was computed to be 12%.

Table 14.11. Event selection and background rejection for signal events and major background processes.

Cut	Signal	tt+nJ	W+nj	Z+nJ	QCD Dijet	WW+nJ
Cross Section (pb)	18.85	371	896	781.84	33076.8	269.91
Events ($10\,\mathrm{fb}^{-1}$)	188500	3.71×10^{6}	8.96×10^{6}	7.82×10^{6}	3.31×10^{8}	2.70×10^{6}
$M\mathrm{Inv} > 2\,\mathrm{TeV/c^2}$	18.71	13.29	6.53	3.85	2634.94	20.53
Tot. Multiplicity > 4	17.72	13.25	6.43	3.84	2613.18	20.42
Sphericity > 0.28	9.27	1.60	0.23	0.10	53.74	0.07
Final No. Events ($10\,\mathrm{fb}^{-1}$)	92740	15990	2328	982	537391	740

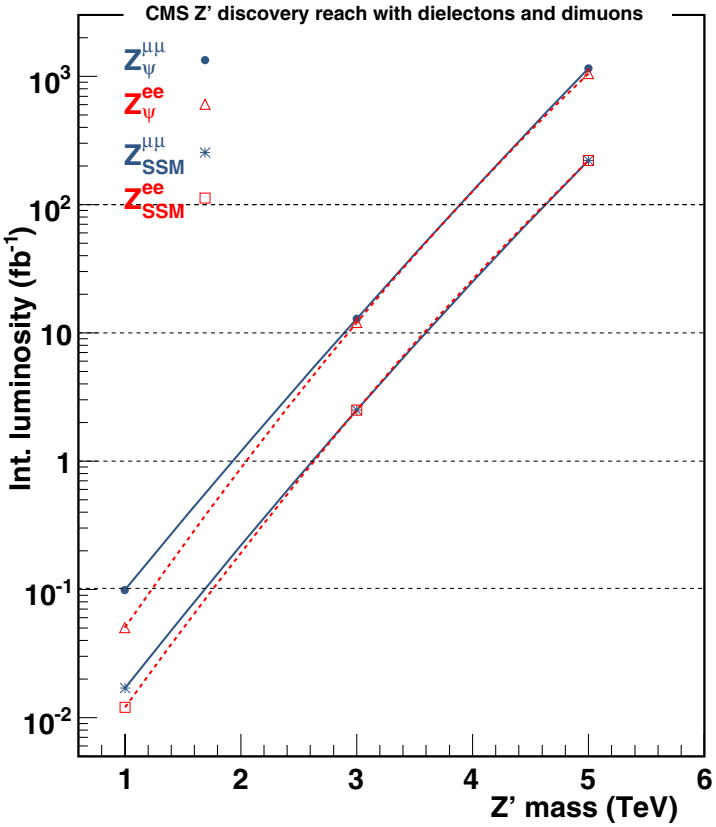

Figure 14.23. Z′ discovery reach for two of the models studied in the dielectron and dimuon channels. The reach for the rest of the models studied is within the band between the two shown here.

14.9. Discussion

The results on Z′s and RS gravitons in the channels studied in this chapter are summarised here.

In Fig. 14.23 the summary of the discovery reach in the dielectron and dimuon channels is shown for two representative Z' models. The reach for the rest of the models studied lies within the band of the two shown in the figure. The results for the dielectron channel are using

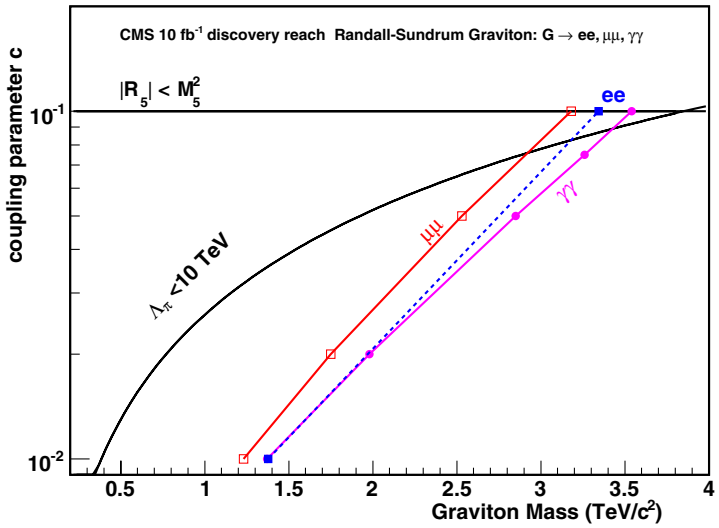

Figure 14.24. RS graviton discovery mass reach as a function of the model coupling parameter in the dielectron, dimuon and diphoton channels for 10 fb^{-1}. The dielectron reach is shown as dashed because only the boundary points ($c = 0.01$ and $c = 0.1$) where studied.

here K-factor of 1.3 for the signal and background in order to be directly compared with the dimuon results[50]. Although the analysis strategies and significance computation is different between the two analyses the results are compatible. For low luminosity and mass reach up to 3 $\mathrm{TeV/c^2}$ the muons suffer from misalignment effects which are recovered after 10 fb^{-1}. For high mass reach (above 3 $\mathrm{TeV/c^2}$) the saturation in the ECAL is causing a degradation of the resolution in the dielectron channel. The reach using the dielectron channel is up to 3 TeV better than the dimuons due to less than 1% resolution. Optimising the analysis in the dielectron channel to extract the background from the data and detailed studies of the saturation is expected to further improve the reach in the dielectron channel for high masses. The combined reach of the two channels requires a detailed analysis and is not presented here. Note that a 1 $\mathrm{TeV/c^2}$ Z' is observable with less than 0.1 fb^{-1} for all models and with a single channel while every $\mathrm{TeV/c^2}$ in mass reach corresponds to approximately an order of magnitude increase in integrated luminosity.

In Fig. 14.24 the summary of the RS graviton discovery reach in the dielectron, dimuon and diphoton channels is shown. Here the results for the diphoton channel are using CTEQ6M PDFs to be directly compared with the dielectron and dimuon channels.[51] Although the branching ratio to photons is roughly twice that of electrons or muons the reach for low coupling and graviton mass is comparable between dielectrons and diphotons due to the QCD and prompt photon backgrounds in the photon channel which are harder to efficiently suppress. For higher masses and coupling the diphoton is leading the reach due to the higher branching ratio. The dimuon channel is trailing the reach compared to the dielectrons merely due to resolution.

[50] Recent calculation of K-factors for several of the processes discussed here can be found in reference [745].
[51] In the main analysis the diphoton channel uses CTEQ5L while the dielectron and dimuon analyses use CTEQ6M where the gluon-gluon contribution is enhanced compared to the CTEQ5L; while the Drell–Yan background is largely insensitive to this choice, at low masses the gluon-gluon is the dominant graviton production process while at high masses the qq dominates where CTEQ5L and CTEQ6M are comparable.

Chapter 15. Alternative BSM Signatures

15.1. Technicolour

15.1.1. The $\rho_{TC} \to W + Z$ channel

Technicolour (TC) provides an alternative to the elementary Higgs mechanism of the Standard Model. It introduces a new strong interaction [746] providing a dynamical nature to Electroweak Symmetry Breaking. Technicolour is a QCD-like force, acting on technifermions at an energy scale $\Lambda_{TC} \sim v_{weak} = 246\,\text{GeV}$. A number N_D of technifermion doublet condensates yield the pseudo-Goldstone bosons π_{TC}, together with a wide spectroscopy of excited technimesons. The present simulation is performed using the phenomenology of the lowest-lying technihadrons, commonly referenced as the "Technicolour Straw Man" model (TCSM) [735]. The colour-singlet sector includes the spin-zero π_{TC} and the spin-one technimesons ρ_{TC} and ω_{TC}. The decay cross-section of the ρ_{TC} is expressed as an admixture of π_{TC} and the Standard Model Z and W bosons:

$$\rho_{TC} \to \cos^2\chi\,\langle\pi_{TC}\pi_{TC}\rangle + \cos\chi\,\sin\chi\,\langle\pi_{TC}V_L\rangle + \sin^2\chi\,\langle V_L V_L\rangle \tag{15.1}$$

where V_L is the longitudinal mode of the $V = Z, W$ and $\sin\chi \simeq 1/\sqrt{N_D} \sim 1/3$. The branching fraction $\text{BR}(\rho_{TC} \to W + Z)$ is competing with the two first terms in Eq. 15.1, hence changing with $\text{M}(\pi_{TC})$.

The decay channel $\rho_{TC} \to W + Z$ is the subject of this analysis [747] as it has the advantage of a very clean final state, namely $3\ell + \nu$. The background contributions arise mainly from Standard Model processes involving weak boson production and decays. Other technicolour decay modes that include jets such as $\rho_{TC} \to \pi_{TC} + W$, have higher branching fractions but are much harder to disentangle from the Standard Model background processes.

15.1.1.1. Event selection. All signal and backgrounds samples used in this analysis are generated with PYTHIA 6.2 [24] with the requirement of at least 3 prompt leptons in the CMS fiducial region. The $Zb\bar{b}$ background is generated using COMPHEP [355] interfaced to PYTHIA. Contributions from processes of type $Z \to 2\ell$ plus an additional fake lepton from a jet have been taken into account in the systematic uncertainties, see Sect. 15.1.1.2. A set of 14 different ρ_{TC} samples are generated within the $[\text{M}(\rho_{TC}), \text{M}(\pi_{TC})]$ phase space.

Nominal CMS Level-1 and High-Level Trigger requirements are applied [76]. The CMS fast simulation [11] is used for detector simulation and event reconstruction. The main reconstructed objects and their efficiencies have been validated against the detailed GEANT-based CMS detector simulation [8, 10].

The analysis is designed to reduce the main Standard Model background contributions WZ, ZZ, $Zb\bar{b}$ and $t\bar{t}$, while retaining high signal efficiency. It is summarised as follows:

(i) Lepton selection: 3 high-p_{T} and isolated electrons or muons.
(ii) Lepton trigger: single- or two-electron or muon mode (Level-1 and HLT).
(iii) Z : same-flavour and opposite-charge ℓ-pair closest to $\text{M}(Z)$, with $p_{\text{T}}\,(\ell_{1,2}) >$ (30, 10) GeV/c.
(iv) W : solution to 3rd lepton with $p_{\text{T}} > 10\,\text{GeV/c}$ + Missing E_{T} + $\text{M}(W)$ constraint.
(v) $|\text{M}(\ell^+\ell^-) - \text{M}(Z)| \leqslant 3\sigma_{\text{M}_Z} \cong 7.8\,\text{GeV/c}^2$.
(vi) $p_{\text{T}}(Z)$ and $p_{\text{T}}(W) > 30\,\text{GeV/c}$. For benchmark points with $\text{M}(\rho_{TC}) = 200\,\text{GeV/c}^2$, the minimum $p_{\text{T}}(Z)$ and $p_{\text{T}}(W)$ threshold is 10 GeV/c.
(vii) $|\Delta[\eta(Z) - \eta(W)]| \leqslant 1.2$.

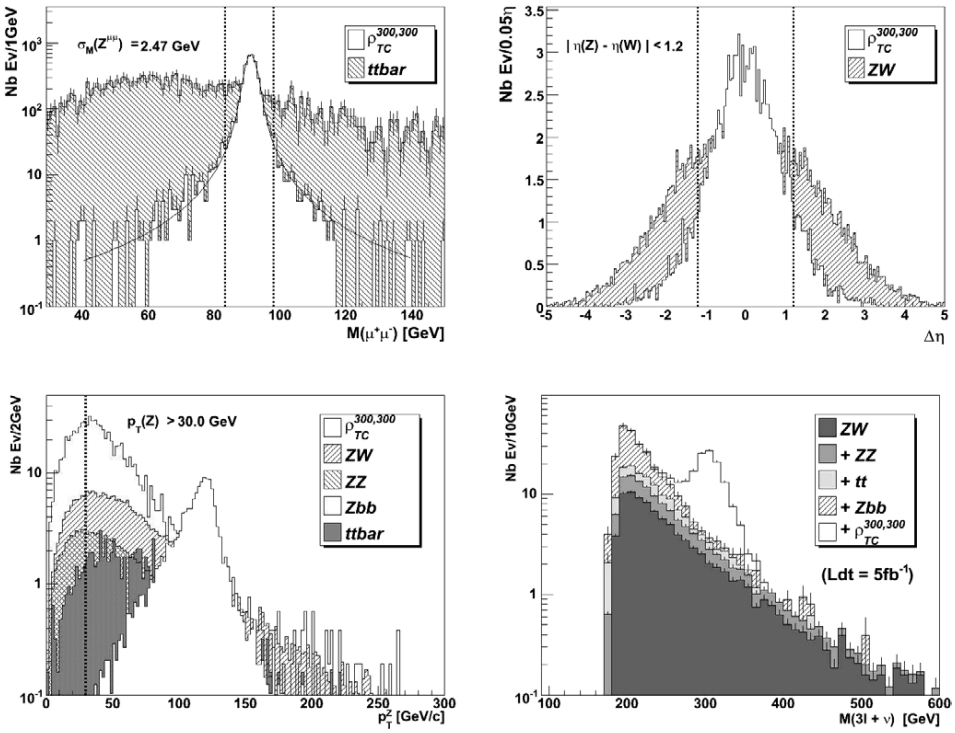

Figure 15.1. (a) $M(\mu^+\mu^-)$ for $\rho_{TC}(300, 300)$ and $t\bar{t}$; (b) $\Delta[\eta(Z) - \eta(W)]$ for $\rho_{TC}(300, 300)$ and WZ; (c) $p_T(Z)$ for $\rho_{TC}(300, 300)$ and all backgrounds ($p_T(W)$ is similar); (d) Reconstructed $M(3\ell + \nu)$ for $\rho_{TC}(300, 300)$ and all backgrounds. The vertical lines indicate the applied requirements.

The Z and W are reconstructed with a purity of $\sim 99\%$, using the 3 highest-p_T leptons in the event, and the Missing Transverse Energy (MET), obtained as the vector sum of the jets and leptons in the event. The $M(W)$ constraint yields a 2 fold ambiguity in the p_Z component of the reconstructed neutrino: it is found that the most efficient choice for the ρ_{TC} signal is the minimum p_Z solution. The kinematic cuts are illustrated in Fig. 15.1. The main $t\bar{t}$ reduction is obtained via the Z-mass window requirement (v). The irreducible background $WZ \to 3\ell + \nu$ is most efficiently separated from the signal via the $\eta(Z) - \eta(W)$ correlation requirement (vii).

The p_T cut on Z and W further improves the signal to background ratio, however it is kept modest in order to preserve the exponential background hypothesis of the $3\ell + \nu$ invariant mass spectrum, used to compute the signal sensitivity. The $\rho_{TC}(300, 300)$ signal and background yields are shown in Fig. 15.1d and the corresponding reconstruction efficiencies are listed in Table 15.1.

15.1.1.2. Signal sensitivity and systematic uncertainties. The sensitivity of each ρ_{TC} benchmark point is computed by taking into account realistic statistical fluctuations for a given integrated luminosity. The sensitivity estimator is defined as the likelihood-ratio S_L, defined in Appendix A.1. The signal probability density function (p.d.f.) is assumed Gaussian (dominated by detector resolution) and the background p.d.f. is exponential in all ρ_{TC} fit regions. The output of the fitting procedure is shown in the contour plot over the

Table 15.1. $\sigma \times \mathrm{BR}(\ell = e \text{ or } \mu)$, 3-lepton pre-selection efficiency, total efficiency and final yield within 3σ of the signal region (Nev), for $\mathcal{L} = 5\,\mathrm{fb}^{-1}$. $\rho_{TC}(300, 300)$ and the main background contributions are shown. The simulation is repeated for all ρ_{TC} benchmark points.

Sample	$\sigma \times$ BR(pb)	ε(3-lept)	ε(Reco) (%)	Nev($5\,\mathrm{fb}^{-1}$)
$\rho_{TC} \to W + Z \to 3\ell + \nu$	0.13	0.635	25.88 ± 0.40	103
$WZ \to 3\ell + \nu$	0.39	0.471	9.91 ± 0.11	27
$ZZ \to 4\ell$	0.07	0.719	15.80 ± 0.14	10
$Zb\bar{b} \to 2\ell + X$	332	0.046	0.23 ± 0.01	12
$t\bar{t}$	489.72	0.065	0.019 ± 0.001	8

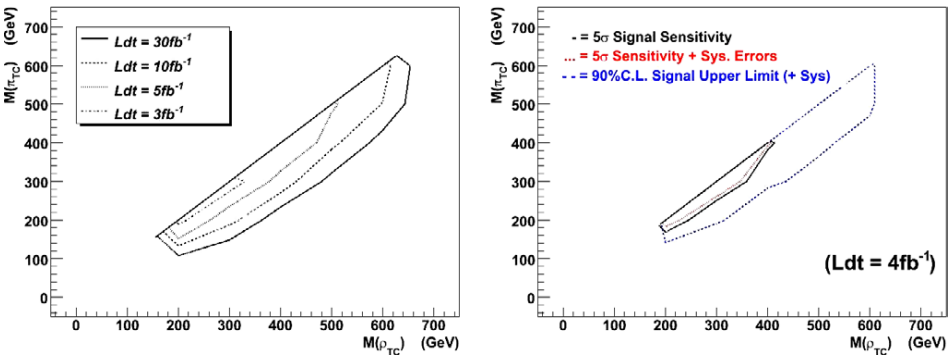

Figure 15.2. Left: Signal 5σ Sensitivity curves for various integrated luminosities. Right: sensitivity for $\mathcal{L} = 4\,\mathrm{fb}^{-1}$: the dotted (resp. dashed) curve shows the sensitivity (resp. the 90% C.L. signal upper limit) after including systematic uncertainties.

$[\mathrm{M}(\rho_{TC}), \mathrm{M}(\pi_{TC})]$ phase space in Fig. 15.2 (left), for various integrated luminosities. A signal sensitivity above 5 is expected for $\mathcal{L} = 3\,\mathrm{fb}^{-1}$ (before including systematic uncertainties).

The ρ_{TC} sensitivity has been simulated for the early CMS data taking phase. Expected detector related systematic uncertainties for $\mathcal{L} = 1\,\mathrm{fb}^{-1}$ are taken into account. While no substantial contribution is found from the tracker and muon system misalignment or the calorimeter miscalibration, the accuracy at which the lepton efficiency will be determined from data affects the result: a 2% uncertainty is considered. Moreover, the lepton fake rate has been simulated on $Zb\bar{b}$ and extrapolated to any $Z + jet(s)$ type background, in order to take into account additional contaminations from pion/kaon decays or from wrongly identified lepton candidates. A production cross-section of 1047 pb per lepton flavour is assumed for $Z + n\text{-}jets$, $n \geqslant 0$. A single lepton fake rate of $\mathrm{O}(10^{-3})$ is obtained using the fast simulation [11], affecting the ρ_{TC} sensitivity as shown below. Finally, a 7.5% uncertainty on the missing transverse energy measurement is considered. The above uncertainties result in the following relative ρ_{TC} sensitivity drop:

$$\Delta^{\mathrm{tot}}_{\mathrm{SYS}} = \sqrt{\left(\Delta^{\mathrm{Eff}}_{\mathrm{SYS}}\right)^2 + \left(\Delta^{\mathrm{Fake}}_{\mathrm{SYS}}\right)^2 + \left(\Delta^{\mathrm{MET}}_{\mathrm{SYS}}\right)^2} = \sqrt{(2.7\%)^2 + (8.5\%)^2 + (6.6\%)^2} = 11\%. \quad (15.2)$$

Introducing K-factors from next-to-leading-order (NLO) expectations for the signal (a K-factor 1.35 is assumed in similarity with the Drell–Yan process) and background leads to a relative signal sensitivity increase of 6%; however the latter estimate has not been included in the final result.

Table 15.2. Contact interaction models.

Model	LL	RR	LR	RL	VV	AA	LL+RR	LR+RL
	Non-parity conserving				Parity conserving			
η_{LL}	±1	0	0	0	±1	±1	±1	0
η_{RR}	0	±1	0	0	±1	±1	±1	0
η_{LR}	0	0	±1	0	±1	∓1	0	±1
η_{RL}	0	0	0	±1	±1	∓1	0	±1

In summary, the technicolour signature $\rho_{TC} \to W + Z$ in the context of the Straw Man model is studied. The 5 sigma discovery reach is obtained for an integrated luminosity $\mathcal{L} \simeq 4\,\text{fb}^{-1}$.

15.2. Search for contact interactions with dimuons

Contact interactions offer a general framework for describing a new interaction with typical energy scale $\Lambda \gg \sqrt{s}$. The presence of operators with canonical dimension $N > 4$ in the Lagrangian gives rise to effects $\sim 1/\Lambda^{N-4}$. Such interactions can occur for instance, if the SM particles are composite, or when new heavy particles are exchanged.

In the following we will consider lepton-pair production. The lowest order flavour-diagonal and helicity-conserving operators have dimension six [123].

The differential cross section takes the form

$$\frac{d\sigma}{d\Omega} = SM(s,t) + \varepsilon \cdot C_{Int}(s,t) + \varepsilon^2 \cdot C_{NewPh}(s,t) \tag{15.3}$$

where the first term is the Standard Model contribution, the second comes from interference between the SM and the contact interaction, and the third is the pure contact interaction effect. The Mandelstam variables are denoted as s, t and u.

Usually the coupling is fixed, and the structure of the interaction is parameterised by coefficients for the helicity amplitudes:

$$\begin{aligned} &g && \text{coupling (by convention } g^2/4\pi = 1), \\ &|\eta_{ij}| \leqslant 1 && \text{helicity amplitudes } (i,\, j = \text{L}, \text{R}), \\ &\varepsilon && \frac{g^2}{4\pi}\frac{\text{sign}(\eta)}{\Lambda^2} \text{ for } f\bar{f}. \end{aligned}$$

Some often investigated models are summarised in Table 15.2. The models in the second half of the table are parity conserving, and hence not constrained by the very precise measurements of atomic parity violation at low energies. The results presented in this contribution cover the LL model, which has the highest sensitivity at LHC energies from the models in the first half of the table. More details can be found in [349].

15.2.1. Analysis

The topology under study is high-mass muon pairs with opposite sign. More details on the analysis are found in [349]. The Global Muon Reconstructor (GMR, described in PTDR, Volume 1, Section 9.1.2) output is used. The dimuon events are triggered by the single and dimuon triggers. We have processed events, generated to cover the whole region of interest

up to dimuon masses of 6 TeV/c^2, through full simulation with OSCAR and reconstruction with ORCA. The dimuon mass resolution is parameterised in two ways:

- as mass dependent one standard deviation (RMS);
- by fitting the mass resolution with a sum of two Gaussians to account for the long tail of less well reconstructed masses.

The results are remarkably stable as a function of the dimuon mass: the second Gaussian contributes around 14% and has a standard deviation 3.3 times bigger than the first Gaussian.

Our strategy is to generate events with PYTHIA and apply parametrisations of the dimuon mass efficiency and resolution obtained from full simulation. We have verified our approach by comparing the resulting mass spectra with the ones obtained with OSCAR/ORCA or FAMOS for Drell–Yan and selected contact interactions samples, observing good agreement in all cases.

Two mass regions: 500–1000 GeV and 1000–6000 GeV are considered. The total cross section and the forward–backward asymmetry as function of the dimuon mass are studied. Our analysis shows that the sensitivity to contact interactions comes almost exclusively from the cross section measurements for the LL model.

In order to reduce the systematic uncertainties both on the experimental and theory sides a "double ratio" method is developed. The number of observed events for a given bin in invariant mass is

$$N_{obs} = L \cdot \sigma \cdot \varepsilon \tag{15.4}$$

where L is the luminosity, σ the differential cross section for the given mass bin, and ε the experimental efficiency. We select a zeroth "normalisation" bin for invariant masses between 250–500 GeV/c^2, both well above the Z pole and in an area well covered by the Tevatron, and define the experimental ratios

$$R_i^{DATA} = \frac{N_i^D}{N_0^D} = \frac{\sigma_i^D \cdot \varepsilon_i^D}{\sigma_0^D \cdot \varepsilon_0^D}. \tag{15.5}$$

Here the cross sections and efficiencies are the ones for the real LHC data. The index i runs for all measured bins with masses above 500 GeV/c^2. The luminosity cancels in the ratio. The choice of this mass bin is not random. If we compare the flavour composition of partons initiating the hard interaction (Table 15.3), at the Z peak 32.1% are heavier flavours (not u or d quarks), with their own parton density functions (PDF) uncertainties. At 250–500 GeV/c^2 the u and d quarks are "initiators" already in 85.6% of the cases, increasing to 96.3% above 1 TeV/c^2, etc. Moreover, at the Z peak d quarks are most abundant, while at higher masses u quarks dominate, asymptotically approaching a ratio 4:1. It is clear that our choice of normalisation bin gives flavour composition much closer to the most interesting high mass events, compared to a normalisation using Z pole events. The PDF uncertainty on cross sections is estimated using LHAPDF [95, 351]. It is interesting to note that this uncertainty reaches a minimum for masses 250–600 GeV/c^2, corresponding to medium values of the parton momentum fractions X, reinforcing our choice of normalisation bin.

We define similar ratios for the Monte Carlo (theory) predictions. The *absolute* values of the cross sections and efficiencies are not important for the ratios, what matters is *the shape* of these quantities as function of invariant mass. For example, the absolute value of K-factors, a way to compensate for missing higher order N(N)LO terms and enable the comparison of leading order Monte Carlo predictions to data (similarly for the electroweak radiative corrections) disappears from the ratios and only the *shape* of the K-function as depending on invariant mass remains – a much smaller effect. And part of the uncertainties introduced due to our limited knowledge of PDFs cancels in the ratio, leaving smaller residual uncertainties due to the change of phase space for changing masses.

Table 15.3. Flavour composition of partons initiating the hard Drell–Yan interaction.The PDF uncertainty on the cross sections (positive and negative asymmetric errors) is estimated using LHAPDF.

Mass [GeV/c^2]	d [%]	u [%]	s [%]	c [%]	b [%]	PDF+ [%]	PDF− [%]
Z peak	35.9	32.1	17.2	9.77	5.10	+4.7	−5.7
250–500	24.3	61.3	6.22	6.64	1.54	+3.4	−4.2
500–600	22.8	68.4	4.03	3.95	0.89	+3.5	−4.1
1000+	21.7	74.6	1.86	1.48	0.33	+5.0	−5.8
2000+	19.9	78.4	0.91	0.63	0.14	+9.0	−7.7

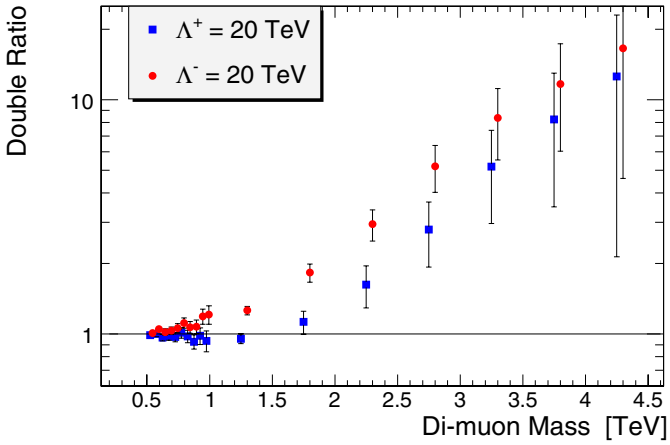

Figure 15.3. Double ratios for contact interactions in the dimuon channel, LL model, scale $\Lambda = 20\,\mathrm{TeV/c^2}$, positive and negative interference, and luminosity $100\,\mathrm{fb}^{-1}$. The errors shown are statistical.

Now let us define the double ratios

$$DR_i = \frac{R_i^{DATA}}{R_i^{MC}}. \tag{15.6}$$

This method is inspired by a study of Drell–Yan events and extraction of proton and pion PDFs at lower masses [748], as well as by the SuperKamiokande double ratio method for measuring atmospheric neutrino oscillations [749]. If our theory understanding and detector modelling are both perfect, we expect $DR_i \equiv 1$. The experimental or Monte Carlo errors introduced in the ratios from the uncertainties in the zeroth bin are negligible, as due to the steeply falling Drell–Yan spectrum this bin has much more data compared to the high mass bins.

An example of double ratios for positive and negative interference is shown in Fig. 15.3. As can be seen, for scale $\Lambda = 20\,\mathrm{TeV/c^2}$ the expected effects are quite sizable (note the log scale), with the sensitivity for negative interference starting around dimuon masses of $750\,\mathrm{GeV/c^2}$, while for positive interference masses above $2\,\mathrm{TeV/c^2}$ are required.

The experimental systematic effects in the cross section measurement are estimated to be 2% from the total muon efficiency and no more than 1.4% from momentum resolution. The former can be controlled quite well with the huge sample of Z events decaying to dimuons, and the effects for TeV muons are taken into account on top of this. The latter is important at high mass as smearing from lower masses from the steeply falling Drell–Yan spectrum can contaminate the high mass measurements, especially if the tails of the momentum resolution

Table 15.4. The PDF uncertainty on the cross section ratios (positive and negative asymmetric errors) as estimated using LHAPDF. Clearly normalising to the 250–500 GeV/c^2 mass bin is superior compared to a normalisation relative to the Z peak (70–120 GeV/c^2).

	$R\left(\frac{M}{250-500}\right)$		$R\left(\frac{M}{Zpeak}\right)$	
Mass [GeV/c^2]	PDF+ [%]	PDF− [%]	PDF+ [%]	PDF− [%]
500–600	+1.5	−1.5	+4.6	−4.2
1000+	+5.2	−4.8	+7.8	−7.1
2000+	+10.7	−7.8	+12.9	−9.4

are not under control. It is estimated by varying the two parametrisations of the mass resolution by ±40%, giving consistent results. The main source of systematic uncertainties on the momentum resolution comes from the alignment of the muon chambers and the central tracker, both at start-up and at high luminosity.

The systematic uncertainties from our limited knowledge of PDFs is estimated using the CTEQ6M PDF set from LHAPDF. From Table 15.4 our estimate of the PDF uncertainty on the cross section ratio is $^{+5.2}_{-4.8}$% above 1 TeV or $^{+10.7}_{-7.8}$% above 2 TeV.

The genuine electro-weak radiative corrections change by ∼10% in the relevant mass range [158, 350]. The K-function changes faster below 250–300 GeV. From our normalisation bin to the highest masses first estimates show a change below 8% on the cross section[52]. Taking conservatively half of these changes with mass as an upper limit on the systematic uncertainty we arrive at 5% and 4% respectively.

Combining all effects in quadrature, we arrive conservatively at systematic uncertainties below 2.5% experimental, 11.5% from theory, 12% total at nominal conditions, 15% shortly after start-up. With the accumulation of data and improved calculations there is hope to improve this number by making progress in our understanding of PDF, electro-weak radiative corrections and K-functions.

The discovery reach for a given model is determined by constructing a negative log-likelihood function combining the deviations between measurements and predictions, including the contact interaction contributions, for all simulated data points. The error on a deviation consists of three parts, which are combined in quadrature: a statistical error, an experimental systematic error and a theoretical uncertainty. The log-likelihood function is integrated in the physically allowed region (all positive Λ for positive interference and all negative Λ for negative interference) to derive the five standard deviations σ discovery reach and one-sided lower limits at 95% confidence level on the scale.

The discovery reach is summarised in Fig. 15.4. The sensitivity is dominated by the cross section measurement, the contribution of the forward-backward asymmetry is minor. The sensitivity for negative interference is substantially better. Even at the highest luminosities the statistical errors at LHC play a major role, as evident from the comparison of the cases with total systematic uncertainties of 3, 15 and 30%. This is not surprising as the Drell–Yan process is probing directly masses up to ∼4–5 TeV/c^2, where due to the steeply falling cross sections the statistical errors remain important for all considered luminosities.

[52] Calculations by M. Schmitt with the program PHOZPRMS [348].

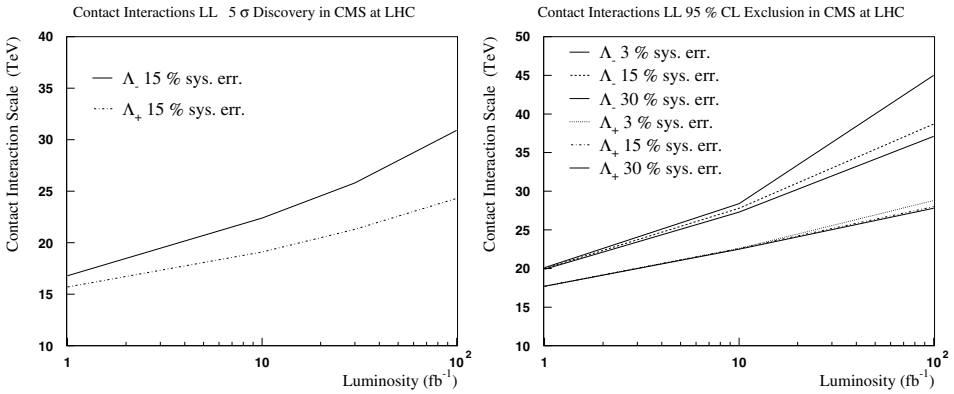

Figure 15.4. Five sigma discovery reach (left) and sensitivity at 95% CL (right) for contact interactions in the dimuon channel for different luminosities and signs of the interference.

15.3. Search for contact interactions with dijets

New physics at a scale Λ above the mass of the final state is effectively modelled as a contact interaction. Here the propagator for a particle of mass $M \sim \Lambda$ exchanged between quarks, or exchanged between constituent particles inside two interacting composite quarks, shrinks to a single point and gives a contact interaction. Quark contact interactions, for example those that arise from a left-handed interaction among composite quarks [123, 124], will always produce a rise in rate relative to QCD at high dijet mass or high inclusive jet E_{T}. However, observation in the mass distribution alone requires precise understanding of the QCD rate as a function of dijet mass, which is complicated by the large systematic uncertainties discussed in Section 4.1.6. Angular distributions benefit from much smaller systematic uncertainties. The contact interaction is often more isotropic than the QCD background, since QCD is dominated by t-channel scattering and produces jets predominantly in the forward direction. Our analysis uses the dijet ratio, discussed in section 4.1.5, to measure the angular distribution as a function of dijet mass, and see any contact interactions which affect the dijet angular distribution [750].

15.3.0.1. Contact interaction sensitivity estimates. The QCD background distribution for the dijet ratio was discussed in section 14.5. In Fig. 15.5 we show a smooth dijet ratio for QCD, estimated at 0.6 from the fit to the full simulation. The error bars shown in Fig. 15.5 are the statistical uncertainties expected with 1 fb^{-1} and the jet trigger prescales discussed in section E.4.3.2. The uncertainties are calculated using Poisson statistics at high dijet mass, where few events are expected and Gaussian statistics is less accurate. In Fig. 4.7 we presented a lowest order calculation of both QCD and a contact interaction among left-handed quarks. The signal in Fig. 15.5 is estimated by scaling the lowest order contact interaction calculation of Fig. 4.7 by the ratio of our full simulation prediction for QCD to the lowest order QCD calculation: signal = contact $\times$ 0.6/QCD. Systematic uncertainties on the dijet ratio are small, as discussed in section 4.1.6 and demonstrated in Fig. 4.8. The calculated chisquared between QCD and the contact interaction signal, including all uncertainties on the dijet ratio, is listed in Table 15.5. In Fig. 15.5 we show the significance in σ, estimated as $\sqrt{\chi^2}$, compared to a smooth fit as a function of $1/\Lambda^+$. The anticipated capability of CMS with 1 fb^{-1} to exclude contact interactions at 95% CL or discover them at 5σ can be read off Fig. 15.5, and they are listed in Table 15.6. This includes the uncertainty on Λ due to the anticipated 5% uncertainty on the observed jet energy. The same analysis is repeated for 100 pb^{-1} and 10 fb^{-1} and the

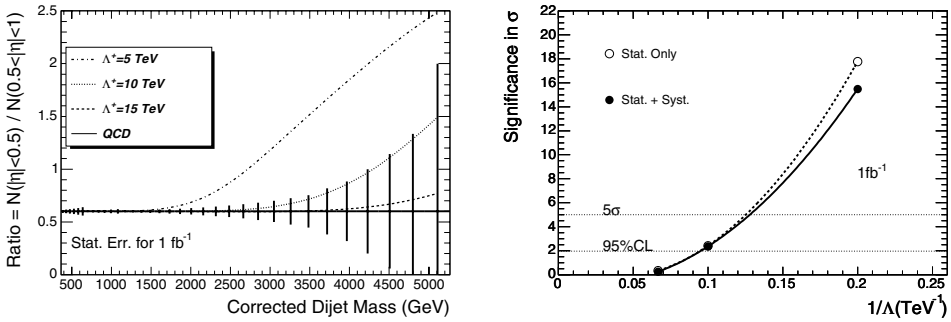

Figure 15.5. Left: The expected value and statistical error of the dijet ratio of QCD in the CMS detector for 1 fb^{-1} (solid) is compared with QCD plus a quark contact interaction at a scale Λ^+ of 15 TeV (dashed), 10 TeV (dotted) and 5 TeV (dot-dashed). Right: The significance with statistical uncertainties only (open circles) and with all uncertainties (solid circles) of the difference between QCD alone and QCD plus a quark contact interaction is plotted vs $1/\Lambda^+$ and fit with a quadratic function. Horizontal lines show the 5σ and 95% CL levels.

Table 15.5. Chisquared between signal and background. For each luminosity and contact interaction scale considered we list the chisquared between QCD alone and QCD plus a contact interaction, for the case where only statistical uncertainties are included (Stat), and for the case where both statistical and systematic uncertainties are included (All).

Luminosity	100 pb^{-1}			1 fb^{-1}			10 fb^{-1}		
Λ^+(TeV)	5	10	15	5	10	15	5	10	15
χ^2 (Stat)	18.3	0.090	0.0037	316	5.82	0.107	3652	133	4.15
χ^2 (All)	16.7	0.082	0.0011	240	5.55	0.061	1340	124	3.56

Table 15.6. Sensitivity to contact interactions with 100 pb^{-1}, 1 fb^{-1}, and 10 fb^{-1}. We list the largest value of the contact interaction scale we expect to be able to exclude at a confidence level of 95% or greater, and the largest value we expect to be able to discover with a significance of 5σ or greater. Estimates include both statistical and systematic uncertainties.

	95% CL Excluded Scale			5σ Discovered Scale		
Luminosity	100 pb^{-1}	1 fb^{-1}	10 fb^{-1}	100 pb^{-1}	1 fb^{-1}	10 fb^{-1}
Λ^+ (TeV)	<6.2	<10.4	<14.8	<4.7	<7.8	<12.0

results are also listed in Table 15.6. The systematic uncertainties on the dijet ratio reduced the CMS sensitivity to a contact interaction between 0.1 and 0.3 TeV/c^2 depending on luminosity and level of significance. To see how quickly CMS jet data will extend the search for new physics, we note that with 100 pb^{-1} our anticipated 95% CL sensitivity, $\Lambda^+ < 6.3$ TeV, is more than twice the sensitivity of the DØ search($\Lambda^+ < 2.7$ TeV at 95% CL) [122]. We note that our contact interaction sensitivity to composite quarks in Table 15.6 is roughly twice our mass resonance sensitivity to excited states of composite quarks in Table 14.5, and is equivalent to observing or excluding a quark radius of order 10^{-18} cm.

15.4. Heavy Majorana neutrinos and right-handed bosons

15.4.1. Introduction

This study is exploring the left–right (LR) symmetric model $SU_C(3) \otimes SU_L(2) \otimes SU_R(2) \otimes U(1)$ [724, 725, 751] at LHC. The model embeds the SM at the scale of the order of 1 TeV

and naturally explains the parity violation in weak interactions as a result of the spontaneously broken parity. It necessarily incorporates three additional gauge bosons W_R and Z' and the heavy right-handed Majorana neutrino states N. The Ns can be the partners (N_l) of the light neutrino states ν_l ($l = e, \mu, \tau$) and can provide their non-zero masses through the see-saw mechanism [726]. Given the results from the atmospheric, solar and reactor neutrino experiments the LR model is very attractive. In the framework of the LR symmetric model, we have studied the production and the experimental signature of heavy Majorana neutrinos and the associated heavy gauge bosons. The detailed analysis is presented in [752].

Existing experimental data constrain the Z' mass to the values $O(1)\,\mathrm{TeV/c^2}$ [753]. The lower bound on the W' mass derived from the $K_L - K_S$ mass difference is quite stringent, $M_{W'} \gtrsim 1.6\,\mathrm{TeV}$ [754], however with some uncertainties from the low energy QCD corrections to the kaon system. The direct searches for W' at the Tevatron yield bounds $M_{W'} \gtrsim 720\,\mathrm{GeV/c^2}$ assuming a light (keV-range) N, and $M_{W'} \gtrsim 650\,\mathrm{GeV/c^2}$ assuming $M_N < M_{W'}/2$ [755]. These bounds are less stringent in more general LR models.

15.4.2. Heavy Majorana neutrino production and decay

The cross sections of $pp \to W_R \to l + N_l + X$ (the process studied here), and $pp \to Z' \to N_l + N_l + X$ (where $N_l \to l + j_1 + j_2$) depend on the value of the coupling constant g_R, the parameters of the CKM mixing matrix for the right-handed sector, the $W_R - W_L$ and $Z' - Z$ mixing strengths, and the masses of the partners N_l of the light neutrino state. In the study presented here the mixing angles are assumed small, the right-handed CKM matrix is identical to the left-handed one and $g_R = g_L$. With these assumptions the Z' is about 1.7 times heavier than W_R and the production cross-section for $pp \to W_R \to eN_e$ is found to be at least one order of magnitude higher than for the $pp \to Z' \to N_e N_e$ process. Finally it is assumed that only the lightest M_{N_e} is reachable at the LHC. In the case of degenerated masses of N_l, the channels with μ's and τ's are open resulting in the increase of the cross section of the process studied here by a factor of $\sim$1.2. The analysis is performed in the M_{W_R}, M_{N_e} parameter space. For the benchmark point considered (referred to as (LRRP)) $M_{N_e} = 500\,\mathrm{GeV/c^2}$ and $M_{W_R} = 2000\,\mathrm{GeV/c^2}$.

For the signal event generation and calculation of cross sections, the PYTHIA Monte Carlo program is used that includes the LR symmetric model with the standard assumptions mentioned above and CTEQ5L parton distribution functions. The fraction of $pp \to W_R^+$ ($pp \to W_R^-$) reactions as a function of M_{W_R} changes from $\simeq$70%($\simeq$ 30%) at $M_{W_R} \simeq 1\,\mathrm{TeV/c^2}$ to $\simeq$ 95%($\simeq$ 5%) at $M_{W_R} \simeq 10\,\mathrm{TeV/c^2}$. For W_R boson masses higher than $M_{W_R} \simeq 2\,\mathrm{TeV/c^2}$ the production of W_R^+ boson dominates. The W_R mass region above $1\,\mathrm{TeV/c^2}$ is studied since smaller masses are excluded by indirect analyses [756].

The signal and background data sample are simulated using the GEANT based CMS full detector simulation [8] and reconstruction package [10].

15.4.3. Analysis

The two major backgrounds considered in this study are the Z+jets and $t\bar{t}$ production. In the event selection two isolated electrons and at least two jets are required. The dielectron invariant mass M_{ee} is required to be above $200\,\mathrm{GeV/c^2}$ to suppress the Z+jets Standard Model background. The invariant mass of each electron with the two leading jets M_{ejj} ($M_{N_e}^{\mathrm{cand}}$ is formed. The M_{eejj} (W_R boson candidate) invariant mass is required to be above $1\,\mathrm{TeV/c^2}$. After this requirement the Standard Model background is suppressed as shown in Fig. 15.6.

The total W_R mass the reconstruction efficiency for $M_{W_R} = 2\,\mathrm{TeV/c^2}$ and for neutrino masses above $500\,\mathrm{GeV/c^2}$ is between 20% and 25% while for neutrino masses much smaller

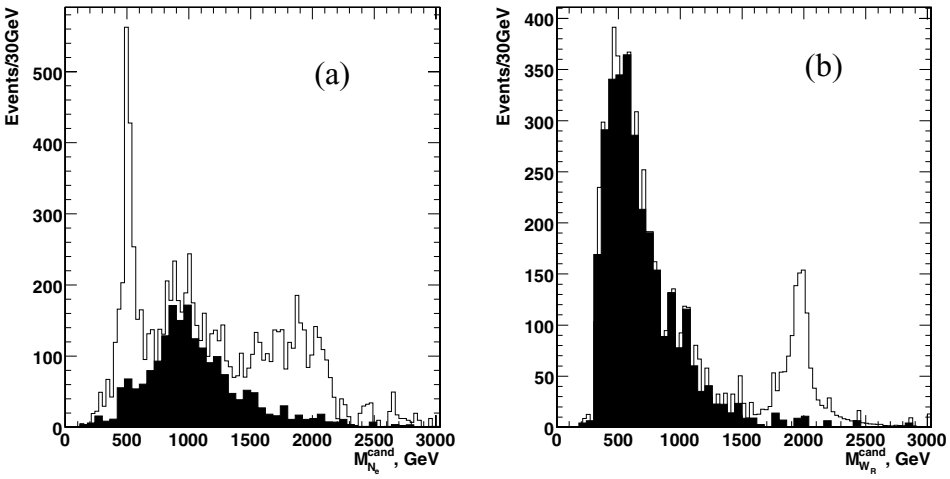

Figure 15.6. M_{ejj} for the signal overlaid with the SM background (shaded histogram) for 30 fb^{-1}: (a) $M_{eejj} > 1\,\mathrm{TeV/c^2}$, (b) $M_{eejj} < 1\,\mathrm{TeV/c^2}$.

than the W_R mass the reconstruction efficiency drops due to the significant overlap of the heavy neutrino decay products in $\eta - \phi$.

15.4.4. Results

The 5 sigma discovery contour in the $(M_{W_R}; M_{N_e})$ plane is shown in Fig. 15.7 for 1 and 30 fb^{-1}. With 30 fb^{-1} a 5 sigma observation of W_R and N_e with masses up to 4 TeV/c^2 and 2.4 TeV/c^2 respectively can be achieved. The signal at the LRRP test point (W_R of 2 TeV/c^2 and N_e 500 GeV/c^2) is observable already after one month of running at low luminosity.

15.5. Little Higgs models

15.5.1. Introduction

The Little Higgs model [656] provides an alternative mechanism of electroweak symmetry breaking keeping a light Higgs boson free from one-loop divergences of SM. It breaks a global symmetry spontaneously and invokes a number of new particles of masses in TeV scale. A heavy singlet quark of charge 2/3, marked as T, is the lightest among them and hence we study the viability of its observation with limited integrated luminosity.

The heavy quark T acquires its mass via Yukawa interactions of two gauge groups with couplings λ_1 and λ_2 which are of similar order. T has three dominant decay modes, the corresponding branching ratios following the relation: $BR(T \to th) = BR(T \to tZ) = \frac{1}{2} BR(T \to bW)$.

15.5.2. Analysis

The decay channel T $\to$ tZ, with leptonic decays of Z and W bosons, provides a clean signature at the LHC environment. This channel has not been previously studied in CMS and the work presented here is a feasibility study. Further details can be found in [757].

The signal samples were generated with PYTHIA 6.227 [24] and the T production was mimicked by activating the fourth quark generation through the W-b fusion. The T quark mass

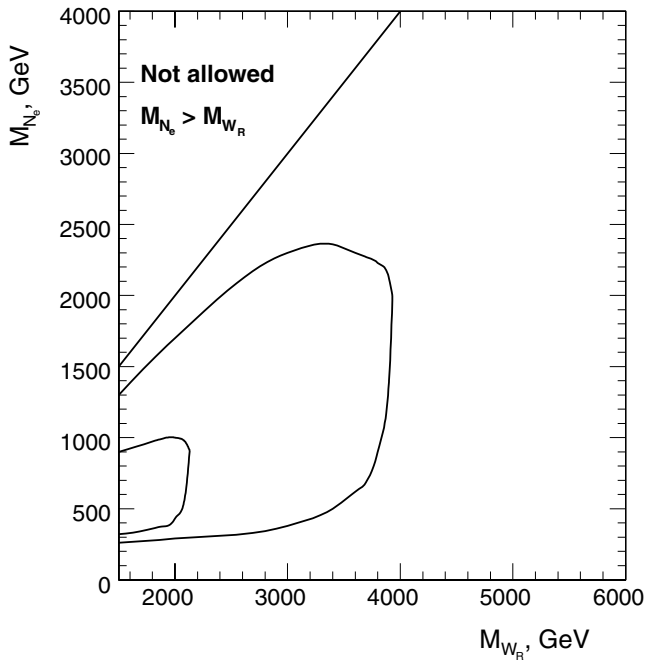

Figure 15.7. CMS discovery potential of the W_R boson and right-handed Majorana neutrinos of the Left–Right Symmetric model for the integrated luminosity $L_t = 30\,\text{fb}^{-1}$ (outer contour) and for $L_t = 1\,\text{fb}^{-1}$ (inner contour).

was set to $1\,\text{TeV/c}^2$ and was treated as a narrow resonance. The CMS full detector simulation was performed with OSCAR [8] and ORCA [10] while pile-up events corresponding to the low luminosity running period of the LHC were taken into account. The major backgrounds considered in this analysis were: $t\bar{t}$, ZW + jets, ZZ + jets, WW + jets, $Zb\bar{b}$, and Z+ jets.

The main selection requirements are summarised below:

- Events are required to pass the "double electron" or "double muon" L1 and HLT trigger criteria.
- Electrons are required to have $p_T > 20\,\text{GeV/c}$ and muons $p_T > 10\,\text{GeV/c}$.
- The combined transverse momentum of the same flavour opposite sign lepton pair is required to be $p_T^{\ell\ell} > 100\,\text{GeV/c}$. The invariant mass of the pair is required to be consistent with the nominal Z mass within $10\,\text{GeV/c}^2$.
- A further third lepton is required in the event ($e^{\pm}$ with $p_T > 20\,\text{GeV/c}$ or $\mu^{\pm}$ with $p_T > 15\,\text{GeV/c}$). The combined transverse momentum of the third lepton with the missing transverse energy is required to be greater than 60 GeV/c. In addition the transverse mass of the third lepton with the missing transverse energy is required to be less than $120\,\text{GeV/c}^2$, to be consistent with the W boson transverse mass.
- Exactly one jet compatible with a b-jet and with calibrated transverse momentum more than $30\,\text{GeV/c}$ is required.
- The combined transverse momentum of the W boson and the b-jet should be more than 150 GeV/c, while their invariant mass is required to be in the range (110–220) GeV/c^2.
- The combined ZWb system invariant mass is required to be in the mass range of the search for heavy quark, namely (850–1150) GeV/c^2.

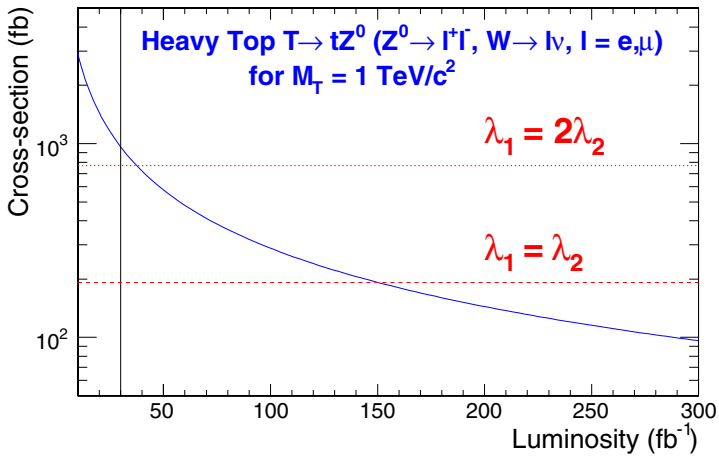

Figure 15.8. Minimum cross section required for a 5σ discovery for a heavy quark of mass $M_T = 1\,\mathrm{TeV/c^2}$ as a function of the luminosity. The horizontal lines correspond to the cross section values for the two cases of λ_1/λ_2. The vertical line indicates the luminosity of $30\,\mathrm{fb}^{-1}$ used for this analysis.

The SM background ZZ → leptonic, is the only background that gives non-zero contribution (still less than 1 event at luminosity $30\,\mathrm{fb}^{-1}$). The total efficiency for the signal selection is $(9.7 \pm 0.4)\%$. Assuming the production cross section of T → tZ to be 192 fb for $M_T = 1\,\mathrm{TeV/c^2}$ (for the case of $\lambda_1 = \lambda_2$) and folding in the branching ratios involved, a total of $N_S = 2.1 \pm 0.1$ signal events are expected for $30\,\mathrm{fb}^{-1}$. This implies that the discovery potential of the channel is rather limited.

The statistical significance of the channel (S_{c12}, defined in Appendix A.1) is 2.5 with a signal-to-background ratio of 41 for $30\,\mathrm{fb}^{-1}$. Taking into account systematic uncertainties from the electron energy scale, jet and missing energy scale and b-tagging efficiency uncertainty, the significance drops down to 2.0. Figure 15.8 shows the signal cross section as a function of the integrated luminosity at the LHC, for establishing at 5σ level, single production of a heavy quark of mass $= 1\,\mathrm{TeV/c^2}$. The luminosity needed for 5σ evidence is estimated to be around $150\,\mathrm{fb}^{-1}(40\,\mathrm{fb}^{-1})$ for choices of parameters $\lambda_1 = \lambda_2$ ($\lambda_1 = 2\lambda_2$). The vertical line corresponds to the luminosity used for this analysis and demonstrates the inadequacy of statistics for a luminosity of $30\,\mathrm{fb}^{-1}$.

15.6. Same sign top

At the LHC dileptonic $t\bar{t}(+jets)$ events can be selected with a relatively high signal-to-noise ratio and efficiency. Within the clean sample of such events, both leptons (electrons and muons) have an opposite electric charge. In several models beyond the Standard Model however, $tt/\bar{t}\bar{t}(+jets)$ topologies are predicted where both leptons have an equal electric charge. The signal excess is highly enhanced by the application of a combined likelihood variable described in [284]. The likelihood variable is designed to differentiate the lepton from the W boson decay from leptons arising for example in QCD jets or from fake reconstructions. The signal of new physics can be diluted by the mis-identification of the electric charge of the leptons in Standard Model $t\bar{t}(+jets)$ events and the mis-identification of the leptons from the W decay themselves. The observability of an excess of same-sign signals above

Table 15.7. Overview of the selection criteria applied on the events using simulated events with pile-up collisions included. The expected number of events are rescaled to a dataset of 1 fb^{-1} taking into account the respective Leading-Order cross-sections of the processes.

	$\mu\mu$	μe and ee	$t\bar{t} \to \tau + X$	Other $t\bar{t}$	$W^{\pm}W^{\mp}$	$Z + jets$	S/N
Before selection	6915.0	20745.0	34606.2	485973.2	189951.7	578033.3	0.0078
Trigger	6114.7	16314.8	17415.6	100137.2	41288.4	266366.7	0.017
Two jets $E_T > 25$ GeV	4398.2	11982.7	13560.9	93858.2	20593.8	66146.7	0.032
b-tag criteria	989.8	2485.4	2289.6	8784.7	133.5	240.0	0.13
Two leptons identified	888.2	30.1	375.8	801.6	1.7	73.3	1.30
Two leptons selected	481.5	0.07	48.4	3.01	0.4	53.3	4.7
Efficiency (in %)	6.96	0.0003	0.14	0.0006	0.00022	0.0092	
Opposite-sign	481.3	0	48.3	2.19	0	53.3	
Same-sign	0.2	0.07	0.1	0.82	0.4	0	
	ee	μe and $\mu\mu$	$t\bar{t} \to \tau + X$	Other $t\bar{t}$	$W^{\pm}W^{\mp}$	$Z + jets$	S/N
Before selection	6915.0	20745.0	34606.2	485973.2	189951.7	578033.3	0.0078
Trigger	5354.8	17074.7	17415.6	100137.2	41288.4	266366.7	0.015
Two jets $E_T > 25$ GeV	3960.9	12420.0	13560.9	93858.2	20593.8	66146.7	0.029
b-tag criteria	802.7	2672.4	2289.6	8784.7	133.5	240.0	0.11
Two leptons identified	724.5	34.6	453.8	2283.6	73.1	126.7	0.57
Two leptons selected	285.0	0.3	37.5	5.2	0.8	53.3	3.1
Efficiency (in %)	4.12	0.0013	0.11	0.0011	0.00044	0.0092	
Opposite-sign	279.6	0.3	36.8	4.1	0.4	46.7	
Same-sign	5.4	0	0.7	1.1	0.4	6.7	
	$e\mu$	$\mu\mu$ and ee	$t\bar{t} \to \tau + X$	Other $t\bar{t}$	$W^{\pm}W^{\mp}$	$Z + jets$	S/N
Before selection	13830.0	13830.0	34606.2	485973.2	189951.73	578033.3	0.016
Trigger	10960.0	11469.5	17415.6	100137.2	41288.4	266366.7	0.030
Two jets $E_T > 25$ GeV	8021.8	8359.1	13560.9	93858.2	20593.8	66146.7	0.061
b-tag criteria	1682.7	1792.5	2289.6	8784.7	133.5	240.0	0.25
Two leptons identified	1500.6	66.4	822.1	3001.6	30.2	20.0	0.88
Two leptons selected	722.7	0.9	85.2	6.3	0.4	0	8.3
Efficiency (in %)	5.23	0.0065	0.25	0.0013	0.00022	0	
Opposite-sign	715.5	0.9	83.8	4.9	0	0	
Same-sign	7.2	0	1.3	1.4	0.4	0	

the mis-reconstruction of the Standard Model background is determined. The details of the analysis are mentioned in [758].

The jets in the final state are reconstructed with an Iterative Cone jet clustering algorithm using a cone size of $\Delta R = 0.5$. Input objects for the cones are selected from all calorimeter towers above a pseudo-rapidity dependent energy threshold determined from the average underlying event energy deposits [165]. The energy scale of the reconstructed jets is calibrated with corrections from Monte Carlo studies. The primary vertices in the proton bunch crossing are determined, and the vertex with the highest transverse momentum is taken as the one of the hard scattering. Via a track-based algorithm, jets are rejected if they do not match with this hard primary vertex.

The leptons are reconstructed and identified using the methods described in [284]. A likelihood variable is used to suppress leptons from the heavy flavour quark background exploiting several reconstruction aspects of leptons in the CMS detector. This likelihood is determined for each muon or electron in the final state in order to enhance the purity of choosing the correct lepton from the leptonic W decay. The combined likelihood

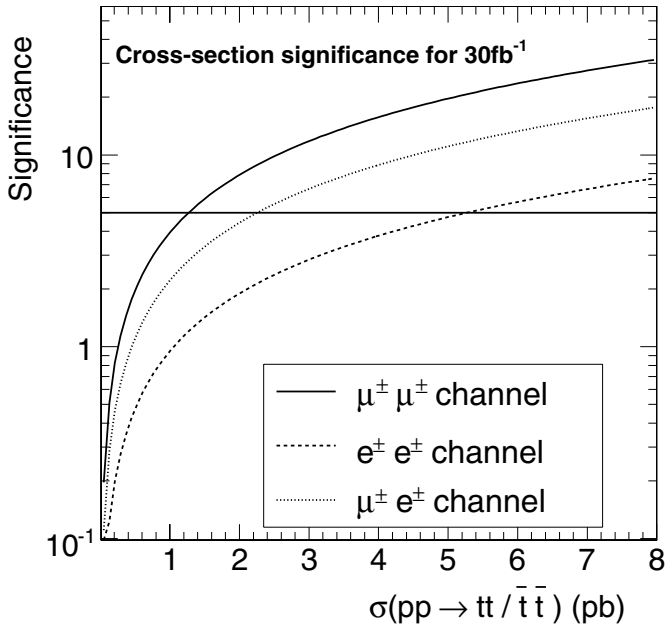

Figure 15.9. For an integrated luminosity of 30 fb^{-1} the significance of the same-sign tt or $\overline{t}\overline{t}$ excess above the Standard Model events is indicated as a function of the cross-section of the inclusive process $pp \rightarrow tt/\overline{t}\overline{t}$.

includes observables as tracker isolation, calorimeter isolation, vertex matching significance, transverse momentum of the lepton and angular distance to the closest jet. For the electron likelihood a variable reflecting the reconstruction quality is added. The two muons or electrons having the largest combined likelihood ratio value are taken as the hard leptons of interest.

The inclusive single-muon, single-electron, double muon and double electron triggers are applied as described in [506]. The event should be triggered in at least one of these streams. In total 88.4%, 77.4% and 79.2% of respectively the $\mu\mu$, the ee and the μe signal events remain after applying the trigger criteria. The event is required to have at least 2 jets with a calibrated E_{T} above 25 GeV. These jets need to have a pseudo-rapidity in the range $|\eta| < 2.4$ and a b-tag discriminant larger than 0.5 [157]. The reconstructed hard leptons are required to have transverse momentum p_{T} exceeding 25 GeV/c in the pseudo-rapidity range of $|\eta| < 2.4$ and a combined likelihood variable larger than 0.05.

In Table 15.7 the efficiencies and signal-to-noise ratios are shown after each selection step. Applying all cuts a signal-to-noise ratio of 4.7, 3.1 and 8.3 is obtained for respectively the $\mu\mu$, the ee and the $e\mu$ final state. Cross-talk between these three considered final states is by construction not possible. As the amount of selected WW and $Z + jets$ events in Table 15.7 is small, their contribution is alternatively estimated by multiplying the efficiencies of the event selection without the b-tagging and the individual b-tagging selection cut efficiency under the assumption that both selection cuts are uncorrelated.

It is illustrated [758] that from the selected topology of dilepton $t\bar{t}$ events, a ratio $R = \frac{N_{++,--}}{N_{+-}}$ can be determined which is sensitive to physics beyond the Standard Model. In the ratio the total amount of events with equally charged leptons is divided by the total amount of events with opposite charged leptons. As the efficiency of reconstructing the leptons electric charge is very high, we can neglect the amount of selected $pp \rightarrow tt$ or $pp \rightarrow \overline{t}\overline{t}$

events observed with two opposite-charged leptons. Using the uncertainty on the ratio R, the significance of the observation of new physics channels $pp \to tt$ or $pp \to \overline{tt}$ is determined as a function of the cross section (see Fig. 15.9). The dimuon channel has a larger sensitivity compared to the decay channels with electrons. This is caused by the electron reconstruction where a large fraction of electron energy clusters are matched with a wrong track resulting in a charge ambiguity.

It is assumed that the new physics processes beyond the Standard Model have a similar kinematic topology compared to the $t\bar{t}$ process, therefore the selection efficiency of the new physics channels is taken equal to that of the Standard Model $t\bar{t}$ process. Several models predict an excess of events with same-sign leptons in this topology, via the process $pp \to tt/\overline{tt}$ or $pp \to tt/\overline{tt} + b/c$. These models are motivated by Flavour Changing Neutral Currents (FCNC) [759,760], topcolour-assisted Technicolour (TC2) [761] or supersymmetry [762]. With a measurement of R these kinematically similar processes $pp \to tt/\overline{tt}$ can be observed with 30 fb^{-1} of integrated luminosity if they have a cross section above 1 pb. Because a ratio of kinematically similar event topologies is measured, most of the experimental and theoretical systematic uncertainties cancel. The uncertainty of the background cross sections on the significances shown in Fig. 15.9 is found to be negligible. A feasibility study is performed to estimate the potential uncertainty on the mis-identification efficiency of the electric charge of electrons and muons from Z boson decays [758]. The effect on the significance of the excess of $tt/\overline{tt}$ events is found to be negligible.